

University of Nottingham
UK | CHINA | MALAYSIA

Continuous Synthesis and Characterisation of Layered Double Hydroxide Nanomaterials for their Application for Dye Wastewater Remediation

Ian Clark MEng

Thesis submitted to the University of Nottingham for the degree of Doctor of Philosophy

May 2018

Abstract

The first part of this research was aimed to improve continuous synthesis of LDHs through a matrix of experiments that investigated the influence of key factors affecting synthesis. These factors; temperature, pressure and reactant concentration were investigated for $Ca_2Al\text{-}NO_3$ LDHs. Alteration of reaction temperature and pressure caused changes to crystal domain length (CDL). As temperature was increased, tune-ability through pressure manipulation was lessened. The effect of the NaOH concentration in the precipitation reaction was found to have an impact on CDL. The highest NaOH concentration was found to produce smaller domain lengths. The initial excess of OH^- causes nucleation of crystals to occur preferentially over sustained growth. High NaOH content caused $Ca(OH)_2$ and $Ca_2Al\text{-}CO_3$ contamination, due to an excess of Ca^{2+} in the precursors and excess NaOH in the reaction. The presence of the impurities alter the chemical makeup of the compounds and the thermal properties. The effect of the changes to CDL was not realised in the other physical characteristics of the LDH, as platelet size remained at an average 2-5μm with no trend corresponding to CDL variations. Specific surface area (S_{BET}) also showed no change in relation to CDL variation or the modification of reaction temperature, pressure or precursor NaOH.

Scale up synthesis of LDHs focused on $Zn_2Al\text{-}CO_3$. Reactions to produce $Zn_2Al\text{-}CO_3$ were carried out at bench, pilot and industrial scale. All variables were kept constant, bar the reactor size and the flow rate. The pilot scale reactor operated at 20-30 times greater than bench scale. The pilot scale LDH exhibited greater CDL, this was attributed primarily to a settling period post-reaction, where the suspension was allowed to settle in the reaction liquor. Platelet diameter increased from 120nm at bench to 177nm at pilot scale and 165nm at industrial scale. The changes to particle size do not correspond

with changes to S_{BET}. Surface area decreased from 58m^2 g^{-1} to 50m^2 g^{-1} between bench and pilot synthesis but the surface area was recorded at 64,1m^2 g^{-1} for the industrial Zn_2Al-CO_3 Industrial synthesis produced a Zn_2Al-CO_3 LDH with CDL (19nm) comparable to the bench scale sample (18nm) but smaller than the pilot scale sample (26nm).

Zn_2Al-CO_3 LDHs for remediation of a synthetic dye was carried out on two types of reactive dye. The LDH was calcined and the resulting mixed metal oxide (MMO) was characterised. Calcination caused an increase in S_{BET} from 50m^2 g^{-1} to 57m^2 g^{-1}. Wet storage of the MMO reformed the LDH crystal phase, partly after 2 weeks and completely after 6 weeks. Adsorption of dye was best modelled by the Langmuir isotherm. The fit of the isotherm model was reduced as adsorption temperature was increased, due to inhibited uptake of dye at low initial concentration (C_0). The maximum uptake capacity (q_m) at 293K, was 589mg g^{-1} and 895mg g^{-1} for Reactive Black 5 and Reactive Orange 16, respectively. Adsorption was also modelled kinetically by a pseudo 2nd order model. Investigation of the impact of competing anions found that, Cl^- had no effect on adsorption of either dye molecule, however addition of Na_2CO_3 and Na_2SO_4 inhibited adsorption. Thermal regeneration of the adsorbent significantly reduced the adsorption capacity in subsequent cycles. Washing with Na_2CO_3 prior to re-calcination mitigated the effect of regeneration. Breakthrough curves were fit with the Yoon-Nelson and Thomas models best, while the Adams-Bohart model was not appropriate. The adsorption capacity (q_e) from the Thomas model was between 7.2mg g^{-1} and 7.6mg g^{-1}, which is considerably lower compared with the batch scale Langmuir q_m value. The reduction is attributed to a number of factors. The empty bed contact time was not enough to allow the adsorption to occur completely and breakthrough occurred after the first, timed sample. The presence of the PMMA in the granules may block adsorption sites also bind the particles, inhibiting the ability to expand and reform LDH layers with the dye

molecules in the interlayer gallery. PMMA is also a hydrophobic which will contribute to a reduced interface between the MMO surface and the adsorbate solution.

Continuous synthesis of LDH composites was carried out in a two-stage reactor system. The core@shell composites were designed to combine properties of the core with the adsorptive capacity of LDHs. For this research ZnO was chosen as the core material due to its photocatalytic capabilities, and $Mg_2Al\text{-}CO_3$ was chosen for the shell, due to the large $Ca_2Al\text{-}NO_3$ particles. $Zn_2Al\text{-}CO_3$ would be difficult to distinguish from the ZnO in chemical analysis. The composite exhibited reflections relating to both ZnO and the $Mg_2Al\text{-}CO_3$ in the diffractogram. The S_{BET} of the composite ($75 m^2 g^{-1}$) was greater than each of the individual materials and a dry mixture of LDH and ZnO powders. There is a reduction in Mg/Al ratio of the LDH from 2:1 to closer to 1:1. This was first attributed to the potential for $Zn_2Al\text{-}CO_3$ LDH production in the second reactor from residual Zn^{2+} ions or dissolution of ZnO. However, further examination of synthesis in the second reactor indicated that NaOH concentration has a dramatic effect on $Mg(OH)_2$ precipitation. Low NaOH caused $Al(OH)_3$ to be prevalent in the brucite-like sheets. This may phenomenon may occur in composite synthesis. Increased $Al(OH)_3$ distorts the layers and caused an increase in S_{BET} to $250 m^2 g^{-1}$. The synthesis of ZnO@LDH composite materials was partially successful as there appears to be some degree of bonding between ZnO cores and $Mg_2Al\text{-}Co_3$ LDH shells. However, more work to fine tune continuous composite synthesis is required, as there is in some instances a mixture of LDH and ZnO nanoparticles that are not part of a composite material.

Publications

Clark, I., Dunne, P. W., Gomes, R. L., Lester, E., Continuous hydrothermal synthesis of $Ca_2Al\text{-}NO_3$ layered double hydroxides: The impact of reactor temperature, pressure and NaOH concentration on crystal characteristics. Journal of Colloid and Interface Science **2017**, 504, 492-499.

Orla Williams, Ian Clark, Rachel Gomes, Tania Perehinec, Jon L Hobman, Dov J Stekel, Robert Hyde, Chris Dodds, Edward Lester, Metal removal from cattle footbath waste water with Layered Double Hydroxide (LDH) adsorbents as a method of Antimicrobial Resistance (AMR) Mitigation on Dairy Farms, *Journal of Cleaner Production*, **2018.** Under review.

Peter Dunne, Edward Lester, Chris Starkey, Ian Clark, The Chemistry of Continuous Hydrothermal/Solvothermal Synthesis of Nanomaterials, Andrew J. Hunt, Thomas M. Attard (Eds), Supercritical and Other High-pressure Solvent Systems for Extraction, Reaction and Material Processing, Royal Society of Chemistry, **2018.** Under review

Conference Contributions

Clark, I., Gomes, R.L., Lester, E. Environmental Applications of Nanomaterials for Wastewater Effluents. University of Nottingham Sustainable Research Symposium. June 15th 2015. Poster Presentation

Clark. I., Gomes. R. L., Tran. T. H. H., Archibald, V., Somerfield. C., Bradley. L. Analysis of Heavy Metals in Canal Sediments to Gain a Better Insight into Current and Future Canal Management Strategies. XV IWRA World Water Congress. May 25th-29th 2015, Edinburgh, Scotland. Oral Presentation

Clark, I., Gomes, R.L., Lester, E. Continuous synthesis of Calcium-aluminium layered double hydroxides for CO_2 adsorption. International Conference on Coal Science and Technology, September 27th – October 1st 2015, Melbourne, Australia

Acknowledgements

I would like to express a huge amount of gratitude towards Dr Rachel Gomes and Prof Ed Lester for their guidance, advice and support as supervisors throughout my studies.

Some special thanks goes to Dr Peter Dunne. Pete helped me with a lot of information and training in the early stages of my PhD and helped by co-authoring my first research publication. My thanks also go to the staff at Promethean Particles Ltd. for allowing me access to large scale production facilities and for help during pilot and industrial scale synthesis reactions. I am indebted to Dr Thomas Huddle, Dr Christopher Starkey, Dr Pablo Caramazana Gonzalez and Ammar Alatta for their support and input into my studies, during our time together as colleagues. A number of other acknowledgements go to Dr Nigel Neate for training in X-ray diffraction and electron microscopy techniques, Vikki Archibald for analysis with ICP-OES and AAS. Mr Martin Roe for training with SEM training. Dave Mee for training with thermal analysis methods. My appreciation also goes to the University of Nottingham and the EPSRC for funding of this PhD and part funding by the European Union's Seventh Framework Programme (FP7/2007–2013), grant agreement no. FP7-NMP4-LA-2012-280983, SHYMAN.

I cannot thank my family enough for their continued support during the more difficult periods of my studies. My mum and dad have helped and supported me in all my decisions, both good and bad. My brother Andrew for keeping me grounded. Finally, I am most grateful to Kate, for putting up with my ups and downs over the last 9 years.

Table of Contents

Abstract i

Publications iv

Conference Contributions iv

Acknowledgements vi

Table of Contents vii

List of Figures xii

List of Tables xvii

List of Abbreviations xx

1. Introduction 1

1.1 Thesis Overview 1

1.2 Research Background 2

1.3 Thesis Aim and Objectives 4

2. Literature Review 6

2.1 The Importance of Water and Wastewater 6

2.1.1 The Water Cycle and Wastewater 6

2.1.2 European Water Legislation and Priority Substances 7

2.2 Textiles and Synthetic Dyes in Water 8

2.2.1 Basics of Textile Dyeing Processes 8

2.2.2 Economic Trends in Textile Dyeing 12

2.2.3 Dyes in the Environment 12

2.2.4 Dye Toxicity 13

2.3 Wastewater Treatments for Dye Wastewater 14

2.3.1 Biological Remediation of Dye Wastewaters 14

2.3.2 Chemical Treatment of Dye Wastewaters 16

2.3.3 Physical Treatment of Dye Wastewaters 24

2.4 Synthesis of Layered Double Hydroxides 49

2.4.1 Co-precipitation Synthesis of Layered Double Hydroxides 49

2.4.2 Separate Nucleation and Ageing Steps Methods for the Synthesis of Layered Double Hydroxides 51

2.4.3 Reverse Micro-emulsions and Aqueous Miscible Organic Solvent Treatment of Layered Double Hydroxides 51

2.4.4 In-Line Dispersion Precipitation Synthesis of Layered Double Hydroxides 53

2.4.5 Hydrothermal Synthesis of Layered Double Hydroxides 54

2.5 Background on the Continuous Hydrothermal Synthesis of Nanoparticles 57

2.5.1 Theory and Reactor Design at Nottingham 57

2.6 Summary 62

3. Materials and Methods 65

3.1 Nanoparticle Synthesis 65

3.1.1 Reagents and Chemicals 65

3.1.2 Continuous Hydrothermal Synthesis Layered Double Hydroxides 65

3.1.3 Pilot and Industrial Scale Synthesis of Layered Double Hydroxides 67

3.1.4 Continuous Hydrothermal Synthesis Zinc Oxide Nanoparticles 68

3.1.5 Continuous Hydrothermal Synthesis of Metal Oxide@Layered Double Hydroxide Core-Shell Nanocomposites 69

3.1.6 Materials Characterisation 71

3.2 Adsorption of Reactive Dyes onto LDHs 81

3.2.1 Batch Experimentation 81

3.2.2 Continuous Experimentation 88

4. Results and Discussion: Continuous Hydrothermal Synthesis of Layered Double Hydroxides 95

4.1 Introduction 95

4.2 Highlights 96

4.3 Continuous Synthesis of $Ca_2Al\text{-}NO_3$ 96

4.3.1 Experimental Conditions 96

4.3.2 Effect of Temperature and Pressure on Crystal Characteristics 100

4.3.3 Effect of Temperature and Pressure on Surface Area Characteristics 107

4.3.4 Effect of Temperature and Pressure on Structural and Chemical Characteristics 110

4.3.5 Effect of Initial Sodium Hydroxide Concentration on Crystal Characteristics 114

4.3.6 Effect of Initial Sodium Hydroxide on Surface Area Characteristics 118

4.3.7 Effect of Initial Sodium Hydroxide on Structural and Chemical Characteristics 120

4.4 Continuous Synthesis of $Zn_2Al\text{-}CO_3$ 122

4.4.1 Experimental Conditions 122

4.4.2 Crystal and Particle Characteristics of $Zn_2Al\text{-}CO_3$ 122

4.4.3 Surface and Characteristics Chemical of $Zn_2Al\text{-}CO_3$ 125

4.5 Summary 129

5. Results and Discussion: Scaling Synthesis of $Zn_2Al\text{-}CO_3$ Layered Double Hydroxides 131

5.1 Introduction 131

5.2 Highlights 132

5.3 Reaction Conditions and Flow Regimes 132

5.4 Materials Characterisation 133

5.4.1 X-ray Diffraction and Changes to Crystal Structure with Increasing Scale 133

5.4.2 Chemical Structure and Morphology 136

5.4.3 Surface Area 141

5.5 Summary 143

6. Results and Discussion: Adsorption of Reactive Dyes onto Calcined $Zn_2Al\text{-}CO_3$ Layered Double Hydroxides 145

6.1 Introduction 145

6.2 Highlights 146

6.3 Calcination of $Zn_2Al\text{-}CO_3$ and Characterisation of Mixed Metal Oxide Adsorbent 146

6.3.1 X-Ray Diffraction and Crystal Structure 146

6.3.2 Surface Area, Topography and Particle Size Distribution Analysis 148

6.4 Stability of $Zn_2Al\text{-}CO_3$ and Calcined Adsorbent (MMO) 152

6.4.1 Stability of Calcined Adsorbent (MMO) and Reference $Zn_2Al\text{-}CO_3$ in Air 153

6.4.2 Stability of Calcined $Zn_2Al\text{-}CO_3$ (MMO) and Reference $Zn_2Al\text{-}CO_3$ in Water 154

6.5 Batch Adsorption of Reactive Orange 16 156

6.5.1 Effect of Initial pH on Adsorption 156

6.5.2 Effect of Adsorbent Dose 157

6.5.3 Effect of Adsorption Temperature on Reaction Kinetics 159

6.5.4 Adsorption Isotherms 165

6.5.5 Thermodynamics of Adsorption of Reactive Orange 16 169

6.5.6 Effect of Competing Anions 171

6.6 Batch Adsorption of Reactive Black 5 173

6.6.1 Effect of Initial pH on the Adsorption of reactive Black 5 173

6.6.2 Effect of Adsorbent Dose 174

6.6.3 Effect of Adsorption Temperature on Reaction Kinetics 176

6.6.4 Adsorption Isotherms 181

6.6.5 Thermodynamics of Adsorption of Reactive Black 5 184

6.6.6 Effect of Competing Anions 186

6.6.7 Adsorbent Regeneration 187

6.6.8 Proposed Adsorption Mechanism 190

6.7 Column Adsorption of Reactive Black 5 192

6.7.1 Adsorbent Granulation – Mechanical stability in water 192

6.7.2 Breakthrough Curve Models 194

6.8 Summary 201

7. Continuous Hydrothermal Synthesis of Metal Oxide@Layered Double Hydroxide Composite Nanomaterials 205

7.1 Introduction 205

7.2 Highlights 206

7.3 Two Stage Counter-Current Reactor Experiments: Composite Synthesis 206

7.3.1 Crystal Structure of ZnO, $Mg_2Al\text{-}CO_3$ and ZnO@$Mg_2Al\text{-}CO_3$ Composite .. 207

7.3.2 Morphology and Particle Size of ZnO, $Mg_2Al\text{-}CO_3$ and ZnO@$Mg_2Al\text{-}CO_3$ Composite 209

7.3.3 Electrochemical Analysis and Band Gap Calculation 213

7.3.4 Surface Area Analysis of ZnO, LDH and ZnO@LDH Composite 215
7.3.5 Chemical Analysis Nanoparticle Materials 218
7.3.6 Thermal Degradation of ZnO, Mg_2Al-CO_3 and Composite Materials 219
7.4 Deconvolution of Reactions in the Two-Stage System 221
7.4.1 Changes to Reaction Flow and Reactor Geometry in LDH Synthesis 224
7.4.2 Effect of Residual Precursor Ions on LDH Synthesis 227
7.5 Summary 233
8. Conclusions and Recommendations for Further Research 236
8.1 Summary of Research and Conclusions 236
8.1.1 Synthesis and Characterisation of LDHs 236
8.1.2 Scale Up of LDH Synthesis 238
8.1.3 Adsorption of reactive Dyes on Calcined LDHs 239
8.1.4 Continuous Synthesis of Zinc Oxide@LDH Composites 241
8.2 Recommendations for Further Research 242
8.2.1 Continuous Synthesis of Layered Double Hydroxides 242
8.2.2 Layered Double Hydroxide Based Adsorbents for Dye Remediation 243
8.2.3 Layered Double Hydroxide Composite Materials 244
References 246
Appendix 268

List of Figures

Figure 2.1 Schematic of the urban water cycle. Taken from Gessner *et al* (2014) [39].... 7

Figure 2.2 Degradation of a) Congo red to organic intermediates including b) benzidine 14

Figure 2.3 Schematic of hydroxyl and super oxide radical formation on the surface of a semiconducting metal oxide photocatalyst 19

Figure 2.4 Layered double hydroxide structural schematic 33

Figure 2.5 Schematic demonstrating the Memory Effect 34

Figure 2.6 Chemical Structure of (a) high molecular weight Evans Blue and (b) low molecular weight methyl orange 38

Figure 2.7 Structure of sodium dodecyl sulfate (SDS) 39

Figure 2.8 a) Water phase diagram approaching the critical region b) Selected properties of sub and super critical water (adapted from Dunne *et al* [12]) 58

Figure 2.9 Pipe-in-pipe counter-current reactor design from the University of Nottingham. Image adapted from Lester *et al* (2006) [176] 60

Figure 2.10 (a) LAI steady state concentration map of the Nozzle Reactor (b) steady state CFD simulation calculated using FLUENT. Both simulations at flow rates of 10ml min^{-1} and 5ml min^{-1} for supercritical water and aqueous metal salt respectively. Used with permission from Lester *et al* (2006) [176]. 60

Figure 3.1 Continuous Hydrothermal synthesis schematic a) reactor system b) technical drawing c) bench scale reactor d) pilot scale reactor 66

Figure 3.2 Computer generated image of the industrial scale SHYMAN reactor system 68

Figure 3.3 Sequential reactor system for core-shell nanocomposites 69

Figure 3.4 Schematic diagrams of reaction arrangements for a) $Mg_2Al\text{-}CO_3$ ($LDH_{initial}$) b) ZnO and c) ZnO@LDH composite synthesis 70

Figure 3.5 Schematic detailing symmetric Bragg reflection [218] 71

Figure 3.6 Schematic diagram of a) Unit cell and lattice parameters b) Repeating unit cells in a crystal lattice [218] 72

Figure 3.7 Schematic of a Scanning Electron Microscope 76

Figure 3.8 Kα generation in Electron Dispersive X-ray Spectroscopy 77

Figure 3.9 Schematic of an imaging column in a transmission electron microscope (TEM) 78

Figure 3.10 Schematic of direct (a) and indirect (b) electron transitions. Adapted from Numai (2015) [223] 80

Figure 3.11 Chemical Structure of Reactive Dyes 81

Figure 3.12a) Annotated schematic showing tube diameter, length and column packing (annotations shown in inches), b) Photograph of adsorption column, pump and wastewater source 90

Figure 3.13 Typical breakthrough curve shape labelled with breakthrough and exhaustion points and the mass transfer zone (MTZ) in a packed column [89] 92

Figure 4.1 Isobaric changes in water density and viscosity with temperature [242] 97

Figure 4.2 X-Ray diffractograms for $Ca_2Al\text{-}NO_3$ LDHs produced at 348K and different pressures 100

Figure 4.3 X-Ray diffractograms for $Ca_2Al\text{-}NO_3$ LDHs produced at 373K and different pressures 101

Figure 4.4 X-Ray diffractograms for $Ca_2Al\text{-}NO_3$ LDHs produced at 423K and different pressures 101

Figure 4.5 X-Ray diffractograms for $Ca_2Al\text{-}NO_3$ LDHs produced at 473K and different pressures 102

Figure 4.6 Schematic of NO_3^- alignment in $Ca_2Al\text{-}NO_3$ layers. Adapted from Renaudin and François [244] 104

Figure 4.7 Effect of changes in pressure on the crystal domain length (CDL) of $Ca_2Al\text{-}NO_3$ (n=2) 105

Figure 4.8 Electron Micrographs of $Ca_2Al\text{-}NO_3$ a) TEM b) SEM 110

Figure 4.9 Thermal Analysis of $Ca_2Al\text{-}NO_3$ samples of produced under varying temperatures and pressures a) 348K b) 373K c) 423K d) 473K 113

Figure 4.10 Diffractograms of $Ca_2Al\text{-}NO_3$ produced at 348K – ($Ca(OH)_2$ – ▼, $Ca_2Al\text{-}CO_3$ – ✶) 115

Figure 4.11 Diffractograms of $Ca_2Al\text{-}NO_3$ produced at 373K ($Ca(OH)_2$ – ▼, $Ca_2Al\text{-}CO_3$ – ✶) 116

Figure 4.12 Changes in Crystal Domain Length with increasing NaOH concentration (n=2) 117

Figure 4.13 Thermal analysis of $Ca_2Al\text{-}NO_3$ with varying initial NaOH concentration, at different temperatures a) 348K b) 373K 120

Figure 4.14 X-Ray diffractogram of continuously produced $Zn_2Al\text{-}CO_3$ with reference points of published $[Zn_4Al_2(OH)_{12}](CO_3)\cdot 4H_2O$ reflections [256] 123

Figure 4.15 TEM micrograph of $Zn_2Al\text{-}CO_3$, inset high resolution image with lattice fringes visible 124

Figure 4.16 Particle size distribution of $Zn_2Al\text{-}CO_3$ LDHs 125

Figure 4.17 Nitrogen adsorption isotherm for $Zn_2Al\text{-}CO_3$, inset - pore size distribution data....126

Figure 4.18 SEM micrograph of $Zn_2Al\text{-}CO_3$, inset low magnification image....128

Figure 5.1 X-ray diffractogram for bench (B-LDH), pilot (P-LDH) and industrial (I-LDH) samples....134

Figure 5.2 SEM micrographs of a) bench b) pilot c) industrial scale samples....138

Figure 5.3 TEM micrographs of a) bench b) pilot c) industrial scale samples....139

Figure 5.4 Platelet size distribution of bench (B-LDH) and pilot (P-LDH) samples, as calculated by image analysis of TEM micrographs....140

Figure 5.5 Nitrogen adsorption isotherms of bench (B-LDH) and pilot (P-LDH) samples. Inset image showing pore size distribution....142

Figure 6.1 Structure of Reactive Dyes used in adsorption experiments....145

Figure 6.2 X-ray diffractograms of $Zn_2Al\text{-}CO_3$ (LDH) and calcined $Zn_2Al\text{-}CO_3$ (MMO)....148

Figure 6.3 Nitrogen adsorption isotherm for $Zn_2Al\text{-}CO_3$ (LDH) and calcined $Zn_2Al\text{-}CO_3$ (MMO). Inset; pore size distribution calculated from the desorption branch of the isotherm....149

Figure 6.4 SEM micrograph of $Zn_2Al\text{-}CO_3$ (LDH)....151

Figure 6.5 SEM micrograph of calcined $Zn_2Al\text{-}CO_3$ (MMO)....151

Figure 6.6 TEM micrographs of $Zn_2Al\text{-}CO_3$ (a, b) and calcined $Zn_2Al\text{-}CO_3$ (c, d)....152

Figure 6.7 Changes in diffraction patterns and crystal structure of mixed metal oxide during dry storage and $Zn_2Al\text{-}CO_3$ (LDH)....153

Figure 6.8 Changes in diffraction patterns and crystal structure of mixed metal oxide during wet storage....154

Figure 6.9 Impact of the initial pH of solution on the adsorption of Reactive Orange 16 after equilibrium (C_0=1500mg L^{-1}; V_{dye}=50mL; adsorbent loading=1g L^{-1}; T=293K)....157

Figure 6.10 Effect of adsorbent dose on Reactive Orange 16 dye concentration and adsorption capacity (C_0=1500mg L^{-1}; V_{dye}=50mL; T=293K)....158

Figure 6.11 Linear pseudo 1st order kinetic model for the adsorption of Reactive Orange 16 (C_0=1500mg L^{-1}; V_{dye}=50mL; adsorbent loading=1g L^{-1})....160

Figure 6.12 Linear pseudo 2nd order kinetic model for the adsorption of Reactive Orange 16 (C_0=1500mg L^{-1}; V_{dye}=50mL; adsorbent loading=1g L^{-1})....163

Figure 6.13 Linear intra-particle diffusion model for the adsorption of Reactive Orange 16 (C_0=1500mg L^{-1}; V_{dye}=50mL; adsorbent loading=1g L^{-1})....164

Figure 6.14 Reactive Orange 16 isotherm data fitted with Langmuir and Freundlich models (V_{dye}=50mL; adsorbent loading=1g L^{-1})....166

Figure 6.15 Van't Hoff plot for the adsorption of Reactive Orange 16 170

Figure 6.16 Effect of additive compounds (Na_2CO_3, Na_2SO_4, NaCl) on the adsorption of Reactive Orange 16 (C_0=1500mg L^{-1}; V_{dye}=50mL; adsorbent loading=1g L^{-1}; T=293K) 172

Figure 6.17 Impact of the initial pH of solution on the adsorption of Reactive Black 5 after equilibrium (C_0=1500mg L^{-1}; V_{dye}=50mL; adsorbent loading=1g L^{-1}; T=293K) 174

Figure 6.18 Effect of adsorbent dose on Reactive Black 5 dye concentration and adsorption capacity (C_0=1500mg L^{-1}; V_{dye}=50mL; T=293K) 175

Figure 6.19 Linear pseudo 1st order kinetic model for the adsorption of Reactive Black 5 (C_0=1500mg L^{-1}; V_{dye}=50mL; adsorbent loading=1g L^{-1}) 176

Figure 6.20 Linear pseudo 2nd order kinetic model for the adsorption of Reactive Black 5 (C_0=1500mg L^{-1}; V_{dye}=50mL; adsorbent loading=1g L^{-1}) 179

Figure 6.21 Linear intra-particle diffusion model for the adsorption of Reactive Black 5 (C_0=1500mg L^{-1}; V_{dye}=50mL; adsorbent loading=1g L^{-1}) 181

Figure 6.22 Reactive Black 5 isotherm data fitted with Langmuir and Freundlich models (V_{dye}=50mL; adsorbent loading=1g L^{-1}) 182

Figure 6.23 Van't Hoff plot for the adsorption of Reactive Back 5 185

Figure 6.24 Effect of competing anions on the adsorption of Reactive Black 5 (C_0=1500mg L^{-1}; V_{dye}=50mL; adsorbent loading=1g L^{-1}; T=293K) 187

Figure 6.25 Adsorption of Reactive Black 5 after two modes of regeneration 188

Figure 6.26 Electron dispersive X-ray spectra of calcined Zn_2Al-CO_3 (MMO) and a regenerated MMO without Na_2CO_3 washing 189

Figure 6.27 Adsorption schematic illustrating the memory effect 191

Figure 6.28 X-ray diffractograms of Fresh LDH and exhausted LDH following RB5 and RO16 adsorption at 293K 192

Figure 6.29 Breakthrough curves of adsorption of Reactive Black 5 (C_0=500mg L^{-1}) .. 195

Figure 6.30 Linear Adams-Bohart breakthrough models at different flowrates (C_0=500mg L^{-1}) 198

Figure 6.31 Linear Thomas breakthrough models at different flowrates (C_0=500mg L^{-1}) 199

Figure 6.32 Linear Yoon-Nelson breakthrough models at different flowrates (C_0=500mg L^{-1}) 200

Figure 7.1 Reactor diagrams of ZnO@LDH composite synthesis with single phase ZnO and LDH ($LDH_{initial}$) 207

Figure 7.2 X-ray diffractograms of composite (ZnO@LDH) and single-phase ($LDH_{initial}$, ZnO) and mixed nanomaterials 208

Figure 7.3 Schematic detailing ZnO and LDH particle size measurement definitions..209

Figure 7.4 SEM micrographs a) ZnO, b) $LDH_{initial}$, c) ZnO@LDH and TEM micrographs d) ZnO, e) $LDH_{initial}$, f) ZnO@LDH.....211

Figure 7.5 Particle size distribution of $LDH_{initial}$ and ZnO compared with ZnO@LDH..212

Figure 7.6a) Reflectance and b) Kubelka-Munk function plots.....215

Figure 7.7a) Nitrogen adsorption isotherms and b) pore distribution plots.....216

Figure 7.8 Mass loss and derivative mass loss profiles of ZnO, LDHinitial and ZnO@LDH 219

Figure 7.9 Mass loss and derivative mass loss profiles of $LDH_{initial}$ and ZnO@LDH compared with $Zn_2Al\text{-}CO_3$ type LDH.....221

Figure 7.10 X-ray diffractograms of $LDH_{initial}$ ($Mg_2Al\text{-}CO_3$), ZnO@LDH composite and $Zn_2Al\text{-}CO_3$.....221

Figure 7.11 Schematic diagram experiments to establish product characteristics of $Mg_2Al\text{-}CO_3$ produced under different conditions in reactor 2 (R_2).....222

Figure 7.12 Diffractograms for LDHs with different Reynolds numbers in R_1 and R_2..225

Figure 7.13 Nitrogen adsorption isotherms of LDH samples produced in reactor 1 ($LDH_{initial}$) and reactor 2 (LDH_3).....226

Figure 7.14 SEM micrographs of a) $LDH_{initial}$ and b) LDH_3.....227

Figure 7.15 Diffraction patterns for isolation experiment LDH samples.....228

Figure 7.16 pH of Layered double hydroxide (LDH) and metal hydroxide phase precipitation. Adapted from A. de Roy et al [289] and V. Rives [148].....229

Figure 7.17 Nitrogen adsorption isotherms of LDH samples produced with 0.15mol L^{-1} and 0.25mol L^{-1} NaOH for residual a) Zn^{2+} b) NO_3^-.....231

Figure 7.18 SEM micrographs of displaying structural the difference between LDH_5 and LDH_6.....232

Figure 7.19 Mass loss profile of LDHs produced to isolate precursor effect.....233

List of Tables

Table 2.1 Dye classification and colour index examples 10

Table 2.2 Dye and chemical oxygen demand (COD) removal by chemical and advance oxidation processes 22

Table 2.3 Chemical Oxygen Demand and Colour Removal, Data from Kim *et al* (2005) [87] 26

Table 2.4 Mixed metal oxide (MMO) uptake capacity of Acid Orange 52 38

Table 2.5 Adsorption capacity of adsorbents and a variety of dye compounds 42

Table 2.6 Comparison of LDH based photocatalysts with advanced oxidation processes 47

Table 3.1 Conditions for continuous hydrothermal synthesis of Layered double hydroxides 67

Table 3.2 Dimensions for laboratory scale adsorption column 90

Table 3.3 Flowrates for column adsorption experiments 91

Table 4.1 Synthesis conditions for $Ca_2Al\text{-}NO_3$ samples 99

Table 4.2 Comparison of surface area (S_{BET}) and crystal domain length (CDL) at different temperatures and pressures 108

Table 4.3 Comparison of Surface Area (S_{BET}) and drying method 109

Table 4.4 Mean platelet diameter of $Ca_2Al\text{-}NO_3$ LDHs, under varying temperature and pressure 111

Table 4.5 Molecular ratio of metals in the $Ca_2Al\text{-}NO_3$ LDH materials under varying reaction conditions 114

Table 4.6 $Ca_2Al\text{-}NO_3$ platelet diameter with varying NaOH concentration 119

Table 4.7 The effect of varying precursor NaOH on the Ca/Al ratio of $Ca_2Al\text{-}NO_3$ 121

Table 4.8 Surface area and pore data for $Zn_2Al\text{-}CO_3$ LDH compared with literature 127

Table 4.9 Molecular content of Zn2Al-CO3 LDH 128

Table 5.1 Flowrate and yield of $Zn_2Al\text{-}CO_3$ with increasing synthesis scale 132

Table 5.2 Reynolds number (Re) of three scales of synthesis for pure water 133

Table 5.3 Crystal domain length (CDL) of scaled $Zn_2Al\text{-}CO_3$ LDH samples 135

Table 5.4 Molecular ratio data from SEM-EDS analysis of bench (B-LDH), pilot (P-LDH) and industrial (I-LDH) samples 137

Table 5.5 Surface area (S_{BET}) and average pore diameter of bench (B-LDH), pilot (P-LDH) and industrial scale (I-LDH) samples....143

Table 6.1 Specific surface are and pore diameter of LDH and MMO materials....150

Table 6.2 Crystal domain length (CDL) calculated for (*003*) and (*110*) reflection for uncalcined Zn_2Al-CO_3 in wet storage....155

Table 6.3 Kinetic rates for the adsorption of Reactive Orange 16....161

Table 6.4 Isotherm constants for adsorption of Reactive Orange 16....168

Table 6.5 Thermodynamic properties of the adsorption of Reactive Orange 16....171

Table 6.6 Percentage reduction of and Reactive Orange 16 (RO16) concentration with competing anions....173

Table 6.7 Kinetic rates for the adsorption of Reactive Black 5....178

Table 6.8 Isotherm constants for adsorption of Reactive Black 5....183

Table 6.9 Maximum uptake capacity of Reactive Black 5 onto selected adsorbents....184

Table 6.10 Thermodynamic properties of the adsorption of Reactive Black 5....185

Table 6.11 Percentage reduction of Reactive Black (RB5) concentration with competing anions....186

Table 6.12 Mechanical breakdown of adsorbent granules and Surface area characteristics....193

Table 6.13 Total adsorption and equilibrium adsorption capacity of Reactive Black 5....196

Table 6.14 Breakthrough curve model constants....198

Table 6.15 Yoon-Nelson 50% breakthrough (τ) parameters....201

Table 7.1 Lattice parameters of single phase and composite materials....208

Table 7.2 Platelet diameter calculated by image analysis of TEM micrographs nanomaterials....212

Table 7.3 Band Gap Energy of ZnO@LDH, ZnO and LDH and artificially mixed sample....214

Table 7.4 Surface area and pore diameter characteristics of ZnO, composite and LDH nanomaterials....217

Table 7.5 Molecular ratio of ZnO@LDH composite....218

Table 7.6 LDH samples and reaction conditions of deconvolution experiments....223

Table 7.7 Reynolds number and flow regime of counter reactors....224

Table 7.8 S_{BET} and pore characteristics of Mg_2Al-CO_3 synthesised in R_1 and R_2....225

Table 7.9 Molecular fraction of metals in LDH structures and residual metal content 229

Table 7.10 Surface are (S_{BET}) and pore size for samples isolating residual ions from ZnO synthesis 231

List of Abbreviations

AAS – Atomic Absorption Spectroscopy

BOD – Biological Oxygen Demand

CDL – Crystal Domain Length

CHS – Continuous Hydrothermal Synthesis

COD – Chemical Oxygen Demand

DTA – Differential Thermal Analysis

EBCT – Empty Bed Contact Time

EQS – Environmental Quality Standard

FWHM – Full Width at Half Maximum

ICP-OES – Inductively Coupled Plasma – Optical Omission Spectroscopy

LDH(s) – Layered Double Hydroxide(s)

RB5 – Reactive Black 5 Dye

RO16 – Reactive Orange 16 Dye

SBET – Specific Surface Area

SEM – Scanning Electron Microscopy

SEM-EDS – Scanning Electron Microscopy / Electron Dispersive X-ray spectroscopy

SHYMAN – Sustainable Hydrothermal Manufacturing of Nanomaterials

TGA – Thermogravimetric Analysis

UV-Vis – Ultra-violet and Visible light spectrophotometry

UWWTD – Urban Wastewater Treatment Directive

WFD – Water Framework Directive

XRD – X-ray Diffraction

1. Introduction

1.1 Thesis Overview

The work in this study is concentrated on a number of key areas. The overarching focus of the body of work is concerned with layered double hydroxides (LDHs). LDHs are an interesting nanomaterial that has been known of, and researched extensively since the 1970s; yet their usage in engineering applications is currently limited. Consequently, the main areas of development were: improving the understanding of continuous synthesis of the layered double hydroxide nanomaterials, their potential application in wastewater treatment, and scaling up of synthesis to make the material more industrially relevant. The second chapter in this thesis is a literature review. The literature review starts with an in-depth look at synthetic dyes, owing to their ubiquitous presence in global society as well as their potential recalcitrance in nature. The literature review also identifies current dye remediation technologies investigated, including the current application of LDHs for dye removal. The final section of the literature review outlines the most common LDH synthesis routes in literature and the potential for continuous hydrothermal synthesis as a means of production. Chapter 3 outlines materials used in this thesis and the experimental and analytical methods. This includes information about the experimental and analytical conditions as well as the theory behind the analytical techniques. Chapter 4 to Chapter 7 describes the results and discussion with, Chapter 4 detailing the synthesis of LDHs via continuous hydrothermal synthesis utilising of a matrix of experiments that examined the effect of changing reaction conditions. The reaction variables studied were temperature, pressure and precursor precipitant concentration. The impact of the variables was evaluated through the characterisation of the materials, looking at material purity, crystal and structural

variations. Chapter 4 also investigates the synthesis of a Zinc based LDH for the purposes of scale up of synthesis. Chapter 5 looks at the scaling up of continuous synthesis of $Zn_2Al\text{-}CO_3$ from bench to pilot scale and then industrial scale synthesis. The subsequent changes that occur as a result of increasing scale of flow rates and changing reactor geometries are evaluated as a function of LDH characteristics. Chapter 6 investigates the use of LDHs as adsorbents for synthetic textile dyes in both batch reactions where kinetic, thermodynamic and adsorption parameters are investigated, as well as column adsorption studies with the modelling of breakthrough curves. Chapter 7 explores the potential for continuous synthesis of core@shell composite nanomaterials using a two-stage reaction system. In this chapter the changing of flow and the effects of residual ions on the $Mg_2Al\text{-}CO_3$ LDH are examined, as well as the influence of a nanoparticle support, on LDH material characteristics, is studied. The experiments were explored with the intention of developing an understanding of the effects of the two-stage synthesis on shell material in the composite. Conclusions drawn and recommendations for further research are outlined in Chapter 8.

1.2 Research Background

Layered double hydroxides (LDHs) are a type of anionic clay that can be produced synthetically [1, 2]. The production of these materials has been researched extensively in small scale batch operations, and therefore, the application of them has been limited [3-7]. The most common form of batch synthesis encountered in published articles is co-precipitation synthesis. [1, 3, 4, 8, 9]. Continuous synthesis is generally accepted as an efficient way of manufacturing on an industrial scale, however continuous synthesis of LDHs is limited in literature The only published paper on continuous hydrothermal synthesis of LDHs, briefly outlines the potential for temperature and pressure

modification to tune the particle properties [10]. Continuous hydrothermal synthesis is more commonly applied to nanoparticle synthesis for ceramics [11, 12].

Remediation of synthetic dyes from textile wastewaters is a difficult task for rudimentary wastewater treatment methods. The recalcitrant nature of many dyes means that advanced treatment methods are required for treatment [13-16]. Left untreated, textile effluent will increase the chemical oxygen demand (COD) of the receiving waters as well as being unsightly. Activated carbon is the most common adsorbent used in tertiary water treatment [17] and is very common in the adsorption of dyes [18-20]. Membrane filtration and ion-exchange resins are highly selective and efficient for removal of dyes [21-24]. Strong anion-exchange resins are selective towards acidic dyes and are easy to regenerate with solvent washing. There are problems though with each of these remediation methods. All require high capital and operating costs to employ. Dye remediation by Layered double hydroxides has been investigated for acid class dyes, in particular methyl orange [25-28]. The vast array of dyes available for use and the growing application of reactive dyes means that this dye class is in need of research where LDHs are the adsorbent to better identify the potential for adsorption applications. LDHs have also been applied as photocatalysts for dye removal where Zn and Ti are constituent elements. Many Ti based LDHs exhibit the capacity for visible light photocatalysis [29-31]. Outside of binary and ternary LDH synthesis, development of core@shell composite materials for enhanced adsorption and other applications have been explored without further significant advances in terms of scaling up of synthesis or adsorption processes [32, 33].

Much of the previous literature regarding the remediation of dye compounds has focussed on either current treatment technologies utilising commercial activated carbons [19, 34], ion-exchange resins [21] and polymer nanofiltration membranes [23];

or a novel twist on a current technology, such as utilising innovative, low costs, carbon sources for activated carbon adsorbents [35, 36]. There has been advancement in terms of scaling of adsorption processes where activated carbons are concerned with published works from the turn of the last decade detailing breakthrough curve modelling for adsorption of acidic and basic dyes. The research utilising completely novel adsorbents is less common, however the adsorption capacity of many LDH based adsorbents overshadows that of activated carbon [37, 38] in batch studies. Despite the adsorption potential of LDHs however there has little progress in the field with respect to this type of adsorbent with no efforts to explore continuous adsorption modes.

1.3 Thesis Aim and Objectives

The aim of this research was to further develop an understanding of LDHs as a viable material for engineering applications with regards to wastewater remediation.

The specific objectives highlighted in order to achieve the research aim were:

1 Develop a better understanding of continuous hydrothermal synthesis of LDHs in order to better recognise the potential for tuneable synthesis of LDHs, by identifying reaction conditions and the impact they have on crystal and structural properties.

2 To utilise the reaction conditions for an LDH material that could be produced at increasing scale. Increased scale of production of LDHs from several grams per hour at bench scale to tens of kilograms in minutes at industrial scale would allow for more robust experimentation in terms of wastewater remediation applications.

3 Examine to the performance of continuously produced LDHs on the adsorption of synthetic dyes in batch and column adsorption modes and the effects of moving from a batch to continuous adsorption.

4 To expand the potential for LDHs to composite nanomaterials, in order to incorporate characteristics of both the core material as well as the shell LDH. By doing so in a two-stage, single process reaction system.

2. Literature Review

The following chapter is a review of published literature relevant to the subject areas in this thesis. The first part of the literature review is concerned with the importance of water, wastewater and textiles. The second part of the review discusses various treatment methods for removal of synthetic dyes, covering the broad topics of biological, chemical and physical remediation methods, including the application of layered double hydroxides (LDHs) for water treatment. The final part of the chapter is concerned the current state of literature regarding synthesis approaches to LDHs and background information into continuous hydrothermal synthesis of nanomaterials at the University of Nottingham.

2.1 The Importance of Water and Wastewater

2.1.1 The Water Cycle and Wastewater

Water is imperative for almost all complex life on earth, and fresh water is needed to sustain life on land. The water cycle demonstrates the importance of water to life and the continual renewal of clean fresh water sources. Such is the need for water that early human settlements were situated along natural water sources, most typically rivers, as the running water courses brought fresh water continuously and took away and waste. London on the Thames, Rome on the Tiber and Paris on the Seine are just a few examples of settlements situated on the banks of rivers that have grown, with the development of current society. With the development of technology and the industrial revolution transforming these settlements into manufacturing hubs, the need to remove waste became more prominent. That change in society brought the development of the urban

water cycle, much like the one outlined by Gessner *et al* in Figure 2.1 [39]. The urban water cycle accounts for municipal and industrial wastewater as well as the remediation and discharge of wastewater [39]. The manufacture of industrial products produced large amounts of potentially toxic waste. At the time of the revolution there was no conscious effort to reduce waste effluent into water courses, however now there is a more determined effort to remediate wastewater to a state as close to natural as economically possible.

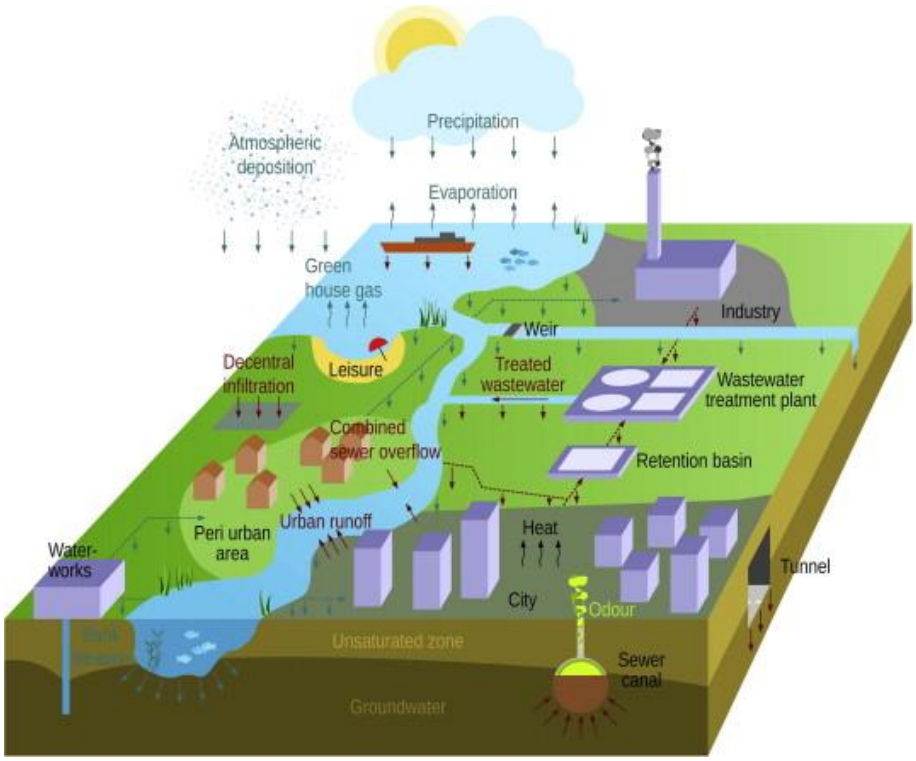


Figure 2.1 Schematic of the urban water cycle. Taken from Gessner *et al* (2014) [39]

2.1.2 European Water Legislation and Priority Substances

With the prominence of industrial and municipal wastewater governing bodies in economically developed countries have set out an array of legislative procedures and practices that must be adhered to. In the European Union (EU) these legislative documents fall under a number of directives with the most prominent including the

Water Framework Directive-2000/60/EC (WFD) [40], the Urban Wastewater Treatment Directive-91/271/EEC (UWWTD) [41] and Environmental Quality Standards in the field of water policy- 2013/39/EU (EQS) [42]. The EQS directive highlights priority substances with which special discharge limits are set. These discharge limits focus on well-known hazardous compounds including heavy metals, halogenated organic compounds such as chloromethanes as well as pesticides. The UWWTD also focussed heavily on industries that are energy intensive and produce large quantities of wastewater like those surrounding drinks manufacture. There is no mention of textile industries in the UWWTD, nor are complex dyes targeted in the EQS directive. The seemingly infinite selection of available synthetic dyes makes them difficult to target specifically. The low amount of textile manufacturing that occurs in the EU makes them lower priority and covered simply by Chemical Oxygen Demand (COD) limits. However, in many cases the materials utilised in textile manufacture can have both environmental and human impacts as dyed surface waters are unsightly. It is worth highlighting the fact that despite a lack of textile manufacture in Europe some of the largest and fastest growing economies rely heavily on the industry. Textile wastes including dye compounds can have significant impacts on the environment and daily life if untreated. There have been historic reports of large scale dye pollution from untreated discharge [43, 44].

2.2 Textiles and Synthetic Dyes in Water

2.2.1 Basics of Textile Dyeing Processes

The application of dyes to textile fibres occurs is a number of ways, but the most common are exhaust, continuous/padding and printing [45]. Exhaust dyeing is the most basic

process and involves the application the fibre substrate to a dye bath, movement of the dyeing liquid or the substrate then ensures uniform colour [45]. In exhaustive dyeing, the dye and substrate are allowed to reach a state of equilibrium, where the dye concentration in the dyeing liquid and on the fibre substrate remain relatively constant, at this stage the dyeing process is complete [45]. Exhaustive dyeing typically involves longer processing times than continuous modes as the adsorption, diffusion and fixation steps of the dyeing, where by the chemical and physical bonding between the dye and the substrate, all occur in the dyebath [45]. Continuous dyeing occurs via two main routes, either by spraying the dye onto the fabric, or by a continuous immersion of the textile fabric into a dyebath. Additional fixation steps may be required in all dyeing processes but particularly in continuous and print dyeing [45]. Despite the various methods available exhaust dyeing remains popular for mass colouring of fabrics due to simplicity and lower operating costs compared with continuous and print dyeing [45].

Depending on the type of textile substrate and the requirements of that substrate; different classes of dye may be used as detailed in Table 2.1. Cellulose fibres (Cotton) utilise the widest variety of dye classes while synthetic polyamide fibres are restricted to typically disperse, reactive, acidic and basic dyes [46]. In general acidic dyes are so named because of the low pH encountered during dyeing, while reactive dyes utilise elevated temperature and the addition of base to enhance fixation [46]. Reactive dyes are arguably the most desirable dyes for cellulose fibres, due to ease of application a superior fastness compared to direct dyes. Acidic dyes are a more than satisfactory in terms of fastness and applicability for polyamide fibres.

Table 2.1 Dye classification and colour index examples

Dye Class	Chemical/Structural properties	Substrate/Fibre	Example – Colour Index (C.I.) Dye	Reference
Direct	High molecular weight Anionic acid functional groups to increase water solubility	Cellulose	Direct Red 28	[45, 47]
Sulphur	Complex chemical structure Water insoluble	Cellulose	Sulphur Brown 1	[45]
VAT	Water insoluble Mechanically bound Carbonyl functional group	Cellulose	Vat Orange 9	[45, 47]
Azoic	Water insoluble Diazonium salts Coupling components	Cellulose	Azoic diazo component 5	[45, 47]
Reactive	Water insoluble Anionic functional groups	Cellulose Polyamide	Reactive Red 3	[45, 47]

Acidic	Reactive functional groups Anionic functional groups Water soluble Low Molecular weight	Protein Polyamide Protein Cellulose	Acid Orange 7	[45]
Basic	Cationic functional groups Water soluble	Polyamide Acrylic	Basic Green 4	[45]
Disperse	Low water solubility Low molecular weight Polar functional groups	Polyamide Polyester	Disperse Orange 25	[47]

The end result of many of these dyeing processes is that there is a wastewater stream with dissolved organic dye compounds [45, 46]. Dissolved dye increases the COD of wastewater streams. High COD levels present an environmental problem if the wastewater is released into surface waters untreated [17].

2.2.2 Economic Trends in Textile Dyeing

The economic landscape of the planet has been changing over the last few decades and developing countries have seen an influx of industry. One industry that has undergone the global shift to developing countries is the textile industry to nations such as China, India, Bangladesh and nations in the Mekong river basin [48]. These nations are now key suppliers in global apparel, as some sources list china as supplying as much as 50% of imports of the U.S. textile market [49], while information on 2012 trade statistics estimates China's net clothing and apparel exports at $160 billion, while India and Bangladesh contributed 14 and 20 billion dollars respectively [48]. International trade agreements as well as changing economic climates have also meant that nations in the Americas (Mexico and the Caribbean) are also contributing to textile trade, particularly in the US as geographical proximity favours trade [50]. The processes involved in traditional textile manufacturing face a number of challenges from meeting commercial demand to increasingly stringent regulations regarding the impact of textile industries on the environment.

2.2.3 Dyes in the Environment

Increased oxygen demand as a result of untreated dye wastewater effluent being discharged into surface water poses environmental problems that amount to more than having coloured fresh water bodies. As much as 15% of dye used in the colouring

processes can be lost [51], while other estimates put dye loss at 9% [52] and reactive dyes can have dye loss rates of 10-50% [53]. The volume of dyeing liquor required to mass dye materials varies widely depending on the information sources. Some estimates assert that as much as 100 litres of liquid is required to dye 1kg of textiles [54], while other source stipulate for a ton of fabric dyed anywhere between $20m^3$ and $350m^3$ is required [55]. Commercial dyeing processes are also rarely completely pure and so there are impurities, including some heavy metals, as well as auxiliary compounds needed during the dyeing and fixation processes [45]. Many textile dyes are required to be resistant to light and the complex chemical structure of many dyes makes them resistant to natural biological degradation [52, 56].

2.2.4 Dye Toxicity

Many textile dyes show little to no acute toxicity to humans and wildlife, with sensory sensitisation being the most common short-term problems associated with dyes [57]. Longer term chronic effects are understood to a lesser extent, with possible mutagenic and carcinogenic effect speculated [54, 56, 58]. Some synthetic dyes are known to be produced from toxic organic compounds or have degradation products that are carcinogenic [45, 51]. Benzidine (Figure 2.2b) is one such degradation intermediate. Congo Red – CI. Direct Red 28 (Figure 2.2a) is known to degrade to benzidine, however there are as many as twenty other aromatic amines that form constituent parts of azo dyes [59]. The manufacture of dyes that are known to produce, or be produced from, toxic aromatic compounds have therefore been banned in parts of Europe [45, 47, 59]. The similarity in structure between toxic and non-toxic means that many dye manufacturers must show care and diligence with the dye compound used [45]. The same similarity in chemical structure has also been seen as an avenue for change, and has been investigated to find alternatives to toxic precursor compounds in de

manufacture [45]. The problem then with newer, non-toxic, dye compounds is the absorption of light and growth inhibition of aquatic flora and fauna that rely on light penetration, as well as the increased chemical oxygen demand loading within the discharge waters making them potentially uninhabitable and unsightly [60].

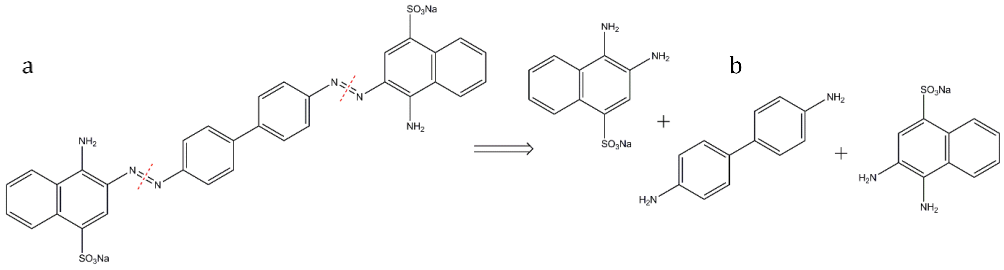


Figure 2.2 Degradation of a) Congo red to organic intermediates including b) benzidine

2.3 Wastewater Treatments for Dye Wastewater

2.3.1 Biological Remediation of Dye Wastewaters

2.3.1.1 Suspended and Fixed Growth Processes for the Remediation of Synthetic Dyes

One of the more common forms of biological treatment is in activated sludge processes (ASP) [17]. ASP is a continuous unit operation involving flocs of microorganisms to biologically degrade organic compounds [17]. ASP treatment occurs typically in two different modes, aerobic or anaerobic, in some cases however these two modes can occur in the same operation in different stages. Following ASP and a second clarification stage, to remove the sludge, the wastewater is discharged [17]. Biological treatments are not often encountered in industrial wastewater treatment [61]. The principle problem with biological degradation is the recalcitrant nature of colourants [53, 62]. The resistance to biodegradation is an inherent property of most synthetic dyes and

therefore the treatment of them using aerobic biological treatment is largely ineffective [62, 63].

Shaul *et al* assessed the applicability of activated sludge in a pilot scale arrangement. Wastewater influent dosed with azo dyes was investigated. The researchers found that of the 18 dyes that were investigated, 11 were left relatively unaffected by the ASP treatment, 4 were adsorbed onto the sludge and 3 were degraded biologically [63]. This study represents a comprehensive investigation of dye wastewater effluents, as a real wastewater effluent was employed in the study, rather than a synthetic solution of dye. The dyes with the least complex structure, those containing the fewest sulfonate functional groups, aromatic rings and the lowest molecular weight were the dyes that were biodegraded. The largest molecules with a greater number of sulfonate groups were left relatively unchanged [63]. This is attributed by the authors to the fact that the increased solubility of more sulfonate functional groups reduces adsorption ability and larger molecules results in an inability for the compound to transport across cell membranes [63].

Other research into the anaerobic reduction of synthetic dyes has been found to have positive results in terms of decolouration of the wastewater. Research by van der Zee *et al* indicates that high decolouration can be achieved from reducing activated sludge for a broad spectrum of low molecular weight simple dyes and high weight complex reactive and direct dyes [64]. Retention time in the reducing reactor ranged from days to weeks depending on the structure of the dye and functional groups present [64]. Panswad and Luangdilok and Nigam *et al* found a similar effect in that anaerobic reduction is more effective at dye remediation compared to aerobic oxidation [65, 66]. There appears to be variability in terms of biological remediation of dyes with anoxic environments being more conducive to degradation, while aerobic oxidation is restricted to more simple

dyes such as Acid Orange 7 [67]. It is notable though that the research combining anoxic and aerobic systems enhances the oxidation of reduction intermediates [64, 65, 68, 69]. Hydraulic retention time is also variable between dye types and structures [64, 65, 69]. The variability in conditions and remediation time required for biological treatment means that in some cases the biological remediation methods are advantageous in terms of cost yet advanced treatment methods such as adsorption and chemical oxidation may be more effective due to the long retention time of the wastewater in biological secondary treatment, compared with more advanced water treatment methods.

2.3.2 Chemical Treatment of Dye Wastewaters

2.3.2.1 Advanced Oxidation Processes in the Remediation of Synthetic Dyes

Oxidising potential is a key characteristic of a chemical oxidant and in some cases where stronger oxidation potential is required the use of hydroxyl free radicals ($HO^{\bullet}$) is required. The formation and application of ($HO^{\bullet}$) in chemical oxidation is often termed advanced oxidation or advanced oxidation processes (AOP) [17]. Advanced oxidation processes (AOP) are more effective in the oxidation of dyes and reaction intermediates than conventional oxidation through chlorine based oxidants, due to the oxidising potential of the $HO^{\bullet}$ (2.80V) being greater compared to that of ClO_2 (1.27) [17]. The recalcitrance of textile dyes and in particular reactive and direct dyes means that in many cases chemical oxidation through the addition of compounds such as molecular oxygen and chlorine-based compounds have not been fully investigated. Instead the application of AOPs to synthetic dye solutions is more common [70-72]. The formation of $HO^{\bullet}$ in most cases involves the use of either O_3 or H_2O_2 in conjunction with UV light [17]:

$$H_2O_2+h\nu \rightarrow HO^{\bullet}+HO^{\bullet}$$

Fenton oxidation also produces HO• by catalysing the breakdown of H_2O_2 in the presence of Fe^{2+} and Fe^{3+} ions. Reactive Black 5 [70] and Reactive Yellow 84 [71] are two dyes that have been oxidised by ozonation. Koch *et al* measured colour reduction as a function of UV-Vis absorption and found that 200mg L^{-1} of dye was completely oxidised and decoloured in 90 minutes with the lowest dissolved O_3 concentration (9.1mg L^{-1}) tested [71]. COD and TOC (total organic carbon) reduction in the dye sample shows that 50% of COD and 30% of TOC remained following oxidation [71]. This article goes no further to characterise the reaction products and intermediates left following the initial dye breakdown. The intermediates still contributing to the COD may also be more toxic than the parent organic compound, depending on the initial dye compound. (Figure 2.2). Work by Wang *et al* goes further in the investigation of ozonation of Reactive Black 5. The study identified similar findings to the ozonation of Reactive Yellow 84, in that there was significant decolouration of the synthetic dye solution, yet mineralisation of organic compounds was poor as COD and TOC remained at 45% and 25% respectively [70]. The reaction intermediates were briefly identified as acidic compounds due to decreasing pH after oxidation. Toxicity screens also identified toxic intermediate compounds that result from the ozonation of Reactive Black 5 [70]. Identification of the toxic intermediates is difficult due to the extensive range large complex structures seen particularly in reactive dyes and the many degradation mechanisms that can be followed. Although not all reactive dyes display the same chemical structure it would not be unreasonable to assume that there are risks associated with the partial oxidation of synthetic dyes [70].

A number of research studies have shown that ozonation was comparable with HO• producing agents and processes, in terms of both colour and COD removal. For O_3,

H_2O_2/UV and Fenton's reagent, COD removal was above 85% for all AOPs in the respective studies [72-74]. Muruganandham and Swaminathan studied the oxidation of Reactive Orange 4 with H_2O_2/UV oxidation process [75]. Decolouration and mineralisation were found to be optimal under acidic conditions [75]. The authors also note that the fixing agents and auxiliary compounds inhibit oxidation through a number of conduits. Soda ash addition, which is common in the fixation of reactive dyes affects the oxidation due to scavenging of $HO^{\bullet}$ by carbonate ions [75, 76]. NaOH is hypothesised to react with the H_2O_2 prior to the formation of $HO^{\bullet}$ thus reducing the amount of available $HO^{\bullet}$ in the oxidation process, and the alkaline nature of OH^- reduces oxidative capacity [75]. These few studies highlight the importance of research in this field as there are a great number of factors that must be considered for AOP application to synthetics dye wastewaters. AOPs are promising however the cost of employing O_3, H_2O_2 and UV light can reduce the appeal as cost efficiency is reduced, especially as dye recovery potential is limited.

Transition metal oxides are known to have photocatalytic semiconductor properties. Titanium dioxide and ZnO are a commonly found additives in sun creams due to the absorption of both UVA (λ = 315-400nm) and UVB (λ = 280-315nm) light that penetrates the ozone layer. The photocatalytic properties of these metal oxides have seen application in the enhancement of UV based oxidation. Semi-conducting photocatalysts produce free radicals when electron-hole pairs are produced under sufficient energy conditions (Figure 2.3). The free radicals produced attack and oxidise the organic pollutants adsorbed to the surface of the photocatalyst [77, 78].

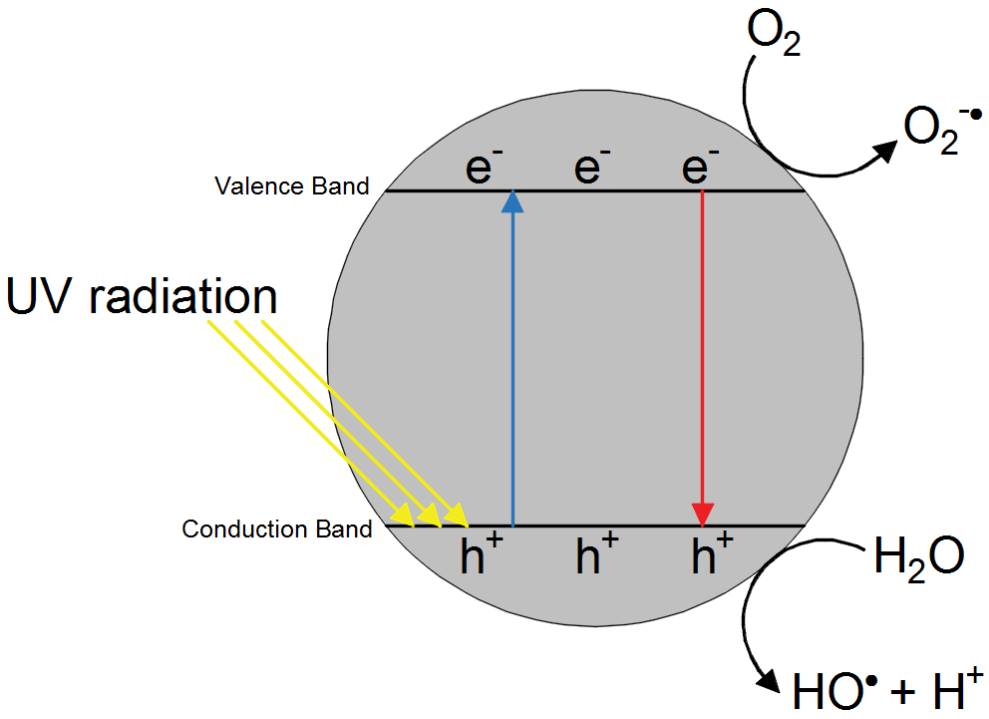


Figure 2.3 Schematic of hydroxyl and super oxide radical formation on the surface of a semiconducting metal oxide photocatalyst

Much of the research surrounding the oxidation of dyes in the presence of photocatalysts has focused on TiO_2 and ZnO based materials in conjunction with UV light at varying wavelengths and in the presence of chemical oxidants to enhance the advanced oxidation processes. When comparing the effectiveness of TiO_2 and ZnO for catalytic efficiency Sakthivel*et al* found that acid brown dye was decoloured and mineralised faster by ZnO than TiO_2, however both photocatalysts achieved full mineralisation [79]. In this instance the concentration of dye was 5×10^{-4} mol L^{-1} while the time taken for mineralisation to occur was 360 and 420 minutes for ZnO and TiO_2 respectively [79]. Other research found that the use of photocatalysts can enhance the degradation of synthetic dyes as the generation of both $HO^{\bullet}$ and $O_2^{-\bullet}$ occurs in the presence of a photocatalyst (Figure 2.3) [78, 80-82]. Despite the success of dye photocatalysis, there are a number of factors that inhibit the use. In the case of nano-size semiconductors, the

issue of a suspension of nanoparticles in the, now dye free, wastewater poses a difficult conundrum. The removal of the suspended of nanoparticles can be difficult, nanoparticles in the environment are also not well understood and release of suspended solids should be minimised. In order to minimise the issue of colloidal nanoparticle suspensions some research has found that immobilisation of semiconductors still provided removal of colour and mineralisation of dyes. Behnajady *et al* immobilised TiO_2 on glass plates in a flow reactor system [80]. Decolouration and mineralisation were achieved at low flow rates while higher flow rates resulted in lower degradation, due to the reduced residence time in the reactor [80]. Comparelli *et al* applied ZnO to glass substrates [83]. Decolouration and degradation was again found to be high however under acidic conditions ZnO dissolves destroying the catalyst [83]. This is a sizeable advantage of TiO_2 over ZnO, as TiO_2 appears to be more robust under acidic conditions. Immobilisation of photocatalysts however shows promise as the maintenance of particles in the nano-scale preserves high surfaces areas for the catalyst.

As previously mentioned, the presence of inorganic auxiliary compounds reduces the effectiveness of $HO^{\bullet}$ based oxidation processes due to the scavenging effects of CO_3^{2-} ions [75, 76]. Alaton *et al* found that O_3 oxidation was superior to TiO_2/UVA and H_2O_2/UVC oxidation systems [13]. Despite relatively high decolouration rates for all oxidation systems mineralisation remained low. The TiO_2/UVA system exhibited the lowest removal, which was attributed to an inability of the UV radiation to penetrate the dye wastewater in order to activate the photocatalyst [13]. The presence of inorganic auxiliary compounds appeared to have little effect on the overall oxidation due to the excess of H_2O_2 in the system. However the authors noted that, in agreement with Muruganandham and Swaminathan [75] and Liao *et al* [76], the H_2O_2/UVC system was affected by the increase in pH and the scavenging effects of OH^- and CO_3^{2-} while the O_3

system was not due to the primary production of $O_2^{-\bullet}$ rather than the primary production of $HO^{\bullet}$ [13]. The oxidation of dyes through AOPs and photocatalytic enhanced AOPs are presented as a potentially feasible remediation method if the problems of light absorption and inhibition of photocatalytic activity and suitable immobilisation can be overcome.

The data in Table 2.2, indicates strong oxidation potential of UV and solar based oxidation with the addition of ZnO or TiO_2 for oxidation of synthetic dye solutions. The use of solar light photocatalysis will reduce the cost of these methods particularly when compared with the oxidation of Solar light with H_2O_2. The problem remains though that the oxidation of the dye is not as sustainable as recovery and reuse of an unused dye in the effluent.

Table 2.2 Dye and chemical oxygen demand (COD) removal by chemical and advance oxidation processes

Oxidising Agent	Contaminant Dye	Decolouration / %	COD removal / %	Reference
O_3	Reactive Black 5	≈100	45	[70]
O_3	Reactive Yellow 84	≈100	50	[71]
Fenton Reagent	Polyester Dye	96	94	[72]
O_3	Polyester Dye	92	90	[72]
O_3/UV	Polyester Dye	94	93	[72]
O_3/H_2O_2/UV	Polyester Dye	90	85	[72]
H_2O_2/UV	Polyester Dye	99	96	[72]
UV	Indigo Dye	7	4	[73]
O_3/H_2O_2/UV	Indigo Dye	99	97	[73]
H_2O_2/UV	Reactive Orange 4	90	60	[75]
H_2O_2/Solar	Reactive Orange 4	80	50	[75]
TiO_2/Solar	Acid Brown 14	100[a]	100[a]	[79]

ZnO/Solar	Acid Brown 14	100[a]	100[a]	[79]
TiO_2/UVC	Acid Red 27	100	100	[80]
ZnO/Solar	Basic Violet 10	100	100	[82]
TiO_2/Solar	Reactive Orange 4	100	100	[81]
Acetate-ZnO/UVC	Acid Orange 52	-	100	[83]
Acetate-ZnO/UVC	Acid Red 2	-	95	[83]

[a]Decolouration and Mineralisation occurred at different rates and mineralisation occurred at least 120 minutes after decolouration

2.3.3 Physical Treatment of Dye Wastewaters

2.3.3.1 Membrane Filtration for Synthetic Dye Remediation

Membranes filters are composed mainly composed of polymer materials [17]. The application of membrane filters for dye removal has been investigated primarily through both the use of ultrafiltration (UF) and Nanofiltration (NF) membranes. Ultrafiltration membranes investigated by Alventosa-deLara *et al* exhibited variable performance in terms of retention of dye [84]. The operating pressure varied from 1 bar to 3 bar, however the increase in pressure resulted in a reduction on retention. At 1 bar the maximum retention was 91.4%, this figure dropped to 73.8% at 3 bar [84]. Influent dye concentration was low at 100mg L^{-1}, and retention, was found to increase with time. An interesting aspect of the research in this study by Alventosa-deLara *et al* is the influence of both pH, on retention, as well as the influence of electrolyte salts. In the study the isoelectric point was at pH 5.3, indicating the net charge on the membrane under tested pH conditions was negative. The sulfonate functional groups in the reactive dye tested were theorised to enhance retention due to static rejection [84]. The presence of electrolytes significantly inhibited retention in the membrane and this is due to the excess of Na^+ ions present in the solution bonding to the negatively charged membrane and eliminating the effects of the static rejection and instead retention was solely due to size exclusion [84, 85]. He *et al* investigated operating conditions including temperature, pressure, flow velocity and influent concentration [86]. Increased operating pressure of the cross flow over the membrane resulted in improved retention of both dye and sodium sulfate [86]. Dye retention was maintained at >99% with increasing rejection when pressure was increased from 0.5 bar to 3 bar [86]. This is contradictory to the work by Alventosa-deLara *et al* where dye retention was inhibited by increased pressure

[84]. The cause of the difference between retention is unclear, particularly as the reasoning behind the phenomenon observed by He *et al* is explained by the fouling and changing flow through the membrane, however it must be noted that the rejection percentage increase in the work by He *et al* is minimal [86]. The pH of the solution appears to have no significant effect on the retention of both dye and electrolyte in the dye solution, across the pH range from 1.5 to 6.5. It is not noted explicitly by the authors, what the isoelectric point of the membrane is, however it appears outside of the tested pH range. Therefore the acidic sulfonate functional groups in the reactive blue dye tested and the noted negative change of the membrane contributed significantly to the rejection of dye through static charge [86]. Increased temperature from 15 to 40°C resulted in zero change to salt retention however there was a decrease in dye retention that was, in a similar vein to the impacts of pressure, almost negligible and approximately 0.6% [86]. The polyethersulphone type membrane investigated by He *et al* was extraordinarily effective at all operating conditions tested.

Nanofiltration in general is a more rigorous treatment method than ultrafiltration, with a microporous structure of the membrane, compared with a mesoporous structure found in UF membranes [17]. Permeate flux of NF and a Reverse Osmosis (RO) membranes was found to be affected by the presence of Reactive Black 5 and Reactive Yellow 145 in a similar way. The presence of the dyes, regardless of specific type resulted in a reduction in flow through the membranes of approximately 0.5 L m^{-2} h^{-1} [87]. The changes in flow, primarily due to fouling resulted in an insignificant change in removal of dye colour for both membranes and both dyes tested, however the retention of Reactive Yellow was significantly higher than the COD rejection for the NF membrane when compared with the RO membrane and the retention of the Reactive Black 5 (Table 2.3) [87]. There is no indication of the zeta potential of the NF membrane however it is

noted that the static charge of the membrane contributes to the success of the filters for dye remediation [87]. It is unclear why there is residual COD in the NF permeate during the removal of Reactive Yellow 145 when compared with the RO membrane or during the removal of Reactive Black 5 [87]. There is no reason offered and the only significant difference in dye structure is a chloride functional group in the Reactive Yellow 145.

Table 2.3 Chemical Oxygen Demand and Colour Removal, Data from Kim *et al* (2005) [87]

Dye	Membrane	COD Remvoal / %	Dye Removal / %
Reactive Black 5	Nanofiltration	96.5	95.5
	Reverse Osmosis	>97%	>97%
Reactive Yellow 145	Nanofiltration	74.0	99.4
	Reverse Osmosis	>97%	>97%

Lin *et al* focused on high molecular weight direct dyes when testing two different types of polymer NF membrane [88]. Regardless of operating pressure, in a cross flow arrangement dye retention was greater than 99% for the Direct Red 80, Direct Red 23 and Congo Red dyes on both types of membrane filter, which were distinguished by flux rate through the membrane [88]. The study aimed to differentiate salt and dye solutions, so in this study the salt retention was an important factor. Salt retention was increased with increasing salt concentration [88]. The lower flux rate membrane exhibited lower salt penetration than the higher flux membrane at low salt concentrations, however as the salt concentration reached its maximum at 40g $^{-1}$ the penetration percentage of the respective membranes converged to a difference of approximately 2% at 96±1% [88]. With the increase in salt concentration in the influent there is a negligible reduction in dye rejection for the three types of direct dye, however the rejection remains greater than 99% [88].

Membrane filters exhibit exception removal of Reactive Dye compounds under optimal conditions where both static and steric rejection of dye compounds results in colour removal rates of greater than 90%, in most cases, from the permeate. Membrane fouling which is a common issue with membrane filters results in insignificant changes to the rejection of dyes and electrolyte salts, however pH plays a potentially important role as the static rejection of dyes is reduced when most commonly when the pH is alkaline. The most interesting aspect of much of the research utilising membrane filters encountered in the review is that despite reactive dyes being the common pollutant of interest, there was no pH adjustment to an alkaline condition which is common in dye baths. Even without the static rejection however, NF and RO membranes remove dyes well due to the microporous structure and semi-permeability of the membranes.

2.3.3.2 Activated Carbon Adsorption of Synthetic Dyes

Activated carbon is one of the most common adsorbents utilised in tertiary water treatment [17]. Activated carbon takes one of two main forms powder activated carbon (PAC) and granular activated carbon (GAC) [17, 89]. Due to the scale of water treatment and engineering difficulties such as pressure drop in packed beds, GAC is more common that PAC in fixed bed adsorption, however PAC is often employed in fluidised bed arrangements [17]. The production of GAC involves heating a carbon source to form char. The char is exposed to high temperature (900°C) gases. These gases develop the micro- and meso-porous structure and high surface area associated with activated carbons. The preparation procedure and the starting carbon source both impact the final physical characteristics of the activated carbon [17].

Kannan *et al* [35] and Hameed *et al* [90] have both investigated the adsorption of methylene blue onto various types of activated carbon. Kannan *et al* investigated

carbons produced by carbonisation at 300°C and steam activation at 700°C, before a final thermal activation at 120°C in air [35]. The investigation compared commercial activated carbon with in-house produced materials from local waste products. The uptake capacity of methylene blue on commercial activated carbon was equal to 980mg g^{-1} while many of the in-house produced adsorbents showed significantly lower uptake ranging from 143mg g^{-1} for bamboo activated carbon to 472mg g^{-1} for straw based activated carbon [35].

Hameed *et al* utilised only bamboo based activated carbon, the activation process was also more complex involving multiple carbonisation/pyrolisation steps and alkaline washing [90]. The activated carbon showed relatively high monolayer adsorption capacity of 454mg g^{-1}. Comparable samples between different activated carbons sources exhibit uptake of methylene blue in the range of 140mg g^{-1} to 472mg g^{-1} [90]. Many acidic dyes exhibit lower uptake with many of the adsorption capacities below 200mg g^{-1} [90].

Al-Degs *et al* investigated the surface chemistry of activated carbon and the effect that the chemistry has on the adsorption of three reactive dyes [34]. Using a commercially available activated carbon (Filtrasorb 400) the research identified a trend of competing dye ions. The workers found that dyes adsorbing more quickly onto the surface of the carbon resulted in lower uptake of dyes that adsorbed at a slower rate [34], this is to be expected as the available active sites and access to finer pores diminishes as dye is adsorbed. It is also interesting to note that the research found an increasing trend in adsorption with decreasing particle size [34]; suggesting that for large bulky dye molecules surface adsorption with little penetration into the micro-pores of the activated carbon is the mode of adsorption. The maximum uptake was also heavily dependent on the dye type with the reactive yellow dye exhibiting a much higher uptake than both the reactive black and reactive red dyes in a single solution reaction system

[34]. The surface chemistry of the activated carbon and the chemistry of the dye are influenced by solution pH, primarily the protonation and de-protonation of the carbon surface influences the attraction between the dye molecule and the carbon surface [91, 92]. It was found by the authors of a number of research studies however that the adsorption process for dyes onto activated carbon involves more than solely electrostatic attractions and hydrogen bonding also occurs [34, 92, 93].

Work by Al-Degs *et al* on the application of activated carbons in fixed bed columns for dye adsorption. The research followed on from batch adsorption studies with a Reactive Black and Reactive Yellow dye on Filtrasorb-400 commercial activated carbon [94]. The results for Reactive yellow high uptake capacity within the column 0.541kg kg^{-1} compared with the monolayer uptake capacity of 0.73kg kg^{-1} as determined by the Langmuir model [94]. The data obtained in the research by Al-Degs *et al* agrees with some basic assumptions, principally that; as the mass of the filter media, and hence bed depth, increases so does the adsorption capacity of the column. Reducing C_0 of the dye feed also increases the service time until breakthrough occurs [94].

Ahmad and Hammed utilised the Adams-Bohart, Yoon-Nelson and Thomas models to linearly model breakthrough curves [95]. The Yoon-Nelson, Adams-Bohart and Thomas breakthrough models are commonly found in literature regarding column adsorption research [95-99]. Similar to Al-Degs, the work concentrated on the bed depth and inlet concentration of the dye as variables affecting the adsorption, but the research also investigated inlet flow rate. Breakthrough curves indicate that breakthrough and exhaustion points are reached more quickly with increasing concentration. Total adsorption and equilibrium adsorptive capacity increase with increasing bed depth, decreasing flow rate and decreasing influent concentration [95]. The reduced adsorption capacity and quicker breakthrough occurs due to increased loading of

adsorbate in the column and reduced residence time [95, 100]. The breakthrough curve models; Thomas, Adams-Bohart and Yoon-Nelson were fitted to the data with the Thomas and Yoon-Nelson models providing the best linear fit to the data [95].

The literature suggests that activated carbon provides an effective adsorbent for synthetic dyes in both batch and column adsorption studies. Adsorption of reactive dyes was found to be more effective in terms of uptake capacity for batch adsorption compared to fixed bed column adsorption [94]. This trend has also been found for adsorption of acid dyes on activated carbon [97]. Reactive dyes may be one of the most widely applied type classes due to their prevalence in dyeing of cellulosic fibres (cotton) and the scale of cotton-based clothing available. The primary issue with activated carbon and the literature surrounding it, is that there are such a variety of materials available and the preparation methods vary between articles that there is no set method for GAC/PAC production other than that in most cases as previously mentioned, high temperature pyrolisation and steam activation is required. Thus, despite activated carbons being a gold standard for water treatment and polishing the high cost of generation and regeneration limits the applicability in some areas of the planet where most large-scale textile and dyeing/finishing processes occur.

2.3.3.3 Ion Exchange Resins for Synthetic Dye Remediation

Ion exchange media are generally utilised in the form of synthetic polymer resins [17]. Ion exchange resins a common in four main types; strong and weak cation and strong and weak anion [17]. Depending on the type of dye designated for removal, the type of resin will change. Most reactive dyes tend to have sulfonate functional groups, and would require anion exchange resins while basic dyes require cation exchange resins for effective removal.

Dulman *et al* utilised both weak and strong anionic exchange resins across an acidic pH range [21]. The work found that a weal anionic exchange resin was more efficient for dye removal under optimum pH conditions than strong anion exchange resins tested. The authors note that in most cases for the exchange resins tested access due to degree of cross-linking within the polymer resin was pivotal in affecting exchange efficiency [21]. The ion exchange resins used in the research were produced in-house and were not commercially available resins. The influence of pH on dye removal was significant for both strong and weak resins, the highest distribution coefficients were achieved primarily under acidic conditions with the weakest ion exchange occurring at near neutral pH [21]. This is problematic in dye adsorption as despite the fact that the dyes are acidic the high alkalinity of dye bath effluents, due to fixation and diffusion enhancement. The alkaline pH will reduce the effectiveness of the anionic resins, according to the research by Dulman *et al* [21]. The desorption and regeneration of the low crosslinked polymer resin tested by Dulman *et al* was found to have outstanding recyclability lasting for 13 cycles, regeneration of the resin is also a simple process of alkaline washing [21]

Work by Greluk and Hubicki on the remediation of Acid Orange 7 suing strong anion exchange resins indicated that there was exceptional colour removal under all conditions tested [101]. The conditions investigated included a wide pH range. The authors note that across the pH range from 2-12 the adsorbent remains positively charged quaternary amine does not undergo deprotonation. This is contrary to the findings of Dulman *et al* yet this appears to be a more logical finding as the resin is basic in nature and the dye molecule remains anionic at both low and high pH [101]. Maximum adsorption capacity was 1370mg g^{-1} at 298K [101]. Desorption of Acid Orange 7 from Amberlite was less effective than that of the resin used for Acid Green 9 removal. An

aqueous hydrochloric acid/methanol mix was found to be most effective, however desorption was lower than 50% of the total adsorbed Acid Orange 7 [101]. NaOH in 50% methanol was found to be the second most effective method of desorption [101]. Dulman *et al* note that in many cases for regeneration of commercial resins, methanol/aqueous mixtures are required to optimise desorption and regeneration [21].

Wawrzkiewicz investigated the removal of Basic Blue 3 on three different types of resin adsorbents. The strong acid cation exchange material was found to be the most efficient at dye removal in batch experiments with the q_m of the dye found to be greater than 560mg g^{-1} at temperatures between 293 and 323K [22]. Dye auxiliary electrolyte have a relatively low impact on removal for the exchange resin, this is primarily due to the fact that both salts used both sodium salts of chloride and sulfate ions [22]. Sodium ions are the exchangeable ion in the sulfonate functional groups in many strong acid cation exchanger resins [17], therefore it is unsurprising that there is little to no effect as a result of their addition, even in such quantities as those used in the study [22]. Desorption and reservation of the cation exchange resin was, much like the regeneration of the resin used by Dulman *et al,* exceptional. Regeneration was found to be 100% effective with HCl washing in 90% methanol [22].

Ion exchange resins are very useful adsorbents for removal of a variety of ionic dyes (Acidic, Reactive and Basic) from aqueous solutions. The adsorption capacity is higher than many other adsorption materials. They lack the versatility of activated carbon, in that an acidic dye required a basic ion exchange resin, however the four varieties of exchange resins can account for the variety of dyes. There has not been a significant amount of research into the area of synthetic polymer ion exchange resins area, possibly because what research has been done has been so successful in terms of adsorption capacity and regeneration. Alternatively, activated carbon is ubiquitous in advanced

water treatment systems and has therefore become the 'weapon of choice' in removal of dye compounds.

2.3.3.4 Anionic Clay Based Adsorbents for the Remediation of Synthetic Dyes

Layered double hydroxides (LDHs) are synthetic anionic clay minerals. LDHs all have the general formula of $[M^{II}_{1-x}M^{III}_{x}(OH)_2](A^{n-})_{x/n} \cdot zH_2O$ [1, 2, 9], where M^{II} is representative of bivalent metal cations (Mg^{2+}, Ca^{2+}, Co^{2+}, Zn^{2+}) and M^{III} denotes trivalent metal ions (Al^{3+}, Fe^{3+}, Cr^{3+}) [2]. The divalent and trivalent cations are randomly disseminated in metal hydroxide sheets that are held together through the electrostatic attraction between the cations and the interlayer anion (A^{n-}) as depicted in Figure 2.4. The interlayer anion can be exchanged, with the affinity of the anion for the LDH dependant on the anion charge density. The order of affinity for simple anions was determined by Parker *et al* as CO_3^{2-}>SO_4^{2-}> F^->Cl^->Br^->NO_3^->I^- [102].

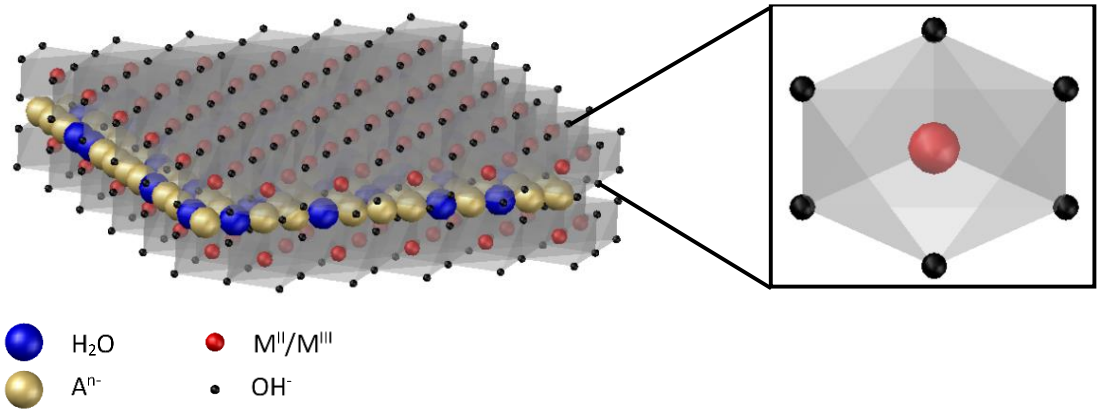


Figure 2.4 Layered double hydroxide structural schematic

LDHs have been receiving growing attention, in the last decade or so, in science and engineering applications from chemical additives [103, 104] and flame retardants [105, 106] to catalysis [107, 108] and adsorption [109-111]. A significant advantage of LDHs

in the field of adsorption is the potential for LDHs to be calcined to form mixed metal oxides (MMO). Upon rehydration, the MMO, in the presence of an aqueous anion, reforms the LDH layers with the anion intercalated in the interlayer region. This phenomenon has been dubbed the memory effect due to the reformation of the LDH (Figure 2.5) [2]. A significant volume of work has been undertaken in the field of adsorption of pollutants from simulated wastewater solutions with a focus on oxyanions such as Cr(VI) and phosphate as well as F^- [112-121].

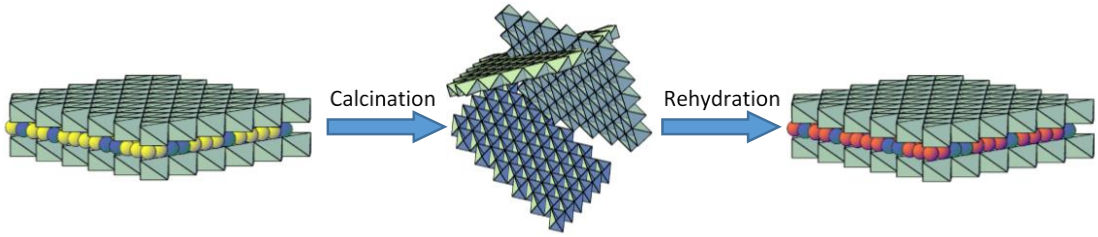


Figure 2.5 Schematic demonstrating the Memory Effect

Ca_2Al type LDHs have not been used extensively for adsorption, only two research articles involving the type of LDH for dye adsorption have been identified. Zhang *et al* applied Ca-Al-Cl type LDHs for adsorption of methyl orange (C.I – Acid Orange 52) and acid scarlet GR (C.I – Acid Red 73) [27]. The authors focussed on the use of infra-red absorption of pre- and post-adsorption LDHs as well as X-ray diffraction to determine the physical changes to the LDH structure. The most interesting result is that despite both dyes being acidic in their structure the methyl orange was intercalated between the individual LDH sheets while the acid scarlet was adsorbed primarily on the outside of the LDH layers and as a result structural changes to the lattice parameters were not observed [27]. No indication as to the differences in adsorption kinetics or uptake capacity was highlighted in the study. Information regarding the differences between the two dyes and the respective modes of adsorption would provide useful information

as to what dyes can be effectively removed by intercalation and ion exchanged and which can only be adsorbed by attraction to the LDH surface.

Ortham *et al* investigated calcined $Mg_3Al\text{-}CO_3$ on the removal of a number of commercial dyes from the acidic, basic and disperse classes [122]. The LDHs were found to exhibit higher adsorption capacity for anionic dyes over cationic due to the anionic attraction of the dye molecule to the positively charged metal hydroxide sheets following rehydration [122]. This study also compares LDHs against activated carbon, a common adsorbent used in dye remediation, for the uptake of Acid Blue 29. Activated carbon exhibited marginally higher adsorption capacity when compared the LDH yet the LDH showed greater adsorption capability at low dye concentrations. The adsorption mechanism is determined as ion exchange or rehydration due to the memory effect, and the dye molecules became part of the rehydrated structure. One benefit of LDHs over activated carbon, as highlighted by Orthman *et al*, is that regeneration of activated carbon adsorbents is costly while the Mg_3Al-dye LDH could be completely regenerated after calcination at 450°C. The regenerated LDH, although only tested for one cycle showed high dye removal [122]. Other studies involving the adsorption of dye onto $Mg_xAl\text{-}CO_3$ have studied the effects of calcination temperature on adsorption capacity, as well as the adsorption capacity and kinetics of various types of dyes.

El Gaini *et al* studied indigo carmine (C.I Acid Blue 74) adsorption on LDHs calcined at temperatures up to 700°C. The adsorption mode varied between $Mg_2Al\text{-}CO_3$ heated to different temperatures [123]. Uncalcined hydrotalcite and samples heated up to 400°C showed predominantly surface adsorption of dye onto the LDH, however calcination of samples between 500°C and 700°C showed complete breakdown of the layered structure, hence on rehydration in the presence of the indigo dye, the primary mode of adsorption was intercalation [123]. It is interesting to note however that calcination at

700°C resulted in lower uptake than calcination at 600°C, suggesting that between these two temperatures, some $MgAl_2O_4$ spinel structures begin to form. The formation of spinel structures is irreversible and reduces adsorption by intercalation and the memory effect [123].

Bascialla *et al* conducted similar experiments using Acid Blue 113 [124]. However, in the study only calcination at 500°C was investigated. Comparable conclusions were drawn with respect to the mode adsorption. In both studies it was found that calcined LDHs followed the Freundlich isotherm model for dye adsorption yet uncalcined adsorbents follow the Langmuir model [123, 124]. Extremera *et al* followed a similar experimental procedure to both El Gaini *et al* [123] and Bascialla *et al* [124], with the exception that the Mg_3Al-CO_3 LDH sample was subject to a variety of pre-treatments prior to adsorption of methyl orange dye [125], samples were subjected to hydrothermal treatment and milling. The investigation concluded that the physical characteristics of the LDH play a key role in the effectiveness of the adsorbent, with characteristics such as crystallinity and pore size distribution cited as examples [125]. The hydrothermally treated LDH performed the best in terms of adsorptive capacity and adsorption rate [125], it is presumably due to the greater meso-pore volume of this sample compared with the milled and untreated LDH. All three adsorbents however appear to follow a pseudo 2nd order rate model, with high temperature increasing uptake. Adsorption followed the Langmuir isotherm model [125]. The majority of literature regarding adsorption of synthetic dyes onto LDHs utilises a small number of dyes for adsorption studies, or in many cases only one [26, 124, 126-129].

Zhu *et al* have investigated the effects of competing inorganic anions in the form of Cl^-, SO_4^{2-} and CO_3^- [130]. The impacts that competing inorganic anions have on the adsorption capacity of the dye are both intriguing and expected. The presence of CO_3^{2-}

has a strong negative influence on uptake due to the high affinity of CO_3^{2-} ion for intercalation [130]. Chloride and sulfate were less influential and the authors note that this is an important finding in terms of selecting LDHs as an adsorbent for dye. Zn_2Al-Cl adsorbents show positive uptake of direct blue dyes (Evans Blue, Chicago Sky Blue 6B and Niagara Blue) even though no calcination occurring prior to adsorption [131]. This suggests that certain interlayer anions present from synthesis salts are exchangeable from the LDH structure notwithstanding the fact that the direct dyes are large, high molecular weight compounds [131]. Uptake of direct blue dyes was highest at higher temperatures [131], Ni and Xia *et al* found that uptake of methyl orange was also maximised at the higher adsorption temperatures, however uptake of methyl orange was relatively low compared with other LDHs (Table 2.4) [126], this result is almost contradictory based on the understanding that the active adsorption sites of an MMO/LDH adsorbent are occupied by the number of anionic functional groups present in the anionic compound, as we can see in the general LDH formula: $[M^{II}_{1-x}M^{III}_{x}(OH)_2](A^{n-})_{x/n} \cdot zH_2O$. An increase in the anionic charge should result in a lower anionic content in the interlayer gallery, yet the report by Marangoni *et al* indicates that Evans Blue uptake was 491mg g^{-1} compared the 200mg g^{-1} reported by Ni *et al* at 25°C, depsite a higher molceular weight and greater number of anionic functional groups [126, 131] (Figure 2.6).

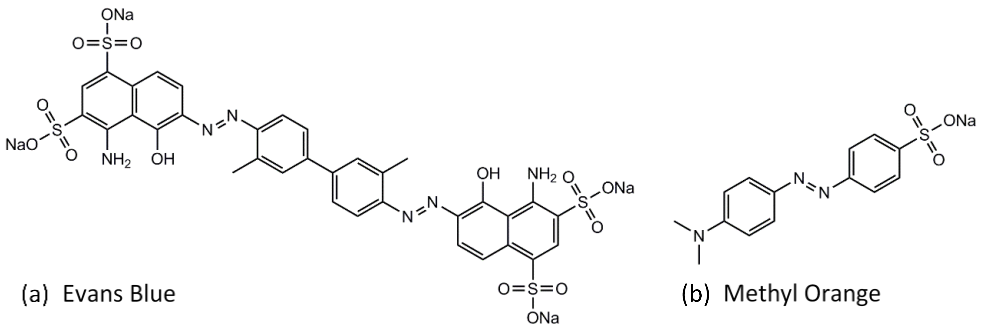


Figure 2.6 Chemical Structure of (a) high molecular weight Evans Blue and (b) low molecular weight methyl orange

Table 2.4 Mixed metal oxide (MMO) uptake capacity of Acid Orange 52

MMO	M^{II}/M^{III}	S_{BET} / m^2 g^{-1}	q_m / mg g^{-1}*	References
NiMgAl	2	246.5	375	[26]
ZnAl	3	–	200	[126]
ZnMgAl	2	82.13	883	[132]
MgFe	3	143	104.27	[133]

Rather than calcination of a CO_3^{2-} type LDH some authors have utilised NO_3^- intercalated materials [128] and also sodium dodecyl sulfate (SDS) [134]. Intercalation of such compounds allows for potentially simple ion exchange as NO_3^- has been shown to have low affinity for LDH layers [102], while the structure of SDS also lends itself to the role of a facile exchange compound, as the molecule is long and has only a single sulfonate functional group (Figure 2.7), resulting in a relatively low charge density in the anion. In terms of exchange-ability the SDS type LDHs may be preferable as the basal spacing (d_{003}) of an SDS intercalated LDH is 2.6nm [134] whereas the d_{003} spacing of a NO_3^- type LDH is between 0.8nm and 0.9nm [1, 135]. Wu *et al* claim that the hydrophobic nature of the SDS intercalated LDH increases dye uptake over traditional LDHs [134], with the maximum uptake capacity of Direct Blue G greater than 700mg g^{-1} at 298K [134].

However, there is no comparison between a Cl and SDS intercalated LDH in the study means that this claim is not entirely substantiated although the theory behind the mechanism for the ion exchange supports their claim that SDS will be readily exchanged due to the low charge density of the SDS molecule. Despite the high adsorption capacity, SDS ion exchange is potentially unwise as the exchange of large amounts SDS should be avoided and by utilising the memory effect and rehydration of LDHs, high adsorption capacity can be achieved without the release of interlayer anions.

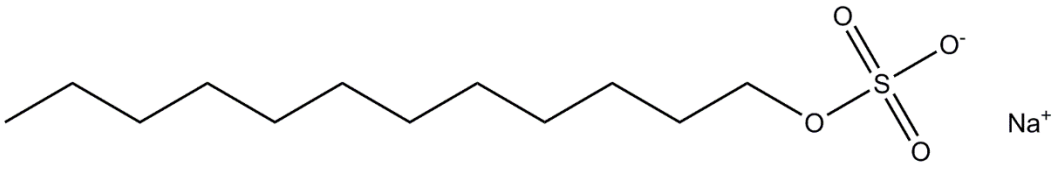


Figure 2.7 Structure of sodium dodecyl sulfate (SDS)

With time more exotic combinations of metal ions have been investigated. Changes to the M^{II} and M^{III} ions, by either by substitution or additional cations, have been investigated by a number of authors. The synthesis of ternary LDHs using Mg^{2+} and Ni^{2+} was investigated by Zaghouane-Boudiaf and Boutahala [26]. Parameters affecting adsorption included pH, temperature adsorbent dose and initial dye concentration. The authors found that the uptake capacity of the calcined LDH was 375mg g^{-1} [26]. The interesting aspect of altering the LDH structure comes with the investigation of maximum uptake capacity with respect to particular dye compounds. Table 2.4 outlines the uptake of methyl orange onto various LDHs with different chemical structures. Transition metal substitutes for M^{II} and M^{III} such as Zn^{2+} and Ni^{2+} and Cr^{3+} and Ti^{4+} have been shown to enhance light absorption of LDHs and increase photocatalytic activity in LDHs [136].

Much of the literature regarding LDHs as dye adsorbents follows a similar pattern focussing on a small number of dyes and one type of LDH. Typical adsorption variables are pH, temperature, dye concentration and in some cases adsorbent loading. These variables serve to elucidate the kinetic and adsorption models that the adsorption process follows. LDHs are, for the most part, subjected to calcination at temperatures near to the thermal decomposition point of the LDH to highlight the requirement for a form of activation prior to adsorption. Very few studies highlight the potential weaknesses in LDH adsorption, such as the presence of CO_3^{2-} in the wastewater. Soda ash is a common auxiliary compound used particularly in reactive dyeing [46]. Carbonate anions are problems for LDHs as adsorbents. The high charge density of CO_3^{2-} ions and their affinity for intercalation means that dyes may either be exchanged or simply not adsorbed if excess CO_3^{2-} is present. As a consequence, the maximum uptake capacity will be lowered. In order to mitigate the effect of soda ash more LDH adsorbent will be required. The other significant obstacle for LDHs is that they are inherently suitable as anion adsorbents, but are less effective for adsorption of cationic dyes. The nature of these dyes makes them difficult to adsorb as Orthman *et al* demonstrated [122]. The remediation of cationic dyes then can potentially follow a route of photocatalysis rather than adsorption, with transition metal cations in the metal hydroxide sheets.

A comparison of a select number of adsorbents covered in Section 2.3.3 in outlined in Table 2.5. The data in Table 2.5 shows that LDHs have been predominantly investigated for acidic dyes due to their inherent ability to adsorb anionic dye compounds. Maximum uptake capacity (q_m) is commonly close to 400mg g^{-1} or greater. Anion and cation exchange resins exhibit q_m greater than that of activated carbons, however the source of the carbon as well as activation methods are integral to achieving the highest maximum

uptake capacity. In general, there are a number of tertiary treatment methods that are capable of removing dyes from solution however the adsorption capacity is not necessarily comparable as it can be seen from the table, not all research studies utilise dyes of the same type for adsorption among different adsorbents. The adsorption capacities can be difficult to then compare, and their merits cannot be ascertained. An example of this is that Reactive Black 5 is a relatively common dye of interest in activated carbon adsorption, however it is not found extensively in literature where LDHs and calcined LDHs are the adsorbent.

Table 2.5 Adsorption capacity of adsorbents and a variety of dye compounds

Adsorbent	Adsorbate	Temperature / K	Adsorption Capacity (q_m) / mg g^{-1}	Reference
Calcined ZnMgAl LDH	Acid Orange 52	Room Temperature	883	[132]
Mg_2Al-SDS	Reactive Yellow 160	308	438	[134]
Calcined MgNiAl LDH	Acid Orange 52	298	375	[26]
Calcined Zn_3Al LDH	Acid Orange 52	298	200	[126]
Calcined Zn_2Al LDH	Direct Blue 53	298	492[b]	[131]
Calcined Mg_3Al LDH	Acid Orange 10	303	665	[125]
Calcined M_2Al LDH	Acid Blue 113	296	2544	[124]
Calcined Mg_2Al LDH	Acid Blue 83	298	614	[130]
Calcined Ca_2Al LDH	Food Yellow 3	Room Temperature	398	[129]
Weak Anion Exchange	Acid Green 9	293	500	[21]
Strong Cation Exchange	Basic Blue 3	293	561	[22]
Amberlite Strong Anion Exchange	Acid Orange 7	298	1370	[101]
Activated Carbon	Basic Red 9	305	127	[137]

Activated Carbon	Reactive Blue 2	298	277[c]	[92]
Activated Carbon	Reactive Black 5	293	294	[94]
Filtrasorb 400 Carbon	Reactive Black 5	293	278	[91]
Filtrasorb 400 Carbon	Reactive Red 22	291	213	[34]
Bamboo Source Activated Carbon	Basic Blue 9	303	454	[90]
Activated Carbon	Basic Blue 9	303	980	[35]
Rice Husk Activated Carbon	Basic Blue 9	303	344	[35]
Coconut Shell Activated Carbon	Basic Blue 9	303	278	[35]

[b]calcualted from M_w of Direct Blue 53 and reported q_m=0.512mmol g^{-1}

[c]calcualted from M_w of Reactive Blue 2 and reported q_m=0.27mmol g^{-1}

2.3.3.5 Layered Double Hydroxides as Photocatalysts

The incorporation of transition metals into LDH layers to enable enhance the photocatalytic potential of LDHs has been investigated by synthesising LDHs with metals with well-known photo-active properties such as Zn and Ti [136]. The added ability of dye adsorption followed by the subsequent degradation of the adsorbed molecules provides a possible solution to the problem identified by Alaton *et al*, when the incident radiation is blocked by the dye. Adsorption of the molecules will render a solution clearer and allow more light to penetrate to the catalyst surface [13].

One of the most common transition metal semiconductors applied in photocatalysis is ZnO, alongside TiO_2 [13, 16, 138]. LDHs containing Zn^{2+} have been shown to exhibit some degree of photocatalytic activity [139, 140]. Zhang *et al* investigated the degradation of C.I Acid Orange 7, in the presence of ZnAl layered double hydroxides. However it must be noted that the synthesis process produced ZnO alongside the LDH. Nevertheless the authors reported that the Zn_2Al-LDH was capable of decolouring Acid Orange 7 by 73% against other more common photocatalysts ZnO and P25-TiO_2, which achieved 9.9% and 30.4% decolouration respectively [141]. The relative success of Zn based LDHs for adsorption and photocatalysis has led to ternary ZnAl LDHs with doped elements that aim to improve the photocatalytic activity

Both Suárez-Quezada *et al* [142] and Zhu *et al* [143]. Both research studies found that addition of Ce into the LDH reduces the band gap of the samples upon calcination, this is due to the presence of CeO_2 within the MMO [143]. Surprisingly however the results indicated that Ce should be applied only as a dopant and not as a significant part of the LDH in the same concentration as Zn^{2+} and Al^{3+}. A 5% addition of Ce to the LDH/MMO material achieved the highest concentration degradation of phenol [142] and

Rhodamine B [143], while the highest concentration of Ce removal rates that were similar or worse.

Instead of doping semiconductors into the LDH structure Parida and Mohapatra utilised the photocatalytic potential of a ZnFe type LDHs [144]. This research relied solely on surface adsorption of a selection of basic dyes as no calcination occurred prior to degradation. The NO_3, Cl and CO_3 intercalated LDHs exhibit low band gap (<2.4eV) with ZnFe-CO_3 showing the lowest band gap energy [144]. An important aspect of this study was the comparison between sole adsorption and photocatalysis. Without irradiation, malachite green removal was ≈20% for all three LDHs, while photocatalysis of the system resulted in significant increases in degradation for all three LDH types with ZnFe-CO_3 exhibiting close to 100% decolouration after 2 hours of visible light irradiation [144]. In spite of the high degradation capability of ZnFe-CO_3 LDHs in visible light, the research fails to identify degradation intermediates and the overall COD reduction of the dye solutions. In previous works on AOPs, COD removal was a key feature of the work and is a more reliable metric for oxidative capacity of the photocatalyst. Other visible light photocatalyst LDHs produced with Zn^{2+} include ZnTi and ZnCr type materials. Initial work with ZnCr LDHs looked at the evolution of H_2 from water [145]. The research highlights the octahedral Cr units in the LDH matrix, similarly to the ZnFe-CO_3 LDH, as the reason for the visible light absorption and low band gap [139, 145]. Later work by Baliarsingh *et al* looked more closely at the effects of Cr in the LDH matrix, with respect to methyl orange oxidation [146]. The research highlights the fact that CoCr-CO_3 was the most effective for methyl orange oxidation, despite having the highest band gap. The CoCr-CO_3 LDH had the largest pore volume however which is most likely the greatest contributor to the results collected [146]. ZnTi LDHs do not exhibit the low band gap energies of ZnCr and ZnFe LDHs. However, ZnTi LDHs still demonstrate visible light

absorption [31, 147]. $Zn_5Ti\text{-}NO_3$ LDHs were shown to readily oxidise Rhodamine B, to a greater extent than the $Zn_3Fe\text{-}NO_3$ LDH. The reason for the enhanced oxidation, despite a larger band gap is due to smaller crystal size present in the $Zn_5Ti\text{-}NO_3$ and $Zn_3Al\text{-}NO_3$ [147], which should result in a higher surface area and larger pore volume, thus more active sites for adsorption and photocatalysis to occur. Small crystals can also help prevent electron hole pair recombination which augments free radical production and thus oxidation [147], while not affecting the bad gap energy. It can be argued then that within reason, the band gap energy and electronic structure of the LDH is not the only critical feature for photocatalysis and physical characteristics play an important role.

In a similar way as the research into utilising LDHs as adsorbents; research into utilising LDHs as photocatalysts is concentrated on a very small selection of dyes, primarily Acid Orange 52 (methyl orange) and Basic Violet 10 (Rhodamine B) [31, 146, 147]. It is apparent from the data in Table 2.6 that there is strong comparison between a few LDHs and two dyes however there needs to be a greater impetus towards expanding the contaminant database for which LDH materials such as ZnTi, ZnFe and doped LDH photocatalyst have been tested on. There is also a need to evaluate total mineralisation of dye contaminants. The effects of auxiliary compounds such as alkaline fixing agents and electrolyte salts on the competency of the LDH based photocatalysts also need to be investigated. These key areas are lacking in the current literature around the use of LDH photocatalysts for dye wastewater remediation.

Table 2.6 Comparison of LDH based photocatalysts with advanced oxidation processes

Photocatalyst	Dye	Decolouration / %	Degradation / %	Reference
H_2O_2/Solar	Reactive Orange 4	80	50	[75]
TiO_2/Solar	Acid Brown 14	100	100	[79]
TiO_2/UVC	Acid Red 27	100	100	[80]
ZnO/Solar	Basic Violet 10	100	100	[82]
Acetate-ZnO/UVC	Acid Orange 52	-	100	[83]
ZnFe-CO_3/Solar	Basic Green 4	98.5	-	[144]
ZnO/Solar	Basic Violet 1	~40	-	[144]
ZnFe-CO_3/Solar	Basic Violet 1	99	-	[144]
ZnTi-NO_3/Visible	Acid Orange 52	>95	-	[147]
ZnAl-NO_3/Vis	Basic Violet 10	98	-	[31]
ZnTi-NO_3/Vis	Basic Violet 10	96	-	[31]
ZnFe-NO_3/Vis	Basic Violet 10	72	-	[31]
ZnFe-Ti-NO_3/Vis	Basic Violet 10	88	-	[31]

Co-Cr-CO_3/Solar	Acid Orange 52	~90	-	[146]
Ni-Cr-CO_3/Solar	Acid Orange 52	~67	-	[146]
ZnCr-CO_3/Solar	Acid Orange 52	~75	-	[146]
Calcined ZnAl-Ce LDH/Solar	Basic Violet 10	97.8	-	[143]

2.4 Synthesis of Layered Double Hydroxides

2.4.1 Co-precipitation Synthesis of Layered Double Hydroxides

Natural hydrotalcite was first discovered in Sweden in 1842 [1], and research in catalysis utilised layered double hydroxides, however the first open source literature regarding LDH synthesis was a publication by Miayta which is now widely cited by many authors as the method for LDH co-precipitation [8]. There were patents filed around the precipitation synthesis of metal hydroxide based catalysts prior to the publication by Miyata *et al* [1]. Following this first publication several more investigations were completed highlighting the effects of interlayer anion type and coordination and the physical and chemical changes that occurs as a result of these variables [3, 4]. Progressive work found that the changing of interlayer anion results in changes to the basal spacing in the crystal structure and thus the lattice parameters of the material [1]. There are few limitations in terms of the interlayer anion that can be included in an LDH structure, however the cationic metals are limited to metals with similar ionic radii to Mg^{2+} Al^{3+} [9].

Co-precipitation occurs in two distinct ways. The first is termed low super-saturation, under this condition a solution of anion salts is prepared. A base solution, typically NaOH is added drop wise until the pH of the anion solution reaches a nominal value for the desired precipitation. A second precursor solution containing mixed metal salts is slowly added drop wise to the anion and base solution under vigorous stirring. The pH is maintained at the nominal value by further addition of either acid or base throughout the precipitation reaction [9]. It must be noted that for co-precipitation to occur the pH must be in a range where the most soluble metal hydroxide will precipitate and the pH where divalent divalent/trivalent metal hydroxides form [9]. A pH range of 7-10 is

typically used for LDH synthesis [1], however this varies depending the cations incorporated into the LDH sheets [148]. Following the complete addition of the mixed metal solution the resulting suspension is then aged [2]. This method, as mentioned was first published by Miyata *et al* to produce Mg_3Al type LDHs and has become the accepted standard procedure for LDH synthesis on small scale [149-155]. The second method of LDH co-precipitation is termed as high super-saturation, due to the degree of saturation occurring as a result of the immediate change in pH [1]. This method involves a similar process as low super-saturation. The only difference being that instead of the pH being set to, and maintained at a nominal value, a set volume of base is added and the pH is more variable throughout synthesis [139]. This method is utilised to a lesser extent as researchers argue that the LDHs produced via this method are less crystalline than those produced by low super-saturation, due to the fact that nucleation rates are higher than growth rates [1, 9, 139].

A modification of co-precipitation is a method that utilises urea hydrolysis to produce the base for the solution. Some authors hypothesise that the slow breakdown of urea to eventually produce OH^- yields a more crystalline LDH. Ogawa and Kaiho utilised urea hydrolysis to produce highly crystalline Mg_2Al-CO_3 LDHs, however the reaction mixture was hydrothermally treated at 120°C [156]. The slow hydrolysis of urea ensures that the growth step in the co-precipitation reaction is more dominant thus producing highly crystalline platelets. Ogawa and Kaiho produced LDH platelets that were greater than 2μm in size [156]. Despite a highly crystalline product following synthesis, the slow additions of reactants to the vessel can result in differential reaction times for the materials and can result in a wider size distribution of crystals. In an effort to mitigate the issues of co-precipitation researchers have endeavoured to establish different methods of LDH synthesis that do not rely on the slow addition of precursor solutions.

2.4.2 Separate Nucleation and Ageing Steps Methods for the Synthesis of Layered Double Hydroxides

One method to overcome the issue of differential nucleation and growth in co-precipitation was devised by Zhao *et al* and involves separate nucleation and ageing steps (SNAS) rather than the two steps being combined in the fashion of co-precipitation [157]. In this method the authors utilise a rapid mixing step, which is carried out in a colloid mill, to nucleate the LDHs that are then aged separately, the method has been utilised since its first publication to produce a range of different LDHs [158-160]. Yang *et al* the SNAS method to produce $Ca_2Al\text{-}NO_3$ type LDHs [161]. The use of the colloid mill produced highly crystalline thin hexagonal $Ca_2Al\text{-}NO_3$ platelets. TEM micrographs show that the material exhibits low amounts of agglomeration and a seemingly narrow size distribution. Rotation speed in the colloid mill in the nucleation stage has a significant impact on the size of LDH platelets. The fastest rotation speed of the mill resulted in finer particles, suggesting a strict control over crystal size can be achieved through variation in mixing speed [161]. To date the work by Yang *et al* appears to be taking steps forward with this synthesis process as it attempts to better understand the variables affecting the LDH products to see if any improvements to the process can be made to tailor to LDHs for specific applications.

2.4.3 Reverse Micro-emulsions and Aqueous Miscible Organic Solvent Treatment of Layered Double Hydroxides

Synthesis by reverse micro-emulsions involves the addition of an anionic surfactant to an organic solvent. The aqueous solutions containing the LDH precursors are added to the emulsion causing the micelles formed by the surfactant in the solvent to expand [162]. The micelles can be thought to essentially form the basis of miniature reactors

where the co-precipitation of a limited amount of LDH can occur. There are however many micelles in the reaction vessel and therefore the synthesis of a suspension of LDHs forms. This limits the potential for differential growth as the micelles all act individually in the reaction vessel [162, 163]. Hu and O'Hare originally published on the use of micro-emulsion synthesis of LDHs in 2005 and it has been used particularly to produce dispersible LDHs for combining with polymer matrices. The primary concern in this aspect is to produce LDHs with as few layers as possible in a crystal to allow for better dispersion [162, 163].

The use of post synthesis treatment via organic solvents was first published by Wang and O'Hare in 2013 [164]. The synthesis of ZnAl-BO_3 and Mg_3Al-BO_3 LDHs were produced using this post synthesis processing. LDHs produced by conventional co-precipitation methods were subjected acetone aging at room temperature. The results of XRD analysis on the dried LDHs indicate that the LDHs are single sheets exhibiting no reflections in the ⟨00*l*⟩ plane that are most commonly associated with an LDH diffraction pattern [164]. The single LDH sheets also exhibit S_{BET} that is significantly higher than conventionally prepared LDHs, as the specific surface area increases by several hundred square meters per gram due to the smaller single sheet crystals [164]. Further research by Yang *et al* into this form of post processing highlighted the effects of different organic solvents. In total 12 solvents were used in the research [165]. Regardless of organic solvent used the surface area of the tested Mg_3Al-CO_3 LDH increased significantly [165] however in this case XRD patterns indicate that (*00l*) basal reflections, and therefore multiple LDH layers are present [165]. TEM micrographs however indicate that the effect of organic solvent washing is not just that it affects the layering but also the stacking and agglomeration of the LDH. An open flower-like pattern is evident in an ethanol washed sample compared to a water washed sample [165, 166]. The AMOST

post processing appears to be one of the stand out advances for LDH synthesis as it holds the ability to alter significant characteristics of LDH materials through the simple production of single LDH nano-sheets after a simple conventional co-precipitation reaction. The method is still relatively novel in that it has only recently come to light in published literature [166-168].

2.4.4 In-Line Dispersion Precipitation Synthesis of Layered Double Hydroxides

One of the few continuous methods of LDH synthesis investigated; in-line dispersion precipitation (ILDP) was developed Abelló and Pérez-Ramírez [169]. The ILDP method showed promise in terms of controlling crystal size by ensuring strict control over reactor residence time. The nucleation of fine LDH crystals was found to occur almost completely within seconds of the combination of precursor [169]. Crystal size remained consistent with residence times up to 18 seconds, yet the longest continuous residence time (36s) yielded significantly larger crystals. The most notable outcome of the research however, was that the textural characteristics of the LDH change with residence time. The texture goes from a vitreous lustre to a dull or waxy with increasing reaction time. However the vitreous material produced by 1 second of reaction was effectively non-porous with a very low S_{BET} [169]. The only other published literature utilising ILDP highlights the effect of residence time on physical characteristics. Thermal stability is increased when reaction time is minimised [170]. The increased thermal stability is attributed by the authors to stronger interactions of the LDH nano-platelets that cause stronger face-face stacking which in turn reduces the pore volume for the gases to evolve from [170]. There is a trade-off between thermal stability and surface area of LDHs produced via ILDP [169, 170].

2.4.5 Hydrothermal Synthesis of Layered Double Hydroxides

Hydrothermal synthesis of LDHs takes several forms. Most commonly the method can be seen more as post synthesis processing for LDHs produced through the high super-saturation method of co-precipitation. Subjecting an as-synthesised LDH suspension to temperatures above 100°C leads to an increase in crystallinity [2]. Investigations into tailoring of LDH products based on reaction temperature and time have been published by Oh *et al* [171] and Kovanda *et al* [172]. Investigating temperature Oh *et al* identified that increased autoclave temperature resulted in a more crystalline diffraction profile resulting from larger hydrotalcite crystals [171]. Increasing the temperature from 100°C to 180°C but keeping reaction time fixed at 48 hours resulted in a crystal size increase of 115nm to 340nm, respectively. While aging time appears to have a smaller impact on size increase; increased hydrothermal treatment time resulted in crystals 120nm in size (after 72 hours) rather than 85nm (after 12 hours) [171]. Kovanda *et al* identified similar trends in their research. It is interesting to note however that with increased temperature, the effect of reaction time becomes more pronounced. After 18 hours of hydrothermal treatment of a conventionally produced LDH (via co-precipitation) the intensity of XRD reflections is greatly increased for samples treated at 180°C and 200°C compared to those treated at temperatures closer to 100°C compared to samples [172].

Continuous hydrothermal synthesis, which is described in greater detail in Section 2.5.1, is more closely associated with the production of inorganic nanoparticles in the form of metal oxides [173-175]. However Wang *et al* [10] utilised the nozzle reactor design from the University of Nottingham [176] to produce two types of LDH, Mg_3Al-CO_3 and Ca_2Al-NO_3. The research highlighted the effect of reaction temperature and pressure, on the crystal size of LDHs [10]. Changes in chemical structure, more specifically the variation of M^{II}/M^{III} with temperature and pressure are also identified [10]. Under supercritical

water conditions AlOOH formed in the LDH [10]. Work from Adschiri *et al* explains the reason for this occurrence as AlOOH forms readily at supercritical conditions [174, 175]. Particle size distribution, determined from TEM, shows a marked increase in particle size with increased temperature for both $Mg_3Al\text{-}CO_3$ and $Ca_2Al\text{-}NO_3$ type LDHs. Crystallite size, from the Scherrer equation, increases with temperature in the Mg type LDH however crystallite size decreases with temperature in the Ca type [10]. There is a significant decrease in M^{II}/M^{III} ratio in the materials produced under supercritical conditions due [10].

2.4.5.1 Two Stage Synthesis of Core@Shell Composite Layered Double Hydroxides

LDH core-shell materials offer an interesting prospect since the LDH shell and core materials are joined without the need for binding agents. Depending the core material; core-shell composites can be tuned to have specific characteristics. Altering the type of LDH has also been found to affect the characteristics of the core-shell material. First synthesised for use as drug delivery vehicles, magnetic core-shell LDHs were produced via a two-step synthesis process, first the magnetic ferrite core was produced and then the LDH shell was grown through co-precipitation reactions in the presence of the magnetic core [177, 178]. More recently, however, a variety of core nanoparticles have been incorporated into composites following the same two-stage synthesis protocol. Silica spheres surround by $MgAl\text{-}CO_3$ shells have been applied to wastewater treatment for the removal of the anti-inflammatory drug diclofenac [179, 180]. Zeolites have been employed as core materials for adsorbent composites for water treatment as a possible way to utilise the high surface area of zeolites coupled with the ion exchange ability of LDHs [168, 181]. It has been found that the micro-pore volume of the zeolite was

reduced when the shell was synthesised in the zeolite@LDH composite due to blocking of pores by the LDH [168]. Cobalt oxide and zinc oxide cores have been produced via a 2 step a batch hydrothermal method rather than by co-precipitation. In this hydrothermal synthesis method a core material is produced in an autoclave and then dried. A second hydrothermal reaction then produces the outer LDH shell. To date, two stage hydrothermal synthesis reactions have been used primarily to produce nanowires on substrates [182-186].

Co_3O_4 and ZnO composites have been applied in electronics and the two step batch hydrothermal method is preferred as it provides materials as readymade electrodes. ZnO@LDHs have also been utilised in photocatalytic applications along with TiO_2@LDHs TiO_2@CoAl-CO_3 core shell materials have been shown to exhibit water splitting capabilities for H_2 production [187-189] as has ZnO@CuAl-CO_3 [186]. By altering the composite from the most common MgAl-, to ZnCr- type; magnetic core-shell composites have also been applied to adsorption and photocatalysis of methylene blue [190]. All reactions, in published literature, to produce core-shell materials have taken place in multi-step processes, be it hydrothermal or co-precipitation based. The two step synthesis methods for core-shell composite materials are time consuming and to the knowledge of the authors, there have been no attempts to incorporate both reactions into a single process.

The LDH synthesis methods highlighted in this review all present positive and negative outcomes within the resulting LDH product. In terms of scalability it appears that the SNAS, ILDP and conventional methods show little scalability. This is highlighted by the fact that despite initial publication some years ago no further progress has been made in terms of scaling the process for what many researchers see as a versatile material in LDHs. The simplicity of continuous hydrothermal synthesis and the already scalable

production of materials via this method [11], shows that it can be an interesting avenue of investigation.

2.5 Background on the Continuous Hydrothermal Synthesis of Nanoparticles

2.5.1 Theory and Reactor Design at Nottingham

Nanotechnology is the manipulation and control of nano-sized materials. Nano-sized materials take a number of forms be it nanoparticles, tubes or platelets; the common trait of all these materials is that they are less than 100nm in size, in at least one dimension. A nanometer is equivalent to 10^{-9}m and this minute size enables the nanoparticles to have a variety of characteristics that larger bulk particles may not have. Such characteristics enable nanoparticles to apply in various fields of science and engineering [191, 192]. Perhaps, the most apparent characteristic of nanoparticles is the high surface area and high surface area to volume ratio, which is beneficial in catalytic applications.

The focus is this work is surrounding the continuous hydrothermal synthesis (CHS) of nanoparticles and nanomaterials. There is an abundance of literature regarding other methods of synthesis including batch hydrothermal and solvothermal synthesis [193, 194], sol-gel [195] and sonochemical synthesis [196, 197]. Water heated to 374°C and subjected to pressures of 22.1MPa becomes a supercritical fluid, possessing the properties of both a liquid and a gas. The simplified phase and property diagrams in Figure 2.8 illustrate the changes the fluid goes through as it goes through the critical region. Supercritical water also has a low dielectric constant and increased dissociation constant (k_w). The reduced dielectric constant indicates significantly reduced polarity

while the increase in k_w results in a higher concentration of H^+ and OH^- [12, 176, 198-200]. The changes to water as a solvent were first exploited by Adschiri *et al* [173]. The research highlighted the fact that at supercritical conditions the dissociation of the solvent and reduced polarity results in a state of supersaturation occurring and so dissolved metal salts are precipitated as metal hydroxides that then undergo a dehydration reaction to form metal oxides [12, 176]:

$$ML_x + xH_2O \rightarrow M(OH)_x + xHL$$

$$M(OH)_x + MO_{x/2} + {}^{x}/_{2}\, H_2O$$

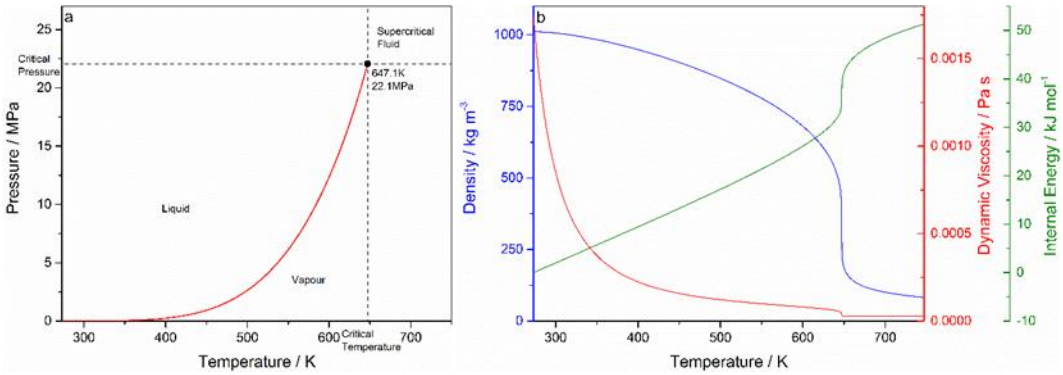


Figure 2.8 a) Water phase diagram approaching the critical region b) Selected properties of sub and super critical water (adapted from Dunne *et al* [12])

Early research in the field of CHS at the University of Nottingham (Nottingham, UK) utilised a Swagelok® stainless steel T-piece reactor, as it was easily obtainable and allowed the rapid heating and mixing of precursor solutions in order to induce the reaction mechanism outlined above. However, it was found that product repeatability and reliability were hindered with this reactor configuration [176]. Research by on the cause of the low reproducibility of the nanoparticle products involved a combination of methods. Light Absorption Imaging (LAI) was performed in a pseudo reactor constructed from Perspex [201]. The Perspex reactor allowed a visual demonstration of

the mixing within the T-piece reactor to be modelled at ambient conditions. Pseudo-fluids were chosen to represent the low density supercritical water stream (methanol) and the cold precursor metal salts (sucrose solution in water) [201]. It was found through observations of the pseudo-fluids that a number of mixing phenomena were the cause of the low reproducibility [201, 202]:

1. Flow partitioning – The different densities of the two reactor inlet streams leads to a separation of flow into discrete channels resulting in little to no mixing.
2. Stagnant zones – Areas of the reactor become cut off from the net flow allowing the potential build-up of product or poor mixed precursors.
3. Inlet mixing – The density difference between the inlet fluids results in pre-mixing and mixing of fluids at one or both inlet streams rather than solely in the mixing zone.

Despite the low flow and the Reynolds numbers of the two inlet flows being low, in some instances, turbulent mixing of liquids was observed [201]. This was due the density difference between the two inlets and the convection/buoyancy of the lower density fluid caused the turbulent mixing in what appears to be a laminar flow system [176, 201, 202]. This facet was utilised to produce a pipe-pipe counter-current flow reactor where by the density difference of the cold and supercritical water induces rapid mixing of precursors without any of the phenomena that inhibited the T-piece reactors [176, 199, 203]. Other reactor shapes that have moved away from the initial T-piece reactor systems include a co-current system developed through research at University College London (London, UK) [204-206].

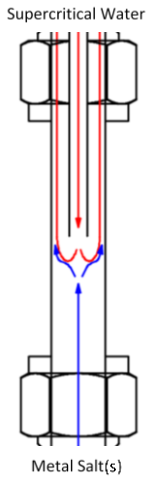


Figure 2.9 Pipe-in-pipe counter-current reactor design from the University of Nottingham. Image adapted from Lester *et al* (2006) [176]

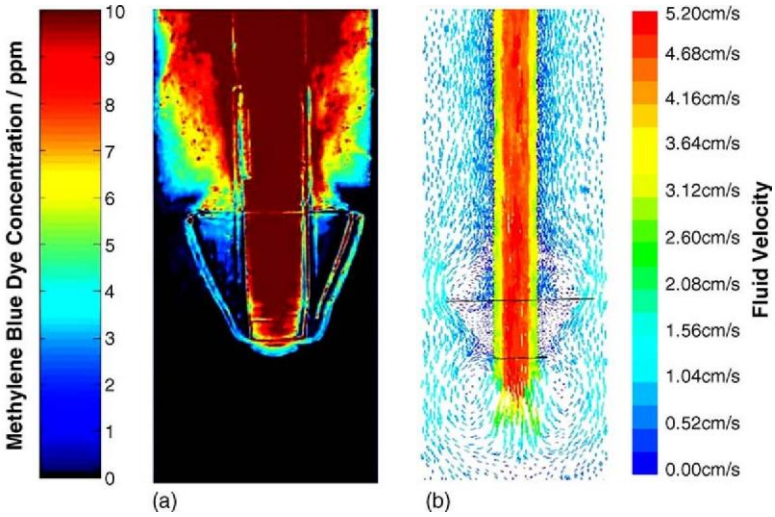


Figure 2.10 (a) LAI steady state concentration map of the Nozzle Reactor (b) steady state CFD simulation calculated using FLUENT. Both simulations at flow rates of 10ml min^{-1} and 5ml min^{-1} for supercritical water and aqueous metal salt respectively. Used with permission from Lester *et al* (2006) [176].

2.5.1.1 Synthesis of Metal Oxide Nanoparticles

A vast array of metal oxide nanoparticles have been produce by continuous hydrothermal synthesis at supercritical and subcritical conditions. These materials

include but are not limited to Fe_3O_4 [175], CeO_2 [175, 207], ZrO_2 [175, 208, 209], Co_3O_4 [175, 199, 210], TiO_2 [175, 176, 192, 211] and ZnO [176, 212-216]. The bias of this research is towards to mitigation of dyes in wastewater, materials such as ZnO and TiO_2 were highlighted as two semiconductors with photocatalytic oxidation potential in Section 2.3.2.1. Therefore the synthesis of ZnO will be reviewed further in this section of the literature study. ZnO has been investigated with many aspects of the synthesis scrutinised heavily by Demoisson *et al* in a number of research articles investigating the influence of both OH^- and Zn^{2+} precursor concentration has on the physical characteristics of the ZnO nanoparticles [214, 215]. The OH^- concentration in relation to the Zn^{2+} concentration was found by the authors to affect the aspect ratio and size of the ZnO. Zn^{2+} was fed into a supercritical flow reactor at two different concentrations, 0.06M and 0.02M, KOH was then fed into the reactor at concentrations between 1 and 8 times the Zn^{2+} concentration [214]. Crystal size analysis indicated that for both concentrations of Zn^{2+}, extremes of high and low KOH concentration resulted in platelet or rod like particles respectively, suggesting that a $[OH-]/[Zn^{2+}]$ ratio of approximately 4 provides the optimum conditions for spherical particles [214]. Zn concentration was found by the authors to have a similar effect as [KOH]. The $[OH^-]/[Zn^{2+}]$ ratio was maintained at 6 and Zn^{2+} was varied between 0.010M and 0.48M. The authors found that the aspect ratio again changes with low Zn^{2+} resulting in rod-like particles while the maximum concentration producing platelets and a concentration of 0.063M producing the most spherical particles [215]. The size and shape control of nanoparticles is of great importance when thinking of applications as these two factors can influence the physico-chemical properties of the nanoparticles [217].

2.6 Summary

The key water and wastewater legislation in Europe covers BOD and COD as the measures of pollution, with total nitrogen and phosphorus as well as priority compounds ranging from heavy metals to pesticides. These target pollutants and pollutant metrics broadly cover the pollutants from the textiles and dyeing industries yet do not cover them explicitly. However, the global nature of the textile industry and the dyeing processes require, and produce large amounts of water. Much of this water needs to be treated to remove residual colour, BOD and COD from the dye compounds themselves and auxiliary salts that aid diffusion and fixation.

The removal of such contaminants is taxing due to the recalcitrant nature of many dyes and advance wastewater treatments are required. Biological treatments are less effective, particularly in aerobic environments at breaking down the most refractory dyes. Advanced oxidation methods are useful at removing colour, yet the residual COD and TOC from oxidation intermediates remains a problem. There is also an issue with AOPs that prevents meaningful recovery of dye compounds.

Physical treatments such as membrane filtration and ion exchange are exceptional when concerned with dye removal and recovery. Steric and static rejection of dye molecules from NF membrane filtration was consistently at >95% across the literature surveyed, while salt rejection remained low. In this case membrane filters represent a strong treatment method for dye/salt separation and water treatment. Polymeric ion exchange resins offer versatility in that they can be cationic and anionic in order to target basic, acid and reactive dyes while solvent washing allows recovery of the dye molecules.

LDHs when activated as a mixed metal oxide offer adsorptive capacity unrivalled by activated carbon and the separation of dye molecules with salts such as NaCl is high. The propensity of MMOs to reform LDHs with intercalated CO_3^{2-} ions can be an inhibiting factor in their use, however the impact of soda ash from dye baths on dye adsorption is dependent on the dye molecule in question and the MMO adsorbent could not be ruled out, especially due to the high adsorption capacity and easy retention through solvent washing. LDHs and Ion exchange resins are comparable materials in terms of dye adsorption. There is however a lack of real world applicability to LDH adsorbents.

There is a substantial amount of research regarding adsorption kinetics and processes in bench scale systems with any notable published works on column adsorption. Column adsorption in a fixed bed is the most common way to find ion exchange and activated carbon absorbers. Work into the possibility of LDH based adsorbents in a fixed bed mode is essential if LDHs are to be utilised as a method of water treatment. There is also a large gap in literature regarding adsorption and degradation by photocatalysis of reactive dyes where LDHs are used as the primary remediation tool. The data in Table 2.5 and Table 2.6, illustrates this fact well. The application of LDHs for adsorption of acidic dyes is has been well documented. Adsorption of other dye classes such as reactive dyes is relatively scarce in comparison. The impact of larger reactive dye molecules with different functional groups compared with acidic dyes is something that must be investigated further; especially as the findings on activated carbon adsorption indicate that for large dye molecules access to microporous structures can be inhibited [34].

The synthesis of LDH nanomaterial has been researched in depth since Miyata *et al* first published the method of co-precipitation synthesis in the 1970s. Since then there have been attempts to improve upon the perceived drawbacks of this mode of synthesis. The SNAS method attempts to separate the nucleation and aging steps as does batch

hydrothermal synthesis, which acts much like a co-precipitation then hydrothermal aging, two-stage process. Then there is the continuous in-line-dispersion-precipitation method (ILDP) which is the only continuous mode of LDH synthesis other than continuous hydrothermal methods Co-precipitation, SNAS and batch hydrothermal methods are most often discussed in small scale batch synthesis in research literature, There are however, industrial scale synthesis processes and commercially available LDHs from Sigma Aldrich, and Sasol Ltd.

Continuous hydrothermal synthesis however, which has been demonstrated in a bench scale reactor at a net flow of 30mL min^{-1}. This reactor design form the University of Nottingham has also been scaled to a pilot scale model that has successfully produced hardened ceramic nanomaterials under the same conditions as a bench scale process. It could be foreseen then, that with refinement of bench scale LDH synthesis in a continuous hydrothermal method could be scaled in a similar way to pilot and then industrial scale synthesis.

3. Materials and Methods

This chapter describes experimental methods used in this thesis as well as the analytical techniques utilised to identify and characterise nanoparticles and LDHs. The experimental methods and analysis of data will also be described in this chapter in a general discussion, covering the theory behind the analysis techniques and the operational conditions employed in the research.

3.1 Nanoparticle Synthesis

3.1.1 Reagents and Chemicals

All chemicals for precursor solutions were reagent grade and were used as received. Aluminium nitrate ($Al(NO_3)_3.9H_2O$ ≥99%), was purchased from Acros Organics (Geel, Belgium). Sodium nitrate ($NaNO_3$ ≥99%), Sodium hydroxide (NaOH ≥98%), Calcium nitrate ($Ca(NO_3)_2.4H_2O$ ≥99%), Zinc nitrate ($Zn(NO_3)_2.6H_2O$ ≥98%), Sodium carbonate (Na_2CO_3 ≥99%), Magnesium nitrate ($Mg(NO_3)_2.6H_2O$ ≥98%) and were purchased from Sigma Aldrich (Dorset, United Kingdom). Prior to synthesis, fresh precursor solutions were prepared by dissolving metal salts in deionised water.

3.1.2 Continuous Hydrothermal Synthesis Layered Double Hydroxides

LDH synthesis was performed using the counter-current hydrothermal reactor designed at the University of Nottingham (Figure 3.1) [176]. A mixed solution of M^{II} and M^{III} metal salts (Solution A) was prepared by dissolving the appropriate amount of nitrate salts in deionised water. A second precursor solution consisting of the base and the anion was again prepared by dissolving the appropriate mass of sodium salt in deionised water

(Solution B). Solution A was fed unheated via the up-flow feed into the reactor system, at 10mL min^{-1}. Solution B was fed via the down-flow, at 20mL min^{-1}, into the top of the reactor having been heated to the desired temperature by a 2kW band heater. The Reaction temperature was monitored and maintained by two thermocouples positioned immediately after the heater and before the reactor in the down-flow feed and after the mixing point in the outer tube of the reactor (T1 and T2-Figure 3.1b). Following synthesis, samples were centrifuged and washed with deionised water. This process was repeated until residual counter ions were removed and the suspension failed to settle following centrifugation. After washing samples were either oven or freeze dried. Freeze dried samples were ground into a fine powder, using a pestle and mortar, ready for characterisation (Chapter 4, Chapter 5 and Chapter 7) and adsorption (Chapter 6) studies.

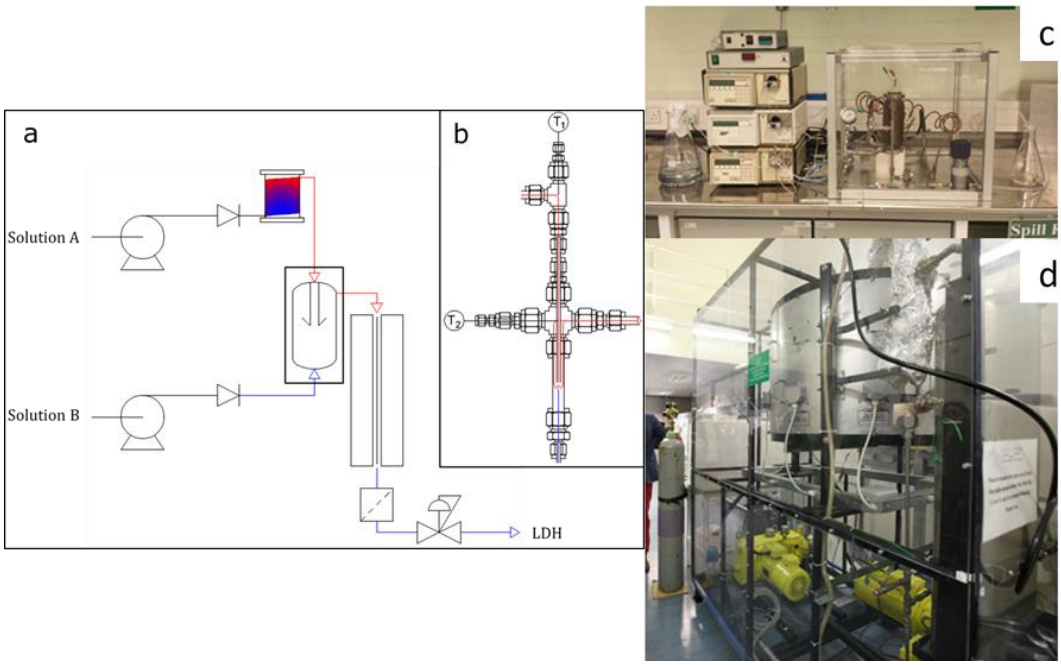


Figure 3.1 Continuous Hydrothermal synthesis schematic a) reactor system b) technical drawing c) bench scale reactor d) pilot scale reactor

Multiple types of LDH were synthesised as part of this research in an effort to identify the most appropriate reaction conditions for crystalline materials with a view to maximise surface area and incorporate enhanced electrical properties to facilitate a broader range of applications. The LDHs produced from this research are summarised in Table 3.1.

Table 3.1 Conditions for continuous hydrothermal synthesis of Layered double hydroxides

Solution A	Concentration / mol L^{-1}	Solution B	Concentration / mol L^{-1}	Temperature / K	Pressure / MPa
$Ca(NO_3)_2$	0.075	NaOH	0.01-1	348-473	5-20
$Al(NO_3)_3$	0.025	$NaNO_3$	0.025		
$Zn(NO_3)_2$	0.067	NaOH	0.125	293	24
$Al(NO_3)_3$	0.033	Na_2CO_3	0.017		

The experiments focusing on the synthesis of $Ca_2Al\text{-}NO_3$, were carried out with changing reaction variables. The primary variables targeted in the experimental matrix were temperature, pressure and precursor NaOH concentration. Synthesis of $Zn_2Al\text{-}CO_3$ was performed under ambient temperature conditions, because under higher temperature conditions (>303K), $Zn(OH)_2$ precipitates can undergo dehydration and form ZnO [213].

3.1.3 Pilot and Industrial Scale Synthesis of Layered Double Hydroxides

Pilot scale synthesis of $Zn_2Al\text{-}CO_3$ type LDH was carried out in a reactor that was scaled to accommodate flows approximately 20-30 times greater than bench scale. This increased flow allows the production to be increased significantly from approximately 5g h^{-1} in the bench scale reactor to 100-150g h^{-1} in the pilot scale reactor. Reaction conditions remained the same when scaling LDH synthesis from bench to pilot scale (24MPa and 293K).The down-flow feed was set at 400mL min^{-1} while the up-flow feed

rate was set at 200mL min^{-1}. $Zn(NO_3)_2.6H_2O$ concentration was set at 0.067mol L^{-1} and $Al(NO_3)_3.9H_2O$ was set at 0.033mol L^{-1}. NaOH concentration was 0.125mol L^{-1} and Na_2CO_3 was 0.017mol L^{-1}. Industrial scale synthesis was performed on the continuous flow reactor at Promethean Particles Ltd. Solutions were prepared as before with concentrations equal to the bench and pilot scale synthesis; however the scale of the synthesis operation was increased by a factor in the region of several hundred times. The flow rate of the industrial synthesis system was 1050L h^{-1} compared to 36L h^{-1} and 1.8L h^{-1} for the pilot and bench scale systems respectively.



Figure 3.2 Computer generated image of the industrial scale SHYMAN reactor system

3.1.4 Continuous Hydrothermal Synthesis Zinc Oxide Nanoparticles

Zinc oxide nanoparticles were produced as a reference point for metal oxide@LDH nanocomposites. $Zn(NO_3)_2.6H_2O$ (0.05mol L^{-1}) was pumped via the up-flow feed at 10ml min^{-1} while NaOH (0.05mol L^{-1})was pumped through the down-flow feed at 20ml min^{-1}. The up-flow was left unheated while the down flow was heated to 623K. Following synthesis samples were centrifuged and washed with deionised water.

3.1.5 Continuous Hydrothermal Synthesis of Metal Oxide@Layered Double Hydroxide Core-Shell Nanocomposites

In order to continuously produce a zinc oxide@LDH nanocomposite, alterations to the reaction system were required. The primary change to the system was the installation of a second counter current reactor. The second reactor is larger than the first, consisting of $^1/_4$" tubing inside $^1/_2$" rather than $^1/_8$" inside $^3/_8$" (Figure 3.3b). The size change was to reduce the potential for blockages, at the outlet of the inner tube. In the synthesis of the core-shell nanocomposite the metal oxide core was produced in the first reactor (R_1) and then the effluent from the first reactor was cooled from the near and supercritical temperatures. This feed was then met with a feed line of Solution B (NaOH and Na_2CO_3). This mixed feed then acted as the down-flow into the second reactor and was heated to the desired temperature. Meanwhile a 4th feed of Solution A was pumped as the up-flow into the second reactor, a schematic of the sequential reactor arrangement is detailed in Figure 3.3a.

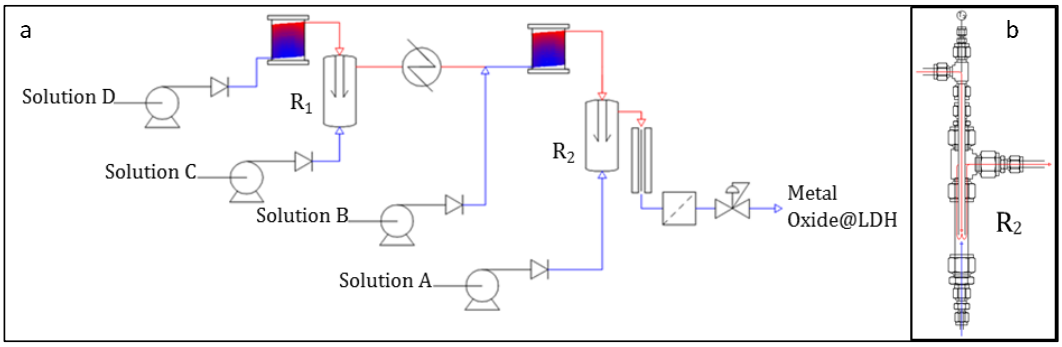


Figure 3.3 Sequential reactor system for core-shell nanocomposites

In order to maintain 2:1 flow ratios within both reactors the feed for solution A was set at 20mL min^{-1} while the feed for solution B was set at 10mL min^{-1}. To accommodate the change in flowrate, the concentrations of solution A were adjusted to 0.033mol L^{-1} and

0.017mol L^{-1}, for Mg^{2+} and Al^{3+} respectively. Solution B was adjusted to 0.15mol L^{-1} and 0.017mol L^{-1}, for NaOH and Na_2CO_3 respectively. The NaOH concentration in solution D was set to 0.05mol L^{-1} and the Zn^{2+} in solution C was also set to 0.05mol L^{-1}. The temperature in R_1 was 623K and the temperature in R_2 was 373K. A comparison of the composite nanomaterial and pure ZnO and pure LDH was also made by producing ZnO following the procedure in Section 3.1.4 and $Mg_2Al\text{-}CO_3$, in a procedure modified from Section 3.1.2 (Figure 3.4). Following synthesis, the suspensions were centrifuged and washed with deionised water and freeze dried.

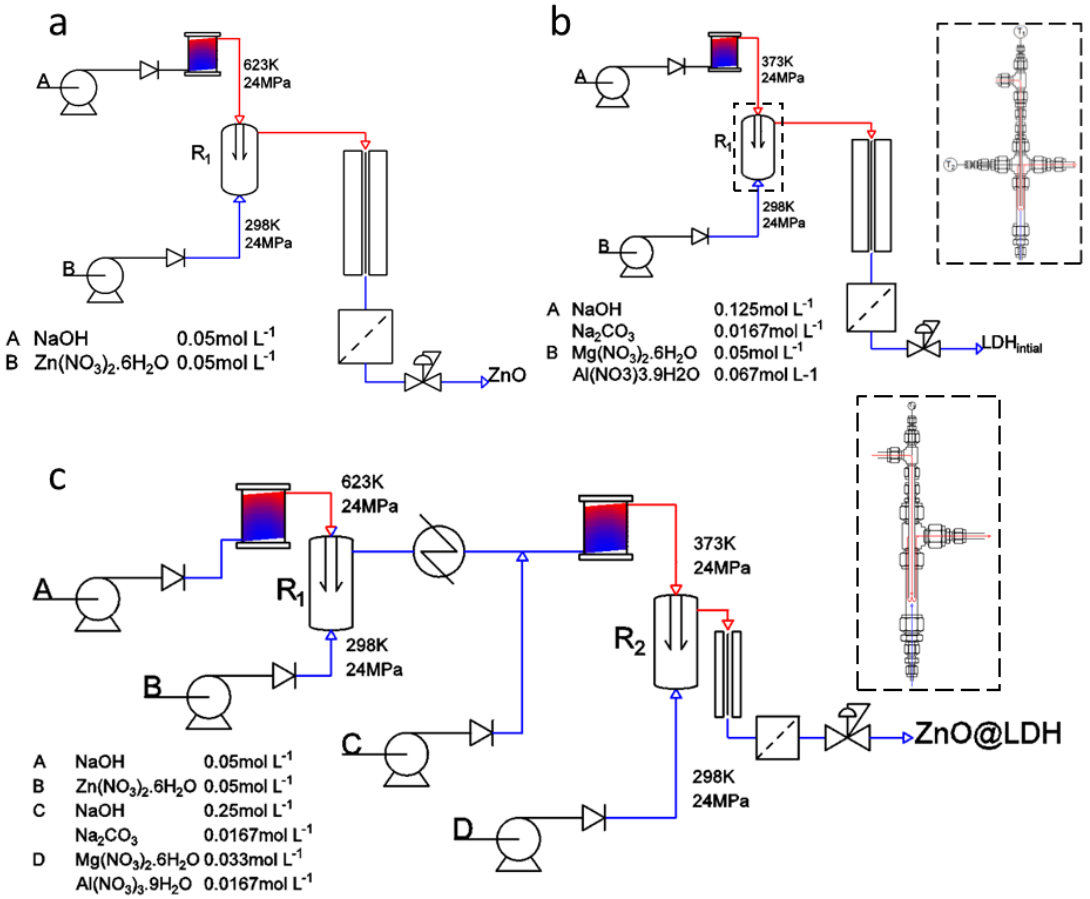


Figure 3.4 Schematic diagrams of reaction arrangements for a) $Mg_2Al\text{-}CO_3$ ($LDH_{initial}$) b) ZnO and c) ZnO@LDH composite synthesis

3.1.6 Materials Characterisation

3.1.6.1 X-ray Diffraction

Materials identification is a key analytical stage in the synthesis and characterisation of LDHs, nanoparticles, nanocomposites. X-ray diffraction is the most common technique used for materials identification in crystalline solids. X-rays are fired from a source into a sample. When the incident X-ray beam impacts the sample, X-rays are scattered (Figure 3.5) [218].

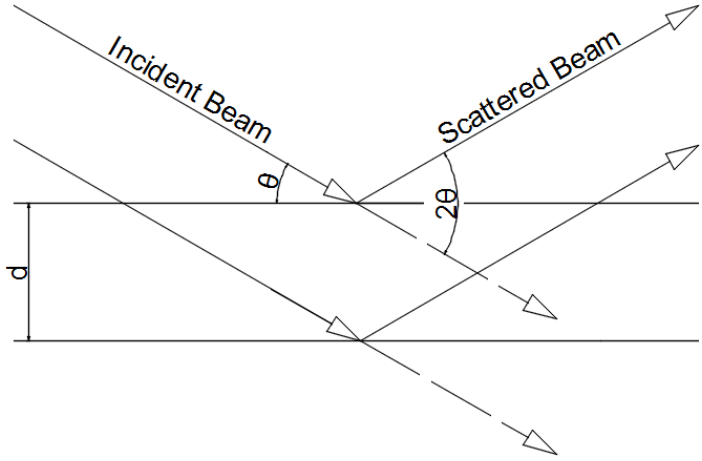


Figure 3.5 Schematic detailing symmetric Bragg reflection [218]

The scattered beam is distributed in relation to the electronic structure of the sample, and as such the X-ray diffraction pattern is specific to the structure of the sample [218]. Crystalline materials can be analysed by X-ray diffraction if they have long range order and periodic arrangements of atoms. Materials lacking repeating periodicity of atoms and long-range order are amorphous. Amorphous materials have diffraction patterns without intense reflections and often show broad asymmetric reflections of low intensity covering a wide range of angles. For a perfect crystal containing no imperfections, a diffraction pattern will contain vertical lines rather than peaks. The structure of a crystalline material and its diffraction pattern can be related by several

equations. For powder diffraction analysis the Bragg law is the simplest way to define the relationship. The Bragg equation defined in (3.1), relates the reflection angle and the wavelength to the inter-planar spacing.

$$n\lambda = 2d\sin\theta \qquad (3.1)$$

Where the n is a constant (n=1), λ is the X-ray wavelength, d is the spacing between crystal planes and θ is the Bragg angle. The inter-planar spacing (d) can be utilised to calculate lattice parameters of a unit cell. A unit cell is the smallest volume of a crystal which has the same order as the overall crystal (Figure 3.6). Repeatedly translating the unit cells in the 3-dimensional space will eventually produce the crystal lattice [218].

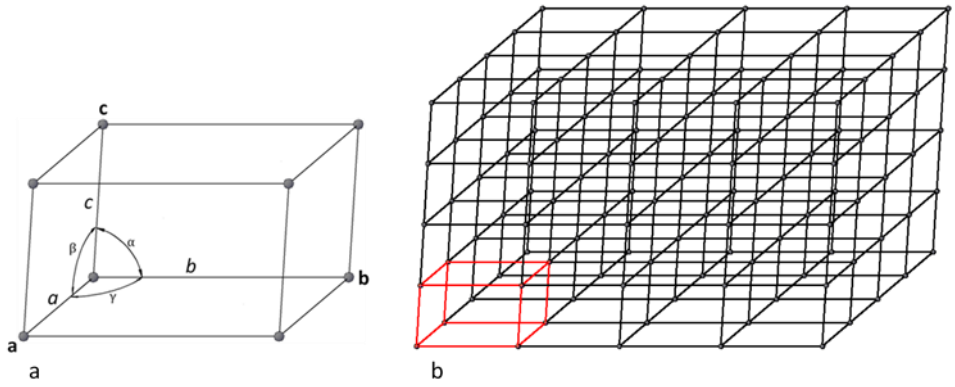


Figure 3.6 Schematic diagram of a) Unit cell and lattice parameters b) Repeating unit cells in a crystal lattice [218]

Unit cells are defined by a number of measurements known as lattice parameters. Lattice parameters are individual to a particular crystal [218]. Lattice parameters are defined as a, b and c which relate to lengths of the unit cell edges between lattice points. The edges of a unit cell run along crystal planes that are defined by miller indices (*h,k,l*) [218]. Lattice parameters relating to the angle of the crystal planes of the unit cell are defined as *α*, *β* and *γ*, however in most cases these values are fixed at either 90° or 120° and are often equal to each other (*α=β=γ/α=β≠γ*) [218]. Depending on the crystal system an

equation can be used to calculate the lattice parameters of the unit cell. In this research hexagonal crystal systems were encountered for most particles. The equations for lattice parameter calculation are detailed below:

$$\frac{1}{d^2} = \frac{4}{3}\frac{(h^2+hk+k^2)}{a^2} + \frac{l^2}{c^2} \quad (3.2)$$

Where d is the inter-planar spacing, h, k and l are miller indices relating to a specific crystal plane, *a* and *c* are lattice parameters. In tetragonal and hexagonal crystal systems *a*=*b* [218]. In practice a crystal is rarely perfect and contains either point, line or plane imperfections. Such imperfections can result in the broadening of reflections in diffraction patterns known as strain broadening. Broadening can also arise from other sources, such as instrumental broadening, which occurs as a result of beam divergence and varies with the Bragg angle; and size broadening, whereby reflection broadening increases with decreasing crystal size. The width of a diffraction peak at half the maximum intensity, the full width at half maximum (FWHM) can be used in conjunction with the Scherrer equation to calculate the crystal domain length in a particular crystal plane [218].

$$CDL = \frac{S\lambda}{B\cos\theta} \quad (3.3)$$

Where CDL is the crystal domain length, S is the Scherrer constant which, in this instance, is taken as 0.9, λ is the wavelength of the X-ray beam, B is the FWHM, and θ is the Bragg angle [218]. In order to account for instrumental broadening, the use of a perfectly crystalline standard to measure instrumental broadening across the 2θ range of the diffractogram. The instrumental broadening of the sample reflections, and the impact it has on the FWHM, can be accounted for in the calculation the CDL. Crystal domain length as calculated by the Scherrer equation will not necessarily give accurate particle size nor

will it give particle size distribution. In order to calculate size distributions of particles and account for potential agglomeration and amorphous content electron microscopy is also employed in material characterisation.

XRD analysis in this research project was carried out on a Bruker D8-A Diffractometer using Cu Kα radiation (λ=0.15418nm) in a 2θ range of 2°-70° and a scanning rate of 0.75° min^{-1}. This range was chosen to cover the range 2θ where LDHs exhibit characteristic reflections. Intense symmetric reflections are found at lower 2θ angles and broader less intense reflections are found at higher angles [9]. A LaB_6 reference material was scanned to enable instrumental broadening to be accounted for. Strain broadening was not accounted for in CDL calculations. Calculation of the *a* and *c* lattice parameters and the CDL of LDHs utilised the (*002*) / (*003*) and (*030*) / (*110*) reflections from X-ray diffractograms. Bragg angle of the reflections was used in the lattice equation (3.2) to calculate lattice parameters.

3.1.6.2 Specific Surface Area and Pore Size Distribution

Specific surface area can be ascertained through adsorption of an inert gas onto the surface of a dried sample. The amount of gas adsorbed with each dose can be calculated using the known volume of the gas added to the sample and the partial pressure of the sealed sample vessel following equilibration. The surface area can be calculated based on the size of the gas molecules and the volume of gas adsorbed. A number of calculations can be used to establish the surface area of a material, most common is the use of the Brunauer-Emmett-Teller theory, which accounts multilayer adsorption of gas molecules and is outlined in equation (3.4) [219].

$$\frac{{}^{P}/_{P_0}}{V\left(1-{}^{P}/_{P_0}\right)} = \frac{1}{V_m B} + \frac{(B-1)^{P}/_{P_0}}{V_m B} \qquad (3.4)$$

Where P/P_0 is the partial pressure, V is the volume of the gas adsorbed at a given partial pressure, V_m is the monolayer capacity of the material and B is an experimental constant. As the dosed gas volume increases all pores will eventually fill. At this stage as desorption occurs the pore size distribution can be calculated using the Berrett-Joyner-Halenda model.

For this research nitrogen was used gas for adsorption at 77K. Prior to adsorption, materials were outgassed overnight at 105°C to remove surface bound water and any impurities that may be present in the sample. Following outgassing, the samples were analysed on a Micromeritics Tristar II 3020 instrument. Isotherms were collected using a pre-loaded dosing program to calculate surface area and meso-pore distribution. Partial pressure dosing for the adsorption branch of the isotherm was between 0.0125 and 0.998.

3.1.6.3 Scanning Electron Microscopy and Energy Dispersive Spectroscopy (SEM-EDS)

Following identification through X-ray diffraction analysis samples can be inspected to ascertain the surface morphology and size distribution of particles within the powder. Particle size may not directly correspond to crystal size as agglomeration and stacking result in crystals packing together as well as some amorphous content within the sample. Scanning electron microscopy (SEM) is the most common method of elucidating surface morphologies of nanomaterials and LDHs. SEM microscopes work by firing electrons at a sample. Acceleration voltage of electrons in SEM imaging is typically in the region of 100V-30kV (Figure 3.7) [220]. Increasing acceleration voltage causes internal structures to become visible in the SEM micrograph, thus the image can become blurred [220, 221].

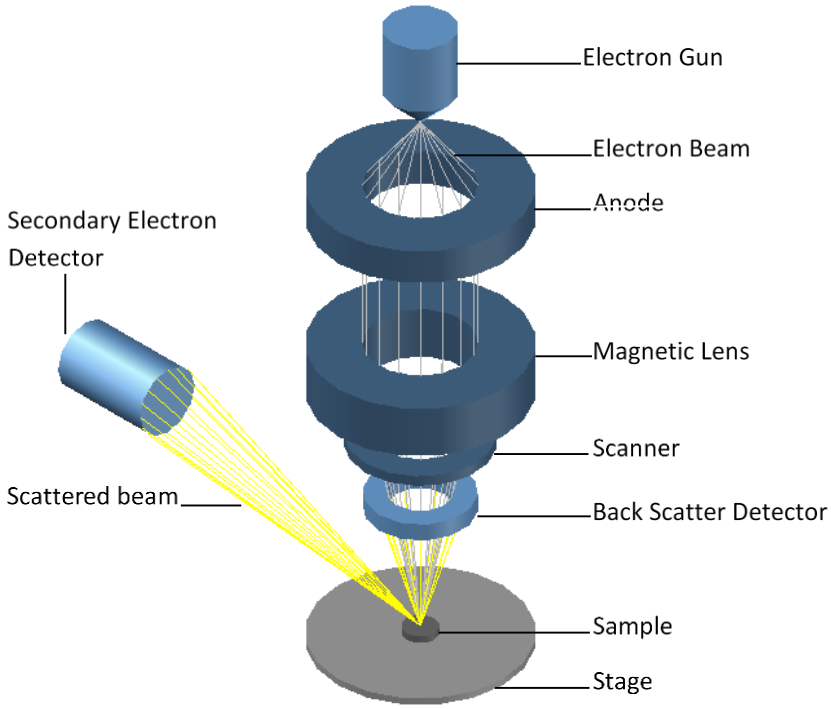


Figure 3.7 Schematic of a Scanning Electron Microscope

SEM micrographs were captured on two different microscopes, one was a Siemens XL30 FEG ESEM and the second was a Siemens XL30 with a tungsten filament (XL30W) using the SE detector. Acceleration voltage was 20kV for both SEM and spot size was fixed at either 3 or 4. Prior to analysis samples were adhered to a carbon tab and a coating was applied to make the surface more conductive. A platinum coating was applied using a sputter coater (Palaron), in a film approximately 15nm thick, in order to improve surface conductivity of the sample. SEM micrographs were then used to evaluate particle stacking characteristics which could be related to surface area.

The ratio of metals in the LDHs and composites was analysed using Energy Dispersive Spectroscopy analysis (SEM-EDS). SEM-EDS analyses the X-rays emitted from the sample as the electron beam impacts the sample. Elements release X-rays of specific energy intensity due to different electron configurations [220, 221] (Figure 3.8) . The

EDS analysis was performed using Oxford Instruments EDS detector and INCA software (Oxford Instruments). Prior to analysis samples were pelleted. Pelleting of sample was used to ensure a flat surface for suitable analysis. Sample pellets were adhered to a carbon tab and then carbon coated. Carbon coating was applied by evaporation coating using a turbo carbon coater (Agar Scientific). The carbon film was approximately 15nm thick.

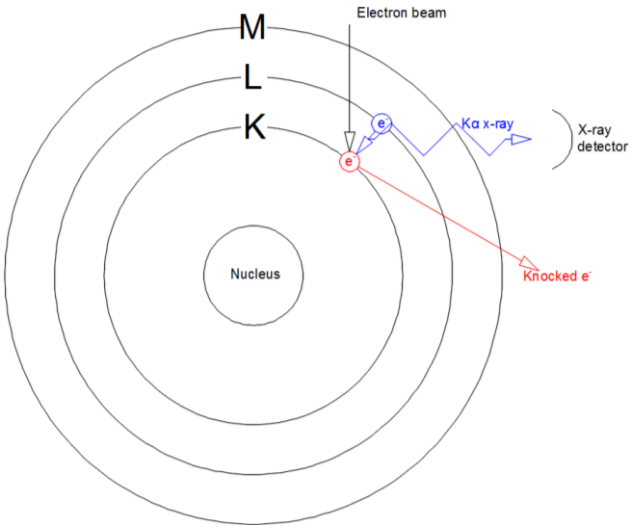


Figure 3.8 Kα generation in Electron Dispersive X-ray Spectroscopy

3.1.6.4 Transmission Electron Microscopy

Transmission electron microscopes (TEM) operate with acceleration voltages >100kV, and the available zoom is ≥x1000000 [220]. Electrons from the emitted beam encounter the sample and are either transmitted or scattered [220, 221]. Transmitted electrons pass through the sample and subsequent lenses to the fluorescent screen at the bottom of the column (Figure 3.9). Scattered electrons do not reach the fluorescent screen and generate contrast in the electron micrograph. Scattered electrons can also be used for elemental analysis with EDS [221].

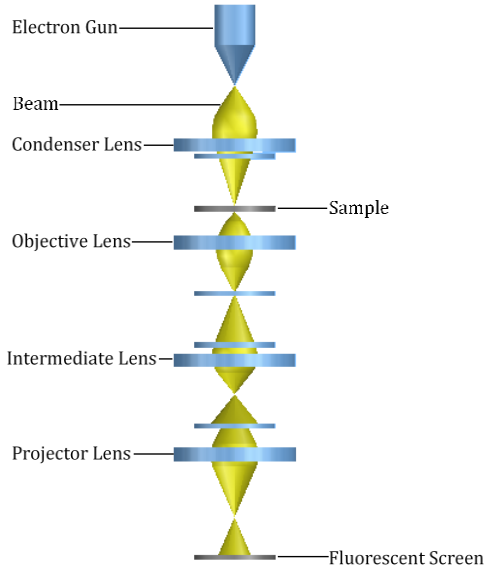


Figure 3.9 Schematic of an imaging column in a transmission electron microscope (TEM)

For the purposes of this research TEM was used to verify crystal and particle size of LDHs and nanoparticles in comparison with the Scherrer crystal size calculated from XRD, and to establish [particle size distribution through image analysis. In general image analysis was performed on micrographs with between 50-200 particles. TEM analysis was performed on a JEOL 2100+ TEM with an acceleration voltage of 200kV. Prior to analysis samples were dispersed in an organic solvent, and sonicated for 15 minutes and then dropped onto lacy carbon films on 300 mesh copper grids (Agar Scientific). Images were captured using a Gatan Orius digital camera.

3.1.6.5 Ultra Violet-Visible Light Spectroscopy

Spectroscopic characterisation in the UV-Visible range of the electromagnetic spectrum (λ=100-700nm) provides information on the optical and electric properties of materials. When an incident beam impacts a material surface the beam experiences various phenomena, absorption, reflectance, transmittance and scattering. Absorption of light by a material is simply described by the Beer-Lambert law in equation (3.5).

$$\text{Absorbance} = \varepsilon Cl \qquad (3.5)$$

The Beer-Lambert equation can be used to calculate the extinction coefficient of a material at a given wavelength using information from the spectrum. Extinction coefficients can then be applied to determine the band gap energy (E_g) of semiconducting materials. The band gap of a semiconducting material is the energy required to promote an electron from the valence band to the conduction band, in general, lower band gap signifies less energy required to promote electrons and so the transition can occur at higher wavelengths of light. The Tauc equation was describes the relationship of band gap and radiation energy [191]:

$$\varepsilon h\nu = A\left(h\nu - E_g\right)^n \qquad (3.6)$$

In the Tauc equation hν is the energy the incident photon, which varies for a given wavelength, A is a constant and n relates to the manner of the electron transition. The value of n varies depending on the type of transition that occurs, these transition types are broadly categorised as direct transitions (n= $^1/_2$or $^3/_2$) and indirect transitions (n=2 or 3). The most common form of transition in a semiconductor is direct allowed (n= $^1/_2$) [222]. Direct and indirect transitions differ in the shared wave vector between the conduction and valence band [223]. Direct transitions occur when the conduction and valence band share a wave vector, whereas indirect transition happen the wave vector is not common between the conduction and valence bands [223] (Figure 3.10).

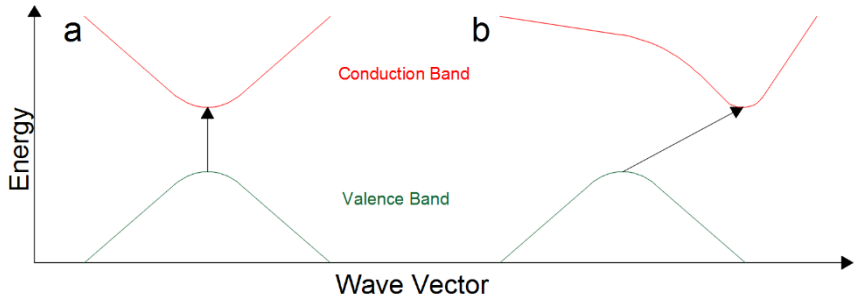


Figure 3.10 Schematic of direct (a) and indirect (b) electron transitions. Adapted from Numai (2015) [223]

The Tauc equation can be expanded to form a linear equation. A modified version of the Kubelka-Munk function can be used for scattering and absorbing particles in the matrix. The modified equation can be used in conjunction with an integrating sphere attachment on a UV-Vis spectrophotometer to collect diffuse reflectance data (DRS). The Kubelka-Munk function [145, 224]:

$$F(R) = \frac{(1-R)^2}{2R} \quad (3.7)$$

Where F(R) is Kubelka-Munk value, R is the diffuse reflectance. The F(R) value can be substituted with ε in the Tauc equation giving rise to:

$$F(R)h\nu = A(h\nu - Eg)^n = (F(R)h\nu)^{1/n} = A(h\nu - E_g) = (F(R)h\nu)^{1/n} = Ah\nu - AE_g \quad (3.8)$$

A plot of $(F(R)h\nu)^{1/n}$ vs hν can then be used to determine E_g, by extrapolating the linear sections of the line to $(F(R)h\nu)^{1/n}$ to the x-axis. UV-Vis-DRS spectra were collected on a Varian Cary 300 UV-Vis spectrophotometer, with an integrating sphere attachment (DRA-CA-30I), in the wavelength range λ=200-700nm.

3.2 Adsorption of Reactive Dyes onto LDHs

3.2.1 Batch Experimentation

3.2.1.1 Adsorbate Dyes

Adsorption of dye onto calcined $Zn_2Al\text{-}CO_3$ LDHs utilised 2 different reactive dyes: Reactive Black 5 (RB5), and Reactive Orange 16 (RO16) (Figure 3.11). Reactive Black 5 (≥50%) and Reactive Orange 16 (≥70%) were obtained from Sigma Aldrich (Dorset, United Kingdom) and were used without further purification. Dye solutions were made fresh before each experiment in deionised water. Both RB5 and RO16 are azo dyes, which are the most common type of synthetic dye accounting for 60-70% of all dyes produced. Compared with RO16, RB5 is a larger molecule with more sulfonate functional groups. The impact of the differences in dye molecules is important for the expansion of LDHs as an adsorbent material for synthetic dyes. Previous research has found that the size of the prospective interlayer anion can affect adsorption efficiency and mode of adsorption [122].

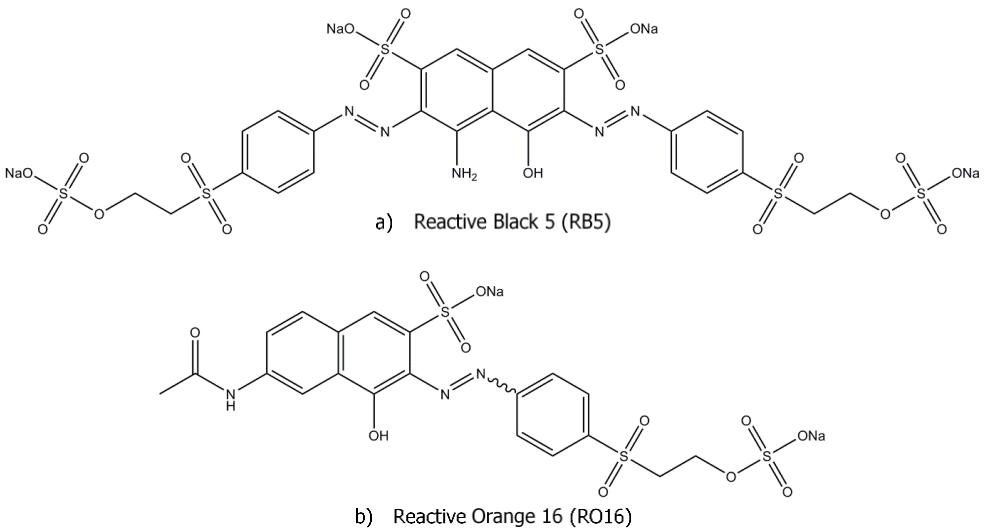


Figure 3.11 Chemical Structure of Reactive Dyes

Batch adsorption experiments were carried out in the dark, in an incubator with magnetic stirring for agitation in order to eliminate any influence of that light may have on the dyes. Prior to adsorption, LDH materials were calcined at 773K for 4 hours to produce a mixed metal oxide (MMO). During adsorption experiments, 1mL aliquots were taken and centrifuged. The supernatant was carefully transferred from the centrifuge tube to a quartz UV cuvette (Hellma), by glass Pasteur pipette. The supernatant was then analysed using a Shimadzu UV-mini 1240 spectrophotometer at the λ_{max} for RB5 (λ_{max}=597nm) and RO16 (λ_{max}=388nm).

3.2.1.2 Adsorption Scoping Studies

Before the effects of reaction parameters were investigated, scoping studies were completed using the proposed conditions for the experiments. An arbitrary concentration set at 1500mg L^{-1}, of dye in deionised water, was chosen and adsorption was measured until equilibrium was reached. The adsorbent loading was 1g L^{-1} and the adsorbent volume was 50mL based on conditions that were similar in literature [25, 123, 225]. The result of the experiment indicated that the time to reach equilibration of RO16 was 2 hours at 293K and 1500mg L^{-1} was an appropriate concentration for the adsorbent to be saturated without complete removal of the dye from solution. For the adsorption RB5 the time to reach equilibration was 195 minutes. The concentration was also high enough for the adsorbent to become saturated without complete removal of the dye from solution. The 1500mg L^{-1} dye concentration was then utilised in the adsorption studies as the upper concentration limit to develop an idea of adsorption. The adsorbent loading was also found to be appropriate at 1g L^{-1} based on the scoping study.

3.2.1.3 Adsorption Studies

For adsorption experiments 50mL of RB5 or RO16 solution and 1g L^{-1} of MMO were used in adsorption experiments. Uptake of dye was calculated from the following equation [225]:

$$q = \frac{(C_0 - C) \times V}{m} \quad (3.9)$$

Where q (mg g^{-1}) is the uptake, C_0 is the initial dye concentration and C is the sample dye concentration (mg L^{-1}) a given time (C_t) or at equilibrium (C_e), V is the volume of the dye solution in litres and m is the mass of the adsorbent (g). Batch adsorption experiments carried out in triplicate with a control solution containing dye in water with no adsorbent loading to track natural changes in dye concentration with time.

3.2.1.4 Effect of Temperature and Adsorption Kinetics

The effect of temperature on adsorption was investigated to establish reaction rates and adsorption mechanisms. The volume of the dye solutions was 50mL. The adsorbent dose was fixed at 1g L^{-1} and initial dye concentration of 1500mg L^{-1}, which was established from the scoping studies. Temperature was varied from 283K to 313K, as this is a common temperature range in literature [128, 225, 226]. Solutions were stirred and samples were taken and analysed every 15 minutes until equilibrium was reached. The most common rate models encountered in literature are the pseudo-first (3.10) and pseudo-second order (3.11) rate equations [126, 225, 227-229] and the intra-particle diffusion model, developed by Weber and Morris [227, 230]. The pseudo-first order rate equation can be expressed in its linear form as [225]:

$$\ln(q_e - q_t) = \ln(q_e) - k_1 t \quad (3.10)$$

Where q_e is the equilibrium dye uptake (mg g^{-1}), q_t is the dye uptake at a given time (mg g^{-1}), t (min) and k_1 (min^{-1}) is the pseudo-first order rate constant. The pseudo-second order rate equation can be expressed linearly as [225]:

$$\frac{t}{q_t} = \frac{1}{k_2 q_e^2} + \frac{t}{q_e} \quad (3.11)$$

Where q_e and q_t are the adsorbed dye amount at equilibrium and time, t, respectively and k_2 is the pseudo-second order rate constant (g mg^{-1} min^{-1}). The intra-particle diffusion model can be presented as [227]:

$$q_t = k_{id}\sqrt{t} + C \quad (3.12)$$

Where q_t (mg g^{-1}) is the adsorbed amount of dye at a given time, t (min) and k_{id} (mg g^{-1} $min^{-1/2}$) is the intra-particle diffusion rate constant.

3.2.1.5 Effect of Adsorbent Dose

For adsorption studies examining the effect of adsorbent dose on the rate of adsorption and the total adsorption capacity, the concentration of each dye was maintained at 1500mg L^{-1}. The temperature was maintained 293K. Adsorbent dose was set at 0.5g L^{-1}, 1g L^{-1}, 1.5g l^{-1} and 2g L^{-1}. Suspensions of dye and adsorbent were stirred and in 15 minute time intervals, 1mL aliquots were taken evaluate the effect that adsorbent dose has on the uptake of dye over time.

3.2.1.6 Effect of Initial Solution pH

The effect of initial pH was assessed at an adsorbent dose of 1g L^{-1} and initial dye concentration of 1500mg L^{-1}. Temperature was maintained at 293K. Solution pH was adjusted using HCl and NaOH between pH 4-10. The pH of the solution was measured

with a pH probe calibrated with pH 4, pH 7 and pH 10 buffer solutions prior to use. The dye solutions were stirred to ensure homogenous pH throughout the solution. Solutions were stirred until equilibrium was reached before samples were analysed by UV-Vis spectrophotometry.

3.2.1.7 Effect of Dye Auxiliary Compounds and Competing Anions

Electrolyte addition and addition of alkaline chemicals to dye baths can also promote dye diffusion fixation and in the substrate [46]. Solutions of dye at 1500mg L^{-1} were prepared with coexisting anions at concentrations between 0 to 10g L^{-1} of the sodium salt. The co-existing anions (CO_3^{2-}, SO_4^{2-} and Cl^-) were prepared in the same solution with the dyes. The samples were stirred at 293K, with 1g L^{-1} of adsorbent, until equilibrium was reached.

3.2.1.8 Adsorbent Recyclability

Regeneration and recyclability of exhausted adsorbents is a key characteristic that enhances sustainability of the adsorption process. Adsorbent regeneration was investigated only for RB5 as the change dye was not the focus of the experiment, but rather the regeneration method and the subsequent performance of the adsorbent. A solution of RB5 (1500mg L^{-1}) was stirred at 293K with 1g L^{-1} of adsorbent until equilibrium was reached. A 1mL aliquot was taken for analysis and the adsorption capacity was calculated. In the first study, the exhausted adsorbent washed with deionised water to remove any residual dye. The adsorbent was then calcined at 773K for 4 hours as per the original activation method. This powder was reused in the next adsorption cycle. The process was followed for four cycles. In the second regeneration study, the exhausted adsorbent was washed with Na_2CO_3 for 2 hours in a static shaker

at 180 strokes per minute, in order to remove and recover the adsorbed dye. After the Na_2CO_3 wash, the adsorbent was calcined at 773K for 4 hours. Subsequent adsorption studies used progressively lower amounts of adsorbent and the volume of the dye solution was adjusted to match the mass for each adsorbent cycle.

3.2.1.9 Adsorption Isotherms

The effectiveness of an adsorbent is typically defined by a number of criteria, chief among these is the adsorptive capacity. This capacity can be obtained from adsorption experiments and modelling of data with isotherm models, which explain the behaviour of adsorbent-adsorbate interactions during adsorption reactions. The principle difficulty where adsorption is concerned is that, due to the vast array of synthetic dyes available and in use; each with its own unique chemistry it may be that one dye is adsorbed readily by a particular adsorbent, while that same adsorbent may not remove dyes with different chemical properties.

Adsorption isotherms such as the Langmuir and Freundlich Isotherm are the most commonly found isotherms in literature regarding adsorption of pollutants from water.

The Langmuir adsorption isotherm when applied to adsorption of contaminants from water is described as [231]:

$$q_e = \frac{q_m k_l C_e}{1 + k_l C_e} \quad (3.13)$$

$$\frac{C_e}{q_e} = \frac{C_e}{q_m} + \frac{1}{k_l q_m} \quad (3.14)$$

Where q_e (mg g^{-1}) is the equilibrium adsorption, q_m (mg g^{-1}) is the maximum adsorption capacity, C_e (mg L^{-1}) is the equilibrium dye concentration and k_l (L mg^{-1}) is the Langmuir constant. The Freundlich isotherm is also commonly used to fit adsorption data. The

Freundlich isotherm is a modification of sorts or the Langmuir isotherm and accounts for heterogeneous adsorbent surfaces [231].

$$q_e = k_f C_e^{\frac{1}{n}} \quad (3.15)$$

$$\ln(q_e) = \ln(k_f) + \frac{1}{n}\ln(C_e) \quad (3.16)$$

Where k_f (mg g^{-1}.(L $mg^{-1})^{1/n}$) is a Freundlich constant and n is the heterogeneity factor.

3.2.1.10 Adsorption Thermodynamics

Reaction thermodynamics for the adsorption process can be evaluated to determine the spontaneity of adsorption, by using the equation for Gibbs free energy [225]:

$$\Delta G = \Delta H - T\Delta S \quad (3.17)$$

Where ΔG is the change is Gibbs energy (kJ mol^{-1}), ΔH is the change in enthalpy (J mol^{-1}), ΔS is the system entropy (J K^{-1} mol^{-1}) and T (K) is the temperature of the adsorption reaction. The approximation of ΔG, ΔH and ΔS vary with the equilibrium constant used in the calculation [225]. A number of approximations for k_a have been used in literature including the distribution coefficient, $(^{q_e}/_{C_e})$ [227, 232, 233], as well as isotherm constants [225, 234, 235]. For the adsorption thermodynamics this thesis, the properties will be calculated from the Langmuir isotherm constant (k_l). The equation for Gibbs free energy can be rearranged as:

$$\Delta G = -RT\ln(k_l) \quad (3.18)$$

Where R is the ideal gas constant (J mol^{-1} K^{-1}) and k_l is the adsorption equilibrium constant(Langmuir). Substitution of (3.17) into (3.18) gives:

$$\ln(k_l) = \frac{\Delta S}{R} - \frac{\Delta H}{RT} \quad (3.19)$$

Where the plot linear plot of $\ln(k_l)$ against 1/T gives the entropy and enthalpy of adsorption as the intercept and gradient of the line respectively.

3.2.1.11 Stability of Mixed Metal Oxides in Air and Water

The stability of the adsorbent was tested to establish changes to the crystal structure and morphology with time and how this would affect adsorption with prolonged adsorbent use. After calcination 6g MMO adsorbent was taken and stored in the dark at 293±1K in 50mL centrifuge tubes. Three grams of dry MMO was stored in a 50mL centrifuge tube in air, and every two weeks a sample (0.5g) was removed for analysis. For wet stored samples, 3g of MMO adsorbent was split equally between four separate centrifuge tubes, and the tubes were filled with 20mL of deionised water. After each two-week interval a wet-stored sample was freeze dried and the powder was taken for analysis. The samples were stored both wet and dry for a total of 8 weeks. Samples were subject to XRD and SEM analysis to identify changes to crystal structure and morphology from the original sample, to each interval.

3.2.2 Continuous Experimentation

Batch adsorption experimentation is a key part of assessing the proficiency of an adsorbent as well as elucidating adsorbent/adsorbate interactions during the adsorption reaction. However, once the data regarding reaction is obtained, this data must then be applied to a more realistic processing environment. As noted in Chapter 2, many adsorption and ion exchange processes occur in the form of a fixed-bed column. In order to establish MMO/dye adsorption behaviour in a continuous mode, fixed-bed column experiments were trialled.

3.2.2.1 Column Adsorbent Preparation and Experimental Conditions

Prior to column studies calcined Zn_2Al-CO_3 MMO was pressed into a 30mm diameter block using 3 different mass loadings of poly(methyl methacrylate) (PMMA) binder. The mass loadings were chosen arbitrarily at 0%, 1% and 5% w/w as this sort of experimentation has not been encountered before in literature. PMMA binder was used, as it was a readily available and low cost, for experiments assessing the impact of pelleting and granulation of LDHs. After pressing the blocks were milled using a Retsch® SM2000 knife mill with a 4mm square screen. The resulting granules were sieved to 1700-1000μm in size. The 1700-1000μm granules were tested for stability in water by shaking at 180 strokes/minute in a Camlab reciprocating shaker. Following shaking and oven drying, the granules were sieved again and weighed and the mass fraction of recorded, to gauge breakdown during the shaking processes. This breakdown data coupled with specific surface area of the granules, formed the basis of the choice for the optimum mass loading of binder for the column adsorption media.

Operation of adsorption columns was based on the empty bed contact time (EBCT), a widely accepted parameter that influences adsorption efficiency and breakthrough in adsorption columns. Due to the lack of available data regarding adsorption of textile dyes onto LDH based adsorbents, a degree of uncertainty surrounds the ideal conditions relating to hydraulic loading and EBCT. The EBCT for this research was based on data available regarding common organic pollutants in water and their respective EBCT and removal rates. EBCT time varies most often between 5-30 minutes [17].

A laboratory scale column measuring 100mm in length and internal diameter of 10.9mm was used, details of the column size can be found in Table 3.2 and Figure 3.12. Based on the size of the column and desired EBCT, three separate experiments were performed

using flow rates of 3.8mL min^{-1}, 1.9mL min^{-1} and 1.1mL min^{-1}, which resulted in EBCT of 2.5, 5 and 8.5 minutes respectively. Flowrates lower than 1.1mL min^{-1} resulted in variable flow rates from the HPLC pump and an accurate and stable EBCT could not be achieved. The three flowrates and the corresponding EBCT and flow velocity through the column are displayed in Table 3.3.

Table 3.2 Dimensions for laboratory scale adsorption column

Outer Diameter (OØ) / mm	Wall thickness / mm	Internal Diameter mm (IØ) / mm	Internal Cross Section Area / mm^2	Column Length (L) / mm	BED volume / mm^3	Bed Volume / cm^3
12.70	0.89	10.92	93.69	100	9369.02	9.37

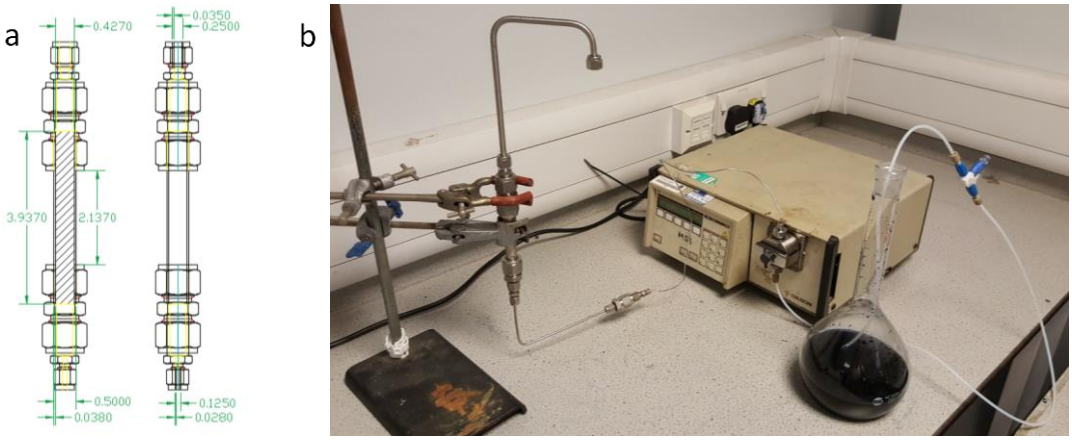


Figure 3.12a) Annotated schematic showing tube diameter, length and column packing (annotations shown in inches), b) Photograph of adsorption column, pump and wastewater source

Table 3.3 Flowrates for column adsorption experiments

Flowrate / mL min^{-1}	Superficial velocity / m s^{-1}	EBCT / min
1.1	$1.96x10^{-4}$	8.5
1.9	$3.38x10^{-4}$	4.9
3.8	$6.76x10^{-4}$	2.5

Column adsorption was only possible for one dye compound (RB5) for three flowrates. An initial study at 3.8mL min^{-1} with the concentration of RB5 equal to 1500mg L^{-1} produced poor breakthrough modelling data as 50% exhaustion occurred within 5 minutes and total exhaustion occurred within 30 minutes. For further studies, a solution of RB5 at a concentration of 500mg L^{-1} was pumped in up-flow mode in order to avoid channelling within the column and samples were taken at five minute intervals up to 1 hour and then 10 minutes up to 2 hours and then every 15 minutes thereafter until bed exhaustion ($C_t/C_0 > 0.95$) occurred for 2 data points and the experiment was stopped. Due to reduced amounts of available MMO granules, it was not possible to run adsorption experiments in duplicate or triplicate. The data from these experiments could have been more reliable with triplicate experimentation.

3.2.2.2 Breakthrough Curve Modelling

Breakthrough curves are used to indicate the change in the adsorption of the packed column with time. With time the mass transfer zone (MTZ), the point in the column where adsorption occurs, moves through the column. Over time the effective column height decreases as the MTZ moves until the contaminant is detected at the column outlet, at which point breakthrough has occurred. Continued operation will eventually lead to the inlet and outlet concentration being equal and the column is exhausted (Figure 3.13) [231].

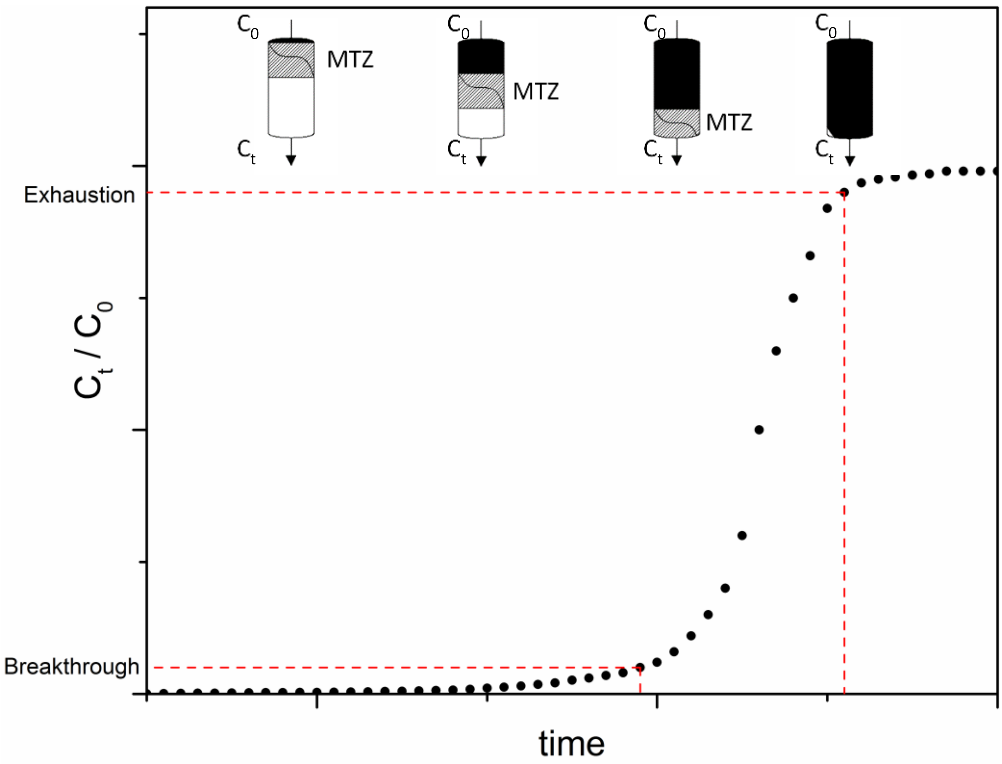


Figure 3.13 Typical breakthrough curve shape labelled with breakthrough and exhaustion points and the mass transfer zone (MTZ) in a packed column [89]

Total adsorption was calculated by integrating the C_0-C_t vs t curve according to equation (3.20) [96].

$$q_{tot} = \frac{Q}{1000} \int_0^t C_{ad}\, dt \qquad (3.20)$$

Where q_{tot} (mg) is the total adsorption, Q (mL min^{-1}) is the flow rate, C_{ad} (mg L^{-1}) is the adsorbed concentration (C_0-C_t), t (min) is the adsorption time. Equilibrium uptake (q_{eq} / mg g^{-1}) in the column was calculated using q_{tot} from equation (3.21) and the following equation [96]:

$$q_{eq} = \frac{q_{tot}}{m} \qquad (3.21)$$

Three commonly found models in literature are Thomas, Adams-Bohart and Yoon Nelson [95, 99] models. The Thomas models follows the assumption that the reaction follows a reversible 2nd order kinetic model and the Langmuir adsorption model [36, 236, 237]. The Thomas model in linear form as [95, 97]:

$$\ln\left(\frac{C_0}{C_t}-1\right)=\frac{k_{Th}q_{Th}m}{Q}-k_{Th}C_0t \qquad (3.22)$$

Where C_t (mg L^{-1}) is the dye concentration at time, t (min), C_0 (mg L^{-1}) is the initial concentration, q_{Th} (mg g^{-1}) is the adsorption at capacity at exhaustion, m (g) is the mass of the adsorbent, Q (L min^{-1}) is the volumetric flowrate through the column, and k_{Th} (mL min^{-1} mg^{-1}) is the Thomas rate constant.

The Adams-Bohart model was originally formulated in 1920 for the adoption phenomena in gas-solid continuous systems [238]. However it has since been applied extensively to model the adsorption of contaminants in liquid-solid continuous systems [36, 95, 97, 236]. The Adams-Bohart model follows the assumption that the adsorption rate is proportional to the residual capacity of the adsorbent and the concentration of the adsorbate in the solid phase and best models the initial part of the curve, before breakthrough occurs [239]. The Adams-Bohart model can be described linearly as [97-99]:

$$\ln\left(\frac{C_t}{C_0}\right)=k_{AB}C_0t-k_{AB}N_0\frac{z}{U_0} \qquad (3.23)$$

Where k_{AB} (L mg^{-1} min^{-1}) is the Adams-Bohart constant, N_0 (mg L^{-1}) is the adsorbate concentration at exhaustion, z (cm) is the column height and U_0 cm min^{-1} is the superficial flow velocity though the column, obtained dividing the volumetric flowrate by the cross section area.

The Yoon-Nelson model was first developed in 1984, again for the adsorption modelling in gas-solid systems [240, 241]. The model assumes that the rate of concentration decrease is proportional to the probability of adsorption and the probability of adsorbate breakthrough in the adsorption column [36, 239]. The Yoon-Nelson model can be expressed in its linear form as [95, 97]:

$$\ln\left(\frac{C_t}{C_o - C_t}\right) = k_{YN}t - \tau k_{YN} \qquad (3.24)$$

Where k_{YN} (min^{-1}) is the Yoon-Nelson rate constant and τ (min) is the time taken for 50% exhaustion to occur. Rate constants from the models were used to identify changes in adsorption rate and characteristics with increased flowrate through the column.

4. Results and Discussion: Continuous Hydrothermal Synthesis of Layered Double Hydroxides

4.1 Introduction

LDH synthesis is most typically carried out in batch co-precipitation reactions, where close control over reactant concentrations can be maintained. The main drawback of co-precipitation is that the reaction is a slow process occurring over several hours as nucleation and aging takes place. Continuous hydrothermal synthesis (CHS) has highlighted the potential for much more rapid synthesis of LDHs with increased throughput. However, with the scarceness of continuous LDH synthesis in literature work was needed to identify the variables that affect the reaction and as a consequence, the LDH characteristics. The work in this chapter is focused on the continuous synthesis and subsequent characterisation of layered double hydroxides (LDHs), with a focus on two types of LDH; $3CaO{\cdot}Al_2O_3{\cdot}Ca(NO_3)_2{\cdot}10H_2O$ ($Ca_2Al\text{-}NO_3$) and $[Zn_4Al_2(OH_{12})](CO_3){\cdot}4H_2O$ ($Zn_2Al\text{-}CO_3$).

The aim was to evaluate the effects of reaction conditions in continuous synthesis and to identify conditions that worked bet to maximise surface area of the LDHs produced. The reaction variables intrinsically linked to the material characteristics were temperature, pressure and precursor concentration. These three primary variables influence reactor residence time, mixing and flow regime as well as the reaction kinetics themselves which in turn can alter the material properties. The effects of the variables were elucidated using X-ray Diffraction (XRD) and the alterations to the crystal domain length (CDL), surface area analysis with the Brunauer-Emmet-Teller isotherm (S_{BET}), Scanning

Chapter adapted from Clark, I.; Dunne, P. W.; Gomes, R. L.; Lester, E. *Journal of Colloid and Interface Science* **2017,** *504*, 492-499.

Electron Microscopy, with energy dispersive spectroscopy (SEM and SEM-EDS), Transmission Electron Microscopy (TEM) and Thermogravimetric and Differential Thermal Analyses (TGA and DTA).

4.2 Highlights

- Synthesis temperature and pressure have an effect on crystal domain length yet particle size characteristics in $Ca_2Al\text{-}NO_3$ LDHs show no trends in changes due to temperature and pressure adjustment.
- Surface area of $Ca_2Al\text{-}NO_3$ remained between 4-7m^2 g^{-1} for all reaction variables investigated as the particle size was 3-5μm.
- $Zn_2Al\text{-}CO_3$ LDHs exhibit a specific surface area of 51m^2 g^{-1} a particle size of 120±53nm

4.3 Continuous Synthesis of $Ca_2Al\text{-}NO_3$

4.3.1 Experimental Conditions

Temperature and pressure can impact on fluid properties, the difference in water density between water at 348K and 473K under a pressure of 5MPa is 110kg m^{-3} (Figure 4.1) [242]. The difference in liquid density results in a variation in flow velocity through the reactor which can alter reactor residence time as temperature increases. Temperature and pressure variation within the reactor should also influence reaction rates because of the energy within the system and rate of successful interactions between the precursor molecules [243]. Modelling of reactor residence time was challenging within the continuous flow reactor because the volume of the reactor is

Chapter adapted from Clark, I.; Dunne, P. W.; Gomes, R. L.; Lester, E. *Journal of Colloid and Interface Science* **2017,** *504*, 492-499.

subject to changes in the mixing volume with flow rates and the temperature variation between the mixing point and the reactor outlet as the suspension cools.

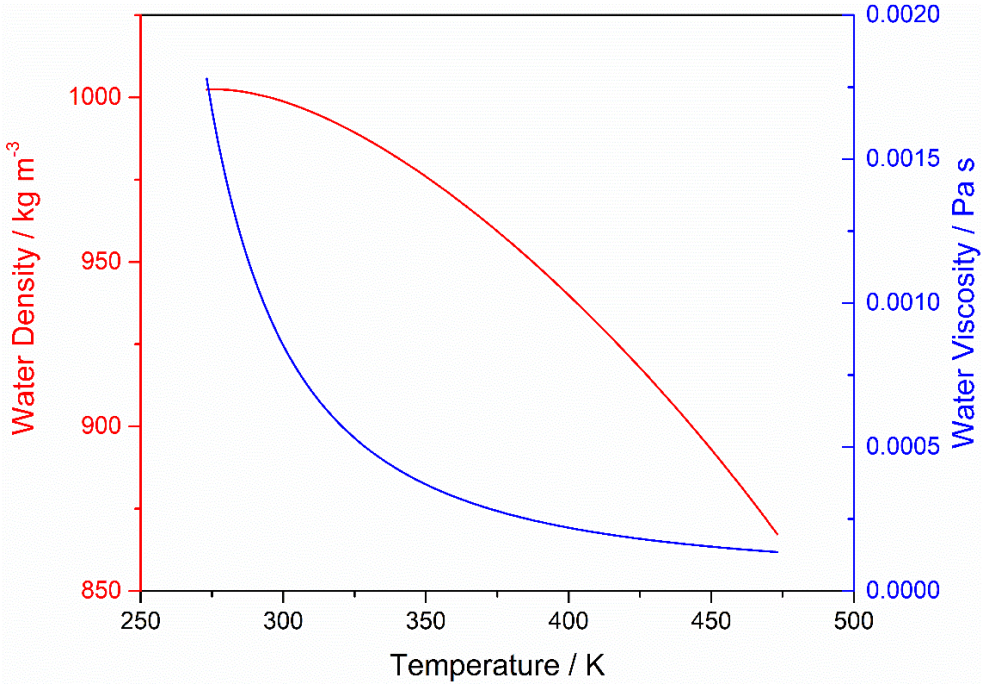


Figure 4.1 Isobaric changes in water density and viscosity with temperature [242]

The effects of temperature and pressure were modelled as a function of product characteristics and tune-ability rather than modelling of reactor flows. The influence of NaOH should alter the precipitation (nucleation and growth rates) within the system, because high NaOH concentration in batch high supersaturation co-precipitation reactions typically results in finer crystals due to the rapid precipitation of $M(OH)_x$, while low supersaturation typically result in larger crystals arising from controlled addition of the base [2]. This is due to the finite amount of NaOH present only allowing for a few crystal to nucleate while the remaining OH^- is sufficient to sustain growth without allowing new crystal to form [2].

Chapter adapted from Clark, I.; Dunne, P. W.; Gomes, R. L.; Lester, E. *Journal of Colloid and Interface Science* **2017,** *504*, 492-499.

All $Ca_2Al\text{-}NO_3$ LDH samples produced under varying reaction conditions are outlined in Table 4.1. The temperatures and pressures chosen in this research looked to build a greater understanding around the work carried out by Wang *et al*, who first published on the continuous hydrothermal synthesis of LDHs [10]. This research investigated an arbitrary set of temperature and pressure conditions and sub and supercritical synthesis. The research indicated that supercritical synthesis was not applicable due to the potential for AlOOH formation [10, 174]. A more comprehensive look at the links between temperature and pressure, as well as the precursor concentration was taken. The sample labels from Table 4.1 will be used throughout this chapter to describe the $Ca_2Al\text{-}NO_3$ LDHs produced. The sample code is Table 4.1, reads as CA, which relates to the type of LDH, which is a $Ca_2Al\text{-}NO_3$ type. The numbers 348, 373, 423 and 473 relate to synthesis temperature and the end numbers; 5, 10, 15 and 20 correspond to synthesis pressure. An example is CA3485, which is a $Ca_2Al\text{-}NO_3$ type LDH, produced at 348K and 5MPa. For samples where NaOH concentration was a variable, the sample code reads as: CA for $Ca_2Al\text{-}NO_3$, the code 002M, 005M, 01M, 02M, 05M and 1M relates to the NaOH concentration in mol L^{-1}. The final number in the sample code is synthesis the temperature, in Kelvin. The example is CA01M348, which is a $Ca_2Al\text{-}NO_3$ type LDH produced using a precursor NaOH concentration of 0.1mol L^{-1} and a temperature of 348K.

Chapter adapted from Clark, I.; Dunne, P. W.; Gomes, R. L.; Lester, E. *Journal of Colloid and Interface Science* **2017,** *504*, 492-499.

Table 4.1 Synthesis conditions for $Ca_2Al\text{-}NO_3$ samples

Sample	Temperature / K	Pressure / MPa	NaOH concentration / mol L^{-1}	
CA3485	348	5	0.125	Pressure and Temperature
CA34810	348	10	0.125	
CA34815	348	15	0.125	
CA34820	348	20	0.125	
CA3735	373	5	0.125	
CA37310	373	10	0.125	
CA37315	373	15	0.125	
CA37320	373	20	0.125	
CA4235	423	5	0.125	
CA42310	423	10	0.125	
CA42315	423	15	0.125	
CA42320	423	20	0.125	
CA4735	473	5	0.125	
CA47310	473	10	0.125	
CA47315	473	15	0.125	
CA47320	473	20	0.125	
CA1M348	348	5	1	NaOH and Temperature
CA05M348	348	5	0.5	
CA02M348	348	5	0.2	
CA01M348	348	5	0.1	
CA005M348	348	5	0.05	
CA002M348	348	5	0.02	
CA1M373	373	15	1	
CA05M373	373	15	0.5	
CA02M373	373	15	0.2	
CA01M373	373	15	0.1	
CA005M373	373	15	0.05	
CA002M373	373	15	0.02	

Sample codes – CA – $Ca_2Al\text{-}NO_3$ LDH 348-373 – Synthesis temperature in Kelvin 5-20 – Synthesis pressure in MPa 002M-1M – Concentration of precursor NaOH in mol L^{-1}

Chapter adapted from Clark, I.; Dunne, P. W.; Gomes, R. L.; Lester, E. *Journal of Colloid and Interface Science* **2017,** *504*, 492-499.

4.3.2 Effect of Temperature and Pressure on Crystal Characteristics

The identification of crystal characteristics by X-ray diffraction is key in establishing product purity. In the diffractograms of continuously produced $Ca_2Al\text{-}NO_3$, the presence of reflections relating to AlOOH and calcium impurities is not desirable. The diffraction profile also allows the calculation of lattice parameters, which are individual to a particular crystal type and the crystal domain length, which is a measure of uniform long range order within the crystals. The X-ray diffraction patterns of all $Ca_2Al\text{-}NO_3$ samples are displayed in Figure 4.2 to Figure 4.5.

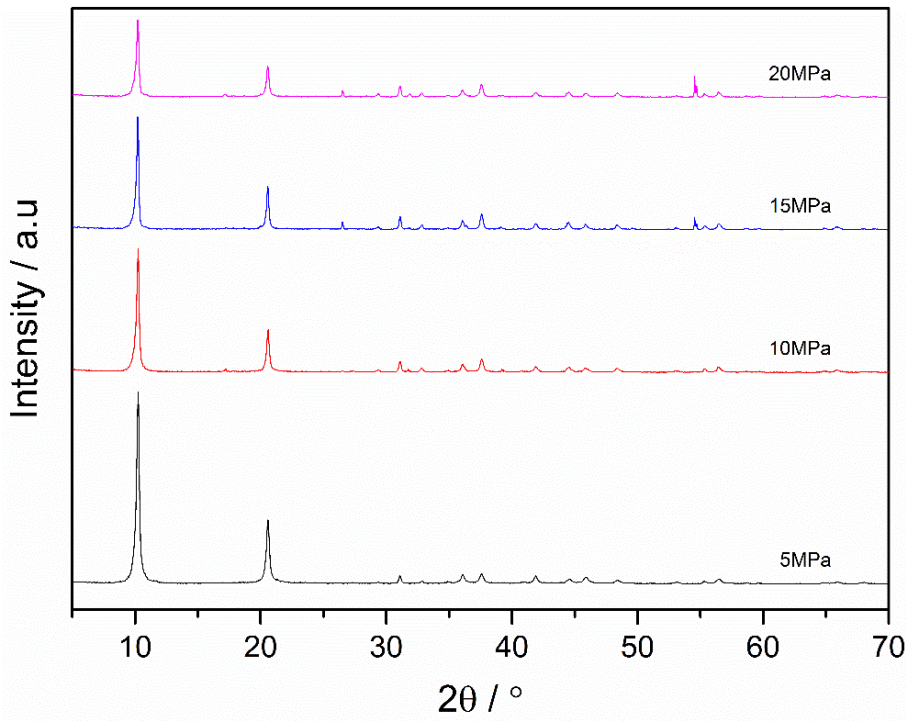


Figure 4.2 X-Ray diffractograms for $Ca_2Al\text{-}NO_3$ LDHs produced at 348K and different pressures

Chapter adapted from Clark, I.; Dunne, P. W.; Gomes, R. L.; Lester, E. *Journal of Colloid and Interface Science* **2017,** *504*, 492-499.

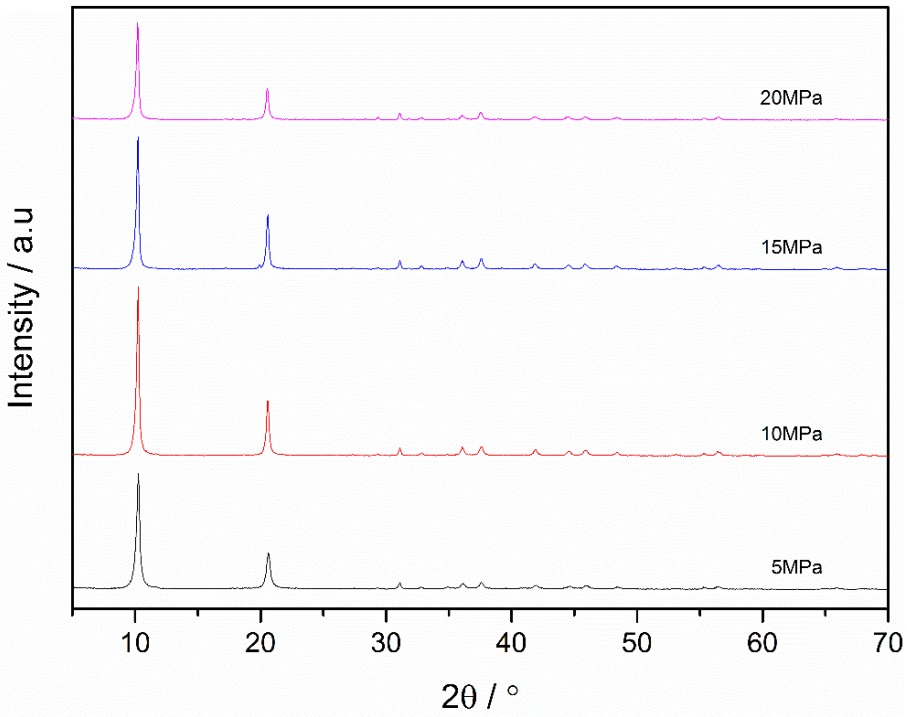


Figure 4.3 X-Ray diffractograms for Ca_2Al-NO_3 LDHs produced at 373K and different pressures

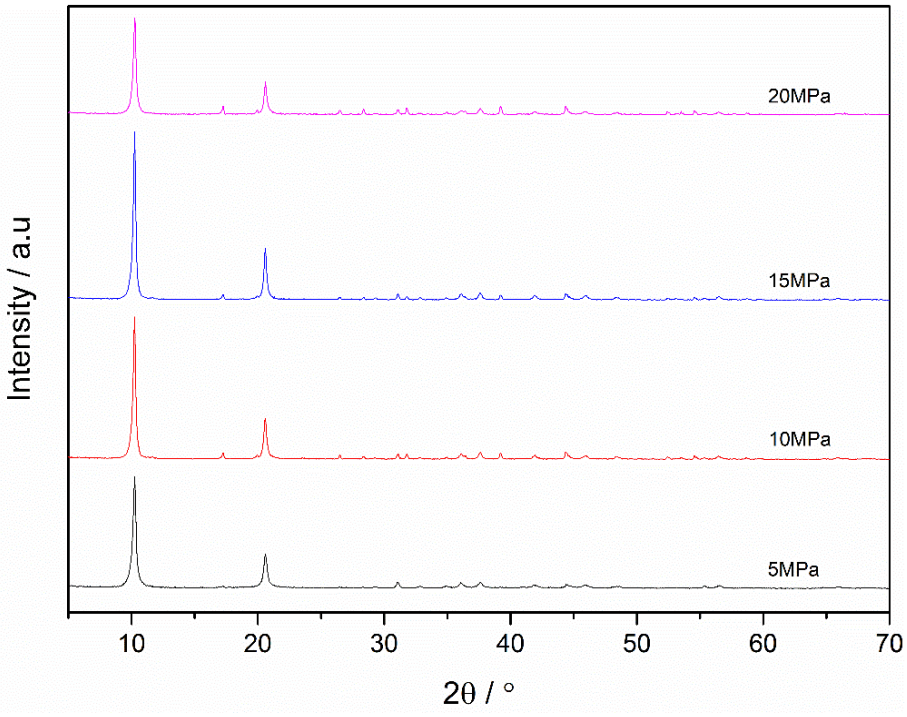


Figure 4.4 X-Ray diffractograms for Ca_2Al-NO_3 LDHs produced at 423K and different pressures

Chapter adapted from Clark, I.; Dunne, P. W.; Gomes, R. L.; Lester, E. *Journal of Colloid and Interface Science* **2017,** *504*, 492-499.

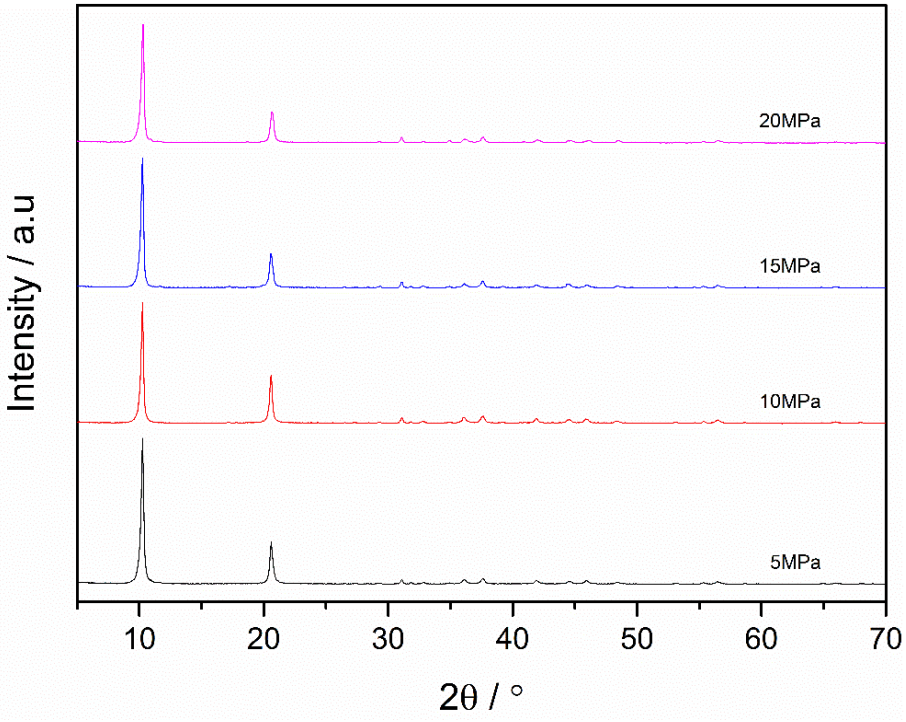


Figure 4.5 X-Ray diffractograms for $Ca_2Al\text{-}NO_3$ LDHs produced at 473K and different pressures

The diffractograms for the samples illustrate intense reflections at low Bragg angle values and less intense reflections at high Bragg angles. This shape of diffractogram is the most acknowledged profile for LDH diffraction patterns [1]. Additional peaks are observed at Bragg angles close to 54° in samples CA34815 and CA34820 due to unidentified impurity phases. The $Ca_2Al\text{-}NO_3$ LDH display a hexagonal crystal symmetry (Space group – $P\bar{3}c1$) [244]. The lattice parameters were calculated from the d_{hkl} value for the (*002*) and (*030*) reflections. These two reflections are chosen due to the hexagonal crystal system and are related to the xy-axes and *l* relates to the z-axis. The d_{hkl} value obtained from the Bragg angle using equation (4.1).

$$n\lambda = 2d\sin\theta \qquad (4.1)$$

Chapter adapted from Clark, I.; Dunne, P. W.; Gomes, R. L.; Lester, E. *Journal of Colloid and Interface Science* **2017,** *504*, 492-499.

Where n is a constant (n=1), λ is the wavelength, d is the inter-planar spacing (d_{hkl}) and θ is the Bragg angle [218]. The hexagonal crystal system and the lattice equation indicates that the *a* and *b* lattice parameters are equal in the lattice and the calculation of the *a* and *b* lattice parameters requires only one of the *h* and *k* indices to be known, while calculation of the *c* lattice parameter requires *l* of the miller indices, as indicated in equation (4 .2). The lattice angles *α*, *β* and *γ* are at fixed angles in a hexagonal crystal system [218].

$$\frac{1}{d_{hkl}^2} = \frac{4}{3}\frac{\left(h^2+hk+k^2\right)}{a^2} + \frac{l^2}{c^2} \qquad (4.2)$$

Where Miller indices *hkl* indicate the lattice plane and *a* and *c* are the lattice parameters. The lattice parameters for all $Ca_2Al\text{-}NO_3$ samples were 0.57nm and 1.72nm for *a* and *c* respectively, the lattice parameters agree with data published in literature [244, 245]. The $Ca_2Al\text{-}NO_3$ LDH structure is different from hydrotalcite and other CO_3^{2-} intercalated LDHs. This is due to the interaction and electrostatic charge between the NO_3^- and the brucite-like layers. The nitrate ion is held more perpendicular to the metal hydroxide layers, which accounts for the larger interlayer spacing found in the $Ca_2Al\text{-}NO_3$ LDH (Figure 4.6) [244].

Chapter adapted from Clark, I.; Dunne, P. W.; Gomes, R. L.; Lester, E. *Journal of Colloid and Interface Science* **2017,** *504*, 492-499.

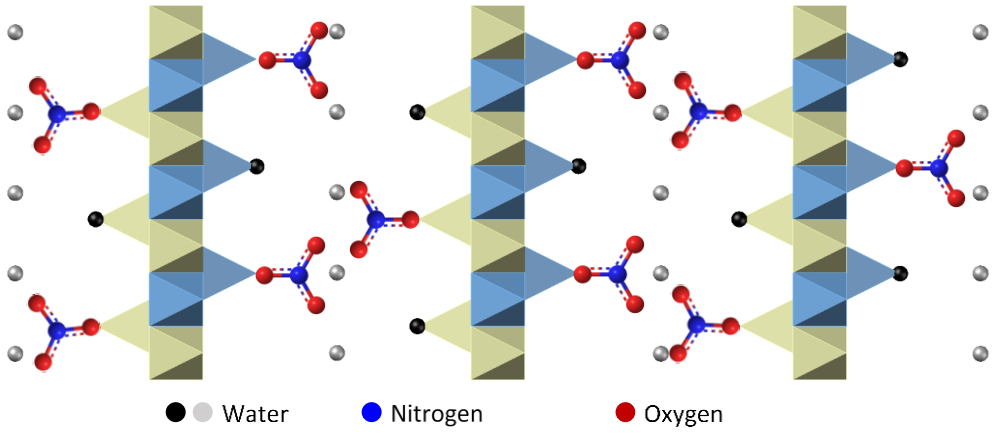


Figure 4.6 Schematic of NO_3^- alignment in $Ca_2Al\text{-}NO_3$ layers. Adapted from Renaudin and François [244]

The effects of temperature and pressure were evaluated by the calculation of the crystal domain length (CDL), through the use of the Scherrer equation (4.3).

$$CDL = \frac{S\lambda}{B\cos\theta} \qquad (4.3)$$

Where CDL is the crystal domain length, B is the full width at half maximum (FWHM) of the reflection, S is the Scherrer constant and is typically assumed to be 0.9-1 [218]. In this research the Scherrer constant was held at 0.9. The Bragg and is denoted by θ and the wavelength of the X-ray beam is represented by λ. The pressure range was chosen to given a wide range of pressures from low pressure to almost critical and the effect that the pressure has on fluid, reaction and LDH characteristics.

Samples produced at 348K show increasing CDL in the ⟨*002*⟩ direction with increasing pressure from 5MPa and 15MPa (Figure 4.7). The CDL for sample CA3485 is 53±0nm, this is comparable with previously reported data by Wang *et* al, who report that the crystallite size of LDHs produced under similar conditions were 62nm [10], while the CDL for sample CA34815 is 74±0nm. At 20MPa there is a reduction in CDL in the ⟨*002*⟩

Chapter adapted from Clark, I.; Dunne, P. W.; Gomes, R. L.; Lester, E. *Journal of Colloid and Interface Science* **2017,** *504*, 492-499.

direction to 65±7nm. Crystal domain length calculated from the (*030*) reflection shows an overall increasing trend with between CA3485 (CDL=92±0nm) and CA34815 (CDL=120±0nm) indicating that growth begins to dominate over nucleation at 15MPa. However, at the lowest temperature investigated a reduction in CDL is observed at the highest pressure, suggesting that the rate of nucleation increases. The CDL of the continuously produced samples in this research is larger than samples produced by separate nucleation and aging steps. A sample of $Ca_2Al\text{-}NO_3$ produced by Yang *et al* exhibited CDL calculated from the (*002*) reflection at 14.66nm, while the CDL from the (*030*) reflection was 10.67nm [161].

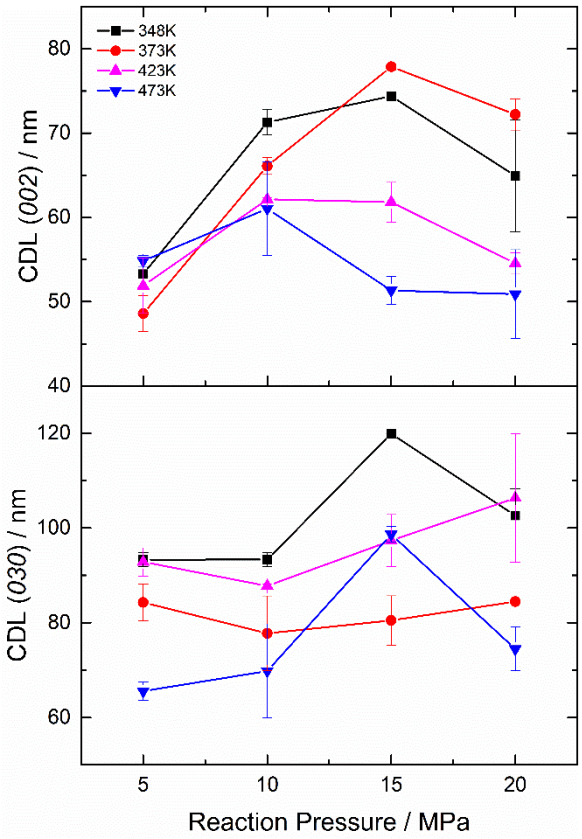


Figure 4.7 Effect of changes in pressure on the crystal domain length (CDL) of $Ca_2Al\text{-}NO_3$ (n=2)

Chapter adapted from Clark, I.; Dunne, P. W.; Gomes, R. L.; Lester, E. *Journal of Colloid and Interface Science* **2017,** *504*, 492-499.

Samples undergoing synthesis at 373K show increases in CDL in the ⟨*002*⟩ direction with increasing pressure. Much like with samples produced at 348K, it is inferred that under a reactor temperature of 373K growth becomes progressively dominant at higher pressures. Conversely there is no significant change in the CDL of these samples from the (*030*) reflection, the CDL ranges from 80-84nm. The CDL calculated from the (*002*) reflection for samples produced at 423K was 51±3nm at 5MPa. This data is comparable to the data computed by Wang *et al* who reported crystallite size from the (*002*) reflection as 57.6nm [10]. Increased reaction pressure from 5MPa to 10MPa resulted in increased mean CDL however further increases in pressure to 20MPa sees the domain length calculated from the samples decreasing to size similar to that calculated for 5MPa. Wang *et al* reported that increased pressure from 5MPa to 20MPa resulted in smaller CDL according to the Scherrer equation [10].

The CDL calculated from the (*030*) reflections indicates that the crystal domain length for samples produced at 423K and 473K the variability in synthesis increases and tune-ability can decrease (Figure 4.7). The range from the smallest to largest CDL is smaller in the ⟨*002*⟩ direction which also indicates that with increasing temperature the tuneable effects from pressure variation is also reduced. Crystal domain length of samples produced at 473K increased in the ⟨*030*⟩ direction from 5MPa (66±2nm) to 15MPa (99±2nm) followed by a decrease in CDL at 20MPa (74±5nm). Materials synthesised at low pressures show the smallest domain lengths in the basal crystal plane, however at the highest temperatures investigated the CDL is similar at both low and high pressure. Samples produced at 373K show little variation in CDL in the ⟨*030*⟩ direction but the greatest variation in the ⟨*002*⟩ direction.

Chapter adapted from Clark, I.; Dunne, P. W.; Gomes, R. L.; Lester, E. *Journal of Colloid and Interface Science* **2017,** *504*, 492-499.

The data indicates that the temperature and pressure tune-ability of the LDH decrease with increased pressure. Reaction temperature is a key component in reaction kinetics. In batch hydrothermal synthesis and treatment of LDHs, increase temperature has been found to produce larger crystallites [4, 171, 172]. In continuous hydrothermal synthesis, increased temperature was found to produce smaller domain lengths. The reduction in CDL is caused by the increase rate of mixing and nucleation compared with batch reactions where the hydrothermal treatment serves to dissolve and re-precipitate to form larger well defined LDH crystals [172, 246]. Pressure also becomes important at higher reaction temperatures (>423K) as the compressibility of water increases with temperature (Figure 4.1) This causes the increased nucleation rates at 473K and the smallest CDL calculated. In continuous hydrothermal synthesis higher temperatures should produce smaller crystals and larger surface areas, because as particles become smaller the surface to volume ratio increase. Depending on the desired characteristics it appears that low temperature synthesis allows for the most tuneable control, while high temperature can lead to increased rates of AlOOH [10, 174].

4.3.3 Effect of Temperature and Pressure on Surface Area Characteristics

Identification of reaction temperature and pressure conditions which produced LDHs with maximised surface area (S_{BET}) was an important feature of the mapping of the continuous synthesis. LDHs produced by batch synthesis reportedly have an S_{BET} typically in the range of 20 to 200 $m^2\ g^{-1}$ [9, 247]. All samples display Type-II adsorption isotherms which arise from macroporous materials, macroporous materials demonstrating Type-II isotherms typically undergo unhindered mono and multilayer adsorption with the thickness of the multilayer increasing constantly with increasing partial pressure up to $P/P_0=1$ [248]. The specific surface area for $Ca_2Al\text{-}NO_3$ type LDHs

Chapter adapted from Clark, I.; Dunne, P. W.; Gomes, R. L.; Lester, E. *Journal of Colloid and Interface Science* **2017,** *504*, 492-499.

have recently been reported at 17.95 $m^2 g^{-1}$ [161], while the S_{BET} of the $Ca_2Al\text{-}NO_3$ LDHs in this thesis was in the range of 4-7$m^2 g^{-1}$ (Table 4.2).

Table 4.2 Comparison of surface area (S_{BET}) and crystal domain length (CDL) at different temperatures and pressures

Sample	Temperature / K	Pressure / MPa	S_{BET} / $m^2 g^{-1}$	CDL (*002*) / nm
CA3485	348	5	6.5	53±0
CA34810	348	10	6.2	71±2
CA34815	348	15	4.9	74±0
CA34820	348	20	4.6	64±8
C3735	373	5	6.0	49±3
C37310	373	10	5.8	65±0
C37315	373	15	5.5	78±2
C37320	373	20	5.6	72±3
C4235	423	5	6.4	52±5
C42310	423	10	4.9	62±0
C42315	423	15	4.1	62±3
C42320	423	20	3.8	55±2
C4735	473	5	5.2	55±1
C47310	473	10	5.9	61±2
C47315	473	15	6.0	51±5
C47320	473	20	5.9	51±7

The changing (*002*) CDL had no definable impact on S_{BET}. The samples produced at 373K follow a trend where the increasing CDL is matched by increases in S_{BET}, however this is not the case for all samples. The lack of defined correlation between CDL and S_{BET} is

Chapter adapted from Clark, I.; Dunne, P. W.; Gomes, R. L.; Lester, E. *Journal of Colloid and Interface Science* **2017,** *504*, 492-499.

exemplified by the samples produced at 348K, where despite and decrease in CDL from 71±2nm to 65±6nm, the S_{BET} decrease from 6.2m^2 g^{-1} to 4.6m^2 g^{-1}, for samples CA34810 and CA34820. The size of particles is the most feasible cause of the low surface area of the Ca_2Al-NO_3 LDHs prepared in this work. Compared with the LDHs produced by Yang *et al* by separate nucleation and aging steps, the surface area is reduced by 10-15m^2 g^{-1}, the CDL of the LDHs in that article are in the range14.66nm compared to 53±0nm for sample CA3485, the increase size of crystals reduces the surface to volume ratio and causes the lower surface area. The surface area of the Ca_2Al-NO_3 LDHs was not desirable and there also appeared to be no control over the S_{BET} through manipulation of reaction conditions.

A brief study highlighting the difference between oven drying and freeze drying indicated that freeze drying of samples can lead to increased surface area. The data outlined in Table 4.3 illustrates the increase in surface area when drying by freeze drying and oven drying. The capillary forces and surface tension of the water acting on nanoparticles can cause unfavourable stacking [249]. This may also contribute to the observed surface areas for the samples as the surface increases when freeze drying, where the capillary forces are negated by sublimation of the water.

Table 4.3 Comparison of Surface Area (S_{BET}) and drying method

Sample	Oven Dried S_{BET} / m^2 g^{-1}	Freeze Dried S_{BET} / m^2 g^{-1}
CA3735	6.0	6.1
CA37310	5.8	9.4
CA37315	5.5	9.7±0.1
CA37320	5.6	11±0.1

Chapter adapted from Clark, I.; Dunne, P. W.; Gomes, R. L.; Lester, E. *Journal of Colloid and Interface Science* **2017,** *504*, 492-499.

4.3.4 Effect of Temperature and Pressure on Structural and Chemical Characteristics

The CDL derived from (*030*) XRD reflections was in the range of 70nm to 150nm for all samples however the platelet size observed in TEM and SEM micrographs indicate much larger platelets are present in the material. The ideal scenario would have nano-scale particles where the CDL matches the particle size more closely, as this would indicate that there are no internal faults or disruptions to long range order and the crystal domains are coherent in the lattice [218]. The individual platelets appear to be a single crystalline structure, however they are in the micrometer scale rather than the nanometer scale, indicating that the CDL calculated from XRD does not match the platelet size (Figure 4.8), this suggests that the LDH platelets suffer from internal disorder of crystal units and the platelets is are made up of smaller crystal domains. The structure of the $Ca_2Al\text{-}NO_3$ LDH appears to favour formation of larger platelets [129, 161].

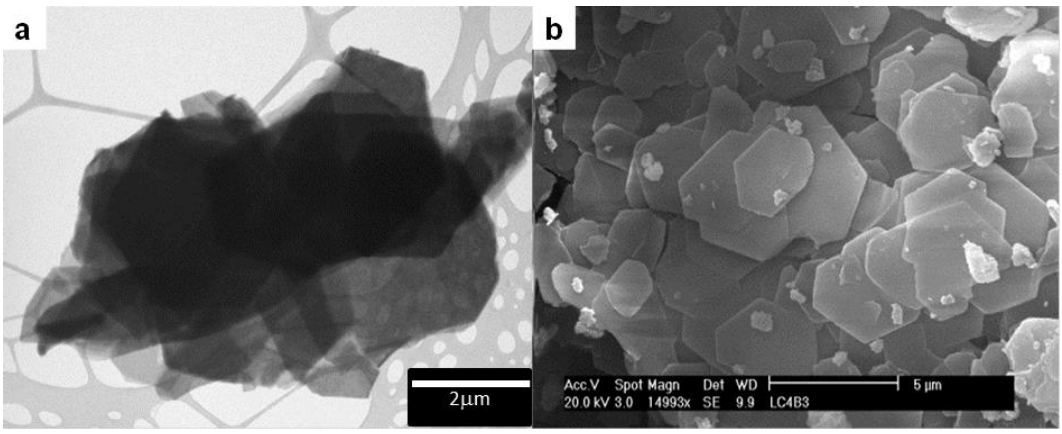


Figure 4.8 Electron Micrographs of $Ca_2Al\text{-}NO_3$ a) TEM b) SEM

The micrometer scale, face-stacked platelets are the reason for the low surface area, so while the CDL within the particles varies as a result of temperature and pressure manipulation, the observable particle size is much larger and the average platelet size is

Chapter adapted from Clark, I.; Dunne, P. W.; Gomes, R. L.; Lester, E. *Journal of Colloid and Interface Science* **2017,** *504*, 492-499.

in the region of 3-5μm with no impact arising from the adjustments made to the reaction conditions (Table 4.4). The stacking and accessibility of N_2 to the surface of the LDHs is a key factor in the low surface area recorded for the LDHs, and can count against the material as a potential adsorbent as increased surface area is favourable in adsorption processes.

Table 4.4 Mean platelet diameter of $Ca_2Al\text{-}NO_3$ LDHs, under varying temperature and pressure

Sample	Reaction Conditions		Platelet Diameter / μm
	Temperature / K	Pressure / MPa	
CA3485	348	5	3
CA34810	348	10	3
CA34815	348	15	3
CA34820	348	20	3
CA3735	373	5	3
CA37310	373	10	3
CA37315	373	15	3
CA37320	373	20	3
CA4235	423	5	3
CA42310	423	10	5
CA42315	423	15	4
CA42320	423	20	4
CA4735	473	5	3
CA47310	473	10	4
CA47315	473	15	3
CA47320	473	20	3

Chapter adapted from Clark, I.; Dunne, P. W.; Gomes, R. L.; Lester, E. *Journal of Colloid and Interface Science* **2017,** *504*, 492-499.

Thermal analysis of the $Ca_2Al\text{-}NO_3$ LDH was used to determine the temperature at which the LDH breaks down and a mixed metal oxide forms. Mixed metal oxides are the main form that LDH based adsorbents take [109, 250-253]. Results from the thermogravimetric analysis of the LDHs show that there were three major stages of mass loss under heating. The first loss (1, Figure 4.9) was attributed to evaporation of surface bound water up to 423K. The second loss (2, Figure 4.9) at approximately 523K is attributed to dehydroxylation of the metal hydroxide layers, and further evaporation of water. The final major mass loss (3, Figure 4.9) around 773K is the breakdown of the layered structure and evolution of the interlayer anion as a gas, N_2 and NO_x in the case of $Ca_2Al\text{-}NO_3$ [254]. The total mass loss for all materials remains constant at 39-43%. The loss of the interlayer anion up to 773K indicates that calcination would need to occur at 773K in order to cause a sufficient breakdown of the interlayer to allow adsorption to occur.

Chapter adapted from Clark, I.; Dunne, P. W.; Gomes, R. L.; Lester, E. *Journal of Colloid and Interface Science* **2017,** *504*, 492-499.

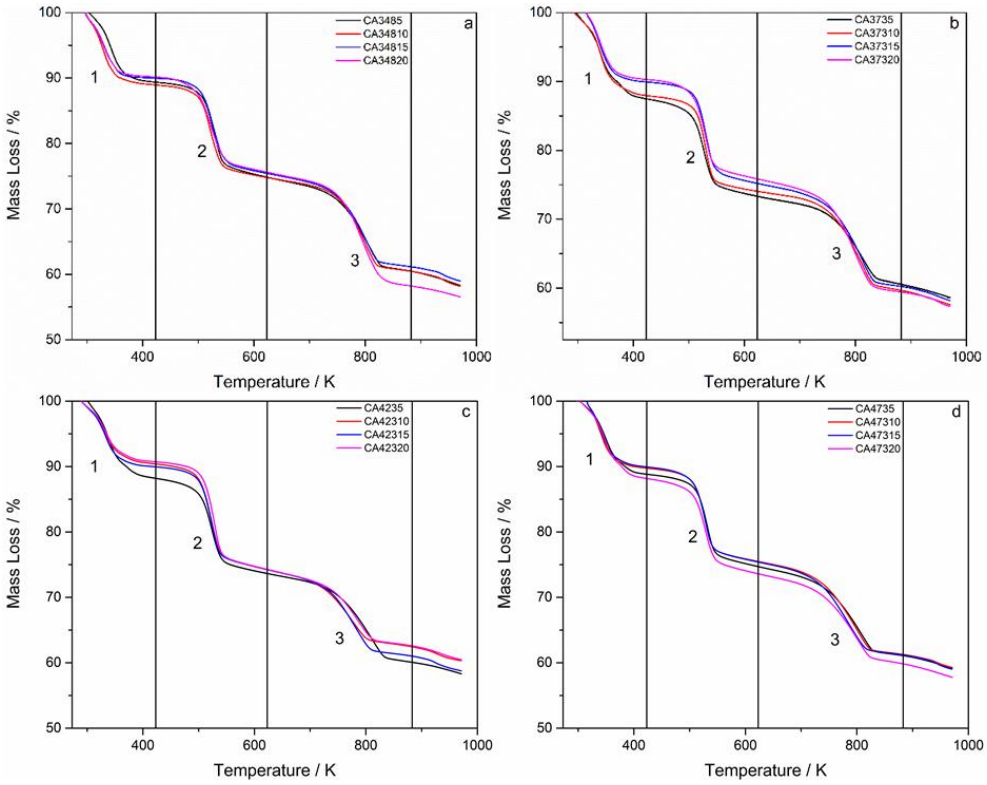


Figure 4.9 Thermal Analysis of $Ca_2Al\text{-}NO_3$ samples of produced under varying temperatures and pressures a) 348K b) 373K c) 423K d) 473K

The molecular ratio of Ca^{2+} and Al^{3+} in the LDHs is outlined in Table 4.5, with the ratio of Ca^{2+}/Al^{3+} equal 2±0.2. The coordination of the Ca^{2+} and Al^{3+} ions is the reason behind the strict ratio of 2, despite the initial excess of Ca^{2+} in the metal salt precursor [244]. The diffractograms in Figure 4.2 do not show any $Ca(OH)_2$ or $CaCO_3$ contamination, despite some reservations by other authors about the presence of $CaCO_3$ impurities being common in the synthesis of $Ca_2Al\text{-}NO_3$; continuous hydrothermal synthesis is able to produce pure materials with Ca/Al level close at the ideal amount [161].

Chapter adapted from Clark, I.; Dunne, P. W.; Gomes, R. L.; Lester, E. *Journal of Colloid and Interface Science* **2017,** *504*, 492-499.

Table 4.5 Molecular ratio of metals in the $Ca_2Al\text{-}NO_3$ LDH materials under varying reaction conditions

Sample	Temperature / K	Pressure / MPa	Ca/Al Ratio
CA3485	348	5	1.97
CA34810	348	10	2.02
CA34815	348	15	1.97
CA34820	348	20	2.09
CA3735	373	5	1.98
CA37310	373	10	1.91
CA37315	373	15	2.05
CA37320	373	20	1.96
CA4235	423	5	2.00
CA42310	423	10	1.94
CA42315	423	15	1.93
CA42320	423	20	2.02
CA4735	473	5	1.98
CA47310	473	10	1.96
CA47315	473	15	2.17
CA47320	473	20	1.93

4.3.5 Effect of Initial Sodium Hydroxide Concentration on Crystal Characteristics

The influence of NaOH on the synthesis of $Ca_2Al\text{-}NO_3$ was examined because of the nature of the CHS process. The NaOH in CHS performs in a similar manner to the base in batch high-supersaturation co-precipitation synthesis. Products produced with 1mol L^{-1} and

Chapter adapted from Clark, I.; Dunne, P. W.; Gomes, R. L.; Lester, E. *Journal of Colloid and Interface Science* **2017,** *504*, 492-499.

0.5mol L^{-1} NaOH exhibit less intense reflections at low Bragg angles relative to $Ca_2Al\text{-}NO_3$ LDHs produced with lower initial NaOH. Reflections relating to $Ca(OH)_2$ and $Ca_2Al\text{-}CO_3$ are impurities present (Figure 4.10 and Figure 4.11). The presence of $Ca(OH)_2$ in the CA1M samples suggest that excessive OH^- present in the reaction causes preferential formation of the $Ca(OH)_2$, due to the excess calcium ions in the precursor solution. Reflections corresponding to $Al(OH)_3$ and AlOOH are not present, therefore it is not unreasonable to assume that the cause of the formation of $Ca(OH)_2$ is the excess Ca^{2+} and the excess NaOH. There are also reflections relating to $Ca_2Al\text{-}CO_3$ LDHs in the samples produced with 1M NaOH. The formation of CO_3^{2-} ions at high pH resulted in the formation of $Ca_2Al\text{-}CO_3$ and some $CaCO_3$ [161].

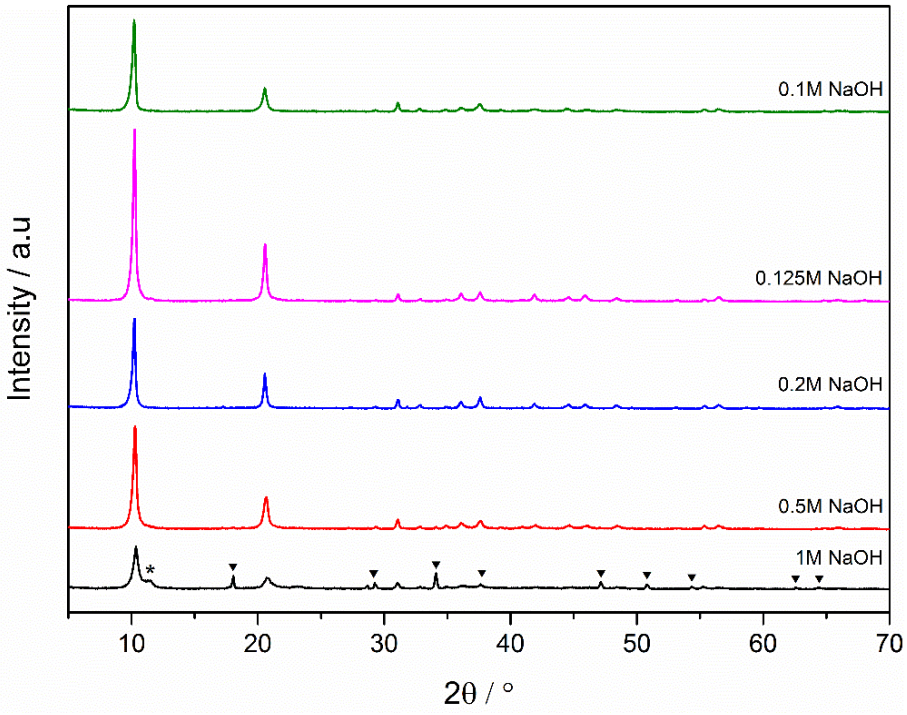


Figure 4.10 Diffractograms of $Ca_2Al\text{-}NO_3$ produced at 348K – ($Ca(OH)_2$ – ▼, $Ca_2Al\text{-}CO_3$ – ★)

Chapter adapted from Clark, I.; Dunne, P. W.; Gomes, R. L.; Lester, E. *Journal of Colloid and Interface Science* **2017,** *504*, 492-499.

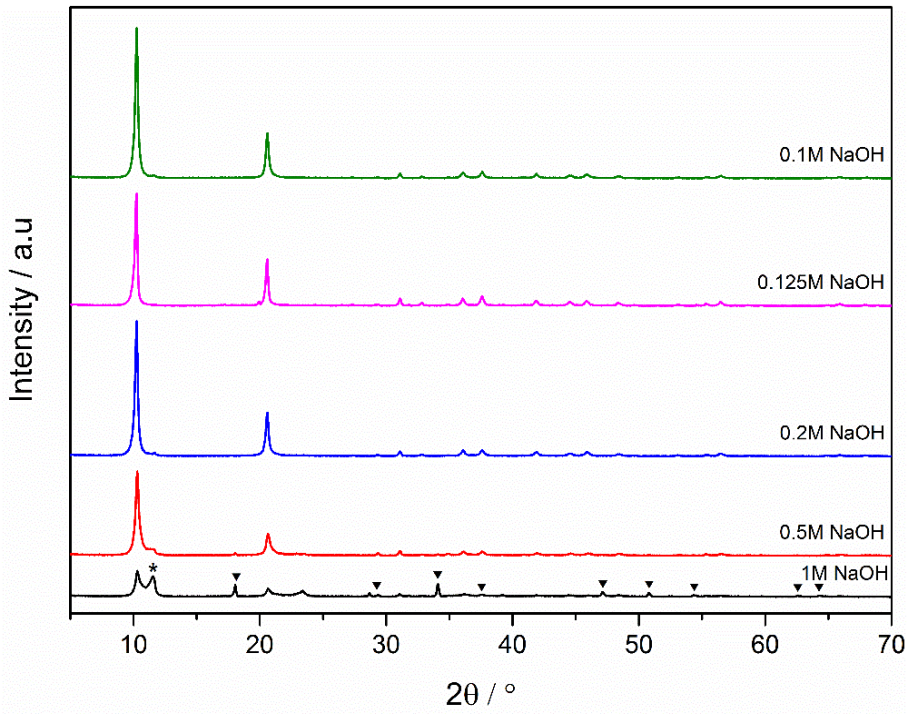


Figure 4.11 Diffractograms of $Ca_2Al\text{-}NO_3$ produced at 373K ($Ca(OH)_2$ – ▼, $Ca_2Al\text{-}CO_3$ – ★)

The ⟨*002*⟩ CDL decreases for samples produced at 348K and 373K with NaOH concentration greater than 0.2mol L^{-1}. This indicates that when the OH^- content is at its highest, nucleation rates increase, and growth of crystals is inhibited (Figure 4.12). The high (>0.5mol L^{-1}) OH^- in the reaction for samples CA1M348, CA1M373, CA05M348 and CA05M373 promoted nucleation in the same way that a high-supersaturation co-precipitation reaction typically results in smaller crystals forming in batch synthesis [2], however it also produced $Ca(OH)_2$ and CO_3^{2-} based impurities. High supersaturation co-precipitation the CDL is typically smaller than for low supersaturation reactions, this is due to the high initial concentration of base in the reaction vessel [2].

Chapter adapted from Clark, I.; Dunne, P. W.; Gomes, R. L.; Lester, E. *Journal of Colloid and Interface Science* **2017,** *504*, 492-499.

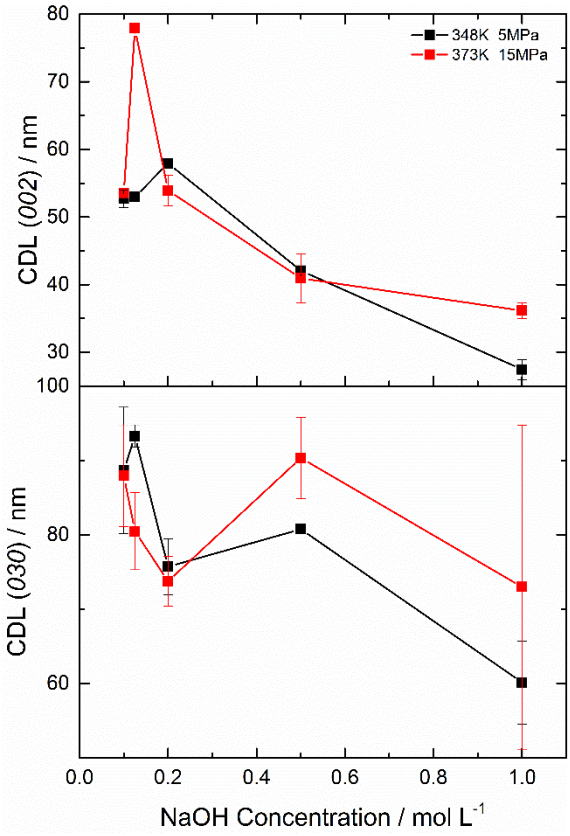


Figure 4.12 Changes in Crystal Domain Length with increasing NaOH concentration (n=2)

CA01M348 and exhibits a greater CDL than CA3485, calculated from the (*002*) reflection. This may result from the lower OH^- sustaining growth of crystals without nucleation occurring at a sufficient rate. There is however, a general downward trend in the CDL calculated form the FWHM of the (*002*) reflection. This is due primarily to the fact that the high initial NaOH causes more rapid nucleation and growth is inhibited as finer crystals form in the early stages of the reaction without sufficient precursor to sustain growth.

Reactions with initial NaOH below 0.1M resulted in no product formation. This was due to the pH being too low for the precipitation of $Ca(OH)_2$ and the LDH did not form, while $Al(OH)_3$ can precipitate at pH 4 [148], the precipitation of single phase $Al(OH)_3$ did not

Chapter adapted from Clark, I.; Dunne, P. W.; Gomes, R. L.; Lester, E. *Journal of Colloid and Interface Science* **2017,** *504*, 492-499.

occur. For this reason these samples were omitted from the rest of the investigation. Concentration. The CDL calculated from the (*030*) reflections shows a great deal of variability and a lack of coherence in changes between the adjustments in NaOH concentration. The reduced crystallinity of the sample produced with high NaOH made the separation of the reflection and the background radiation more challenging, and as a result the FWHM of the reflections is more variable between repeated analyses, which caused the variability in the CDL calculation, this was not a problem when calculating the FWHM and the CDL for the (*002*) reflection as it was much more intense.

The synthesis of $Ca_2Al\text{-}NO_3$ LDHs is adversely affected by excessively high (>0.2mol L^{-1}) and low (<0.1mol L^{-1}) precursor base. The ideal synthesis conditions to produce a stable crystal structure is around stoichiometric amount based on the general LDH formula: $\left[M^{II}_{1-x}M^{III}_{x}(OH_2)\right](A^{n-})_{x/n} \cdot zH_2O$ [9], at 0.1-0.125mol L^{-1}.

4.3.6 Effect of Initial Sodium Hydroxide on Surface Area Characteristics

The S_{BET} of the LDH sample produced under varying NaOH conditions was evaluated for the effect that the more rapid nucleation has on the material surface characteristics. Specific surface area for the samples with varying pH is similar to samples produced under constant NaOH conditions, with the S_{BET} values are in the range of 4-7 $m^2\ g^{-1}$ (Table 4.6). The precursor NaOH concentration appears to have little impact on S_{BET} despite resulting in changes to the ⟨*002*⟩ and ⟨*030*⟩ CDL. This is because the particle size may again be in the micrometer scale, because despite the trend visible in CDL, which has been reported to affect surface area [166], the S_{BET} shows no trending towards higher NaOH samples having higher surface areas (Table 4.6).

Chapter adapted from Clark, I.; Dunne, P. W.; Gomes, R. L.; Lester, E. *Journal of Colloid and Interface Science* **2017,** *504*, 492-499.

Table 4.6 $Ca_2Al\text{-}NO_3$ platelet diameter with varying NaOH concentration

Sample	Reaction Conditions			S_{BET} / $m^2\ g^{-1}$	Platelet Diameter / μm
	Temperature / K	Pressure / MPa	NaOH concentration / mol L^{-1}		
CA1M348	348	5	1	6.0	3
CA05M348	348	5	0.5	6.5	3
CA02M348	348	5	0.2	6.7	3
CA01M348	348	5	0.1	6.8	2
CA1M373	373	15	1	4.7	2
CA05M373	373	15	0.5	5.4	4
CA02M373	373	15	0.2	6.4	3
CA01M373	373	15	0.1	6.6	3

The diameter shows little variation between the different concentrations of NaOH in the precursor solutions, however some broad trends can be identified. For the samples produced at 348K, the sample produced with 1mol L^{-1} of NaOH is had the smallest platelet size with the samples produced whereas lower concentrations of base exhibited larger diameters of 3-4μm. Samples produced at 373K however indicate that the sample produced with the lowest NaOH level in the precursor had the smallest diameter, indicating that 0.1mol L^{-1} could not sustain growth to the same degree at sample produced with a slight excess of base. The implication is, that optimum concentration for nucleation and growth, as well as the minimisation of $CaCO_3$ and $Ca(OH)_2$, impurities is a slight excess of OH^-. The NaOH concentration should be above 0.1mol L^{-1} in this reaction arrangement.

Chapter adapted from Clark, I.; Dunne, P. W.; Gomes, R. L.; Lester, E. *Journal of Colloid and Interface Science* **2017,** *504*, 492-499.

4.3.7 Effect of Initial Sodium Hydroxide on Structural and Chemical Characteristics

Thermogravimetric analysis of the samples CA1M348 and CA1M373 shows different mass loss profiles compared to the other samples produced at lower NaOH concentrations (Figure 4.13). Most noticeable is the reduced mass loss in both samples; 38% for CA1M348 and 37% for CA1M373, compared to mass loss of 41±1% in all other samples. In addition to the weight loss steps observed in all other LDH samples, these samples prepared with higher NaOH concentrations show additional mass losses at 373K and 613K. These additional mass loss events and the overall lower total mass losses can be attributed to the presence of both calcium hydroxide and the calcium aluminium carbonate observed in the X-ray diffraction patterns [255].

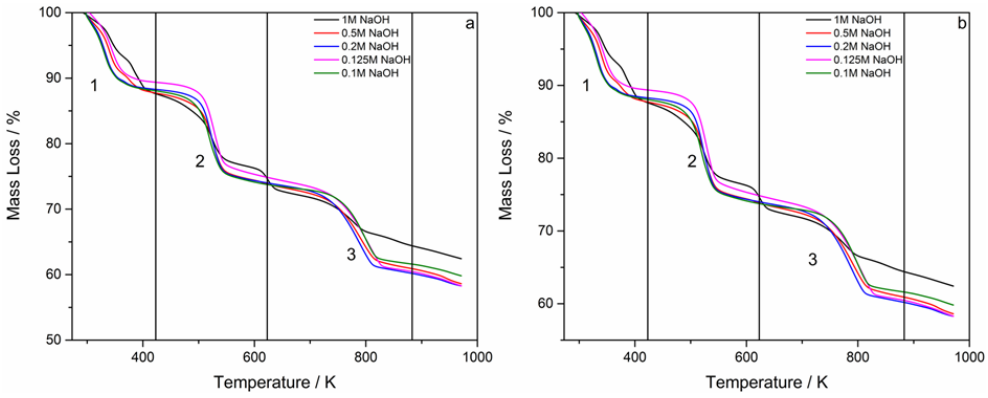


Figure 4.13 Thermal analysis of Ca_2Al-NO_3 with varying initial NaOH concentration, at different temperatures a) 348K b) 373K

The molar content of Ca^{2+} to Al^{3+} in the LDHs, produced with varying NaOH content in the precursor solutions, is outlined in Table 4.7. The Ca/Al ratio was 2±0.1 for all but CA1M samples, which suggests a chemical formula approximate to $[Ca_2Al(OH)_6](NO_3)\cdot zH_2O$ for the samples. The Ca/Al ratio was 2.16 and 2.37 for CA1M348

Chapter adapted from Clark, I.; Dunne, P. W.; Gomes, R. L.; Lester, E. *Journal of Colloid and Interface Science* **2017,** *504*, 492-499.

and CA1M373 respectively. Inflated M^{II}/M^{III} ratios for CA1M348 and CA1M373 point to the fact that there is excess of calcium in the sample which is due to the presence of $Ca(OH)_2$ (Figure 4.10). The diffraction patterns for the CA1M samples do not show detectable AlOOH and $Al(OH)_3$, indicating that the initial precursor ratio can affect the product in extreme cases when conditions for preferential precipitation occur. The ideal ratio that the M^{II} and M^{III} ions form at in the $Ca_2Al\text{-}NO_3$ LDHs left the excess Ca^{2+} to form other compounds when there is an imbalance in the precursor concentrations. These impurity compounds impact on the $Ca_2Al\text{-}NO_3$ material, particularly when looking at it from an adsorption stand point. The $Ca(OH)_2$ and $CaCO_3$ are not adsorptive in the same way as $Ca_2Al\text{-}NO_3$ and their presence in the sample would reduce the effectiveness of the LDH/MMO adsorbent.

Table 4.7 The effect of varying precursor NaOH on the Ca/Al ratio of $Ca_2Al\text{-}NO_3$

Sample	Heater Temperature / K	Pressure / MPa	NaOH concentration / mol L^{-1}	Ca/Al Ratio
CA1M348	348	5	1.0	2.16
CA05M348	348	5	0.5	2.01
CA02M348	348	5	0.2	2.00
CA01M348	348	5	0.1	2.05
CA1M373	373	15	1.0	2.37
CA05M373	373	15	0.5	2.00
CA02M373	373	15	0.2	2.05
CA01M373	373	15	0.1	2.07

Chapter adapted from Clark, I.; Dunne, P. W.; Gomes, R. L.; Lester, E. *Journal of Colloid and Interface Science* **2017,** *504*, 492-499.

4.4 Continuous Synthesis of $Zn_2Al\text{-}CO_3$

4.4.1 Experimental Conditions

The synthesis of $Zn_2Al\text{-}CO_3$ LDHs cannot be strictly termed as hydrothermal due to the fact that no increase of temperature is utilised in the reaction. The continuous flow reactor served primarily as a high pressure mixing vessel, as mentioned in Section 3.1.2. The research by Demoisson *et al* on the hydrothermal synthesis of ZnO nanoparticles indicated that at lower temperatures and higher pressures (<323K / >20MPa) there is a preference for $Zn(OH)_2$ formation [213]. Thus synthesis occurred at room temperature (293±2K) and 24MPa.

4.4.2 Crystal and Particle Characteristics of $Zn_2Al\text{-}CO_3$

4.4.2.1 X-Ray Crystallography

$Zn_2Al\text{-}CO_3$ exhibited hexagonal cell characteristics with the rhombohedral symmetry (Space group – $R\bar{3}m$). The crystal system of $Ca_2Al\text{-}NO_3$ is somewhat unique among LDHs, and other metal configurations exhibit the same $R\bar{3}m$ crystal symmetry [2, 172]. The difference in crystal structure between the $Ca_2Al\text{-}NO_3$ and $Zn_2Al\text{-}CO_3$ should lead to crystal and structural characteristics that are more appropriate for adsorption. The X-ray diffractogram of $Zn_2Al\text{-}CO_3$ LDH is displayed in Figure 4.14, and the pattern of the material matched well with published data regarding structure. The lattice parameters of the material were calculated from equation (3.2) were 0.30nm and 2.29nm for *a* and *c* respectively, with a d_{003} spacing of 0.76nm. These data relate well to lattice parameters for $Zn_2Al\text{-}CO_3$ LDHs, in published literature which indicates the continuously produced LDH in this thesis is comparable to batch synthesised materials in terms of crystal

Chapter adapted from Clark, I.; Dunne, P. W.; Gomes, R. L.; Lester, E. *Journal of Colloid and Interface Science* **2017,** *504*, 492-499.

structure [30, 140]. Crystal domain length calculated using the Scherrer equation is 18±0nm relating to the (*003*) reflection and 39±1nm relating to the (*110*) reflection. The crystal system and CDL of the $Zn_2Al\text{-}CO_3$ LDHs is different from the $Ca_2Al\text{-}NO_3$ LDHs. This is due to the nature of the $CaAl\text{-}NO_3$, and the coordination of the Ca^{2+} and Al^{3+} ions. The coordination of these ions results in a different crystallographic profile compared to the $Zn_2Al\text{-}CO_3$ LDH [140, 244], and therefore different domain length characteristics.

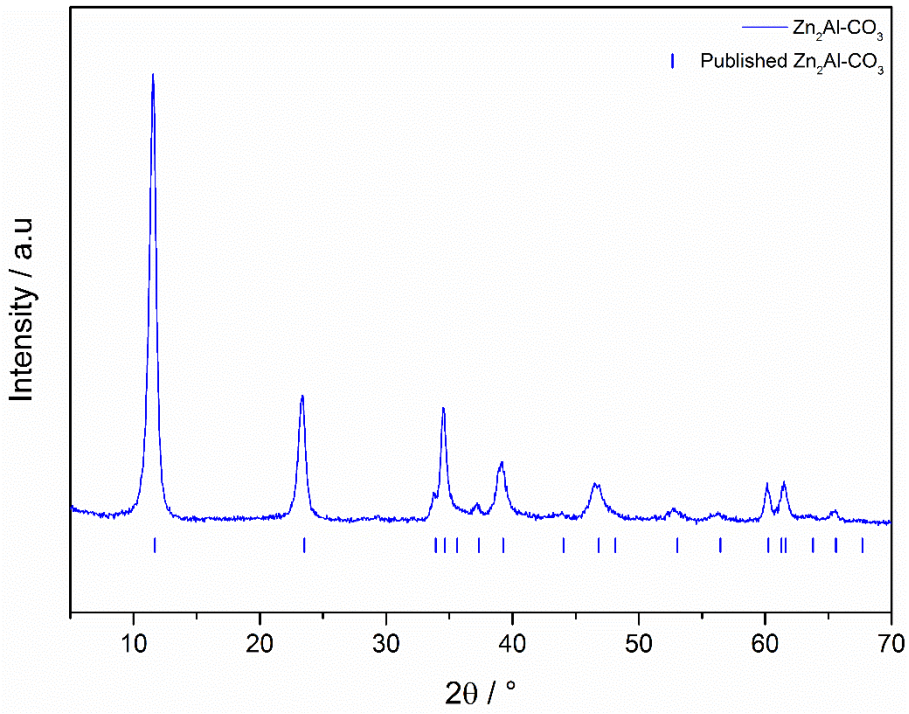


Figure 4.14 X-Ray diffractogram of continuously produced $Zn_2Al\text{-}CO_3$ with reference points of published $[Zn_4Al_2(OH)_{12}](CO_3)\cdot 4H_2O$ reflections [256]

4.4.2.2 Transmission Electron Microscopy and Particle Size Distribution

In contrast with the data calculated from XRD, the particle size distribution obtained from TEM micrographs indicated that the particles are somewhat larger (Figure 4.15 and Figure 4.16). The particle size calculated from TEM micrographs was 120nm while the CDL calculated from the (*110*) reflection in the XRD diffractogram (39±1nm).

Chapter adapted from Clark, I.; Dunne, P. W.; Gomes, R. L.; Lester, E. *Journal of Colloid and Interface Science* **2017,** *504*, 492-499.

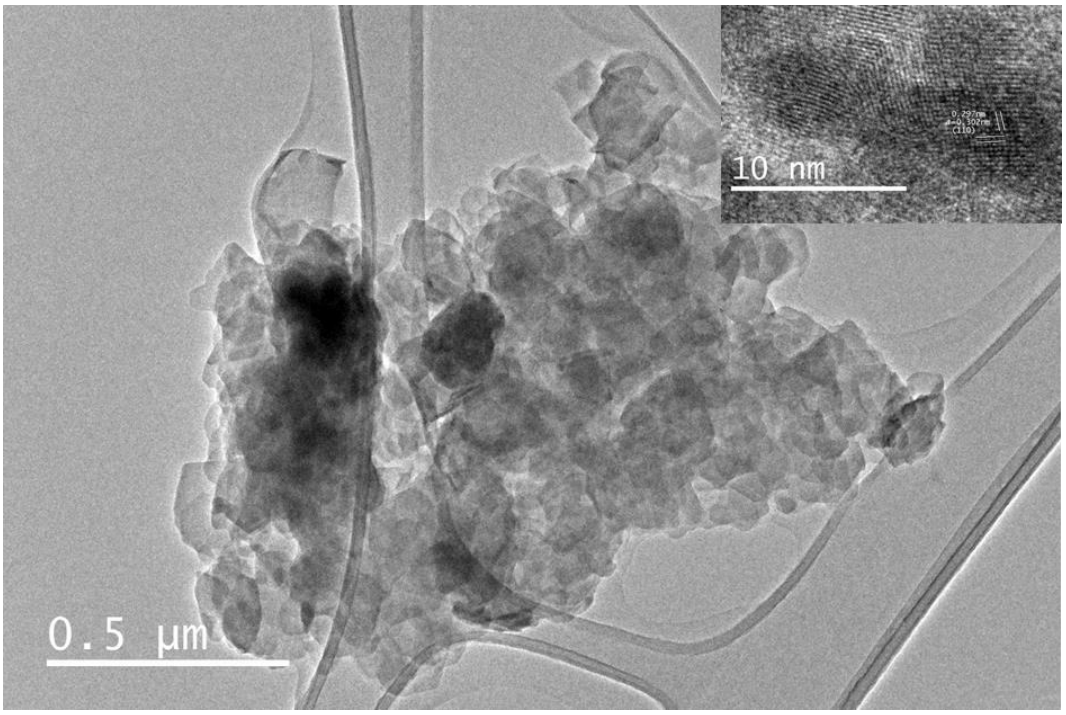


Figure 4.15 TEM micrograph of Zn_2Al-CO_3, inset high resolution image with lattice fringes visible

The lattice fringes, in the inset image in Figure 4.15, are visible and can be corresponded well with the value of the *a* parameter calculated from equation (4.2). The CDL is subject to scrutiny, however it must be noted that the CDL calculated by XRD cannot account for intrinsic disruptions in the long range order and therefore the crystal domain length may not be representative of the average platelet size, in a similar way to the calculation of the CDL in the Ca_2Al-NO_3 LDH samples in Section 4.3. The size of the particles in this research is 120nm, with a range between 30 and 290nm. Compared with separate nucleation and aging synthesis (SNAS), particle size is similar; with the SNAS method producing LDHs with an average size of 170nm and 90% of particles <370nm [158].

Chapter adapted from Clark, I.; Dunne, P. W.; Gomes, R. L.; Lester, E. *Journal of Colloid and Interface Science* **2017,** *504*, 492-499.

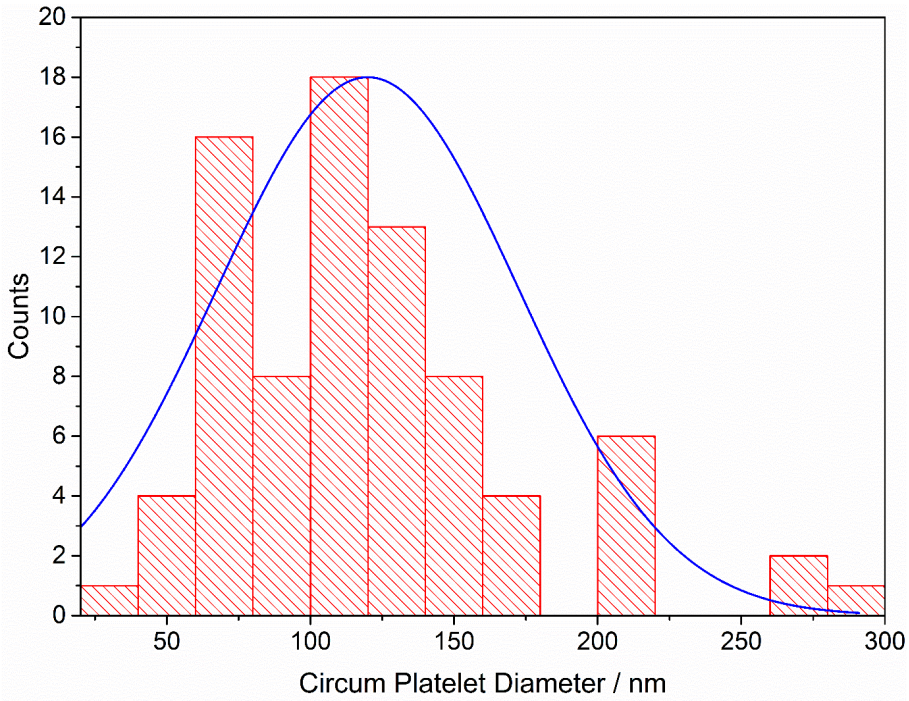


Figure 4.16 Particle size distribution of Zn_2Al-CO_3 LDHs

4.4.3 Surface and Characteristics Chemical of Zn_2Al-CO_3

4.4.3.1 Surface Area and Pore Size Characteristics

Surface area analysis by nitrogen adsorption at 77K indicated a Type-IV isotherm for the continuously produced Zn_2Al-CO_3 (Figure 4.17) [248]. The Type-IV shape suggests that there are meso-pores present within the material. The adsorption branch of the isotherm resembled that of a Type-II isotherm and shows that there is mono and multilayer adsorption on pore walls up to high P/P_0, which is followed by condensation in the meso-pores [248]. There is a hysteresis loop on the desorption branch of the isotherm, giving the Type-IV shape. The hysteresis most closely resembled H3 hysteresis [248]. There is no plateau at the highest point on either the adsorption or desorption branches of the isotherm, this indicated that the gas adsorption was occurring between loosely packed agglomerates of platelet like particles [248]. The inset pore size

Chapter adapted from Clark, I.; Dunne, P. W.; Gomes, R. L.; Lester, E. *Journal of Colloid and Interface Science* **2017,** *504*, 492-499.

distribution, calculated from the BJH method, inset in Figure 4.17 indicated that there is a large volume of pores that are macroporous (>50nm), however there is still some pore volume in the mesoporous (2-50nm) range giving the material its Type-IV isotherm, while no micro-pores (<2nm) are present in the LDH.

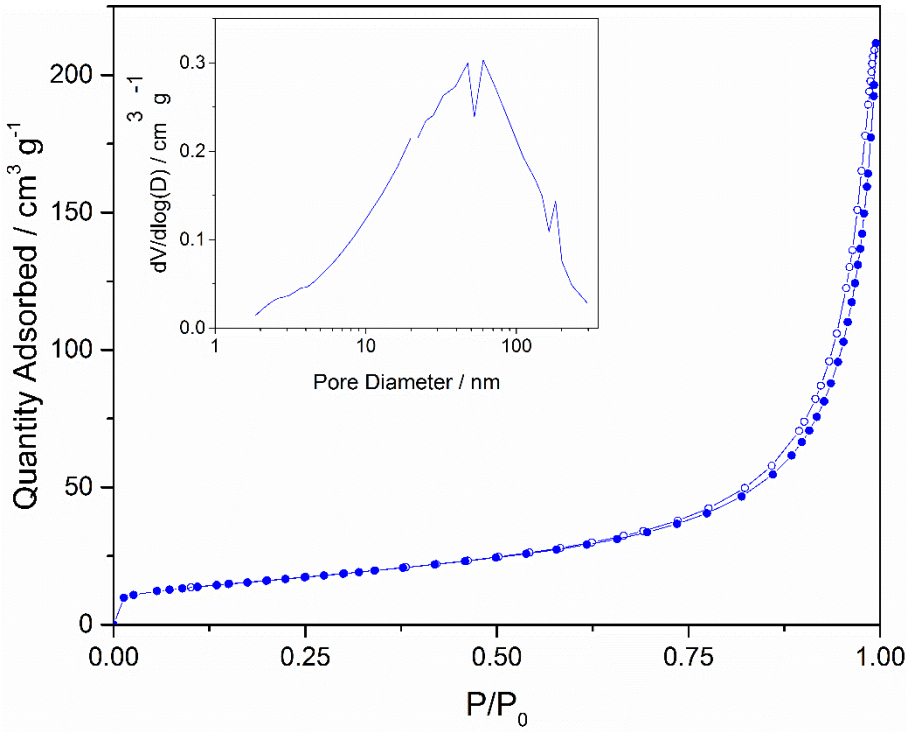


Figure 4.17 Nitrogen adsorption isotherm for Zn_2Al-CO_3, inset - pore size distribution data

The surface area and pore data for the LDH are outlined in Table 4.8, along with surface areas of Zn_xAl-CO_3 samples produced by different methods published in literature. From the data in the table it can be seen that Zn_2Al LDHs typically display S_{BET} values of approximately 50-60m^2 g^{-1} with pore volumes between 0.1cm^3 g^{-1} and 0.3cm^3 g^{-1}. The sample from Yang *et al* exhibited high surface area due to the ratio Zn^{2+}/Al^{3+} equal 1 [257]. With decreasing molar ratio there is a breakdown in the uniformity and coordination in the brucite-like layers due to the size of the ionic radii of the M^{II} and M^{III} ions. This disruption results in a more porous structure, this is discussed further in

Chapter adapted from Clark, I.; Dunne, P. W.; Gomes, R. L.; Lester, E. *Journal of Colloid and Interface Science* **2017,** *504*, 492-499.

Chapter 7, regarding the continuous hydrothermal synthesis of metal oxide@LDH nanocomposites. The surface area of the continuously produced LDH is comparable with literature and larger than the S_{BET} recorded for all the $Ca_2AL\text{-}NO_3$ samples in this thesis which were <11$m^2\ g^{-1}$ and <7$m^2\ g^{-1}$ for freeze dried and oven dried samples respectively.

Table 4.8 Surface area and pore data for $Zn_2Al\text{-}CO_3$ LDH compared with literature

Sample	Synthesis route	S_{BET} / $m^2\ g^{-1}$	Pore Diameter / nm	Pore Volume / $cm^3\ g^{-1}$	Reference
$Zn_2Al\text{-}CO_3$	Continuous Flow	50.1±0.2	15.3	0.2	This work
$Zn_2Al\text{-}Cl$	Co-precipitation	51.87	20.04	0.26	[258]
$Zn_2Al\text{-}CO_3$	Batch Hydrothermal	64.9	11.7	0.19	[259]
$ZnAl\text{-}CO_3$	Co-precipitation	135	4.42	0.151	[257]
$Zn_2Al\text{-}CO_3$	Co-precipitation	44	16.6	0.158	[110]

4.4.3.2 Surface Topography and Chemical Structure of $Zn_2Al\text{-}CO_3$

Where TEM allows the sizing of individual particles and crystals of the LDH, lower resolution SEM allows the mapping of the surface structure. The SEM images in Figure 4.18 show stacking of LDH platelets on top of each other into micron sized agglomerates. While many platelets are clearly visible, the presence of the large agglomerates possibly explains the reason for the surface area of close to 50$m^2\ g^{-1}$. Tight face-face stacking can reduce the available surface of the individual particles for adsorption. Nevertheless, there does appear to be cavitation within the agglomerates suggesting loose packing.

Chapter adapted from Clark, I.; Dunne, P. W.; Gomes, R. L.; Lester, E. *Journal of Colloid and Interface Science* **2017,** *504*, 492-499.

The loose packing of the platelet particles is well represented by H3 hysteresis in the nitrogen adsorption isotherm.

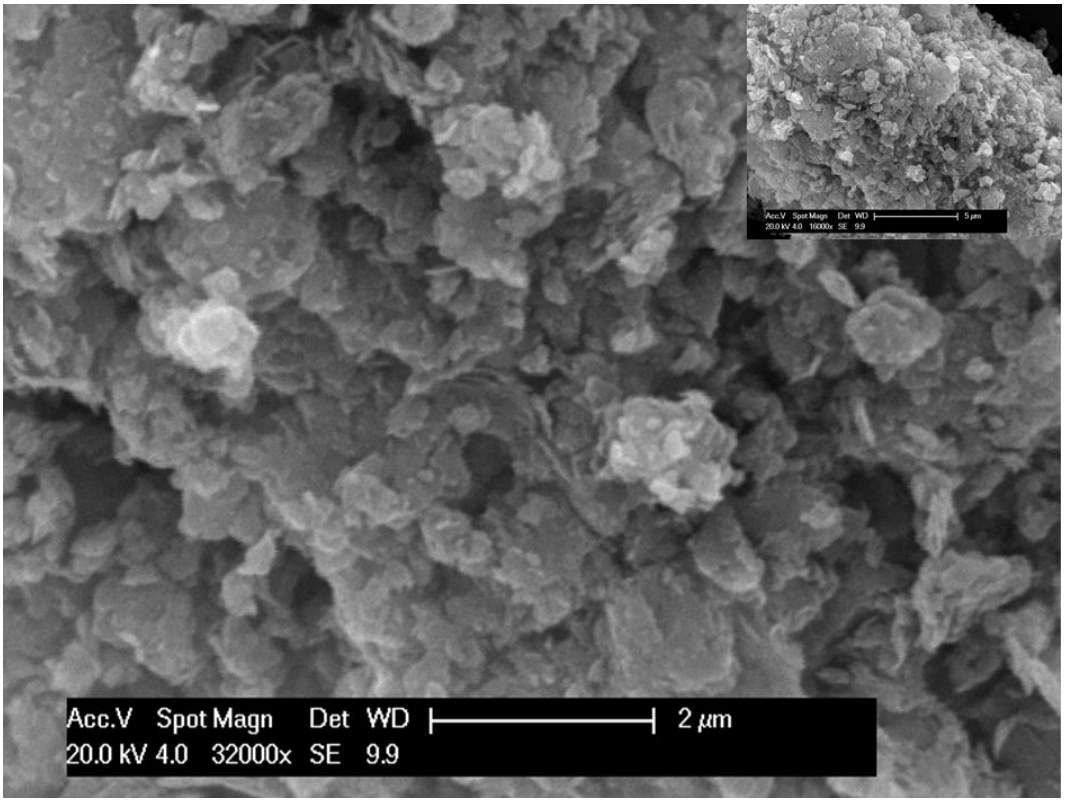


Figure 4.18 SEM micrograph of Zn_2Al-CO_3, inset low magnification image

SEM-EDX was used to establish the molecular ratio between the metallic species in the brucite-like layers. The data in Table 4.9 illustrates the actual M^{II}/M^{III} was similar the theoretically ideal ratio from the precursor salt solution. This suggests that the reaction conditions and NaOH concentration did not produce small amounts of ZnO, not inhibit $Al(OH)_3$ precipitation, which were not detected in XRD analysis.

Table 4.9 Molecular content of Zn2Al-CO3 LDH

Sample	Zn Content / %	Al Content / %	Zn/Al
Zn_2Al-CO_3	29.6	16.3	1.8

Chapter adapted from Clark, I.; Dunne, P. W.; Gomes, R. L.; Lester, E. *Journal of Colloid and Interface Science* **2017,** *504*, 492-499.

4.5 Summary

The synthesis of two types of LDH with differing crystal characteristics was performed in a counter-current continuous flow reactor. The synthesis of $Ca_2Al\text{-}NO_3$ highlighted the reaction variables that impact on the final product during synthesis. These variables were temperature, pressure and initial NaOH concentration. The initial NaOH concentration primarily affects nucleation rates, with 1mol L^{-1} NaOH resulting in CDL of 27nm and 60nm for (*002*) and (*030*) reflections respectively. The CDL increased to 53nm for samples produced with 0.125M NaOH in the down-flow reactor feed. The reducing NaOH causes a shift in prominence of nucleation to growth. However the greatest change brought about through OH^- manipulation was the synthesis of $Ca(OH)_2$ impurities resulting from excess OH^- and excess Ca^{2+} in the reaction. These impurities affected the thermal stability and chemical composition of the final powder. Pressure and temperature are more intimately affected by each other and the result is that as temperature increases the control over CDL through pressure alteration is reduced, particularly in the (*002*) crystal plane. The effect of CDL change between different samples is minimal as all samples investigated at varying pressure and temperature displayed similarly low surface area (4m-7m^2 g^{-1}). The changes in temperature, pressure and NaOH concentration appear to have little effect on the diameter of LDH platelets as there are no definitive trends present and mean platelet size ranges from 3-5μm.

The synthesis of $Zn_2Al\text{-}CO_3$ meanwhile, was a precursor study to Chapter 5 and Chapter 6. Following on from the lack of variability in the characteristics of $Ca_2Al\text{-}NO_3$ LDHs, only one set of reaction conditions was used. After the successful synthesis of crystalline $Zn_2Al\text{-}CO_3$; the conditions outlined in Chapter 3, worked well and were carried forward to other experiments involving $Zn_2Al\text{-}CO_3$. The surface area is higher than that of Ca_2Al-

Chapter adapted from Clark, I.; Dunne, P. W.; Gomes, R. L.; Lester, E. *Journal of Colloid and Interface Science* **2017,** *504*, 492-499.

NO_3 type LDHs, at 51m^2 g^{-1} compared to <11m^2 g^{-1}, primarily due to the larger platelets in the Ca_2Al LDHs compared with the Zn based LDH. The nature of the agglomeration may also play a part in the larger surface area. Regardless of material the conversion of precursors to LDHs is acceptable using continuous synthesis methods and the surface characteristics of continuously produced Zn_2Al-CO_3 is comparable with batch synthesis materials.

Chapter adapted from Clark, I.; Dunne, P. W.; Gomes, R. L.; Lester, E. *Journal of Colloid and Interface Science* **2017,** *504*, 492-499.

5. Results and Discussion: Scaling Synthesis of Zn_2Al-CO_3 Layered Double Hydroxides

5.1 Introduction

The continuous synthesis of Zn_2Al-CO_3 at bench scale conditions detailed in Chapter 4 were utilised in pilot and industrial scale reactions. The perceived improvements in material characteristics of Zn_2Al-CO_3 when compared with Ca_2Al-NO_3 type LDHs were the primary reason for using Zn based LDHs. The reaction conditions of the bench scale synthesis were carried forward to a set of synthesis experiments with increasing scale to determine the feasibility of scale up of LDH synthesis for adsorption experiments, and the changing material characteristics that occur with increased scale of synthesis. Pilot scale synthesis was completed at a scale of twenty times greater than the bench scale, thus in order to increase the scale of the synthesis the flow rate was increased from 30mL min^{-1} to 600mL min^{-1}. Industrial scale synthesis was then scaled up from the pilot scale reactor to a flow rate of 1050L h^{-1}. The experiments were completed at 293±5K, while the pressure was maintained in the reactor by a back pressure regulator at 24MPa. Changes in lattice parameters, crystal domain length (CDL), chemical and structural characteristics between the three scales of synthesis were elucidated using XRD, SEM, TEM, BET, TGA and SEM-EDS. Table 5.1 outlines the difference in flowrate between the different synthesis scales and the effect that the increased scale has on the yield of the process. The theoretical yield is based on the concentration of salts in the precursor solutions and the molecular formula of the LDH product while the yield is based on the mass loading of the lquid suspension from the synthesis process.

Table 5.1 Flowrate and yield of Zn_2Al-CO_3 with increasing synthesis scale

Scale	Flowrate / L h^{-1}	Theoretical Yield / g h^{-1}	Yield / g h^{-1}
Bench	1.8	11	5
Pilot	36	217	100
Industrial	1050	6300	3000

5.2 Highlights

- First pilot and industrials scale continuous synthesis of Zn_2Al-CO_3 LDH nanomaterials reported.
- Material characteristics comparable between bench and industrial samples, indicating that there is potential for continuous industrial scale synthesis of LDH nanomaterials.

5.3 Reaction Conditions and Flow Regimes

The increased flow rate from bench scale to pilot scale and then again from pilot scale to industrial scale synthesis results in changes to the flow regime within the reaction system. The Reynolds number (Re) of the flow system immediately after mixing and up to the cross piece at the reactor outlet was calculated using the equation for Re (5.1):

$$\mathrm{Re} = \frac{\rho D u}{\mu} \qquad (5.1)$$

Where Re is the Reynolds number, ρ is the density of the water in kg m^{-3}, μ is the viscosity (Pa s), u is the fluid velocity (m s^{-1}) and D is the hydraulic diameter of the reactor tubing (m). The volumetric flowrate through the bench scale reactor at 293K and 24MPa results in a calculated Re of 68. The flow regime for the Re in this reaction is well within the

limits of laminar flow. Flow becomes transitional at Re>2300 and turbulent flow occurs when Re>4000 [231]. The dramatically increased flow rate of the reaction and the different reactor geometries between scales are the principle changes observed. The comparative Reynolds numbers of the pilot and industrial scale reaction were 310 and 9050 (Table 5.2). These numbers along with the changes to reactor geometry may be the cause of any changes to CDL and particle size, and subsequent surface area characteristics. The fact that the pilot scale reaction, despite operating at a higher flow rate, the flow regime is still linear. The dimensions of the tubing utilised in the pilot scale reactor are greater than the bench scale and similar in size when compared to the industrial scale reactor. Therefore the Reynolds number increases in line with the flow rate.

Table 5.2 Reynolds number (Re) of three scales of synthesis for pure water

Scale	Flowrate / L h^{-1}	Re
Bench	1.8	68
Pilot	36	310
Industrial	1050	9050

5.4 Materials Characterisation

5.4.1 X-ray Diffraction and Changes to Crystal Structure with Increasing Scale

The X-ray diffraction profile of the bench scale material (B-LDH) is outlined with the pilot (P-LDH) and industrially (I-LDH) produced samples in Figure 5.1. The diffractograms of three samples produced at progressively larger scale, display reflections representative

of a crystalline $Zn_2Al\text{-}CO_3$ LDH. The continuously produced $Zn_2Al\text{-}CO_3$ samples from exhibit rhombohedral symmetry in a hexagonal setting with the space group ($R\bar{3}m$) [9]. Lattice parameters were calculated using information from the Bragg equation (5.2) and the lattice equation outlined in (5.3).

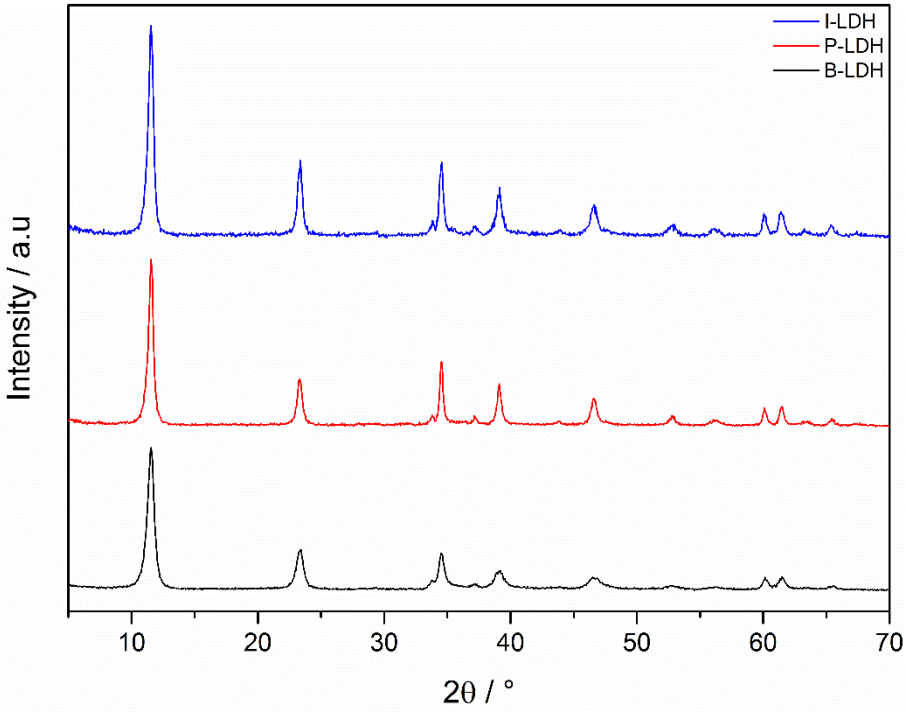


Figure 5.1 X-ray diffractogram for bench (B-LDH), pilot (P-LDH) and industrial (I-LDH) samples

$$n\lambda = 2d\sin\theta \qquad (5.2)$$

$$\frac{1}{d_{hkl}^2} = \frac{4}{3}\frac{(h^2+hk+k^2)}{a^2} + \frac{l^2}{c^2} \qquad (5.3)$$

Where n is a constant (n=1), λ is the wavelength of the X-ray, d is the inter-planar spacing (nm) and θ is the Bragg angle, in degrees. Miller indices *hkl* indicate the lattice plane of a particular reflection and *a* and *c* are the lattice parameters. Lattice parameters for B-LDH are 0.30nm and 2.29nm for *a* and *c* respectively. The lattice parameters of P-LDH calculated from the (*003*) and (*110*) reflections were 0.31nm and 2.29nm for *a* and *c*, while the lattice parameters for the I-LDH sample were calculated at 0.31nm for *a* and

2.30nm for *c.* The lattice parameters were in agreement with published information regarding the characteristics of Zn_2Al-CO_3 LDHs [9, 260]. The crystal domain length for the LDH samples calculated was using the Scherrer equation (5.4) and the full width at half maximum (FWHM) of (*003*) and (*110*) reflections.

$$CDL = \frac{S\lambda}{B\cos\theta} \qquad (5.4)$$

Crystal domain length is denoted by CDL, S is the Scherrer constant, assumed to be 0.9 [218], λ is the wavelength of the x-ray ($Cuk_{1\alpha}$=0.15406nm), B is the full width at half maximum (FWHM) of the reflection. The Bragg and is denoted by θ. The data in Table 5.3 illustrates an increase CDL in both ⟨*003*⟩ and ⟨*110*⟩ directions when scaling the synthesis from 30mL min^{-1} on the bench to 600mL min^{-1} in the pilot reactor.

Table 5.3 Crystal domain length (CDL) of scaled Zn_2Al-CO_3 LDH samples

Sample	CDL in ⟨*003*⟩ plane / nm	CDL in ⟨*110*⟩ plane / nm
B-LDH	18	39±1
P-LDH	26	50±4
I-LDH	19	31±1

This trend has previously been demonstrated in the scaling of continuous hydrothermal synthesis of $Ba_xSr_{(1-x)}TiO_3$ nanoparticles between bench and pilot scale reaction systems [11]. The cause of the observed growth in CDL is attributed to a number of factors. The combination of changes in turbulence of the flow in the pilot scale reactor, compared with the bench scale reactor (Table 5.2), is a possible cause for the change. The flow regime may be likely as the $Ba_xSr_{(1-x)}TiO_3$ nanoparticles produced in the work by Dunne *et al* were also produced in the same reactor with comparable increases in flow between the bench and pilot scale reaction schemes [11]. The CDL of the industrial scale sample (19nm) was comparable to the CDL of the bench scale sample (18nm). The increase in

crystal domain length between B-LDH and P-LDH was primarily attributed to the post synthesis period where the P-LDH suspension was allowed to settle, in order to reduce the overall volume liquid product. The reduction of liquid volume was essential to enable washing and drying of the sample. During this settling period, some degree of Ostwald ripening may occur, continued precipitation of any residual precursor may also be a contributing factor in the increase in CDL.

5.4.2 Chemical Structure and Morphology

The molecular ratio of Zn and Al metal hydroxides in the LDH samples can be identified by the respective mass and molecular ratios of the metals as determined by SEM-EDS. The M^{II}/M^{III} ratio of both the bench and pilot scale LDH is outlined in Table 5.4. The Zn/Al for both B-LDH and P-LDH samples is close to the ideal value of 2, based on the precursor concentrations of 0.067mol L^{-1} of Zn^{2+} and 0.033mol L^{-1} of Al^{3+}. The pilot scale, P-LDH, sample exhibits a molar ratio of 2.2, which is slightly in excess of the ideal ratio value. The bench scale, B-LDH, sample however, appears to show a greater degree of $Al(OH)_3$ precipitation compared with $Zn(OH)_2$ in the reactor. This is evident from the M^{II}/M^{III} ratio in Table 5.4. The closeness of the actual Zn/Al ratio of the bench and pilot scale LDH samples indicates that the scaling of LDH synthesis and changing of flowrate, between bench and pilot scale, does not impact greatly on the co-precipitation rates of the metal hydroxides in the LDH. Industrial scale synthesis appeared to favour $Zn(OH)_2$ precipitation as the Zn/Al ratio is skewed away from the theoretical ratio of 2. However, the Zn/Al ratio of the I-LDH sample is closer to 3, thus indicating that the precipitation of $Al(OH)_3$ in the industrial scale LDH is not as efficient. This has implications towards LDH synthesis at industrial scale and modification of precursor ratios may be required to mitigate the changes to the Zn/Al ratio in the LDH.

Table 5.4 Molecular ratio data from SEM-EDS analysis of bench (B-LDH), pilot (P-LDH) and industrial (I-LDH) samples

Sample	Molecular % Zn	Molecular % Al	Zn/Al
B-LDH	29.6	16.3	1.8
P-LDH	17.6	8.1	2.2
I-LDH	9.1	3.3	2.8

The bench scale LDH sample analysed by SEM is illustrated in Figure 5.2a. The powder of the B-LDH sample show platelet-like particles ranging from several hundred nanometers to 1-2μm. The platelets appear to show a degree of face-face stacking in agglomerates much larger than the platelets themselves. Face–face stacking of particles is a familiar characteristic of LDHs and was prominent in the bench scale synthesis of Ca_2Al-NO_3 LDHs and is also found in other examples of LDHs [165]. Agglomerates of the platelet-like particles are greater than 10μm across and in some instances are greater than 40μm. The P-LDH particles observed by the SEM (Figure 5.2b) appear to be similar in size, however in contrast with the B-LDH samples, the platelets exhibit less face-face stacking and are instead arranged in more edge-face stacked agglomerations. The edge-face stacking of platelets results in the more open flower-like micro-structure depicted in the SEM micrograph in Figure 5.2b. Edge-face stacking is also observed in the TEM micrograph in Figure 5.3b. The agglomerates found in the P-LDH sample are a similar size to those present in the B-LDH SEM samples. The SEM micrograph of the I-LDH sample looks similar to the P-LDH sample, suggesting that the agglomeration of crystals in the reactor is affected by the increased mixing of higher flows. The TEM micrograph however, shows an agglomerate that consists predominantly of face stacked platelets.

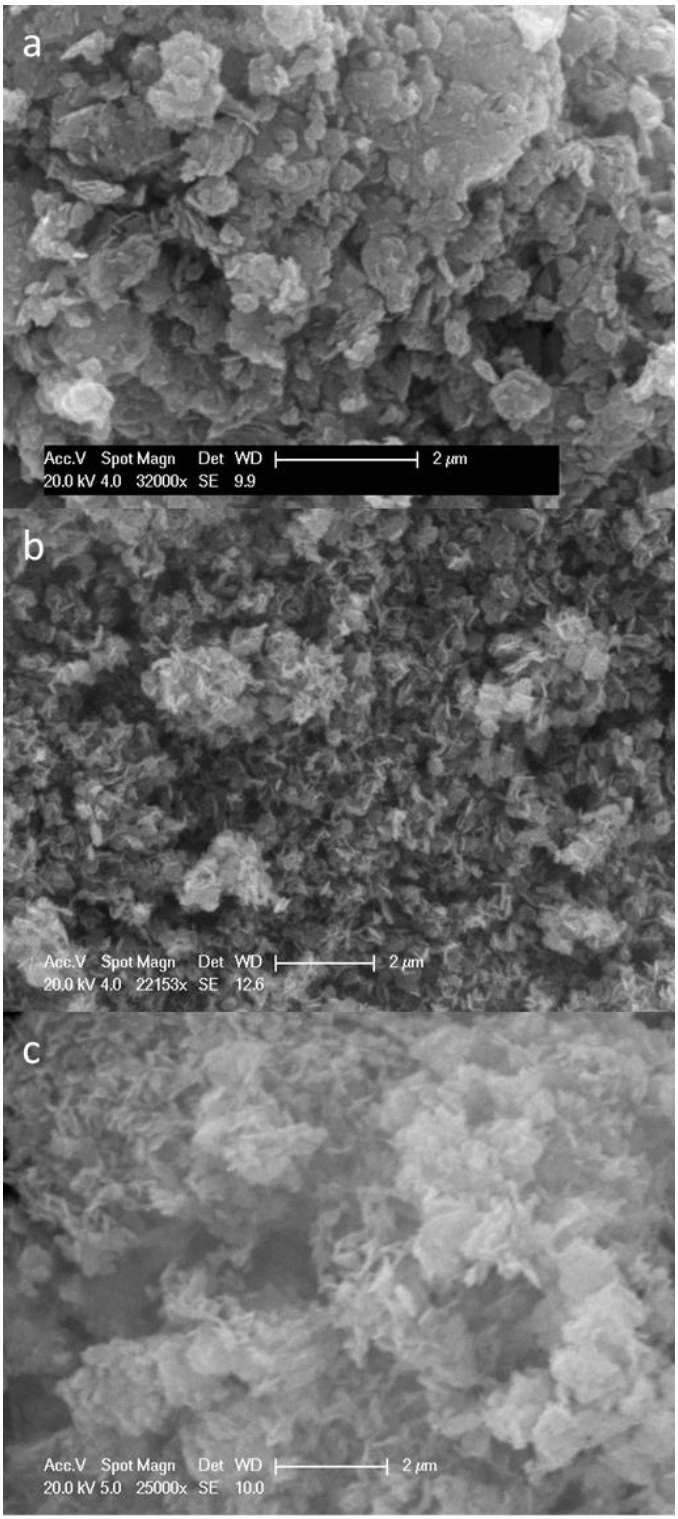


Figure 5.2 SEM micrographs of a) bench b) pilot c) industrial scale samples

TEM micrographs of the LDH samples are detailed in Figure 5.3. Image analysis indicated that the mean diameter of B-LDH platelets is 120±53nm (n=81). The image analysis of

the P-LDH particles was found to be 177±74nm (n=74), while I-LDH had a similar distribution to the B-LDH sample, yet the platelet diameter was 165±54nm (n=206).

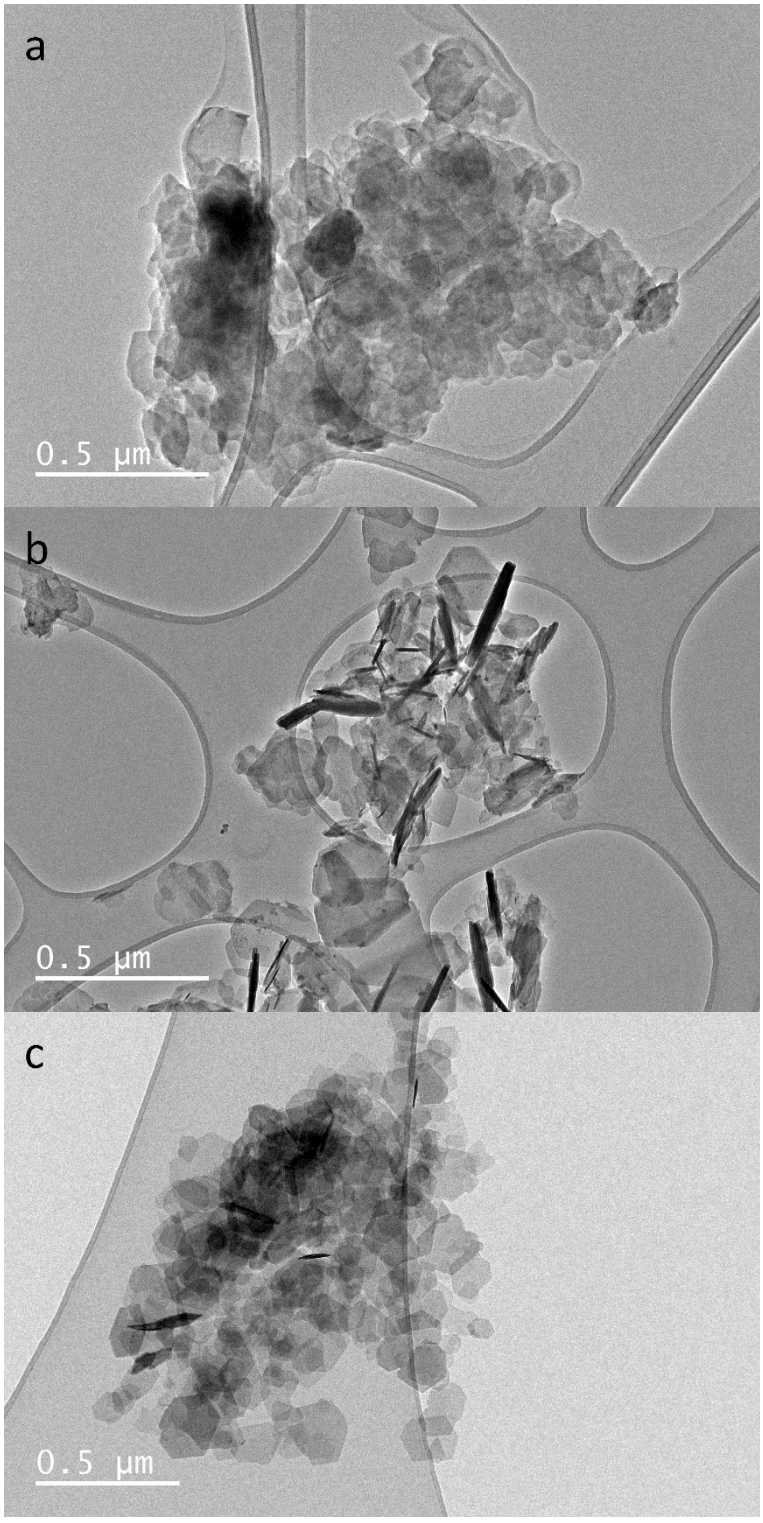


Figure 5.3 TEM micrographs of a) bench b) pilot c) industrial scale samples

The particle size distributions of the samples are detailed in Figure 5.4. From the data in Figure 5.4 it is clear that the bench scale reaction has a greater concentration of particles with a diameter in the region of 50-150nm while the distribution of the P-LDH sample exhibits a greater proportion of platelets in the 200-300nm platelet size. This is clearly visible in the example TEM micrographs where there are larger platelets visible in the middle of the micrograph in Figure 5.3b compared with Figure 5.3a. The larger size distribution and greater mean platelet size is possibly the result of the same changes that affected the calculation of CDL. The standard deviation of the I-LDH sample is comparable with the B-LDH sample, while the mean diameter is closer to the P-LDH particle size. This suggests that the increased reactor size may cause increased growth in LDH synthesis.

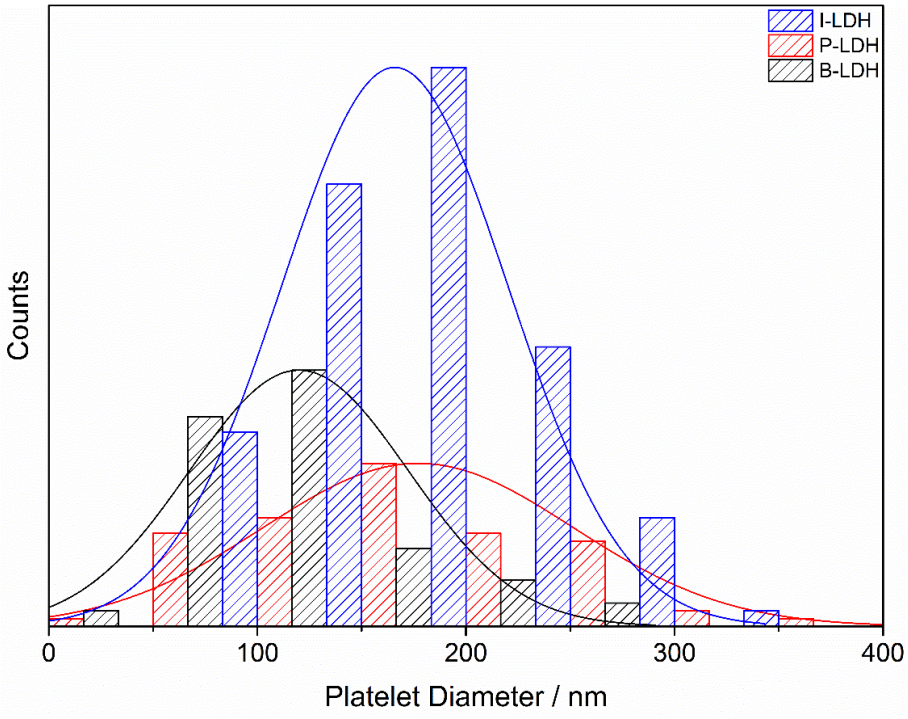


Figure 5.4 Platelet size distribution of bench (B-LDH) and pilot (P-LDH) samples, as calculated by image analysis of TEM micrographs

The CDL as calculated by the Scherrer equation shows the same trend with the image analysis of TEM micrographs, in that there is an increase is size between the bench and pilot scale samples. The image analysis produced significantly greater estimations of platelet diameter. This is attributed to the fact that the calculation of CDL and Scherrer equation is a measure of internal order and of the repeating units in the lattice. The presence of faults or disruptions to the order in the crystal structure and amorphous regions in the material are not accounted for. Broadening due to faults and strain is also not accounted for in the calculation of the CDL, which may also contribute to the large discrepancy between the CDL and the platelet size.

In contrast with the difference between the CDL and the platelet diameter; there is an agreement between the platelet thickness, of the few perpendicular particles visible in TEM micrographs, and the CDL calculated from the FWHM of (*003*) reflection. The CDL is 26nm for P-LDH while the thickness of the darker rod-shaped particles was 25±11nm (n=26).

5.4.3 Surface Area

The nitrogen adsorption isotherms are detailed in Figure 5.5. All three LDH samples exhibited Type-IV isotherms with H3 hysteresis. This indicates the material is mostly a mesoporous material created by loose agglomerates of lamellar, non-porous and macroporous, particles [248]. The pore size distribution suggests that there is a high concentration of pores in both bench and pilot samples close to the boundary between meso-pores (2nm-50nm) and macro-pores (>50nm) [248], indicating that macro-pores are present in the agglomerates of finer particles.

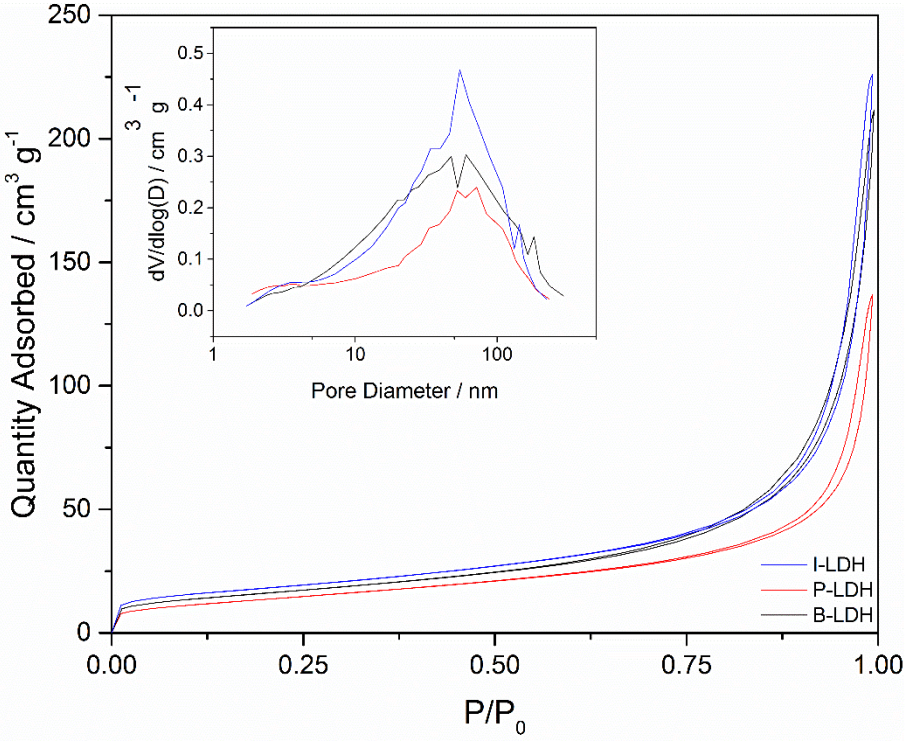


Figure 5.5 Nitrogen adsorption isotherms of bench (B-LDH) and pilot (P-LDH) samples. Inset image showing pore size distribution

The data in Table 5.5 shows the average pore diameter calculated from the desorption branch of the isotherm. The average pore diameter is larger in the bench scale sample compared with the pilot scale sample, however the total pore volume in the B-LDH sample is 1.5 times greater than the volume in the P-LDH sample. This is due to the greater volume of smaller mesopores in the sample (inset Figure 5.5). Therefore despite the greater proportion of face-stacked particles in the B-LDH sample the size increase in the platelets impacts more on the surface area characteristics. The result would suggest that the bench scale LDH sample would be preferential for adsorption. The pore diameter of the I-LDH sample is comparable to the B-LDH sample however the greater surface area and pore volume would suggest that there is a difference in the agglomeration of the particles, which results is a larger volume of mesopores at close to 50nm.

Table 5.5 Surface area (S_{BET}) and average pore diameter of bench (B-LDH), pilot (P-LDH) and industrial scale (I-LDH) samples

Sample	S_{BET} / m^2 g^{-1}	Pore Diameter / nm	Pore Volume / cm^3 g^{-1}
B-LDH	58.0±0.1	19.1	0.3
P-LDH	50.1±0.2	15.3	0.2
I-LDH	64.1±0.2	19.6	0.4

5.5 Summary

The difference in Zn_2Al-CO_3 LDH materials produced by continuous flow synthesis at bench (flow rate – 1.8L h^{-1}), pilot (flow rate – 36L h^{-1}) and industrial scale (1050L h^{-1}) has been investigated across a range of characteristics. The crystal structure of the materials remains similar with small differences in domain length in both ⟨*003*⟩ and ⟨*110*⟩ directions between the P-LDH sample and the other two scales. B-LDH shows smaller CDL in both crystal planes compared to P-LDH with CDL in the (*003*) plane at 18nm and 26nm for B-LDH and P-LDH respectively while the CDL in the (*110*) plane is larger for both materials and P-LDH again displaying the longer domain length at 50±4nm compared with 39±1nm for B-LDH. The crystal domain length of the repeated industrial scale LDH sample was 19nm and 31±1nm in the⟨*003*⟩ and ⟨*110*⟩ directions, respectively. The CDL of the I-LDH sample indicated that the increased domain length in the P-LDH sample is most likely due to post synthesis settling in the reaction liquor, prior to washing.

Platelet size determined from TEM micrographs showed that the P-LDH average platelet size was 177±77nm while the B-LDH was 120nm±53 and I-LDH was 165±54nm. This data indicates that the difference in reactor geometry and the time allowed for product

settling post synthesis impacted on particle size characteristics. M^{II}/M^{III} ratio can be seen as a measure of efficiency of conversion, as the ideal ratio is 2, the P-LDH sample has a ratio of 2.2 while the B-LDH has a ratio of 1.8, this is differentiation from the ideal value is insignificant and the pilot scale synthesis allows for good conversion of precursors even at higher flow rates.

Specific surface area does not change significantly between the bench, pilot and industrial scale samples. The decrease in S_{BET} between B-LDH and P-LDH samples may be due to larger particles present in the pilot scale sample, while stacking of the particles after drying results in a hierarchical structure resulting in more accessible pores in the microstructure. The greater surface area of the I-LDH sample appears to be as a result of particle thickness and stacking arrangements of the sample.

.

6. Results and Discussion: Adsorption of Reactive Dyes onto Calcined $Zn_2Al\text{-}CO_3$ Layered Double Hydroxides

6.1 Introduction

The work in Chapter 6 focuses on the application of the pilot scale $Zn_2Al\text{-}CO_3$ materials produced for and analysed in Chapter 5. Adsorption of two different reactive dyes; Reactive Orange 16 (RO16) and Reactive Black 5 (RB5), was investigated. These two dyes are similar in chemical structure, both are reactive anionic dyes with sulfonate functional groups ($R\text{-}SO_3^-$) (Figure 6.1). However, the size of the molecules is different; with RB5 having a molecular weight of 992g mol^{-1} and RO16 being 618g mol^{-1}. There is also a difference in the number of sulfonate groups present in each molecule. The sulfonate functional groups are the primary reacting component in the dye molecules during adsorption onto calcined LDH materials.

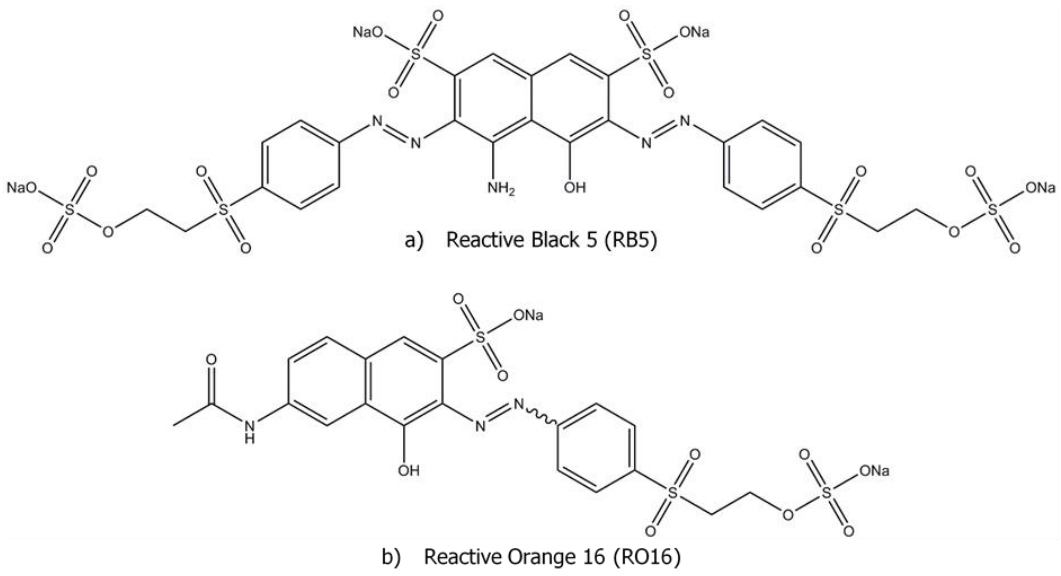


Figure 6.1 Structure of Reactive Dyes used in adsorption experiments

6.2 Highlights

- The crystal structure of calcined $Zn_2Al\text{-}CO_3$ does not change with time in when stored in air, however prolonged storage in water causes reformation of $Zn_2Al\text{-}CO_3$ LDH crystal phase a mixed metal oxide.
- Monolayer adsorption capacity of Reactive Orange 16 (895mg g^{-1}) is greater Reactive Black 5 (589mg g^{-1})
- All adsorption follows 3 distinct stages of adsorption and is best fit with a pseudo 2nd kinetic model indicating the rate controlling step in the reaction is the intercalation of the dye molecules into the interlayer gallery.

6.3 Calcination of $Zn_2Al\text{-}CO_3$ and Characterisation of Mixed Metal Oxide Adsorbent

Prior to studying adsorption, the pilot scale produced $Zn_2Al\text{-}CO_3$ material was subjected to calcination heat treatment at 773K for 4 hours. This temperature is the mid-range value for many adsorption experiments utilising the memory effect of LDHs found in literature, and typically yields the highest adsorption capacity [261]. Higher temperatures form spinel structures that cannot then be used in adsorption due to the inability for the spinels to reform the LDH structure through the exploitation of the memory effect [119, 121].

6.3.1 X-Ray Diffraction and Crystal Structure

X-ray diffraction was required for the examination of the crystal phases present in the $Zn_2Al\text{-}CO_3$ LDH and the calcined $Zn_2Al\text{-}CO_3$ (MMO). The diffractograms for the $Zn_2Al\text{-}CO_3$

(LDH) and calcined $Zn_2Al\text{-}CO_3$ (MMO) samples are detailed in Figure 6.2. Intense basal reflections are clearly defined in the diffractogram for LDH at Bragg angles; 11.5° and 23.2° relating to (*003*) and (006) respectively. Reflections decrease in intensity as the Bragg angle increases, which is a relatively a common feature of an LDH diffraction profile [9]. The LDH has hexagonal crystal symmetry in a rhombohedral setting (Space group – $R\bar{3}m$) [10]. Lattice parameters were calculated as 0.31nm and 2.29nm for *a* and *c* respectively, these lattice parameters match well with those published for $Zn_2Al\text{-}CO_3$ type LDHs [30, 140]. Crystal domain length (CDL) was calculated using the integral breadth, calculated from the FWHM of the (*003*) and (*110*) reflections and the Scherrer equation. CDL of the LDH was calculated as 26±0nm in the ⟨*003*⟩ direction and 50±4nm in the ⟨*110*⟩ direction.

The diffractogram for the MMO sample shows significantly reduced intensity of reflections and the only observable reflections in the pattern pertain to ZnO. There are no visible reflections relating to the LDH or and spinel $ZnAl_2O_4$ structures. This implies the calcination temperature was not high enough to form spinel structures and the main component of the mixed metal oxide is a semi-crystalline ZnO and Amorphous Al_2O_3 and AlOOH. Lattice parameters for the ZnO in the MMO sample were calculated 0.32nm and 0.52nm for *a* and *c* respectively. Information from literature indicates that, calcination at higher temperatures will increase the intensity of the ZnO reflections and cause $ZnAl_2O_4$ reflection to appear in the diffractogram [119, 121]. Heating the LDH causes losses surface bound in interlayer water through evaporation and boiling. It then undergoes dehydroxylation of the brucite-like layers and then the interlayer CO_3^{2-} is evolved as CO_2 [140, 253].

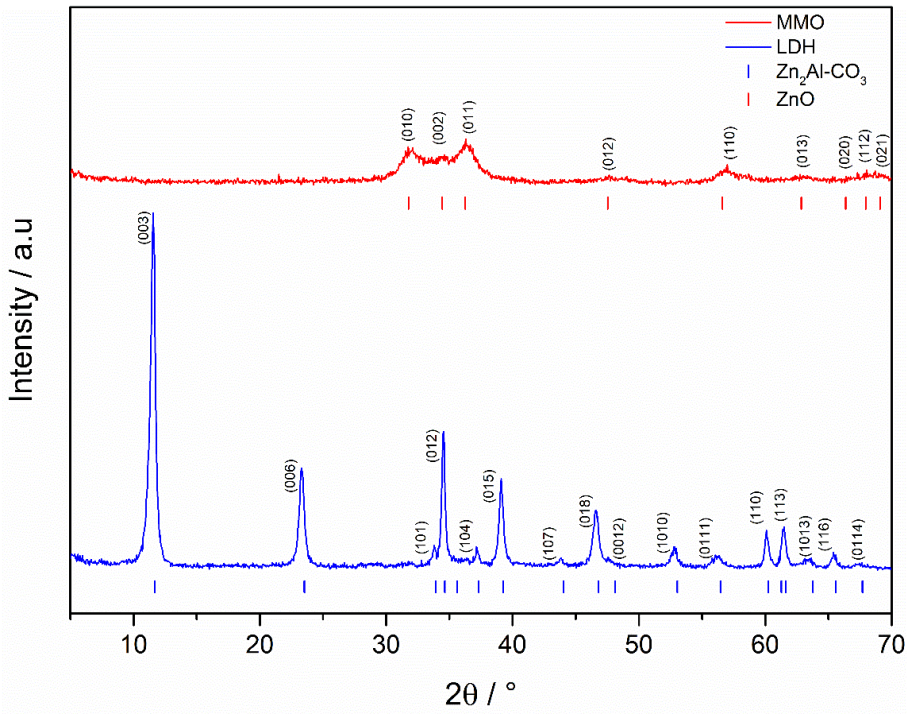


Figure 6.2 X-ray diffractograms of $Zn_2Al\text{-}CO_3$ (LDH) and calcined $Zn_2Al\text{-}CO_3$ (MMO)

6.3.2 Surface Area, Topography and Particle Size Distribution Analysis

The nitrogen adsorption isotherms for the LDH and MMO materials are detailed in Figure 6.3. Isotherms exhibit a Type-IV isotherm shape which suggests mesopores are present in both the LDH and MMO materials. The adsorption branch of the Type-IV isotherm resembles a Type-II isotherm and shows that there is mono and multilayer adsorption to high P/P_0. The hysteresis loop on the desorption branch of the isotherm most closely resembles H3 hysteresis (according to IUPAC classifications) [248]. This indicates that the gas adsorption was occurring between loosely packed agglomerates of platelet like particles [248].

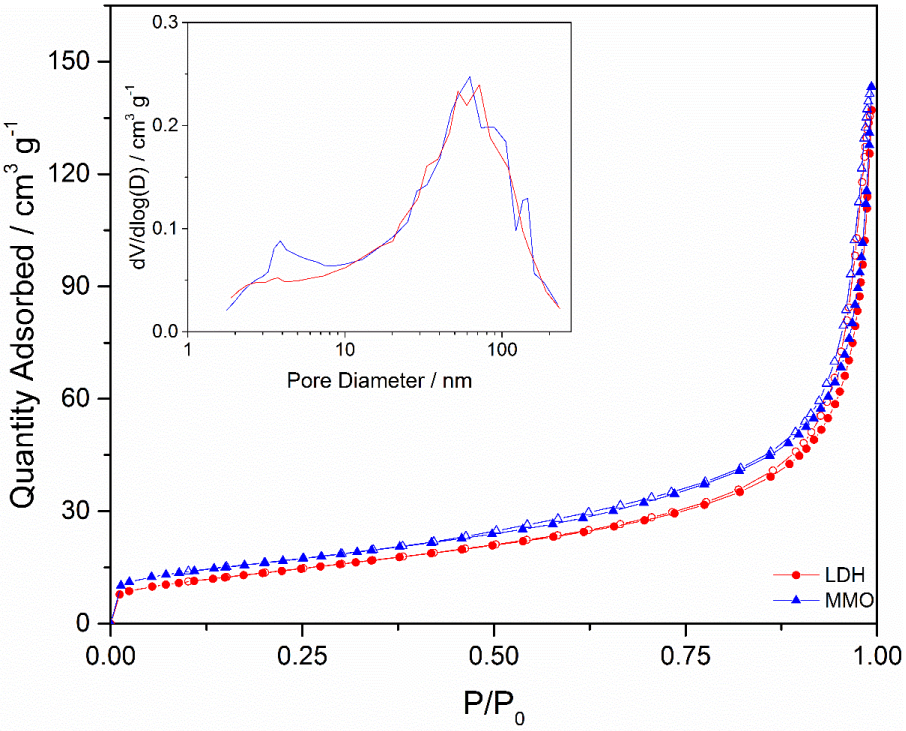


Figure 6.3 Nitrogen adsorption isotherm for $Zn_2Al\text{-}CO_3$ (LDH) and calcined $Zn_2Al\text{-}CO_3$ (MMO). Inset; pore size distribution calculated from the desorption branch of the isotherm

The surface area and pore diameter are detailed in Table 6.1. The slight increase in S_{BET} and decrease in pore diameter between the LDH and MMO is attributed to increased access to smaller pores in the agglomerates post calcination with the break-down of the strict layered structure of the LDH. Increased specific surface area of MMO samples compared to LDH samples is common in adsorption research, however in some cases the increase is far more dramatic than the increase observed in this research [119, 121, 151]. For example, the calcination of $Zn_2Al\text{-}CO_3$, at 500°C, to a mixed metal oxide reported by Mandal and Mayadevi, increases the S_{BET} from 52.3mg g^{-1} to 126.8mg g^{-1} [121].

Table 6.1 Specific surface are and pore diameter of LDH and MMO materials

Sample	S_{BET} / m^2 g^{-1}	Pore Diameter / nm
LDH	50.1±0.2	15.3
MMO	57.8±0.1	14.1

The SEM micrographs of the LDH and MMO samples are displayed in Figure 6.4 and Figure 6.5. The SEM micrographs indicate that there is no change in the agglomeration of the particles in the LDH and MMO samples. The large agglomerates of particles are larger than 20μm across and exhibit similar morphology. The individual platelets show no distinct order to stacking although a slight open criss-cross structure in both the LDH and MMO samples is visible. The structure and size of the agglomerates supports the information garnered from N_2 isotherms that the materials consist primarily of agglomerates of platelet like particles. TEM micrographs in Figure 6.6 show some slight changes in the surface of the platelets under high resolution. Prolonged exposure of the LDH to the electron beam causes a breakdown in the material and the platelets become pitted. This can be observed to a small degree in the platelets in Figure 6.6a. However, the phenomenon is more pronounced in Figure 6.6c and Figure 6.6d. Aside from the pitting of platelets there are no significant changes to size or shape of platelets following calcination. The implication of the difference in diffractograms and the similar shape of the MMO platelets compared with the LDH platelets is that the layers of material are comprised of areas of ZnO and amorphous aluminium oxide compounds.

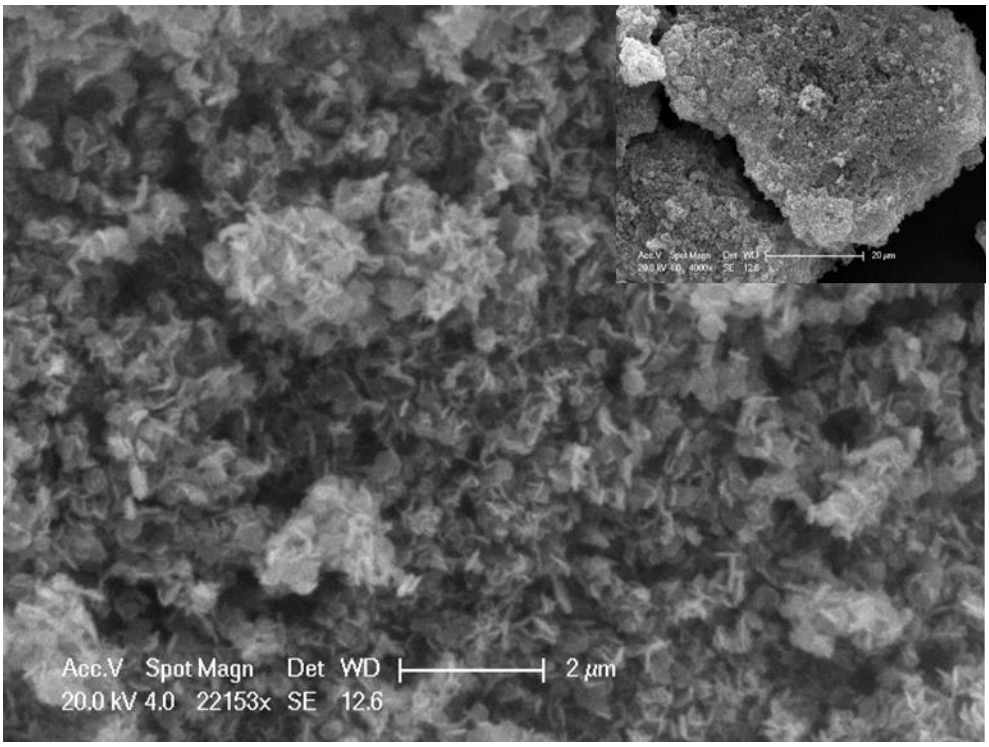


Figure 6.4 SEM micrograph of $Zn_2Al\text{-}CO_3$ (LDH)

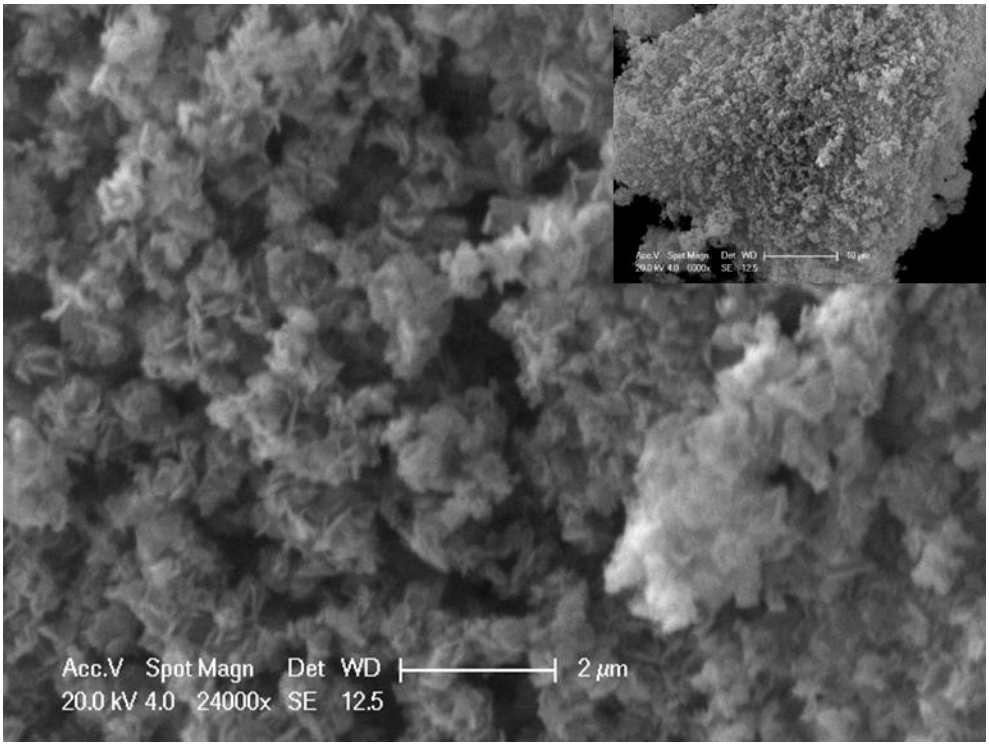


Figure 6.5 SEM micrograph of calcined $Zn_2Al\text{-}CO_3$ (MMO)

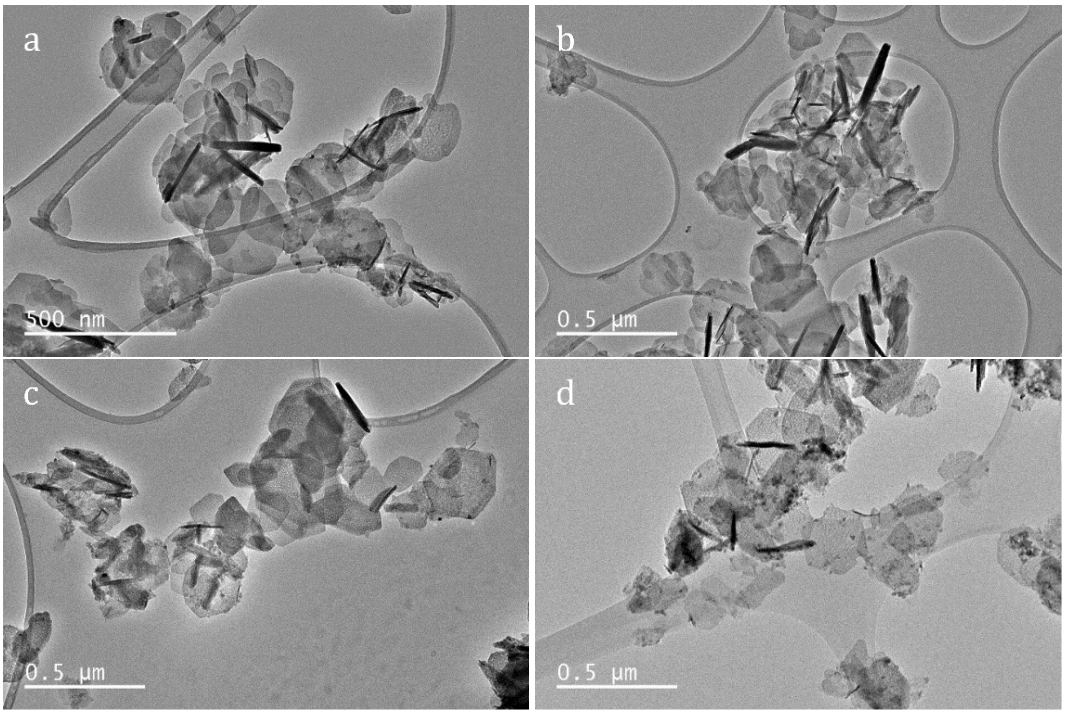


Figure 6.6 TEM micrographs of $Zn_2Al\text{-}CO_3$ (a, b) and calcined $Zn_2Al\text{-}CO_3$ (c, d)

6.4 Stability of $Zn_2Al\text{-}CO_3$ and Calcined Adsorbent (MMO)

Stability of adsorbents is a key feature that is not often investigated in literature. The stability of an adsorbent can impact on whether the material is suitable for purpose, regardless of its surface area and other characteristics. This is the case if the material is unstable under the conditions of the adsorption; like ZIF-8 which, has extraordinary surface area but breaks down rapidly in water [262]. The stability of the MMO adsorbent was tested in both dry and wet storage and changes to X-ray diffractograms were used as the primary metric by which stability was measured. Samples of the MMO were held in storage for 8 weeks in centrifuge tubes, in the dark at 291K. Dry samples were left in air while, samples held in wet storage were left in deionised water. After two-week intervals, samples were taken and analysed using X-ray diffraction. Samples stored wet storage were frozen and freeze dried prior to analysis. LDH samples were also stored in

deionised water experiments using LDH samples were also taken to measure changes that occur to the LDH during wet dry storage.

6.4.1 Stability of Calcined Adsorbent (MMO) and Reference $Zn_2Al\text{-}CO_3$ in Air

The X-ray diffractograms for the dry stored MMO samples are presented in Figure 6.7. The diffraction patterns show no significant changes in the shape or relative intensity of reflections for the MMO samples held in dry storage. The lack of any significant changes to the diffraction patterns indicates that in dry storage the MMO samples can be held for extended periods without changes to the structure and therefore potential for adsorption.

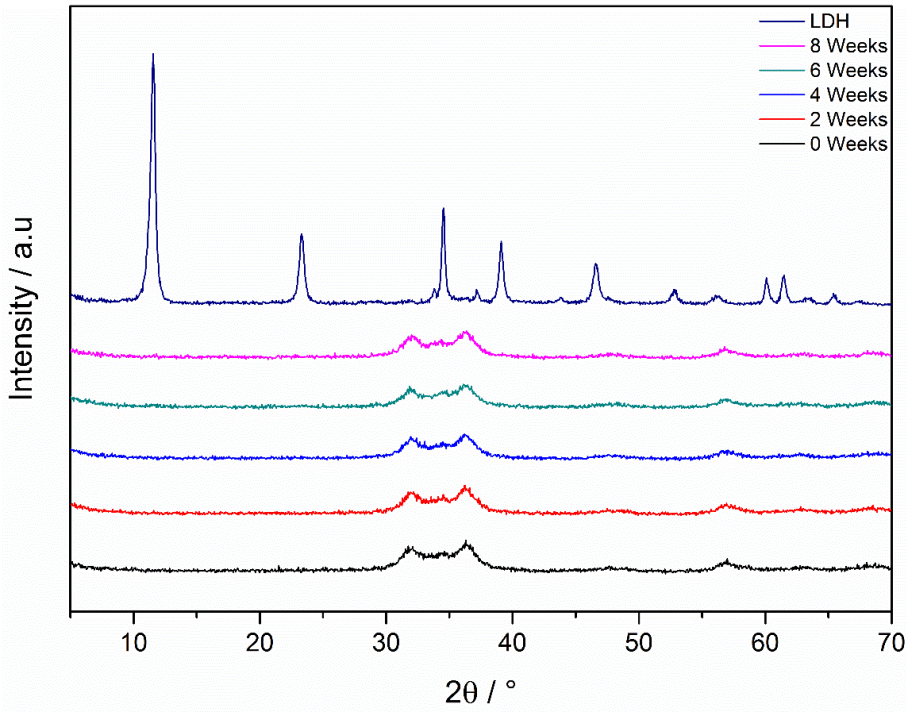


Figure 6.7 Changes in diffraction patterns and crystal structure of mixed metal oxide during dry storage and $Zn_2Al\text{-}CO_3$ (LDH)

6.4.2 Stability of Calcined $Zn_2Al\text{-}CO_3$ (MMO) and Reference $Zn_2Al\text{-}CO_3$ in Water

Extended periods of time in storage of MMO in deionised water resulted in rehydration and reformation of the $Zn_2Al\text{-}CO_3$ LDH. The reformation of the LDH was slow and the increasing crystallinity with storage time suggests that unspent MMO adsorbent will likely reform LDH layers and the adsorption capacity will decrease. This is phenomenon partly due to the formation of CO_3^{2-} from dissolved CO_2 in the presence of the buffering zone around reformed LDH layers. The affinity of CO_3^{2-} for the LDH interlayer region means that carbonate intrusion will most likely always reduce adsorption capacity.

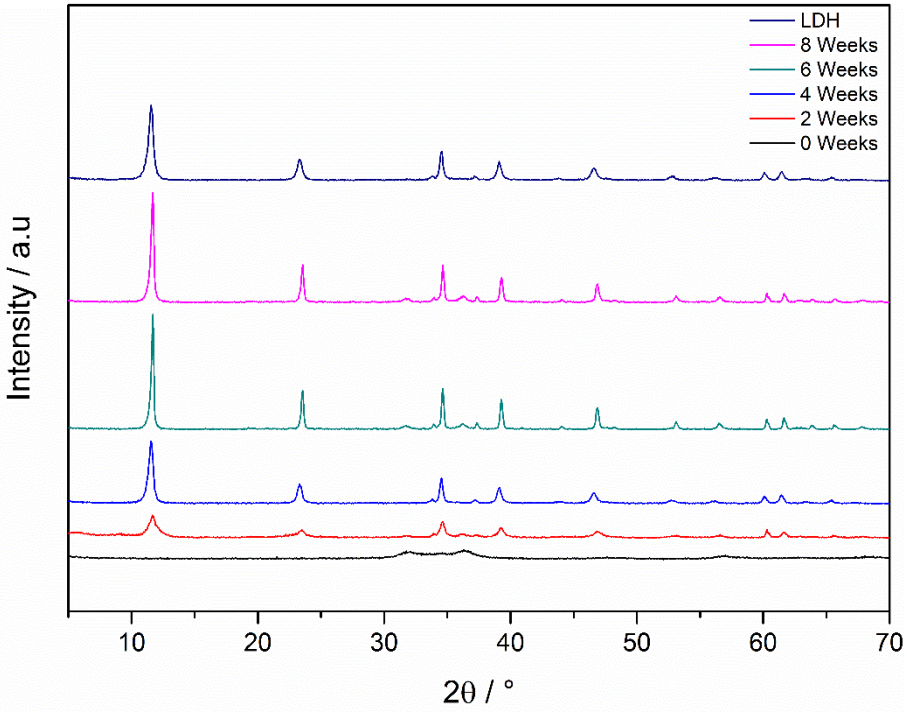


Figure 6.8 Changes in diffraction patterns and crystal structure of mixed metal oxide during wet storage

Despite the reformation of the LDH within the samples there are reflections present at 32° and 36° relating to the (010) and (011) reflections of ZnO. These reflections are not

present in the diffractogram of the LDH (Figure 6.8). This is most likely a result of some irreversible ZnO formation during calcination treatment. It may be beneficial therefore, to calcine the $Zn_2Al\text{-}CO_3$ at a lower temperature to ensure minimal irreversible ZnO formation. The regenerated samples after 6 and 8 weeks of storage show relative reflection intensity that is comparable to the fresh LDH, and each other. This suggests that further regeneration is unlikely to occur after this time period and dye adsorption capacity is minimised.

The data in Table 6.2 relates the CDL of LDH samples that have not been calcined and stored in deionised water. The CDL calculated from the (*003*) reflection again shows little change and no significant trend in changes with storage time are observed. The CDL calculated from the (*110*) reflection however is more variable, despite the variability the 95% confidence intervals indicate that the domain lengths are within acceptable limits and change deemed insignificant.

Table 6.2 Crystal domain length (CDL) calculated for (*003*) and (*110*) reflection for uncalcined $Zn_2Al\text{-}CO_3$ in wet storage

Sample	Storage	CDL (*003*) / nm	CDL (*110*)/ nm
$Zn_2Al\text{-}CO_3$	0	26	50±4
	2	26	50±2
	4	26	55±3
	6	28	54±5
	8	26	57±2

6.5 Batch Adsorption of Reactive Orange 16

6.5.1 Effect of Initial pH on Adsorption

High alkaline conditions are ideal for fixation of reactive dyes onto cellulose substrates during dying, due to the effect that high pH has on the cellulose substrate making bonding between the dye and the substrate more favourable [46, 47]. A range of pH conditions were investigated to establish the effects that alkaline and acidic conditions have to the adsorption performance of MMO adsorbents. The adsorption performance was examined across the pH range from 4-10. LDHs readily precipitate under alkaline conditions, thus in the presence of a suitable anion, in this case the reactive dye, the LDH should readily reform the LDH-dye material even at pH greater than 10 [225]. LDHs breakdown significantly under acidic conditions (pH<4) therefore under such conditions adsorption would be unsuccessful [148, 151]. There is no observable trend in adsorption performance across the pH range tested as detailed in Figure 6.9. Adsorption of RO16 was found to be in the range of 700mg g^{-1} to 800 mg g^{-1} with the experimental error covering difference in mean adsorption capacity. A previously mentioned, adsorption under increasingly acidic conditions (pH<4) will diminish due to the dissolution of the MMO/LDH structure [263]. The pH of solution is also important with activated carbon adsorption and influences dye removal as static charges on the carbon vary with pH, as does the protonation of the dye molecule [92].

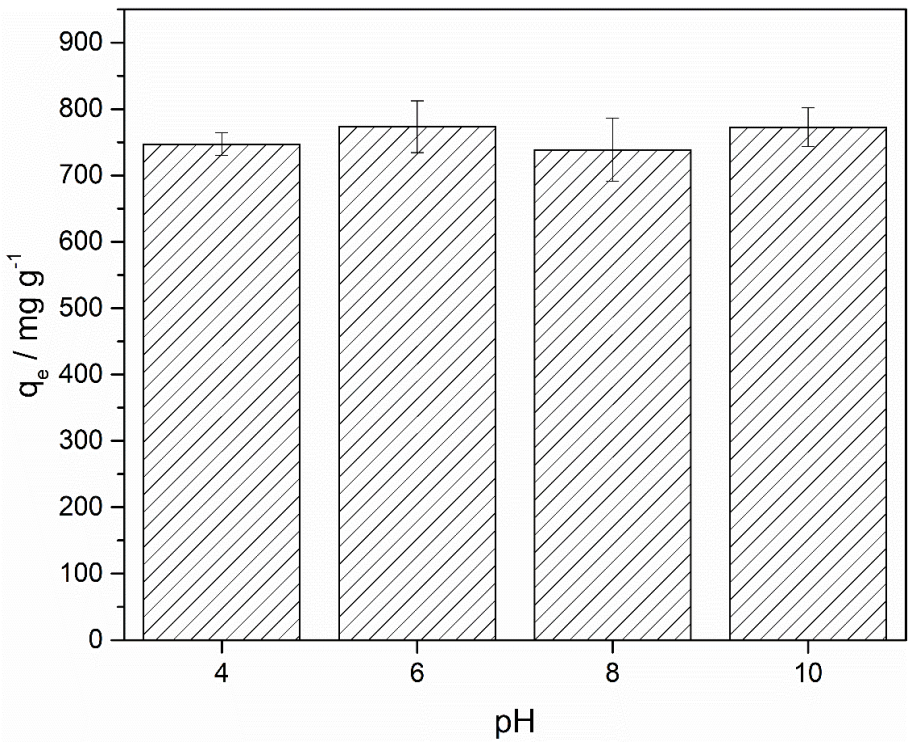


Figure 6.9 Impact of the initial pH of solution on the adsorption of Reactive Orange 16 after equilibrium (C_0=1500mg L^{-1}; V_{dye}=50mL; adsorbent loading=1g L^{-1}; T=293K)

6.5.2 Effect of Adsorbent Dose

The effect of adsorbent dose on adsorption performance of RO16 is detailed in Figure 6.10. The adsorbent dose was varied from 0.5g L^{-1} to 2g L^{-1} in order to establish a wide range of mass loadings and the effect that this has on adsorption performance both kinetically and in terms of adsorption capacity. The graph shows decreases in concentration of dye across the two-hour reaction time between the 4 mass loadings. Concentration after 2 hours (C_e) for 0.5g L^{-1} of adsorbent was 1103±28mg L^{-1}, whereas the C_e for an adsorbent loading four times greater (2g L^{-1}) was 48±19mg L^{-1}. This is an increase in dye reduction of approximately 4.5 with a mass loading increase of a multiple of four. However, the increase in mass loading from 0.5g L^{-1} to 1g L^{-1} caused an increase in q_e. At high adsorbent loading qe would diminish as C_e approached zero and the

adsorbent is left unsaturated. Similar observations have been identified in literature with adsorption of dye and with adsorption of inorganic pollutants [26].

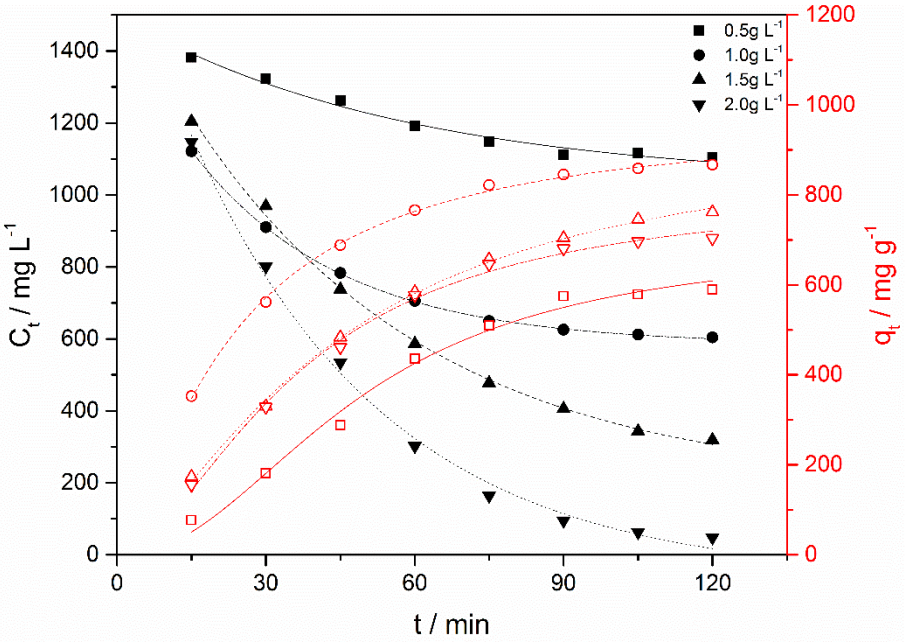


Figure 6.10 Effect of adsorbent dose on Reactive Orange 16 dye concentration and adsorption capacity (C_0=1500mg L^{-1}; V_{dye}=50mL; T=293K)

In the adsorption of methyl orange report by Zaghouane-Boudiaf *et al* it is described that increased adsorption dose causes adsorption capacity (q_e) decreases exponentially while dye removal plateaus as q_e tends toward C_0 [264]. The instance in this research indicates that the dye removal plateaus as adsorbent dose increases beyond a critical point where the availability of adsorption site is greater than the adsorbate level [265]. However in this research the lowest adsorbent loading also has the lowest q_e. The implication then is that the adsorbent loading of the MMO adsorbent influences the dye removal but the rate of removal remains unaffected, and depending on the dye adsorbed the adsorbent loading can be optimised for both q_e and C_e.

6.5.3 Effect of Adsorption Temperature on Reaction Kinetics

The temperature of dye bath effluent can vary due to the temperature required of the dyeing process [45, 47]. The impact that temperature has on adsorption performance of MMO adsorbents is outlined through kinetic modelling. The data from adsorption experiments at different temperatures was modelled against the pseudo 1st order, pseudo 2nd order and the intra-particle diffusion models, these are the three most common kinetic models applied to adsorption data in published literature. The pseudo 1st order model is expressed in linear forms as [266] :

$$\ln(q_e - q_t) = \ln(q_e) - k_1 t \qquad (6.1)$$

Where q_t (mg g^{-1}) and q_e (mg g^{-1}) are the adsorption at time (t / min) and at equilibrium respectively and k_1 (min^{-1}) is the pseudo first order rate constant. The pseudo 2nd order model can be expressed in linear form as follows [266] :

$$\frac{t}{q_t} = \frac{1}{k_2 q_e^2} + \frac{t}{q_e} \qquad (6.2)$$

Where k_2 (g mg^{-1} min^{-1}) is the 2nd order rate constant. The third model fitted to the experimental data was the Weber-Morris intra-particle diffusion model [35]:

$$q_t = k_{id}\sqrt{t} + C \qquad (6.3)$$

Where k_{id} is the intra-particle diffusion constant. The plot of the linear pseudo 1st order model for adsorption of RO16 is presented in Figure 6.11. The pseudo 1st order model fits similarly to adsorption data at 293K and 303K. Adsorption at 283K occurs at a lower rate (k_1=0.0316min^{-1}) whereas the reactions between 293K and 313K have k_1 rate constants between 0.045 and 0.055min^{-1} (Table 6.3). There is however, a discrepancy

between the $q_{e,exp}$ and $q_{e,cal}$ values from the pseudo 1st order rate model. In all instances $q_{e,cal}$ is greater than $q_{e,exp}$, however adsorption at 303K indicates the closest relationship between the pseudo 1st order model and the experimental data. The data indicates that the pseudo 1st order reaction equation is not appropriate to model the adsorption data. This is in agreement with published data regarding LDH/MMO adsorption of dye compounds [26].

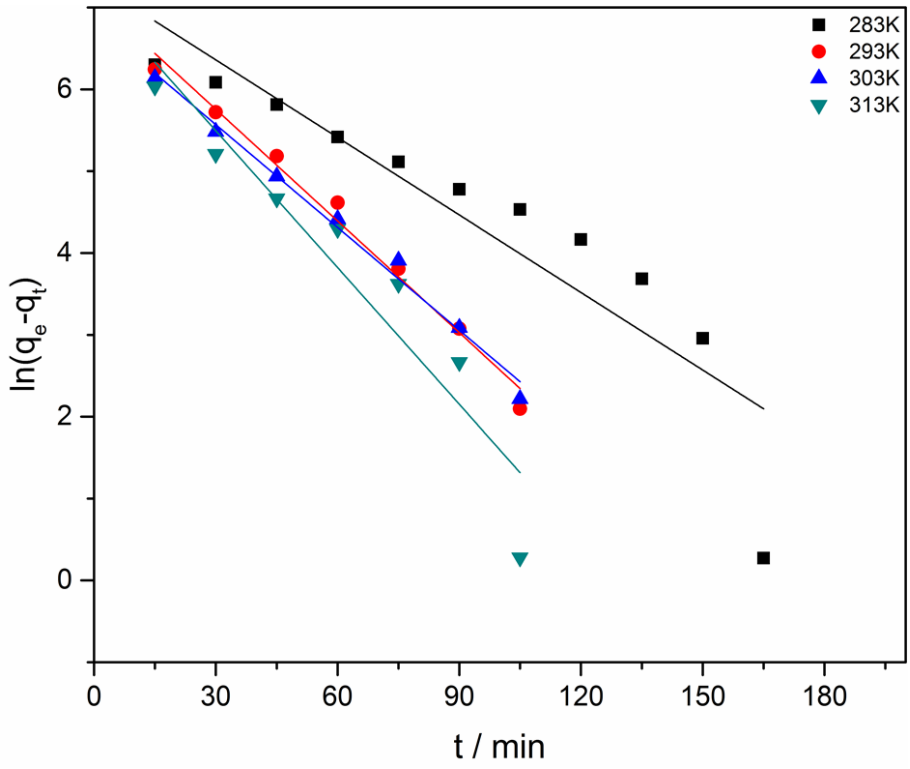


Figure 6.11 Linear pseudo 1st order kinetic model for the adsorption of Reactive Orange 16 (C_0=1500mg L^{-1}; V_{dye}=50mL; adsorbent loading=1g L^{-1})

Table 6.3 Kinetic rates for the adsorption of Reactive Orange 16

Dye	Temperature / K	$q_{e,exp}$ / mg g^{-1}	Pseudo 1st order			Pseudo 2nd order		
			k_1 / min^{-1}	$q_{e,cal}$ / mg g^{-1}	R^2	k_2 /g mg^{-1} min^{-1}	$q_{e,cal}$ / mg g^{-1}	R^2
RB16	283	690	0.0316	1492	0.829	$1.104x10^{-5}$	1058	0.982
	293	895	0.0455	1238	0.987	$3.269x10^{-5}$	1094	0.995
	303	919	0.0419	921	0.917	$5.302x10^{-5}$	1067	0.999
	313	998	0.0557	1294	0.902	$7.760x10^{-5}$	1105	0.999

The linear fit of the pseudo 2nd order model with the data is outlined in Figure 6.12. The linear equation fits better with the data than the pseudo 1st order model. This is due to the fact that in the pseudo first order model the initial dye concentration is not in excess observe negligible changes in the concentration of the dye during adsorption [267]. The pseudo 2nd order model is linked with chemisorption, which is the main mode of adsorption through the electrostatic attraction between the brucite-like layers and the dye anions [225]. The pseudo 2nd order rate constants for RO16 adsorption appear to increase at regular intervals of approximately $2x10^{-5}$, however the fit of the adsorption at 283K is less than that of the reactions at the three higher temperatures. Not only that but the reaction takes approximately three hours to reach equilibrium compared with two hours for the higher temperatures. This indicates that as temperature decreases the rate slows dramatically, this is key as ambient water temperatures in dye systems vary with the process [45, 46].

Despite the goodness of fit of the experimental data to the pseudo 2nd order model (Table 6.3). The shape of the linear pseudo 2nd order model indicates that at 283K temperatures early stages of adsorption (t<45 min) are slower than the models predict, accounting for the inferior fit of adsorption of RO16 and the longer time to reach equilibrium. The initial surface adsorption of dye molecules would appear to be slower at the lower temperature due to less energy in the system. The value of k_2 for each temperature investigated of the for RO16 adsorption are lower than rates of adsorption of acid dyes on LDHs. Data published by Guo *et al* on the adsorption of Acid Brown 14 shows k_2 to be an order of magnitude larger than the adsorption of RO16 at comparable temperatures [225]. The implication is that the chemisorption and reformation of the LDH layers intercalated with dye is slower for the larger molecule and would need to be accounted for in adsorption processes.

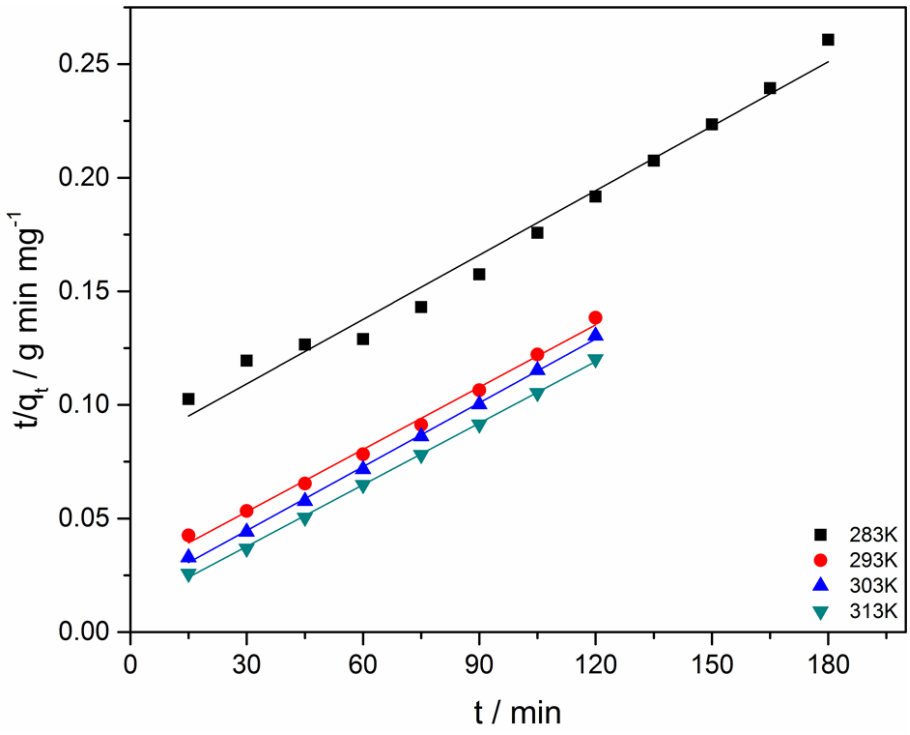


Figure 6.12 Linear pseudo 2nd order kinetic model for the adsorption of Reactive Orange 16 (C_0=1500mg L^{-1}; V_{dye}=50mL; adsorbent loading=1g L^{-1})

The intra-particle diffusion plots can be separated into three sections for adsorption (Figure 6.13). The first stage of the adsorption is linked to the surface adsorption of the dye molecules onto the surface of the MMO, while the second stage of the adsorption is the migration the adsorbed dye molecules into the interlayer and the resulting regeneration of the LDH. The third stage of adsorption is the reaching of a state of equilibrium in the adsorption system and the adsorbent has become saturated [259]. At higher temperatures the initial stage of surface adsorption occurs more quickly, due to increased molecule energy and increased energy and rate of collisions resulting in adsorption occurring. The second and third stages of diffusion into the interlayer region and reaching equilibrium occur at a similar rate between 293K and 313K. The data indicates that, for adsorption of RO16 at higher temperatures (≥293K), the diffusion of

dye into the interlayer region is the rate limiting step in the adsorption reaction [259, 268].

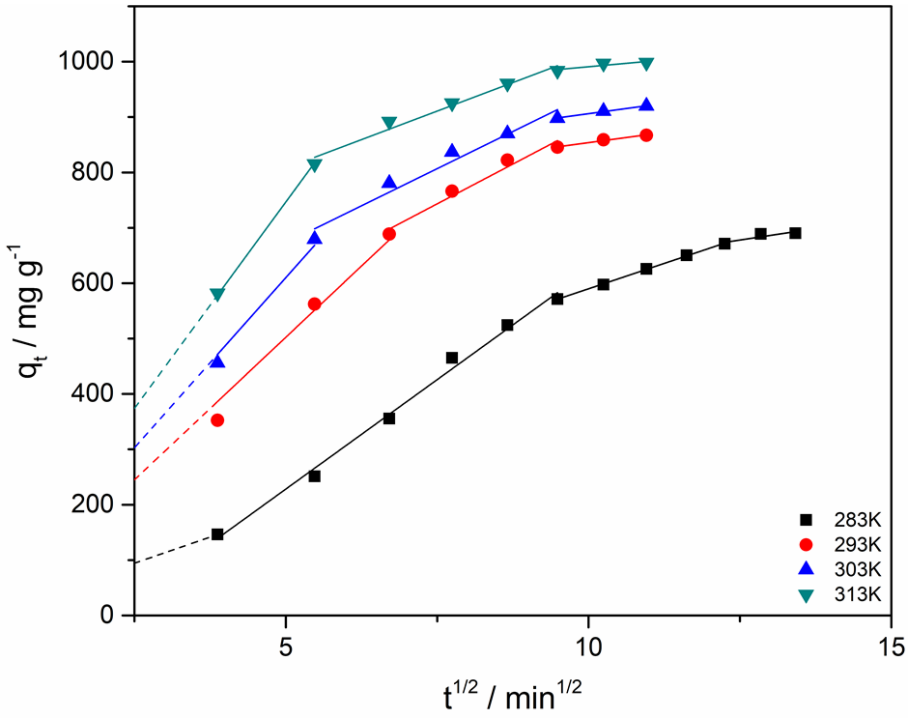


Figure 6.13 Linear intra-particle diffusion model for the adsorption of Reactive Orange 16 (C_0=1500mg L^{-1}; V_{dye}=50mL; adsorbent loading=1g L^{-1})

At 283K the gradient of the linear portion; from the start of the reaction (t=0 min) to the first sampling point (t=15 min) is shallower than the gradient for temperatures ≥293K. The second stage also appears to occur at a lower rate than the other temperatures tested. There also appears to be 4 stages to the adsorption, indicating that there may be two phases to the surface adsorption or two phases to the diffusion stage of the adsorption process. This has not been encountered in literature. The reason for the multiple phases is possibly due to the low rate of adsorption at 283K. The slow surface adsorption continues as the intra-particle diffusion and reformation of the LDH occurs

giving rise the added stage of adsorption which is a combination of surface adsorption and intra-particle diffusion.

6.5.4 Adsorption Isotherms

The adsorption isotherms help to elucidate the adsorbent-adsorbate surface interactions as well as some important adsorption characteristics such as maximum uptake capacity (q_m). The Isotherms for adsorption of RO16 were calculated from experiments with adsorbent loading and varying initial dye concentration (C_0), where C_0 varied between 100mg L^{-1}-1500mg L^{-1}. The initial concentration was based on the concentrations encountered in literature and the results of the scoping studies [141]. It was also chosen to ensure that the MMO adsorbent would be saturated so the maximum concentration of the isotherm experiments could be appropriately determined. Experiments were allowed to reach equilibrium before aliquots were taken and analysed. Isotherm were modelled using the Langmuir and Freundlich isotherm models as these are the most common in literature [129, 141]. The Langmuir isotherm model can be described in linear form [269]:

$$\frac{C_e}{q_e} = \frac{C_e}{q_m} + \frac{1}{k_l q_m} \quad (6.4)$$

Where k_l (L mg^{-1}) is the Langmuir constant, q_m (mg g^{-1}) and q_e (mg g^{-1}) are the maximum uptake capacity and the equilibrium uptake capacity, respectively, C_e (mg L^{-1}) is the equilibrium adsorbate concentration. The non-linear form of the Freundlich isotherm can be described as [269]:

$$\ln(q_e) = \ln(k_f) + \frac{1}{n}\ln(C_e) \quad (6.5)$$

Where k_f (mg g^{-1}.(L $mg^{-1})^{1/n}$) is the Freundlich isotherm constant and 1/n is the heterogeneity factor. The Langmuir and Freundlich models for RO16 are illustrated in Figure 6.14. The parameters from models are outlined in Table 6.4. The fit of the Langmuir isotherm RO16 decreases with increasing temperature. The q_m calculated for RO16 increases with increasing temperature. The q_e value for high C_0 at 303K is close to 900mg g^{-1} while the calculated q_m value is 1004mg g^{-1} (Table 6.4). For adsorption at 313K the q_e with increasing C_0 is more variable. In the case of these two conditions though, the high q_m value comes from the poorer fit of the isotherm model to the data, primarily because at higher temperatures, with low C_0 adsorption is inhibited. The data is fit by the Langmuir isotherm more appropriately isotherm model.

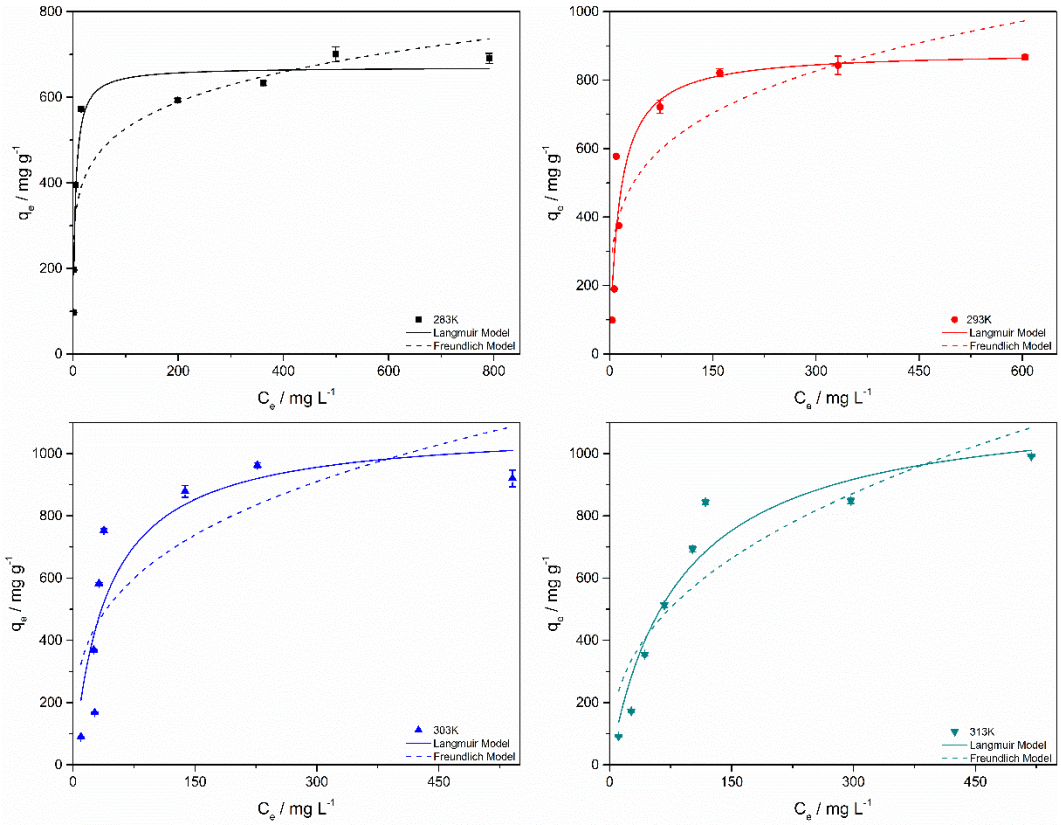


Figure 6.14 Reactive Orange 16 isotherm data fitted with Langmuir and Freundlich models (V_{dye}=50mL; adsorbent loading=1g L^{-1})

The data is fit better by the Langmuir isotherm than the Freundlich due to the monolayer adsorption that occurs as a result of the intercalation and surface adsorption through electrostatic attractions between the positively charged brucite-like sheets and the anionic dye molecules. The Langmuir isotherm is found to fit well with adsorption calcined LDHs [129, 225]. The maximum uptake capacity of RO16 onto the MMO adsorbent is superior to some other adsorbents investigated in literature. Adsorption capacity for RO16 was reported by Marrakchi *et al* as 105.8mg g^{-1} onto mesoporous carbon 30°C [270] and 190.97mg g^{-1} onto sepiolite at the same temperature [271]. The comparative temperature in this work yielded a q_m value of 1004mg g^{-1}. This indicates that based purely on uptake capacity MMO based adsorbents are exceptional for the removal of RO16.

Table 6.4 Isotherm constants for adsorption of Reactive Orange 16

Dye	Temperature / K	Langmuir			Freundlich		
		k_l / L mg^{-1}	q_m / mg g^{-1}	R^2	k_f / mg g^{-1}. (L mg^{-1})$^{1/n}$	n	R^2
RO16	283	0.089	694	0.997	178.074	4.392	0.707
	293	0.053	895	0.999	122.362	2.837	0.712
	303	0.029	1004	0.973	53.082	1.891	0.641
	313	0.009	1210	0.962	26.944	1.567	0.867

6.5.5 Thermodynamics of Adsorption of Reactive Orange 16

The thermodynamic parameters relating to an adsorption reaction are important to know and understand when designing an adsorption system. Thermodynamics parameters investigated are enthalpy (ΔH) entropy (ΔS) and Gibbs free energy (ΔG). These parameters inform on the energy within the system and the spontaneity of the reaction. Gibbs free energy can be calculated using two different equations [225]:

$$\Delta G° = \Delta H° - T\Delta S° \quad (6.6)$$

$$\Delta G° = -RT\ln k_a \quad (6.7)$$

Where ΔG (kJ mol^{-1}) is Gibbs free energy, ΔH (kJ mol^{-1}) and ΔS (kJ K^{-1} mol^{-1}) are system enthalpy and entropy respectively, T (K) is the adsorption temperature, R is the gas constant (J K^{-1} mol^{-1}) and k_a is the adsorption coefficient, in this case taken from the Langmuir constant; k_l (L mol^{-1}). Combining the equations for Gibbs free energy produces:

$$\Delta G° = -RT\ln k_l = \Delta H° - T\Delta S° \quad (6.8)$$

$$\ln k_l = \frac{\Delta S}{R} - \frac{\Delta H}{RT} \quad (6.9)$$

The parameters can be evaluated using a Van't Hoff plot (Figure 6.15), illustrating the relationship between adsorption and temperature. The gradient of the regression line from the Van't Hoff plot can be used to calculate ΔH and the intercept is used to calculate ΔS.

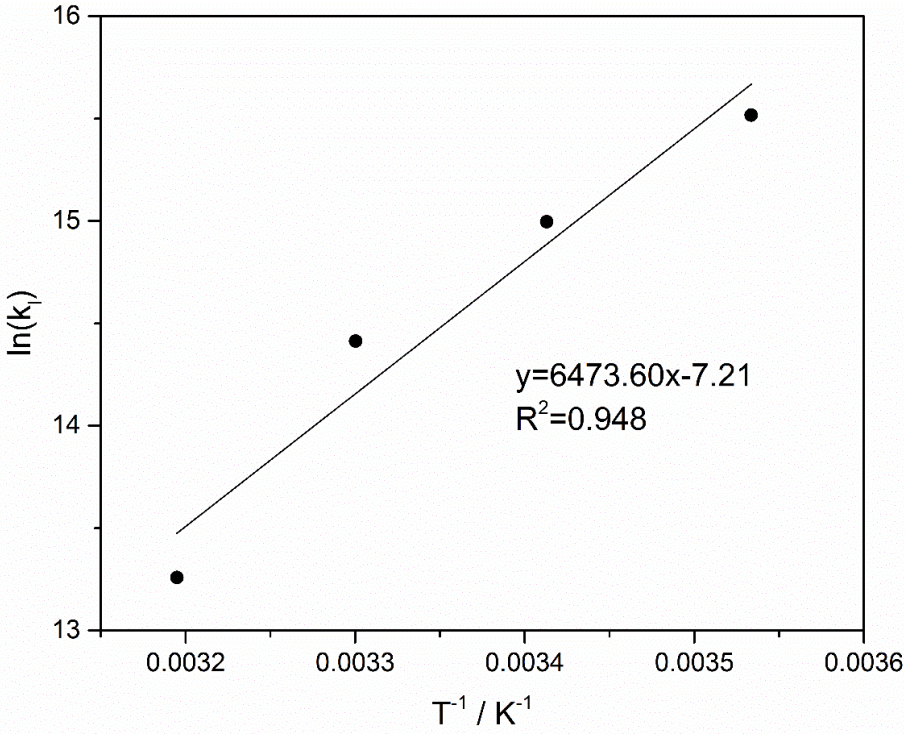


Figure 6.15 Van't Hoff plot for the adsorption of Reactive Orange 16

The thermodynamic parameters for adsorption of RO16 indicate that adsorption RO16 onto the MMO is a spontaneous process, as evidenced by the negative ΔG value for temperatures 283-313K (Table 6.5). This data is in agreement with previously published findings regarding dye adsorption onto LDH/MMO adsorbents [26, 225]. The ΔH value for RO16 (-56.07kJ mol^{-1}) is indicative of an exothermic adsorption process. The enthalpy values also indicate that the process was primarily chemisorption rather than physisorption [225], occurring as a result of the electrostatic attractions between the R-SO_3^- functional groups and the regenerated brucite-like layers of the Zn_2Al-Dye [26, 125]. The negative entropy suggests a reduction in freedom of the adsorbent-adsorbate interactions at the surface of the adsorbent, however the total ΔS of the system would remain negative as the exothermic nature of the reaction releases energy into the surrounding reaction vessel The data regarding both enthalpy and entropy is contradictory with much of the published literature regarding dye adsorption onto MMO

and LDH based adsorbents, in which many of the processes are found to be endothermic in nature with positive ΔS [26, 38, 125, 225, 272].

Table 6.5 Thermodynamic properties of the adsorption of Reactive Orange 16

ΔH / kJ mol^{-1}	ΔS / kJ K^{-1} mol^{-1}	ΔG / kJ mol^{-1}			
		283K	293K	303K	313K
-56.07	-0.06	-39.11	-38.51	-37.91	-37.31

6.5.6 Effect of Competing Anions

Electrolyte salts and alkaline chemicals are added to dye baths to enhance diffusion of dye through the substrate and to augment fixation [45, 46]. These additives are ubiquitous in the dye bath effluent and so investigating their effects on the adsorption processes is essential. Competing anions investigated were Cl^-, SO_4^{2-} and CO_3^2 as these are often utilised in literature. Soda ash (Na_2CO_3) is a common additive in reactive dyeing to aid fixation and while the sodium chloride and sodium sulfate are used to aid with of the dye through the substrate [46]-. Sodium salts of the anions were added to dye solutions at four concentrations, which were 0g L^{-1}, 1g L^{-1} 5g L^{-1} and 10g L^{-1}. The range of concentrations for the competing species was determined from literature regarding competing anions [126, 225]. It must be noted however that the concentration of the competing anions was lower than, and equal to the concentration of the dye compound in the studies by Ni *et al* [126] and Guo *et al* [225] respectively; consequently there is some ambiguity as to what appropriate concentrations of the anions actually are. The impact that the additives had on the adsorption of the RO16 is outlined in Figure 6.16.

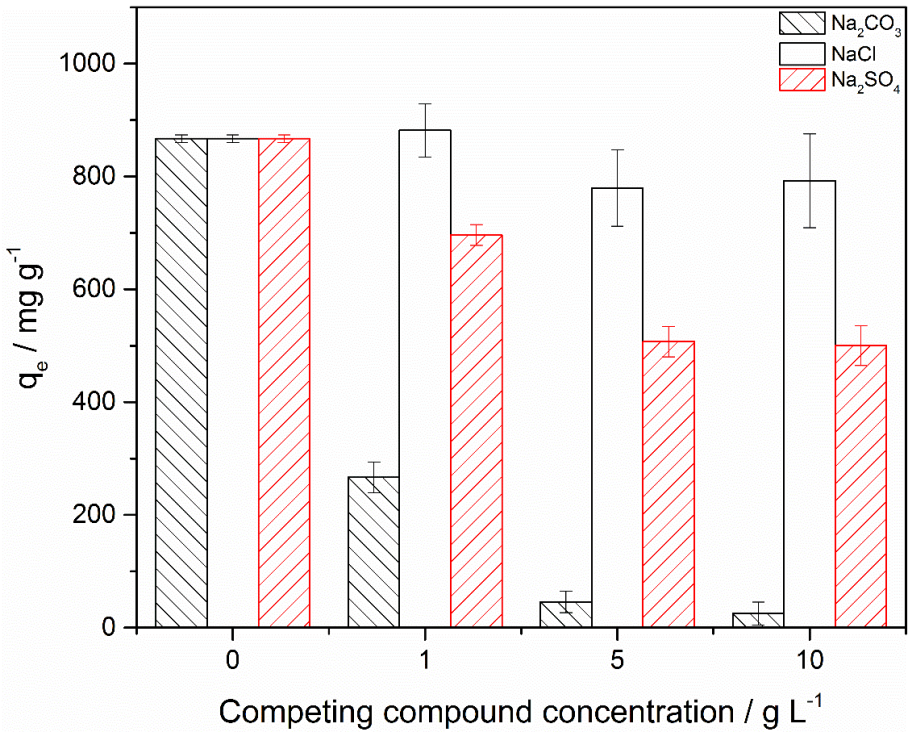


Figure 6.16 Effect of additive compounds (Na_2CO_3, Na_2SO_4, NaCl) on the adsorption of Reactive Orange 16 (C_0=1500mg L^{-1}; V_{dye}=50mL; adsorbent loading=1g L^{-1}; T=293K)

Increasing Na_2CO_3 and Na_2SO_4 content, even to 1g L^{-1}, results in reduction in adsorption capacity of RO16. The charge density of CO_3^{2-} and SO_4^{2-} ions outweigh the adsorbate molecules, resulting in a greater affinity for the brucite-like sheets and reducing the adsorption of dye from solution as the data in Table 6.6 outlines. Sodium sulfate has less of an impact on adsorption compared with CO_3^{2-}, due to the fact that the charge density of CO_3^{2-} is greater than SO_4^{2-} [102]. Adsorption was almost completely inhibited when 5g L^{-1} of Na_2CO_3 was added. Dye removal, at 10g L^{-1} of Na_2CO_3, was reduced further and C_e was 98±4% of C_0. In contrast the addition of sodium sulfate results in C_e/C_0=66±6%, and q_e is reduced by 42% compared to no addition of Na_2SO_4. The presence of NaCl in solution appears to have little impact on adsorption suggesting that Cl^- do not present a large enough charge density to impact adsorption. The reduction in capacity as a result of CO_3^{2-} and SO_4^{2-} presence is of concern as the presence of alkaline carbonates is

common in the fixation of dyes and additional adsorbent would be required to remove the carbonate due to the high specificity of MMO/CO_3^{2-} interactions.

Table 6.6 Percentage reduction of and Reactive Orange 16 (RO16) concentration with competing anions

Additive /Mass g L^{-1}	RO16			
	0	1	5	10
Na_2CO_3	59±4	18±2	3±2	2±2
Na_2SO_4	59±4	46±2	34±3	34±3
NaCl	59±4	60±8	54±9	55±6

6.6 Batch Adsorption of Reactive Black 5

6.6.1 Effect of Initial pH on the Adsorption of reactive Black 5

The effect of pH was examined for the adsorption of RB5 in the same way as RO16 to clarify the impact that changing pH has on the adsorption capacity of the MMO adsorbent. The structure of RB5 is different from RO16 and as a result the dye may behave differently under conditions of variable pH, and therefore affect adsorption. The effect of pH investigated from 4-10 is shown in Figure 6.17. Equilibrium uptake of RB5 remains constant at 500-600mg g^{-1}. The error of samples at pH 6 and pH 8 shows more variability in the data, yet the q_e value remains within the error bars and no clear trends in uptake change are observed in the data. The data regarding adsorption of RB5 is similar to that of RO16 in that the effect of pH is negligible. The presence of increase OH^- ions does not inhibit adsorption despite being the secondary effect of increased pH, being that more OH^- ions competing for active sites on the adsorbent. The MMO

adsorbent is therefore applicable for RB5 absorption across the investigated pH range and will not suffer from reduced adsorption capacity due to changes to the surface charge of either the adsorbent or adsorbate.

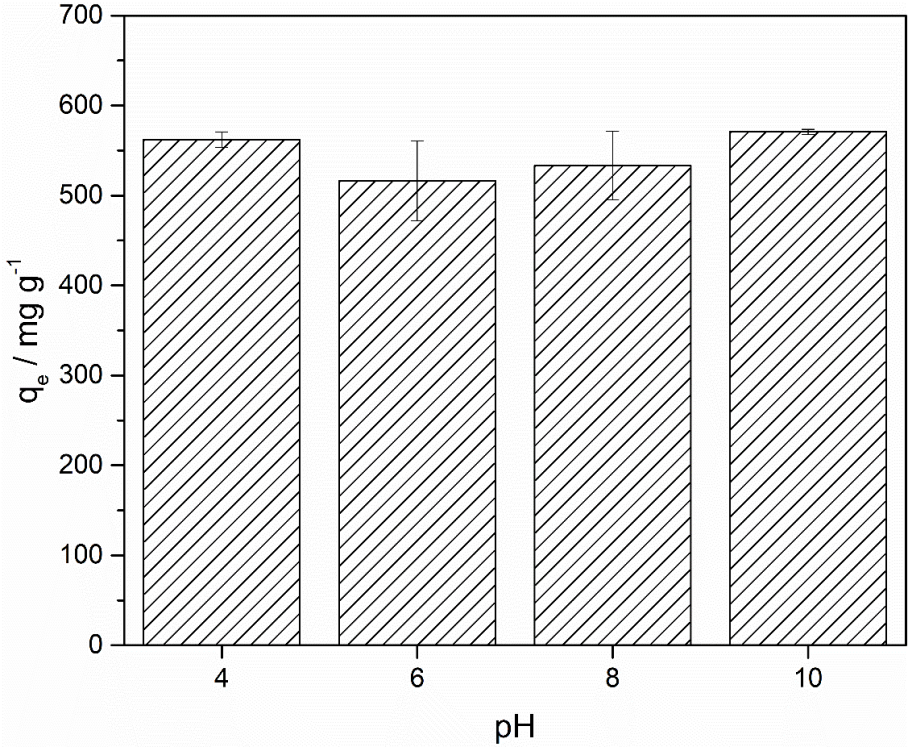


Figure 6.17 Impact of the initial pH of solution on the adsorption of Reactive Black 5 after equilibrium (C_0=1500mg L^{-1}; V_{dye}=50mL; adsorbent loading=1g L^{-1}; T=293K)

6.6.2 Effect of Adsorbent Dose

The adsorbent dose was again investigated in order to establish the effect on the different dye structure of RB5. The impacts variable adsorbent loading on adsorption of RB5 are detailed in Figure 6.18. The data indicates that there is a small change in adsorption at equilibrium, however the rate of uptake remains constant across adsorbent loading from 0.5-2g L^{-1}.

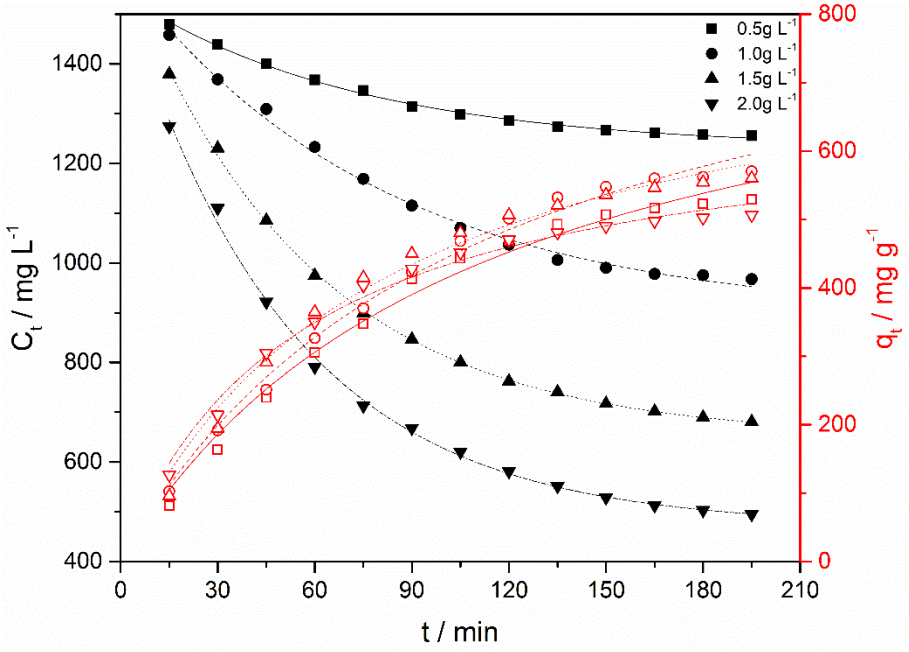


Figure 6.18 Effect of adsorbent dose on Reactive Black 5 dye concentration and adsorption capacity (C_0=1500mg L^{-1}; V_{dye}=50mL; T=293K)

The final adsorbate concentration (C_e) decreases with increasing adsorbent loading which is to be expected, due to the availability of active sites across the larger mass of adsorbent within the reaction system. The reduction in C_e is more pronounced between 0.5g L^{-1} and 1g L^{-1} compared to1.5g L^{-1} and 2g L^{-1}. The reason behind this occurrence is due to the fact that as adsorbent loading increases the equilibrium uptake will decrease as some adsorbent remains unsaturated. Some authors also attribute agglomeration of excess adsorbent particles, to inhibition of adsorption [265]. Adsorption capacity is in the range of 500-600mg g^{-1} while C_e reduced from 1256±9mg L^{-1} to 495±9mg L^{-1} when increasing the adsorbent dose. The reduction C_e with increased adsorbent loading was approximately 290mg L^{-1} per 0.5g $^{L-1}$ increased in adsorbent mass up to 1.5g L^{-1}. However, as the adsorbent loading increases, the reduction in C_e is lessened. The reduced q_e of RB5 requires greater adsorbent loading compared to RO16, before the reduction in C_e plateaus and q_e diminishes as adsorbent sites are left unsaturated efficient.

6.6.3 Effect of Adsorption Temperature on Reaction Kinetics

The temperature of adsorption is an important feature of the reaction. The adsorption of RB5 was tested over four temperatures, in the same way as RO16, at 283K-313K. These temperatures are commonly investigated in literature as they can impact on the reaction and are also potentially feasible temperatures to encounter in dyebath effluent [273]. The data was modelled using three commonly found kinetic models [225]. The pseudo 1st order, pseudo 2nd order and intra-particle diffusion models were used to model the data for the four temperature tested. Data modelled by the pseudo 1st order the adsorption of RB5 is displayed in Figure 6.19.

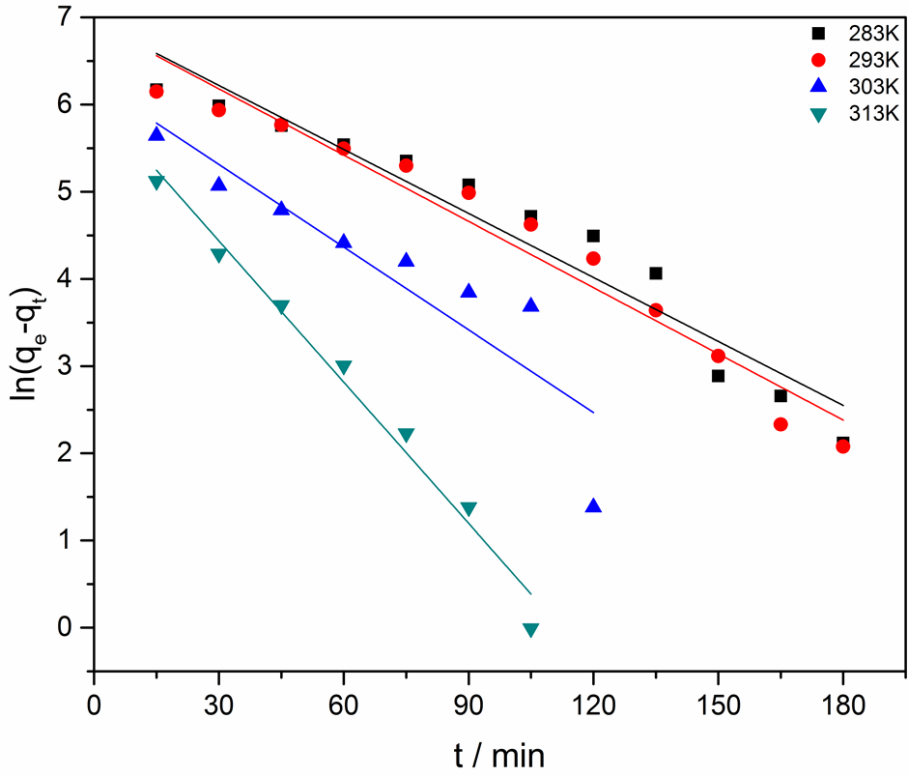


Figure 6.19 Linear pseudo 1st order kinetic model for the adsorption of Reactive Black 5 (C_0=1500mg L^{-1}; V_{dye}=50mL; adsorbent loading=1g L^{-1})

From the Figure 6.19, it is clear that for the adsorption of RB5, adsorption at 283K and 293K occurs at similar rate, while the rate of adsorption increases with increasing temperature to 303K and 313K occurs at increased rates. This is due to the increased energy within the system at 303K and 313K and the reaction rate is increased. The adsorption at 283K and 293K occurs at a similar rate due to the rate of film diffusion, of the dye molecules. For temperatures ≤293K the $q_{e,cal}$ value is almost double the $q_{e,exp}$ value (Table 6.7). This is indicative of the model not fitting well with the data, however the closest $q_{e,cal}$ and $q_{e,exp}$ values occur at 303K, where the pseudo 1st order model has the poorest fit (R^2=0.818). The $q_{e,cal}$ value is based on the expected value at equilibrium given the adsorption at a specific time point, this low adsorption in the early stages of the experiment result in the disproportionality between $q_{e,cal}$ and $q_{e,exp}$ at 283K and 293K. The rapid adsorption occurring at 313K causes the model to predict a q_e value lower than was observed experimentally. The pseudo 1st order model is not appropriate to model the data similarly to the model being unfit to model the adsorption of RO16.

Table 6.7 Kinetic rates for the adsorption of Reactive Black 5

Sample	Temperature / K	$q_{e,exp}$ / mg g^{-1}	Pseudo 1st order			Pseudo 2nd order		
			k_1 / min^{-1}	$q_{e,cal}$ / mg g^{-1}	R^2	k_2 /g mg^{-1} min^{-1}	$q_{e,cal}$ / mg g^{-1}	R^2
RB5	283	572	0.0245	1046	0.925	$7.211x10^{-6}$	1016	0.981
	293	570	0.0253	1032	0.957	$8.949x10^{-6}$	952	0.983
	303	523	0.0316	524	0.818	$7.434x10^{-5}$	602	0.999
	313	542	0.0540	427	0.992	$2.377x10^{-4}$	562	0.999

The pseudo 2nd order rate model developed by Ho *et al* [266] provides a better fit of data compared to the pseudo 1st order model. Linear regression analysis indicates a good fit R^2=0.999) for temperatures ≥303K. The shape of the linear pseudo 2nd order models indicates that at low temperatures early stages of adsorption are slower than the models predict (Figure 6.20) in the same fashion as the pseudo 2nd order model fits to adsorption of RO16 at 283K.

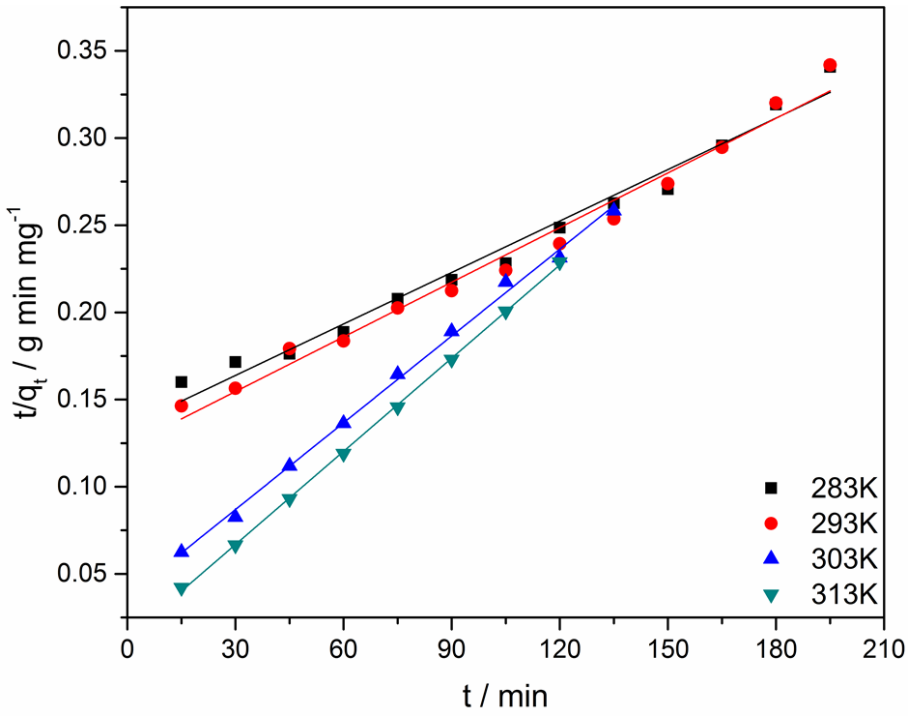


Figure 6.20 Linear pseudo 2nd order kinetic model for the adsorption of Reactive Black 5 (C_0=1500mg L^{-1}; V_{dye}=50mL; adsorbent loading=1g L^{-1})

The pseudo 2nd order rate constants (k_2) for RB5 adsorption are between $7x10^{-6}$ and $9x10^{-6}$ g mg^{-1} min^{-1} for temperatures 283K and 293K (Table 6.7). There is an increase, almost in an order of magnitude, when increasing the temperature from 293K to 303K. The $q_{e,exp}$ and $q_{e,cal}$ grow increasingly close with increasing temperature as does the fit of the models. This suggests that at higher temperatures the pseudo 2nd order model becomes more appropriate as the early stages of adsorption occur more rapidly and as

a result the full adsorption reaction is better modelled by the pseudo 2nd order equation. Likewise with the pseudo 1st order equation, the low rate of adsorption in the early stages of the reaction results in an overestimate of the $q_{e,cal}$ value which decreases with increasing temperature and rate of the reaction.

The intra-particle diffusion model for adsorption of RB5, the model can generally be separated into three sections for adsorption. The first stage of the adsorption is the surface adsorption of the dye molecules onto the surface of the MMO, the second stage is the migration the dye molecules into the interlayer. The third phase is the reaching of the state of equilibrium in the adsorption system [128]. At higher temperatures the initial stage of surface adsorption and film diffusion occurs more quickly, due to increased molecule energy and increased energy and rate of collisions in the early stages of the adsorption. The second and third stages of diffusion into the interlayer region and reaching equilibrium occur at a similar rates between all temperatures tested. The data indicates that, for RB5 adsorption the diffusion of dye into the interlayer region is the rate limiting step in the adsorption reaction for temperatures above 303K [259, 268], while the adsorption at lower temperatures is limited by the surface adsorption phase of the reaction, as indicated by the more shallow gradient of the initial stage of the reaction (Figure 6.21). After the initial stage of surface adsorption, the intra-particle diffusion and film diffusion stages of adsorption occur simultaneously resulting in an extended middle stage of the intra-particle diffusion graph in Figure 6.21.

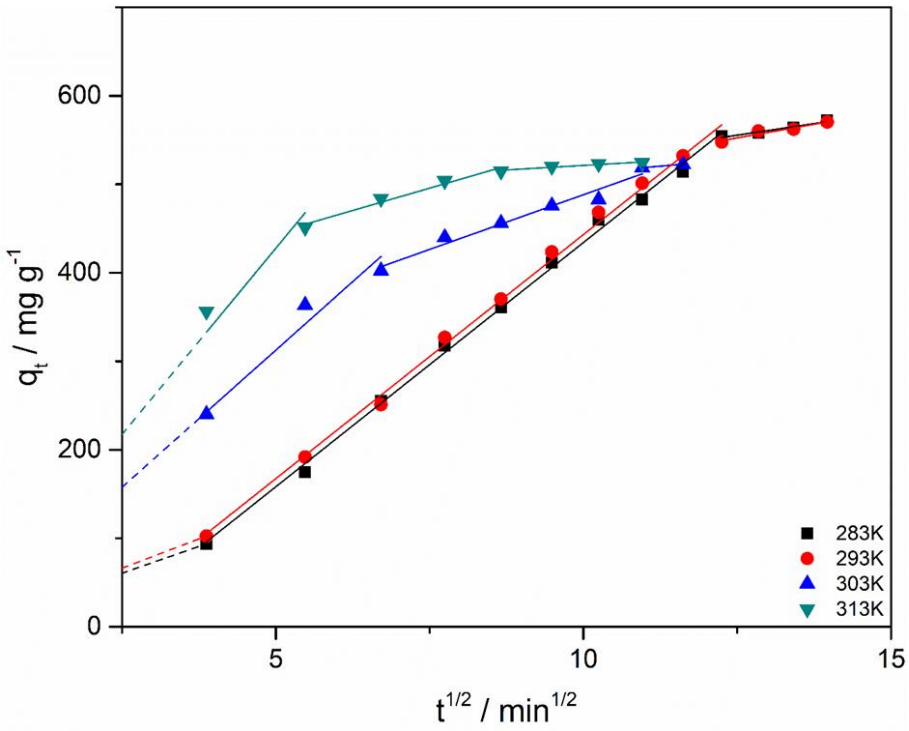


Figure 6.21 Linear intra-particle diffusion model for the adsorption of Reactive Black 5 (C_0=1500mg L^{-1}; V_{dye}=50mL; adsorbent loading=1g L^{-1})

6.6.4 Adsorption Isotherms

Adsorption isotherm models reveal the adsorbent-adsorbate interactions and the surface behaviour of the adsorbent [219]. The Langmuir and Freundlich models for adsorption of RB5 are illustrated in Figure 6.22. The parameters for the Isotherm models are outlined in Table 6.8. The models outlined in Figure 6.22 illustrate that the Freundlich model did not fit the data as well as the Langmuir model. Adsorption of RB5 follows a similar pattern as adsorption of RO16 with increasing temperature. The goodness of fit decreased as the adsorption temperature rises. The inhibited adsorption at low C_0 and high temperatures is the cause of the poorer fit of the Langmuir model as C_e is larger than would be expected by the model.

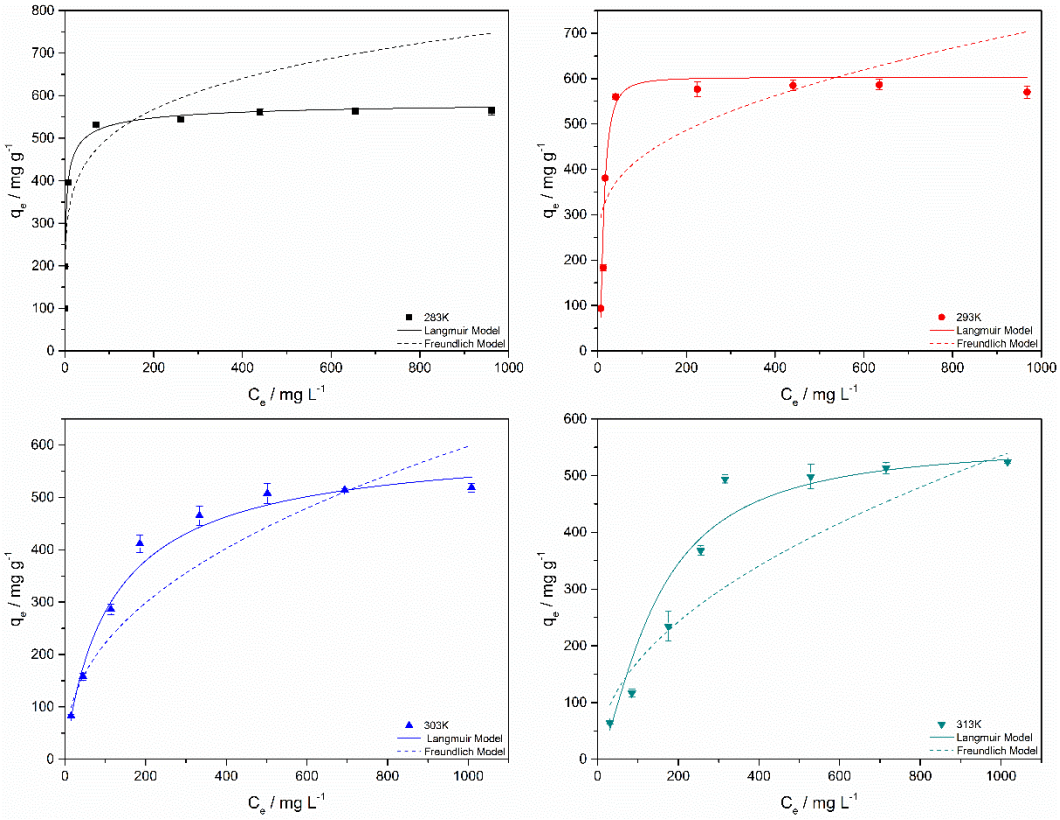


Figure 6.22 Reactive Black 5 isotherm data fitted with Langmuir and Freundlich models (V_{dye}=50mL; adsorbent loading=1g L^{-1})

The q_m value of the MMO for adsorption of RB5 is in the region of 500-600mg g^{-1} compared to >694mg g^{-1}, which was calculated for RO16 at 283K. This is due primarily to the fact that the adsorption of the dye molecules is through the memory effect and regeneration of the LDH from the MMO [119]. RB5 contains four R-SO_3^- functional groups where as RO16 contains only two, therefore based on the general LDH formula the increased negative charge of RB5 anion results in reduced molecular capacity within the interlayer region. The molecular weight difference between RO16 and RB5 is not linear in line with the increase in negative charge which is why there is a decrease in adsorption capacity.

Table 6.8 Isotherm constants for adsorption of Reactive Black 5

Dye	Temperature / K	Langmuir			Freundlich		
		k_l / L mg^{-1}	q_m / mg g^{-1}	R^2	k_f / mg g^{-1}. (L mg^{-1})$^{1/n}$	n	R^2
RB5	283	0.217	566	0.999	180.92	5.269	0.900
	293	0.068	589	0.998	105.443	3.521	0.639
	303	0.018	550	0.989	28.783	2.195	0.928
	313	0.*003*	544	0.931	7.684	1.52	0.914

The data in Table 6.9 shows that the MMO adsorbent exhibits a much higher adsorption capacity for RB5 dye compared with other adsorbents that have been investigated. Only chitosan exhibited a significantly higher maximum uptake for the dye compared with the MMO adsorbent and many of the reference adsorbents exhibit uptake below 100mg g^{-1}. This suggests that MMO adsorbents can compete strongly with other adsorbents in terms of capacity for dye uptake and could make them a useful material for dye wastewater remediation [274-276].

Table 6.9 Maximum uptake capacity of Reactive Black 5 onto selected adsorbents

Adsorbent	q_m mg g^{-1}	Reference
Zn_2Al MMO	589	This work
Biomass Fly Ash	4.38	[274]
Peanut Hull	50	[275]
Aspergillus foetidus	65	[276]
Laminaria sp.	73.2	[277]
Chlorella vulgaris	476.2	[278]
Zeolite	63.6	[279]
Activated carbon (Powdered)	58.823	[280]
Chitosan	1100	[281]

6.6.5 Thermodynamics of Adsorption of Reactive Black 5

The parameters outlined in equation (6.6) and (6.7) can be evaluated using the Van't Hoff plot (Figure 6.23). The data in thermodynamic parameters calculated from Figure 6.23 are detailed in Table 6.10. The data in Table 6.10 indicates that for all temperatures investigated, adsorption is a spontaneous process, as evidenced by the negative ΔG. This

data is in agreement with previously published observations regarding LDH/MMO adsorption [26, 225].

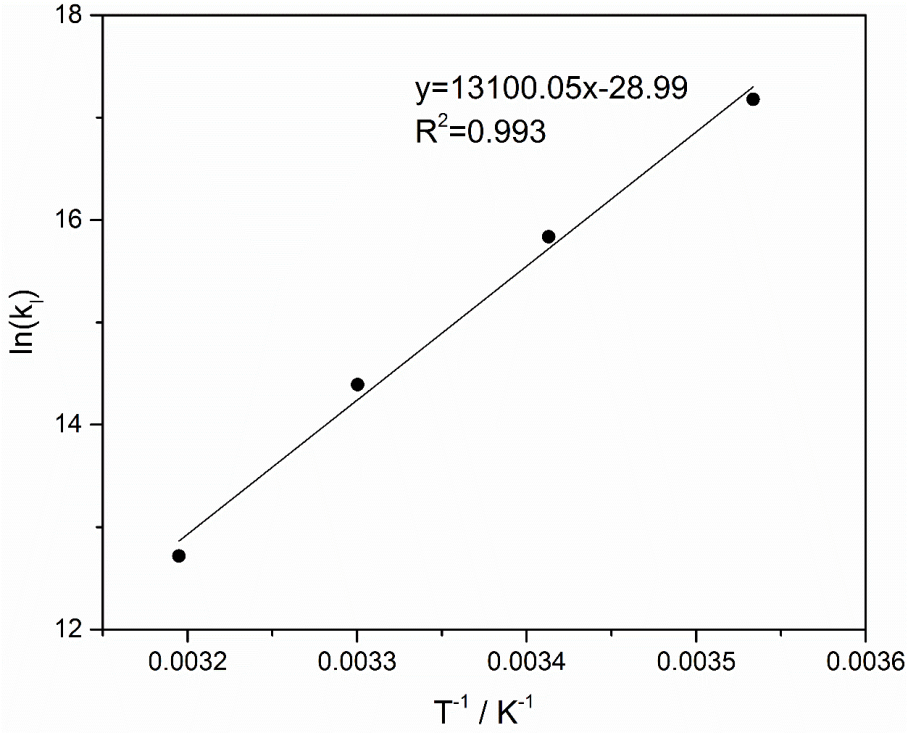


Figure 6.23 Van't Hoff plot for the adsorption of Reactive Back 5

Table 6.10 Thermodynamic properties of the adsorption of Reactive Black 5

ΔH / kJ mol^{-1}	ΔS / kJ K^{-1} mol^{-1}	ΔG / kJ mol^{-1}			
		283K	293K	303K	313K
-102.33	-0.22	-40.21	-38.01	-35.82	-33.62

The ΔH value for RB5 (-102.33kJ mol^{-1}) indicates that the adsorption process was exothermic and should result in a better adsorption process at low temperatures. This hypothesis, at least in terms of is q_m, is supported by the data which illustrates reduced q_m with increasing temperature. The enthalpy values also indicate that the process was primarily chemisorption, occurring as a result of the electrostatic attractions between the sulfonate functional groups of the dye and the regenerated brucite-like layers of the

new LDH [26, 125]. The negative entropy suggests a reduction in freedom of the adsorbent-adsorbate interactions at the surface of the adsorbent, as the free moving solute is bound to the surface of the adsorbent.

6.6.6 Effect of Competing Anions

The effect competing anions from electrolyte salts and alkaline chemicals, on the adsorption of RB5, is outlined in Figure 6.24. Much like the adsorption of RO16, NaCl and has a negligible impact on adsorption due to the charge density of the Cl^- ion being insufficient to replace the dye molecules in the interlayer region. Unlike the adsorption of RO16 however, the presence of Na_2SO_4 results in a greater reduction in adsorption. The addition of 10g L^{-1} Na_2SO_4 results in a similar reduction in adsorption of RB5 as 10g L^{-1} of Na_2CO_3. The concentration of RB5 was reduced by 6±2%, for 10g L^{-1} of Na_2SO_4 and 7±2% for Na_2CO_3 (Table 6.11). This information is important regarding the adsorption of dyes, as the adsorption capacity of the MMO for the dye, is closely affected by the the charge density of competing anions in solution. The charge density of RB5 appears to be lower than both CO_3^{2-} and SO_4^{2-}, whereas the charge density of RO16 appears to be closer to SO_4^{2-} yet still lower than CO_3^{2-}.

Table 6.11 Percentage reduction of Reactive Black (RB5) concentration with competing anions

Additive mass / g L^{-1}	RB5			
	0	1	5	10
Na_2CO_3	37±4	17±3	7±3	7±2
Na_2SO_4	37±4	23±4	8±2	6±2
NaCl	37±4	35±5	36±5	38±4

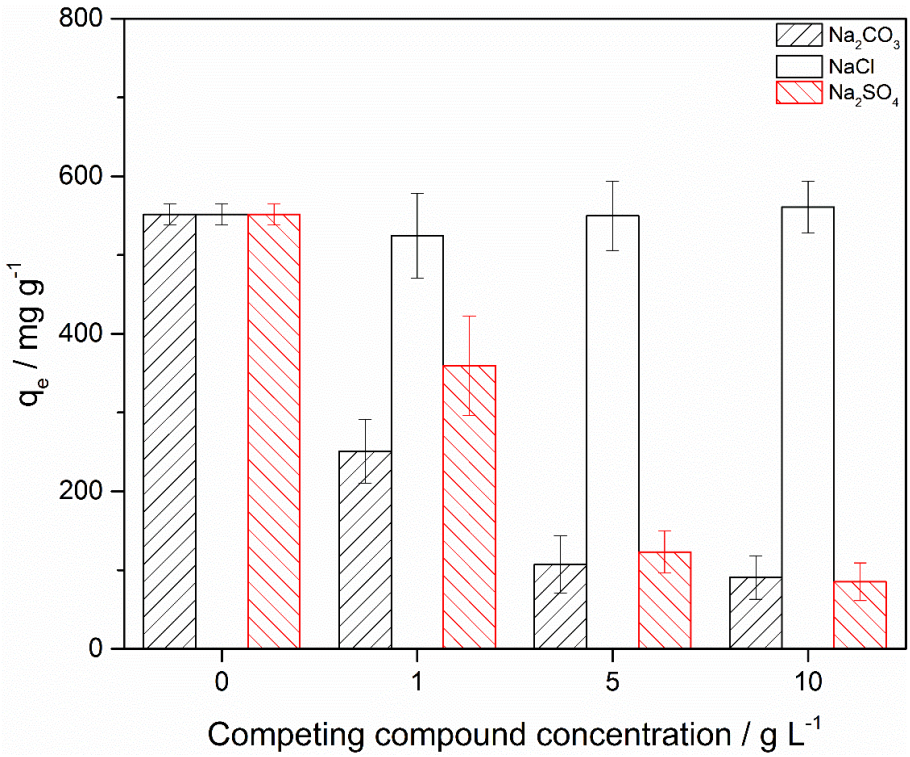


Figure 6.24 Effect of competing anions on the adsorption of Reactive Black 5 (C_0=1500mg L^{-1}; V_{dye}=50mL; adsorbent loading=1g L^{-1}; T=293K)

6.6.7 Adsorbent Regeneration

Regeneration and sustained adsorption capacity in successive cycles is one of the key aspects in the choice of adsorbent. The recyclability of the adsorbent and adsorption capacity impact on the operating costs of the adsorption process. Regeneration of the MMO adsorbent has been investigated in previous research and thermal treatment has been typically utilised for regeneration [225]. Two methods of regeneration were employed; firstly the most common thermal regeneration, by reheating the spent adsorbent to 773K in order to reactivate the adsorbent by oxidising the interlayer anion, and causing dehydroxylation of the brucite-like sheets to produce the MMO from the LDH. The second regeneration method involved an extra step of washing with Na_2CO_3 to

remove adsorbed dye molecules prior to thermal reactivation at 773K in air. Straight thermal regeneration does not allow the recovery of the adsorbed dye. However, washing with Na_2CO_3, which has been shown to exchange with and prevent dye adsorption (Figure 6.24) allows adsorbed dye to be recovered and potentially reused.

Thermal regeneration alone, resulted in reduced uptake capacity, from 546±11mg g^{-1} to 24±35mg g^{-1} after the second adsorption cycle. Adsorption was completely diminished (q_e=1±10mg g^{-1}) after four adsorption cycles with the potential for adsorption to be reduced completely after the first adsorption cycle (Figure 6.25).

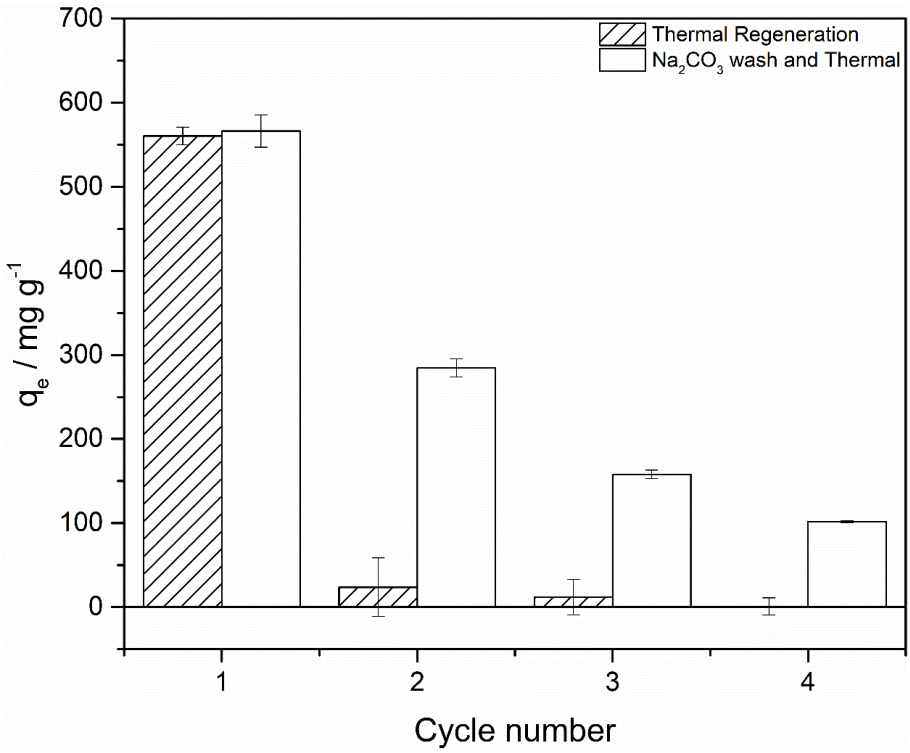


Figure 6.25 Adsorption of Reactive Black 5 after two modes of regeneration

The reduced uptake is attributed to thermal degradation products of the adsorbed dye due to incomplete mineralisation. After heating, decomposition products from the adsorbed RB5 such as; carbonaceous material and residual sulfur are be left in the MMO

matrix due to the incomplete mineralisation (Figure 6.26). During the second adsorption cycle these products reduce the crystallinity of the adsorbent and reduce the number of active sites for the sulfonate groups to bond to the brucite-like layers. This phenomenon has been postulated previously regarding thermal regeneration of LDH/MMO adsorbents [225].

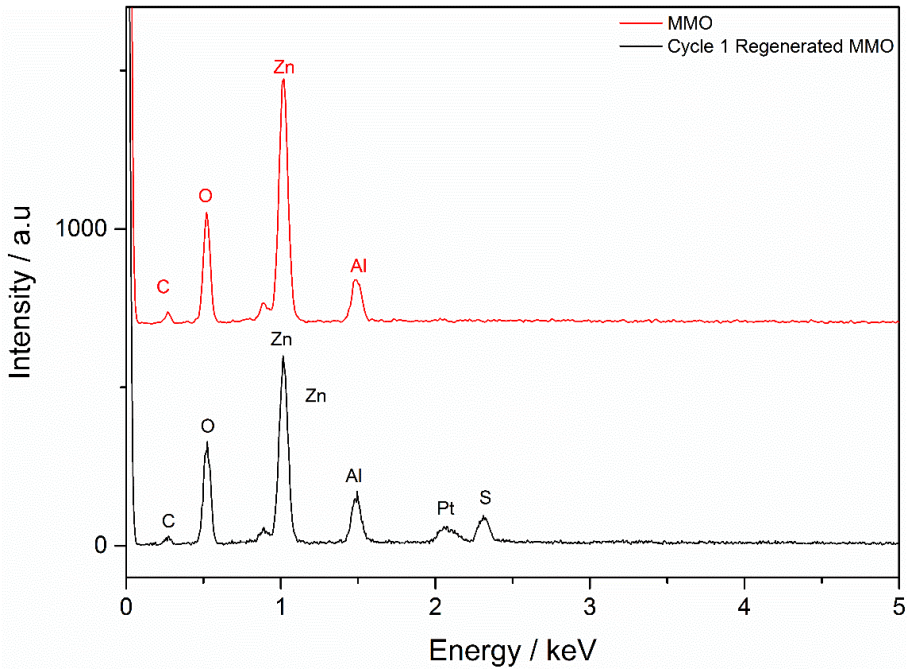


Figure 6.26 Electron dispersive X-ray spectra of calcined $Zn_2Al\text{-}CO_3$ (MMO) and a regenerated MMO without Na_2CO_3 washing

Thermal regeneration following sodium carbonate exchange was primarily investigated in an effort to reduce residual degradation products from the adsorbed RB5. Washing the spend MMO adsorbent with Na_2CO_3 resulted in an increase in adsorption capacity compared with simply thermally regenerating the MMO. After cycle two q_e was 285±11mg g^{-1} compared to 24±35mg g^{-1}, for thermal and Na_2CO_3 washing respectively (Figure 6.25). The adsorption capacity after cycle 4 (q_e=102±1mg g^{-1}) is still reduced compared to that of cycle 1 and is reduced with each subsequent cycle. The continually

reduced adsorption capacity is attributed to incomplete exchange between the R-SO_3^- functional groups in the RB5 molecules and CO_3^{2-} during the post adsorption washing stage. This may be due to the high negative charge in the RB5 dye resulting in a strong attraction to the brucite-like layers. Greater amounts of Na_2CO_3 and longer washing times may mitigate the impact of regeneration. This is a key area of research that will need to be investigated further if LDHs and MMOs are to serve as a useful adsorbent for dye wastewaters. Some other research investigations have however found that regeneration of LDH/MMO adsorbents yields high adsorption for more than one adsorption cycle [126, 282]. However, the initial dye concentration is not divulged in these studies, so it is difficult to determine if the regeneration is successful for exhausted adsorbents.

6.6.8 Proposed Adsorption Mechanism

The primary mode of adsorption is the regeneration of LDH platelets and intercalation of dye molecules into the interlayer region (Figure 6.27). This is evident from the shift to lower Bragg angle of the most intense reflections in the LDH diffractograms (Figure 6.28). The diffractogram for the fresh LDH, has an intense reflection at 11.5° 2θ relating to the d_{003} basal spacing. The basal spacing of the Zn_2Al-CO_3 LDH is 0.76nm, however this reflection has shifted to 4.5° (d_{003}=1.94nm) and 3.1° (d_{003}=2.83nm) for the RB5 and RO16 regenerated samples respectively. This shift in basal spacing is due to the greater molecular weight and size of the dye molecules compared to CO_3^{2-} ions present in the fresh LDH.

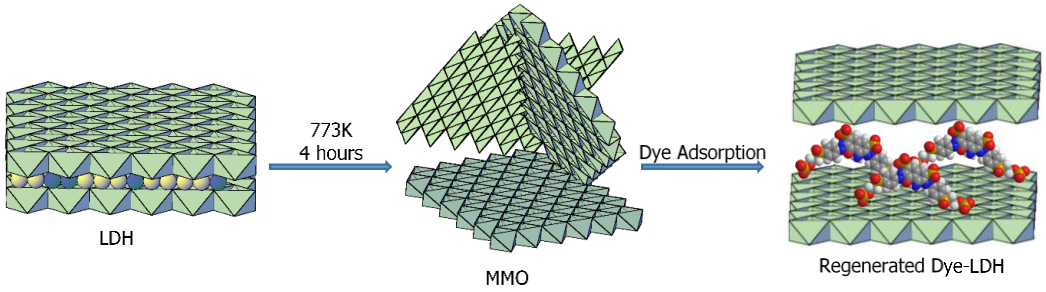


Figure 6.27 Adsorption schematic illustrating the memory effect

The thickness of the brucite-like layers in an LDH are generally accepted as approximately 0.48nm [1], thus the interlayer region occupied by RB5 molecules is 1.42nm and the interlayer region occupied by RO16 is 2.32nm. There are also some minor reflections relating to the d_{003} basal spacing of CO_3^{2-} intercalated LDHs in Figure 6.28. This suggests that without complete de-carbonation of the water some $Zn_2Al\text{-}CO_3$ will regenerate alongside the dye intercalated LDH, due to the ability of CO_3^{2-} ions to displace dye molecules in the interlayer region. However, in the presence of excess CO_3^{2-} from the alkaline additive to dye bath effluent, it is already indicated that there is a need for additional MMO to account for the affinity of CO_3^{2-} to the interlayer region.

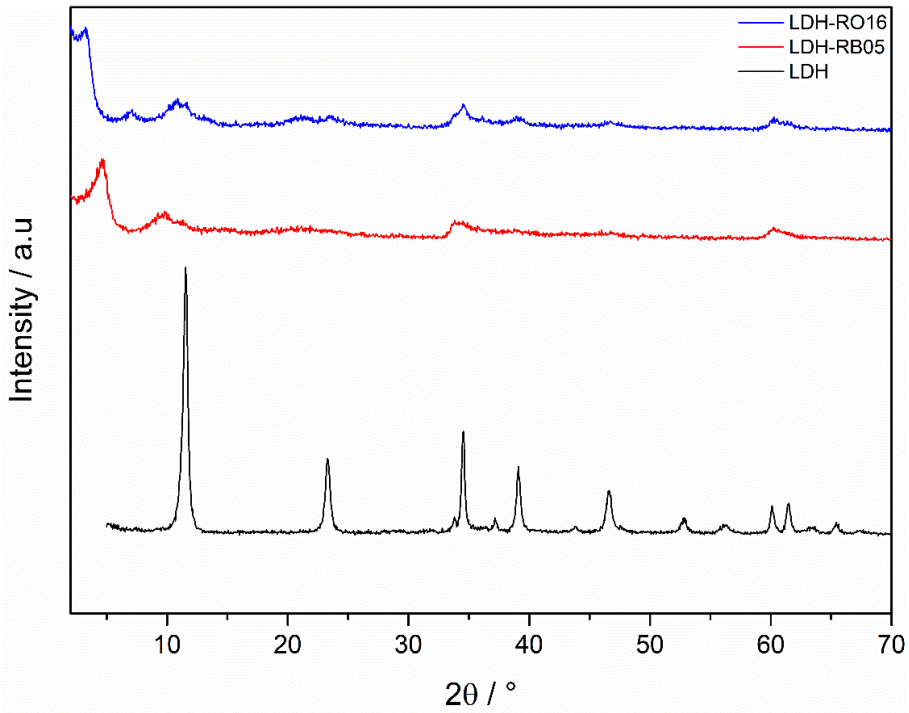


Figure 6.28 X-ray diffractograms of Fresh LDH and exhausted LDH following RB5 and RO16 adsorption at 293K

6.7 Column Adsorption of Reactive Black 5

Column adsorption studies offer a more industrially appropriate experiment when compared with a batch scale system. Column adsorption in a fixed bed is typically utilised in wastewater treatment operations with granular bed media [17, 61, 231]. Column adsorption of only one reactive dye, RB5, was utilised as a test to examine how the pelleting and granulation of MMO materials would affect adsorption. Adsorption column experiments were set up according to the arrangement in Section 3.2.2.

6.7.1 Adsorbent Granulation – Mechanical stability in water

The block pelleting and granulation of powders was chosen as a means to allow more uniform flow through the fixed bed column. Three mass loadings of poly(methyl

methacrylate) (PMMA) binder were used. As there has been no method of column testing for MMO adsorbents where granulation is used, the mass loadings were arbitrarily chosen. The pellet with 0% binder added, was broken down to the powder again and insufficient material was held in a 1mm sieve, and so it was no longer investigated. A portion of the granules were analysed for surface area changes following pelleting and granulation, the surface area and pore size distribution of the granules is outlined in Table 6.12. The sample with 5% PMMA suffered from a greater S_{BET} reduction from 57.8±0.1m^2 g^{-1} to 47.0±0.1mg^2 g^{-1}, whereas the granules with 1% PMMA were only reduced to 49.8±0.1m^2 g^{-1}. The stability of the granules was tested to ensure they could withstand water flow through a column without breaking down during operation. The stability of the granules after shaking in water indicates that the 5% granules are more robust with a greater mass fraction of the granules remaining in the 1mm-1.7mm range (Table 6.12).

Table 6.12 Mechanical breakdown of adsorbent granules and Surface area characteristics

Mass Loading of PMMA / %w/w	Mass Fraction 1 - 1.7mm	Mass Fraction 0.5 – 1mm	Mass Fraction <0.5mm	S_{BET} / m^2 g^{-1}	Pore Diameter / nm
1	91±1	9±1	0	49.8±0.1	6.2
5	98±7	2±7	0	47.0±0.1	6.3

Based on the data displayed in Table 6.12, the decision was taken to use a PMMA loading of 5% in the granules due to the superior mechanical stability and only a small reduction in surface area compared with the granules with 1% w/w PMMA binder.

6.7.2 Breakthrough Curve Models

Breakthrough curve modelling helps to establish adsorption rate constants and adsorption capacity of the material. Three empty bed contact times (EBCTs) were used for adsorption as it is common method for column testing of new adsorbents in literature [97]. The impact of changing flow rate and EBCT is also important to understand the adsorption rate changes and the time to reach breakthrough for a given flowrate. The breakthrough and exhaustion points of a breakthrough curve are detailed in Section 3.1.8.4. Plotting C_t/C_0 vs t produced the breakthrough curves of RB5 (Figure 6.29). The breakthrough curve data can then be modelled using various equations to predict adsorption kinetics and adsorption capacity. Total adsorption can be calculated by integrating the C_0-C_t vs t curve according to equation (6.10) [96].

$$q_{tot} = \frac{Q}{1000}\int_0^t C_{ad}\, dt \qquad (6.10)$$

Where q_{tot} (mg) is the total adsorption, Q (mL min^{-1}) is the flow rate, C_{ad} (mg L^{-1}) is the adsorbed concentration (C_0-C_t), t (min) is the adsorption time. Equilibrium uptake (q_{eq} / mg g^{-1}) in the column can be calculated using q_{tot} from equation (6.10) and (6.11) [96].

$$q_{eq} = \frac{q_{tot}}{m} \qquad (6.11)$$

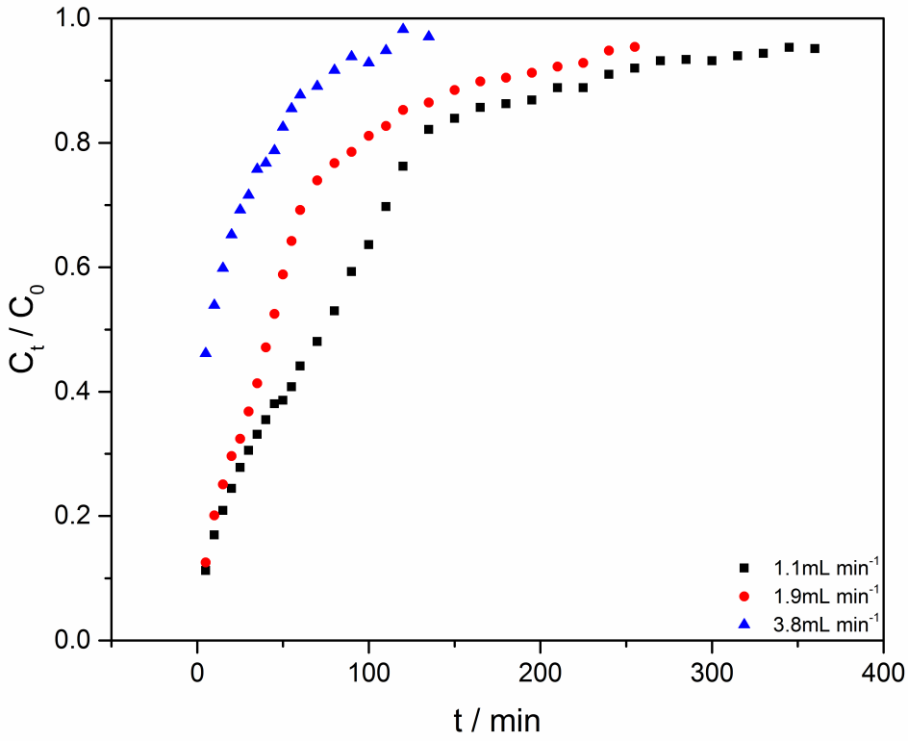


Figure 6.29 Breakthrough curves of adsorption of Reactive Black 5 (C_0=500mg L^{-1})

Total amount adsorbed and equilibrium adsorption of RB5 onto pelleted MMO adsorbents is outlined in Table 6.13. From the data, it can be seen that there is a reduction in adsorption comparing the batch powder material with the pelleted material in the column adsorption experiments; q_e at 293K was 570±13mg g^{-1}, whereas in column testing q_{eq} was <10mg g^{-1}. There are several possible reasons for such a substantial discrepancy between the two adsorption modes. The EBCT was not sufficient to allow complete adsorption of the RB5 onto the MMO. The equilibration time for batch experimentation was typically 2 to 3 hours, thus the slow adsorption kinetics of the RB5 results in incomplete adsorption and an incomplete "S" shape in the breakthrough curve [94, 95]. The surface area does not diminish meaningfully when the MMO is transferred from powder to granules. However, the presence of PMMA in the granules leads to obstruction of pores and prevention of interlayer expansion to cause problems with

adsorption of dye from water. Surface adsorption of dyes onto the surface of LDHs without interlayer adsorption is much lower than the adsorption of dyes onto MMOs with interlayer penetration [225]. PMMA is also hydrophobic and may have prevented the necessary interface between the solute and the adsorbent surface to allow for film diffusion.

Table 6.13 Total adsorption and equilibrium adsorption capacity of Reactive Black 5

Flow Rate / mL min^{-1}	EBCT / min	q_{tot} / mg	q_{eq} / mg g^{-1}
1.1	8.5	51.7	8.4
1.9	4.9	60	9.7
3.7	2.5	45.5	7.4

The breakthrough curves were fit by linear regression to the Thomas, Adams-Bohart and Yoon-Nelson adsorption models. These are the most common three found in literature regarding column breakthrough curve modelling [94, 95, 97]. The linear form of the Thomas model is [95, 97]:

$$\ln\left(\frac{C_0}{C_t} - 1\right) = \frac{k_{Th} q_{Th} m}{Q} - k_{Th} C_0 t \qquad (6.12)$$

Where C_t (mg L^{-1}) is the dye concentration at time, t (min), C_0 (mg L^{-1}) is the initial dye concentration, q_{Th} (mg g^{-1}) is the adsorption at capacity at equilibrium, m (g) is the mass of the adsorbent, Q (L min^{-1}) is the volumetric flowrate through the column, and k_{Th} (mL min^{-1} mg^{-1}) is the Thomas rate constant. The Adams-Bohart model can be described linearly as [97-99]:

$$\ln\left(\frac{C_t}{C_0}\right) = k_{AB} C_0 t - k_{AB} N_0 \frac{z}{U_0} \qquad (6.13)$$

Where k_{AB} (L mg^{-1} min^{-1}) is the Adams-Bohart constant, N_0 (mg L^{-1}) is the adsorbate concentration at the point of exhaustion, z (cm) is the column height and U_0 (cm min^{-1}) is the superficial flow velocity though the column, obtained dividing the volumetric flowrate by the cross section area. The Yoon-Nelson model can be expressed in non-linear and linear forms as [95, 97]:

$$\ln\left(\frac{C_t}{C_o - C_t}\right) = k_{YN}t - \tau k_{YN} \qquad (6.14)$$

Where k_{YN} (min^{-1}) is the Yoon-Nelson rate constant and τ (min) is the time taken for 50% exhaustion to occur. The linear plots of the breakthrough curve models show relatively pore fits in all instances.

The Adams-Bohart model is the least appropriate equation for modelling the adsorption in these column experiments (Figure 6.30). This is primarily due to the fact that the Adams-Bohart model is best used for modelling early stages of adsorption and the lower end of the ideal breakthrough curve [36]. However, the data in these experiments does not have these adsorption points due to the insufficient EBCT to allow adsorption prior to breakthrough (C_t/C_0=0.05). The Adams-Bohart models appear to fluctuate and due to the poorness of fit, the R^2 value is less than or equal to 0.75 for all three EBCT (Table 6.14). The k_{AB} value obtained from the models shows not trending between different flow rates and not reliable due to the poor linear fit with the experimental data. Therefore the Adams-Bohart model cannot be considered useful for modelling the adsorption data in this research

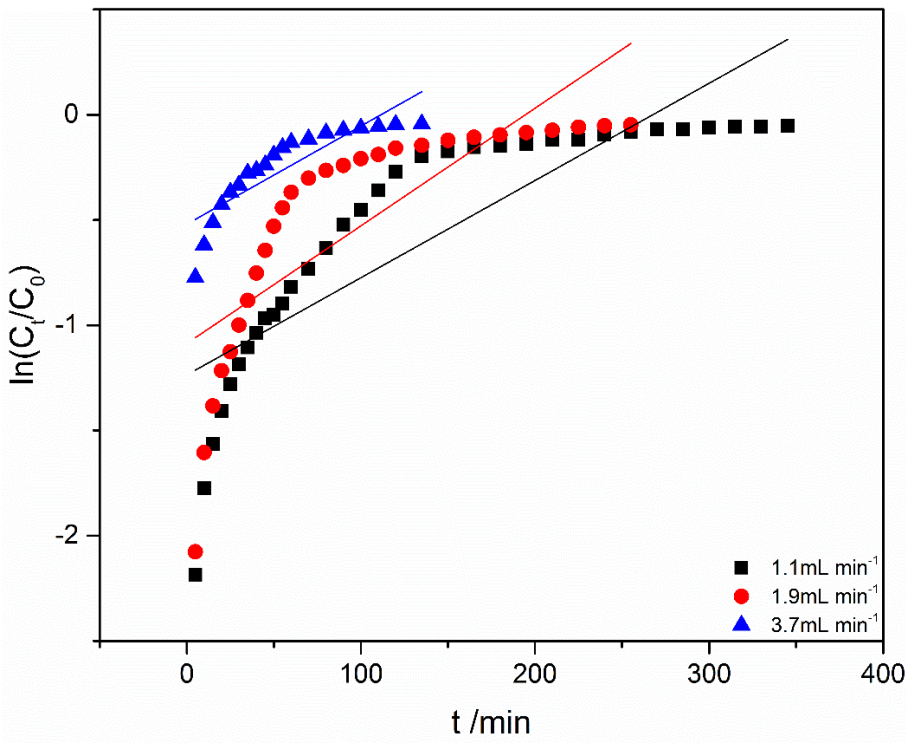


Figure 6.30 Linear Adams-Bohart breakthrough models at different flowrates (C_0=500mg L^{-1})

Table 6.14 Breakthrough curve model constants

Flow Rate / mL min^{-1}	EBCT / min	k_{Th} / mL min^{-1} mg^{-1}	R^2	k_{AB} / mL min^{-1} mg^{-1}	R^2	k_{YN} / min^{-1}	R^2
1.1	8.5	0.027	0.926	0.009	0.741	0.054	0.926
1.9	4.9	0.033	0.874	0.011	0.614	0.018	0.885
3.7	2.5	0.047	0.947	0.009	0.750	0.017	0.956

The Thomas and Yoon-Nelson models provide more appropriate fits to the data. The Thomas model assumes a reversible pseudo 2nd order reaction and Langmuir adsorption characteristics, this is the reason for the close fit of the data to the adsorption model. The Thomas model rate constants increase with increasing flow rate, however the equilibrium uptake capacity shows little change between 1.1mL min^{-1} and 1.9mL min^{-1} as the q_{Th} values are 7.3mg g^{-1} and 7.6mg g^{-1} respectively. This is similar to the q_{eq} calculated from the integration of the experimental curve data. The Thomas kinetic

model rate constant increases with increased flow through the column indicating that the rate of adsorption increases due to the increased flow rate through the column and that equilibrium is reached more quickly, however the q_{Th} value for 3.7mL min^{-1} is negative due to the shape of the model curve.

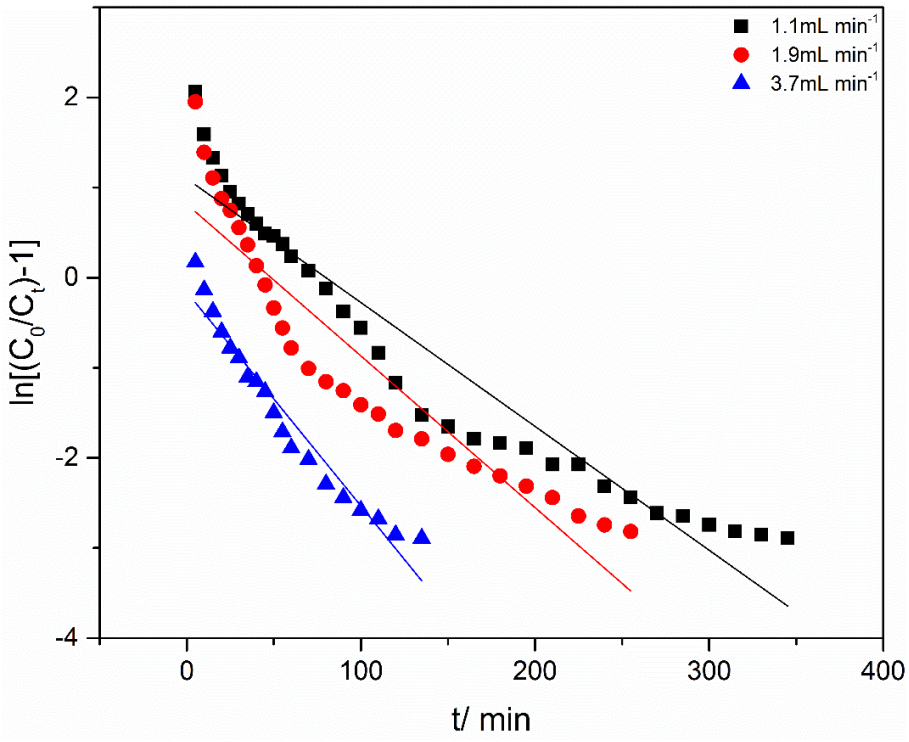


Figure 6.31 Linear Thomas breakthrough models at different flowrates (C_0=500mg L^{-1})

The Yoon-Nelson model is similar in form to the Thomas model, however the Yoon-Nelson model does not account for adsorbent characteristics. The rate constant decreases with increasing flow rate, the implication is that as the flow rate increases the rate of adsorption decreases. The increased flow reduces the adsorption due to the slow adsorption kinetics identified in the batch adsorption studies. With increased flow rates through the column the volume of water and the amount of dye passing through decreases as adsorption slowly occurs through a combination of surface adsorption and intercalation of dye molecules as breakthrough and exhaustion occurs.

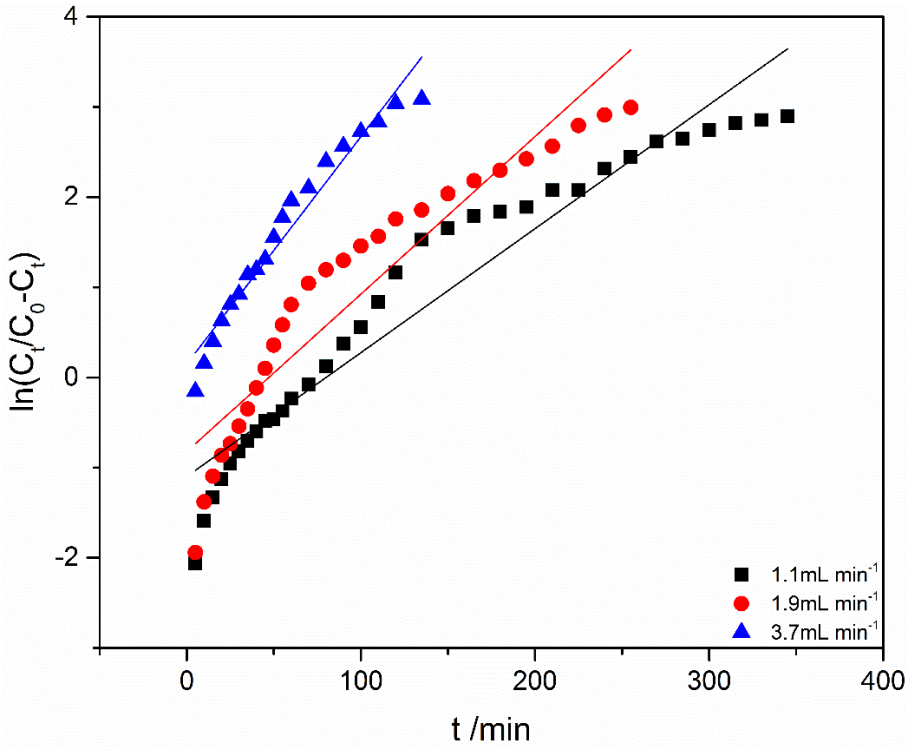


Figure 6.32 Linear Yoon-Nelson breakthrough models at different flowrates (C_0=500mg L^{-1})

The τ_{cal} and τ_{exp} parameters are detailed in Table 6.15. These breakthrough parameters indicate that the time to reach 50% exhaustion of the entire column decreases with increased flowrate. The τ_{cal} values are modelled well for the shorter EBCTs while the τ_{cal} for the longest EBCT (8.5min) is modelled poorly and is less than 50% of the τ_{exp} value. The indication is, that with increased flow through the column, the slow adsorption kinetics of RB5 are inhibited further by flooding the unspent adsorbent ahead of the initial mass transfer zone (MTZ) with dye. This phenomenon elongated the MTZ and reduced the efficiency of the adsorption process. In contrast, when a lower flowrate is used, the slow kinetics are not accentuated as much, and a better adsorption efficiency can be achieved [94].

Table 6.15 Yoon-Nelson 50% breakthrough (τ) parameters

Flow Rate / mL min^{-1}	EBCT / min	τ_{cal} / min	τ_{exp} / min
1.1	8.5	38	80
1.9	4.9	47	45
3.7	2.5	13	10

The implications of the kinetics parameters identified from the data are inconclusive due to the fact that none of the models fit well with the data (<0.98). The column adsorption experiments did not allow for complete adsorption to occur with proper modelling of the breakthrough point. The Yoon-Nelson and Thomas models provide an indication that increased flowrate and reduced EBCT are detrimental to adsorption of RB5 onto granulated MMO adsorbents. The reduced EBCT coupled with slow adsorption kinetics results in low uptake capacity and rapid time to reach breakthrough and exhaustion. Longer EBCT through larger columns would be beneficial in modelling the data and achieving better adsorption.

6.8 Summary

The capability of $Zn_2Al\text{-}CO_3$ based MMO adsorbents for the remediation of two types of reactive dye (RB5 and RO16) from water. A range of factors influence the capability of the MMO adsorbent including stability in operation adsorption kinetics and thermodynamics. The stability of the MMO adsorbents in air and in water was investigated to determine the necessary storage conditions for the MMO as well as the stability in operation for prolonged periods in contact with water. In air there is no change to the MMO adsorbent. Storage in water results in the regeneration of the carbonate intercalated $Zn_2Al\text{-}CO_3$ LDH; after 6 weeks the $Zn_2Al\text{-}CO_3$ LDH was fully

reformed. This indicates that even in de-ionised water, low concentrations of CO_3^{2-} still impact on the MMO and cause LDH regeneration. The basic nature of the reforming LDH, causes more CO_2 to dissolve in the deionised water, which in turn increases the LDH regeneration. This fact should be accounted for in operation by using more MMO adsorbent. The CO_3^{2-} adsorption of the MMO reduces its applicability as an adsorbent when compared with other materials such as activated carbon or membrane filters.

Post adsorption characterisation of adsorbents indicates that intercalation of dye molecules is the mode of adsorption, which causes the regeneration of the original LDH structure through the memory effect, however the CO_3^{2-} intercalated anion is replaced by the anionic dye molecules. The Langmuir isotherm model of adsorption data indicates that maximum adsorption capacity (q_m), of RO16 was generally greater than that of RB5, which were 895mg L^{-1} and 589mg L^{-1} at 293K respectively. This is attributed to the size of the dye molecules and the number of R-SO_3^- functional groups present in the molecule. Reactive Black 5 has more sulfonate functional groups and when following the general LDH formula, a greater anionic charge on the interacted ion results in lower amounts being intercalated. The lowest maximum adsorption capacity of RB5 onto Zn_2Al based MMO is greater than most other adsorbents found in literature, indicating that fresh MMO adsorbents are comparable to current remediation methods.

The influence of competing anions on adsorption, was investigated. Carbonate ions had a greater impact than SO_4^{2-} and Cl^- resulting in almost complete inhibition of dye adsorption with 5g L^{-1} of Na_2CO_3. Dye removal was reduced to 7±3% and 3±2% for RB5 and RO16 respectively. Chloride ions had a negligible effect on adsorption. As a result, the presence of Na_2SO_4 and Na_2CO_3 in dye wastewater effluent would need to be accounted for in adsorption using MMO based adsorbents.

The pH of dye bath effluents may vary with dyeing conditions and the pH investigated in the adsorption experiments for RO16 and RB5 was 4-10. Initial pH was found to have little impact on adsorption of both RB5 and RO16, with no significant trends observed across the pH range. Regeneration was found to reduce q_e after the first adsorption-regeneration cycle and continued to reduce with subsequent cycles, this was most prevalent when a simple thermal regeneration approach was employed. Washing with Na_2CO_3 was found to mitigate the loss of adsorption capacity.

The pelleting and granulation of the MMO adsorbent appeared to have little impact on the surface area of the material despite an increase in size from micron size agglomerates in powder form, to ≥1mm granules. Despite the insignificant change in surface area the adsorption capacity at equilibrium, determined by the integration of the breakthrough curves, was reduced from a maximum capacity of 589mg g^{-1} at 293K in batch reactions to 9.7mg g^{-1}, at an EBCT of 4.9 minutes, in column testing. The significant reduction in q_{eq} is attributed to a number of factors. The first is that the PMMA binder used to granulate the MMO; although it may not have impacted on surface area it blocked the active sites and layer expansion during regeneration of the MMO. PMMA is also hydrophobic and can obstruct the solute-adsorbent interface and reduce the adsorption of the dye. The second possible reason for the low adsorption is the low EBCT achieved in the experimentation coupled with slow adsorption kinetics identified in batch adsorption, Longer EBCT may have resulted in better removal, this is however unsubstantiated in this research.

Modelling of the breakthrough curves by the Adams-Bohart model yielded poor linear fits to the data. The Adams-Bohart model is best fit to the early stages of a breakthrough curve, before breakthrough occurs, this is the reason for the woeful linear fitting and

unusable data. The Yoon-Nelson and Thomas models follow a similar linear equation and so generate similar fits for the data. The half-time breakthrough parameter (τ) from the is fit reasonably well with experimental data for dye flowrates of 1.9mL min^{-1} and 3.7mL min^{-1}, however for 1.1mL min^{-1} the calculated time to reach 50% breakthrough (38 minutes) is half of the experimental value (80 minutes). Indicating that the slow adsorption kinetics benefit from longer EBCTs. The Thomas model allows the calculation of the maximum uptake capacity. The Thomas model uptake capacity (q_e) is comparable with the equilibrium uptake capacity calculated from the integration of the breakthrough curves. However for the experiment where the flowrate was 1.9mL min^{-1}, the fit with the Thomas model is lowest of the three investigated. The column testing in this research must be improved upon if LDHs are to be investigated fully as adsorbents and precursors for adsorbents. The recommendation for further research are outlined in Chapter 8.

7. Continuous Hydrothermal Synthesis of Metal Oxide@Layered Double Hydroxide Composite Nanomaterials

7.1 Introduction

There has been an effort to improve the capabilities of LDH nanomaterials by forming core@shell composites with other materials [179, 188, 283]. The core materials range from nano sized particles to micron sized. The synthesis process has always been in batch experiments where several grams is formed over the course of a number of hours, which varies depending on the synthesis route used. In some cases it is as long as 9 hours for synthesis [284]. In many cases the core material is formed from a metal oxide and the LDH shell bonds across an electrostatic attraction [282]. The motivation for this study was to utilise the continuous hydrothermal reactor to facilitate a single process for the synthesis of core@shell LDH materials without separate batch formulations, to increase the rate of synthesis to grams per hour rather than grams per day. ZnO was chosen as it has photocatalytic capabilities which may be useful in the oxidation of synthetic dye compounds, which has already been highlighted in Section 2.3.2. The problem with using either $Ca_2Al\text{-}NO_3$ or $Zn_2Al\text{-}CO_3$ LDHs as the shell material was that; the $Ca_2Al\text{-}NO_3$ LDHs are larger than any nanomaterials produced by the counter-current hydrothermal reactor where the platelet size was 2-5μm, and particle size of metal oxides is in the nanometer scale [194, 285], thus it may prove difficult to sustain nucleation and growth on the core. The difficulty with using $Zn_2Al\text{-}CO_3$ comes from the ZnO core; elemental analysis would be unable to differentiate between the ZnO in the core and the $Zn(OH)_2$, therefore a core of ZnO and a hydrotalcite ($Mg_2Al\text{-}CO_3$) shell were

utilised in the core-shell composite synthesis. The core-shell composite material was then tested against single phase ZnO core and $Mg_2Al\text{-}CO_3$, as well as a synthetic mixture of the two in the mass fraction obtained in the composite, as well as an array of different $Mg_2Al\text{-}CO_3$ LDH produced in order to elucidate the changes to the material during composite synthesis compared with single phase synthesis.

7.2 Highlights

- Two stage single process synthesis of ZnO@$Mg_2Al\text{-}CO_3$ core-shell LDH composite occurred, however reaction conditions required optimisation to ensure bonding and coverage are improved.
- Composite material exhibits increased surface and band gap energy compared to single phase $Mg_2Al\text{-}CO_3$.
- Reduced NaOH amount during synthesis of $Mg_2Al\text{-}CO_3$ results in distortion of brucite-like layers resulting in significant reduction in crystallinity but increases in surface area.

7.3 Two Stage Counter-Current Reactor Experiments: Composite Synthesis

For the synthesis of ZnO@LDH in the two-stage reactor system; the synthesis of the core occurred in the same manner as the standard ZnO and LDH synthesis, however, NaOH (0.15M) and Na_2CO_3 (0.017M) were fed at 293±1K temperature into the reaction system using a third pump to meet the ZnO, again at 10mL min^{-1}. This mixed feed was heated to 373K as the down-flow feed into the second reactor. LDH metal salts were pumped into

the up-flow for the second reactor, unheated at 20mL min^{-1}. The reaction is outlined in a schematic (Figure 3.4). Concentrations of reagents were modified in order to match the alterations in flow rates when transferring from a single to a sequential reactor system.

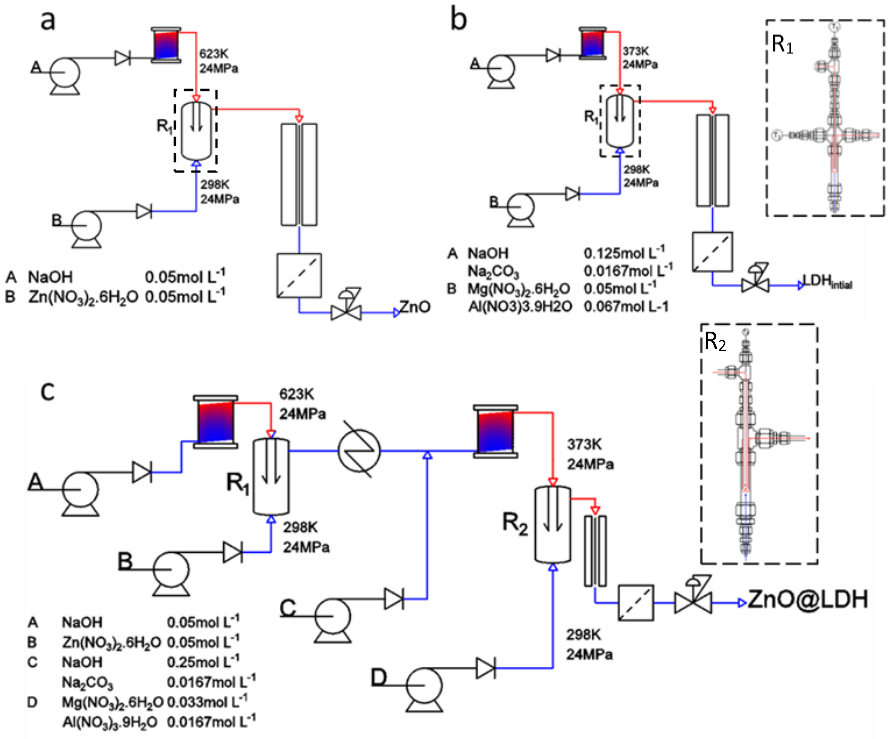


Figure 7.1 Reactor diagrams of ZnO@LDH composite synthesis with single phase ZnO and LDH ($LDH_{initial}$)

7.3.1 Crystal Structure of ZnO, Mg_2Al-CO_3 and ZnO@Mg_2Al-CO_3 Composite

Mg_2Al-CO_3 in $LDH_{initial}$ exhibits $R\bar{3}m$ rhombohedral crystal symmetry whereas ZnO exhibits $P6_3mc$ symmetry. The LDH_{mix} is a combination of ZnO and $LDH_{initial}$ samples, thus the crystal phases for each of the induvial samples are present in the diffractogram. The diffraction pattern for ZnO@LDH shows reflections for both ZnO and Mg_2Al-CO_3 phases Figure 7.2. The lattice parameters in Table 7.1 show variation between single phase

$LDH_{initial}$, ZnO and ZnO@LDH. However, the lattice parameters correspond well with published data [3, 10, 157, 286, 287].

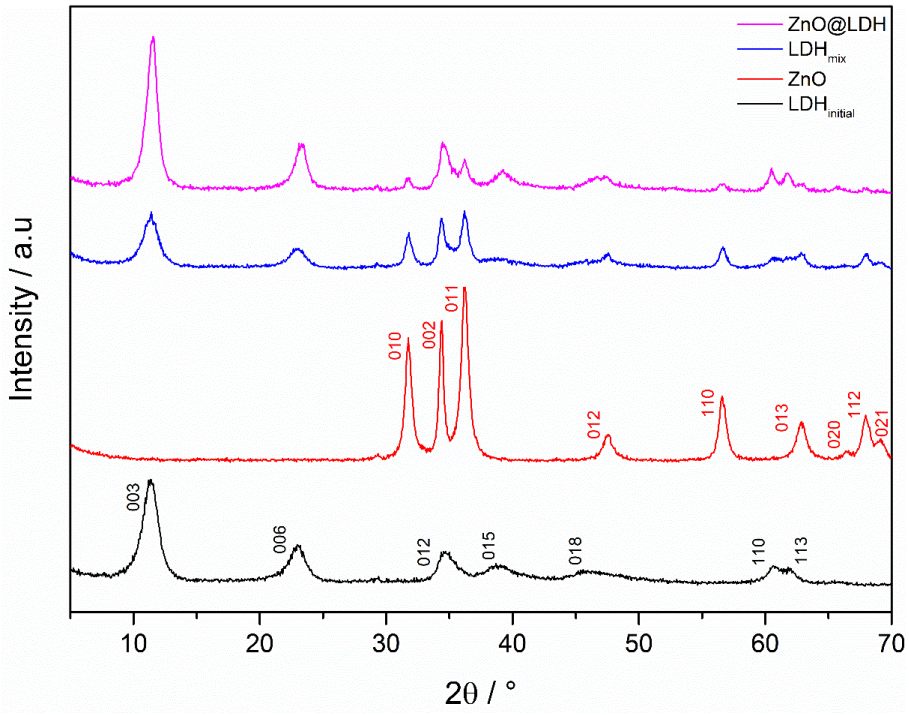


Figure 7.2 X-ray diffractograms of composite (ZnO@LDH) and single-phase ($LDH_{initial}$, ZnO) and mixed nanomaterials

Table 7.1 Lattice parameters of single phase and composite materials

Sample	*a* (nm)	*c* (nm)	CDL (*112*) / nm	CDL (*003*) / nm	CDL (*110*) / nm
ZnO	0.33	0.52	25±0		
$LDH_{initial}$	0.30	2.3		8±0	31±5
ZnO@LDH	0.32	0.52	42±2	12±0	27±4
	0.31[c]	2.2			

Crystal domain length (CDL), approximated from the Scherrer equation, indicates differences between single phase and the composite diffractograms (Table 7.1). The CDL calculated from the (*112*) reflection of the ZnO phase in ZnO@LDH is 17nm larger than

in single phase ZnO. Domain length relating to the (*003*) and (*110*) reflections in the LDH phase in ZnO@LDH are marginally larger, and smaller than that of $LDH_{initial}$ for the ⟨*003*⟩ and ⟨*110*⟩ planes respectively. The larger ZnO CDL in ZnO@LDH may be due to the fact that some Zn^{2+} remained unconverted following the first reaction. Elemental analysis of reaction liquor from ZnO indicated that conversion of Zn^{2+} is 94%. The remaining Zn^{2+} is then converted into ZnO prior to the second reactor, forming in the band heater prior to R_2, growing on the already formed crystals. Dissolution of ZnO in the secnd heater, and recrystallisation may also contribute the increased CDL in the zinc oxide phase of the ZnO@LDH sample.

7.3.2 Morphology and Particle Size of ZnO, Mg_2Al-CO_3 and ZnO@Mg_2Al-CO_3 Composite

Image analysis of particles visible in TEM micrographs was used to compare the CDL obtained from XRD analysuis with particle sizes as well as determining particle size distribution. The diameter of LDH platetelts which were typically hexagonal in shape, was approximated based on the circuim diameter of a regular hexagon. The size of ZnO rods was approximated based on the length of the rod along the longest edge (Figure 7.3).

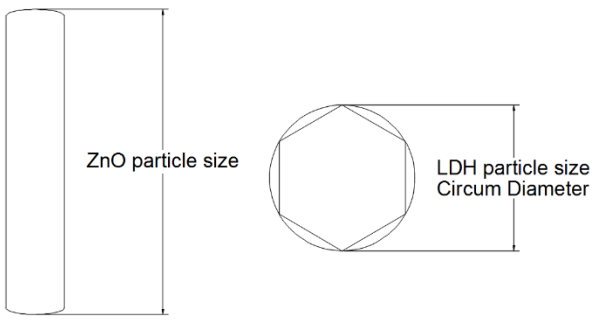


Figure 7.3 Schematic detailing ZnO and LDH particle size measurement definitions

The ZnO agglomerates outlined in the SEM micrograph in Figure 7.4a are >2μm in size, however smaller particles in the agglomerates are visible. The SEM micrographs illustrating the morphological differences between the ZnO@LDH composite and the $LDH_{iniital}$ sample show face-face stacking and agglomeration is prevalent in the $LDH_{initial}$ sample, whereas the ZnO@LDH composite material shows more criss-crossed arrangements of $Mg_2Al\text{-}CO_3$ platelets and a hierachical struxcture to the agglomerates compared to the flatter faced blocks of the $LDH_{initial}$ (Figure 7.4b). There are also rods visible in the middle section of the SEM micrograph showing the ZnO@LDH composite material where there is a break in the LDH shell (Figure 7.4c).

The ZnO nanoparticles in the TEM micrograph are elongated into eliptical and short rod-like particles. The rods appear to be smaller than in the ZnO sample (Figure 7.4d) compared with the ZnO@LDH composite (Figure 7.4f). The LDH platelets depicted in Figure 7.4e are less defined in terms of shape, compared with the ZnO nanoparticles, the platelets also appear to thinner when not particle of an agglomerate (Figure 7.4e). There is a distinct difference in the TEM micrograph of $LDH_{initial}$ and ZnO@LDH. There is a large rod sahpe particle visible in the ZnO@LDH TEM micrograph, with thinner disordered platelets arranged around the rod like particle suggesting that there is a degree of potential growth of LDH platelets onto a ZnO core. The zeta potential of LDHs is postive, while the zeta potential at pH 10 is approximately 0mV, however as the pH increases towards 11 the zeta potential decreases and the ZnO becomes negatively charged [288]. Synthesis of the ZnO@LDH smaple occurs between pH 9 and pH 11, suggesting that in areas of localised higher pH, there is likely to be some electrostatic attractions, between the ZnO and brucite-like layers of the $Mg_2Al\text{-}CO_3$, as evidenced by Figure 7.4f.

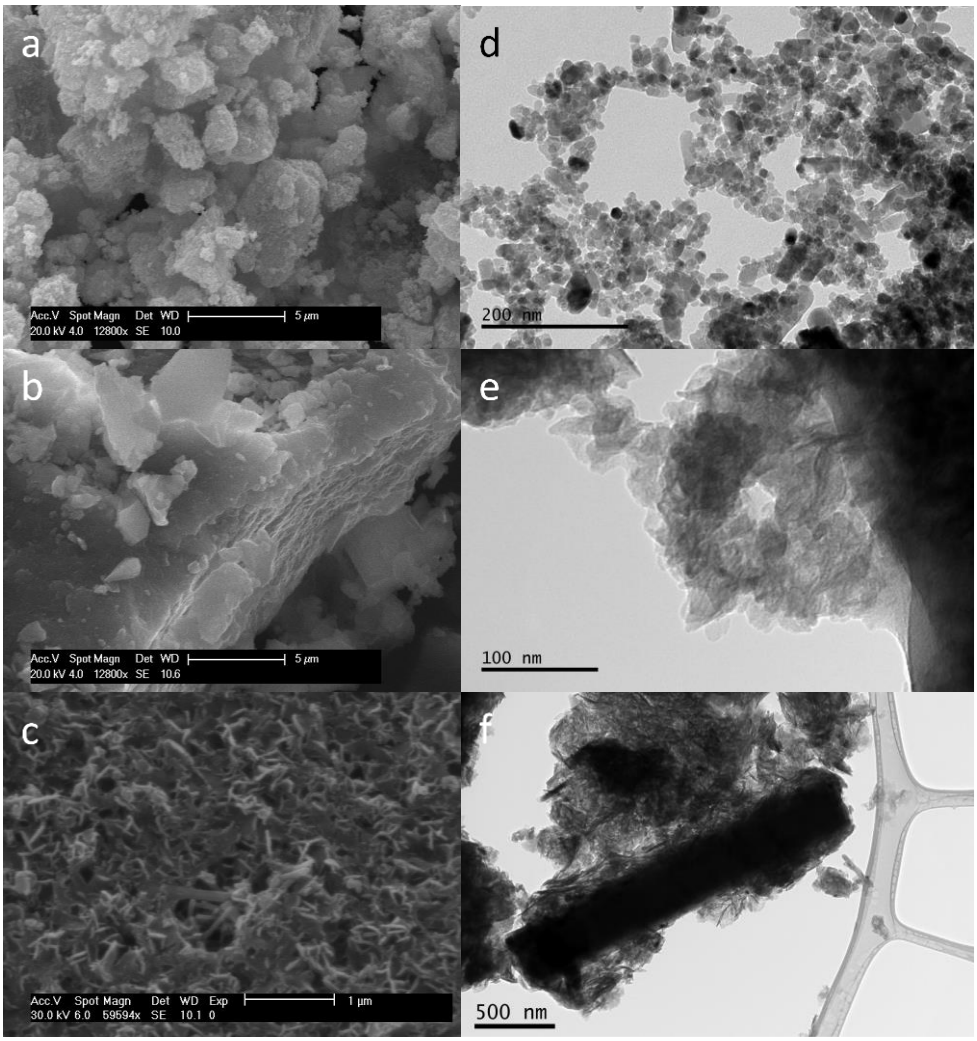


Figure 7.4 SEM micrographs a) ZnO, b) $LDH_{initial}$, c) ZnO@LDH and TEM micrographs d) ZnO, e) $LDH_{initial}$, f) ZnO@LDH

The data from image analysis particles in TEM micrographs is outlined in Table 7.2 and Figure 7.5. The size distribution of the LDH phases in the $LDH_{initial}$ and ZnO@LDH samples are similar, however the mean particle size has increased. Analysis of TEM micrographs for ZnO, $LDH_{initial}$ and ZnO@LDH included more than 100 individual particles for each sample and crystal phase in the case of ZnO@LDH.

Table 7.2 Platelet diameter calculated by image analysis of TEM micrographs nanomaterials

Sample	TEM	
	[b]Particle Size / nm	[b]Particle Size / nm
ZnO	22±14	
$LDH_{initial}$		34±34
ZnO@LDH	53±41	51±21

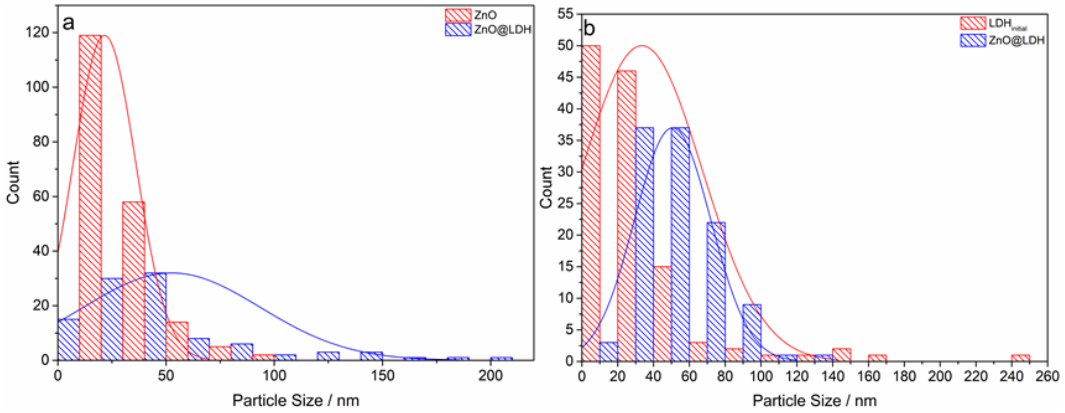


Figure 7.5 Particle size distribution of $LDH_{initial}$ and ZnO compared with ZnO@LDH

The particle size for the ZnO rods is comparable to the CDL. The image analysis of the rods in the ZnO and ZnO@LDH micrographs indicates a size increase in-line with the increase observed from the CDL calculation. There is an increase of approximately 30nm in rods length between the single phase ZnO and the ZnO@LDH material compared with an increase of approximately 17nm in the CDL. There are also some exceptionally larger ZnO rod particles (Figure 7.4f) . The size distribution is also wider in the ZnO@LDH sample compared with the single phase ZnO where the modal particle size is twice the second most frequent.

The increase in platelet size of the Mg_2Al-CO_3 in the ZnO@LDH sample is greater compared with the CDL calculated from the (*110*) reflection in the respective

diffractograms for $LDH_{initial}$ and ZnO@LDH. The increase in platelet size between the $LDH_{initial}$ sample and the ZnO@LDH sample indicated that growth mechanics are different in the secodn reactor as a result of the changes to the reaction systme by the presence of the ZnO and possibly, the reactor sizing and the changing of growth has lead to reductions in crystallinity that are not accounted for in XRD analysis. The distribution of particle sizes is wider across the 20-140nm range in the ZnO@LDH composite, however in the single phase $LDH_{initial}$ sample there are some particle that are as large as 250nm, which were not observed in the composite. In general though the size distribution of the LDH platelets appears to be affected by the chaning of reaction conditions between single phase and composite synthesis.

7.3.3 Electrochemical Analysis and Band Gap Calculation

For semiconductors, the onset of light absorption is also known as the band gap. In general, a lower band gap is considered more desirable as a lower band gap requires less energy to cause electron transition to occur (Section 3.1.6.5). The Beer-Lambert law relates the absorbance of a substance to the path length through the substance and concentration of the substance, which is also impacted by the extinction coefficient which is affected by the substance itself and the radiation energy. The Tauc equation relates the extinction coefficient to the energy of radiation and the electron transmission occurring. The Tauc equation can be described as [191]:

$$\varepsilon h\nu = A\left(h\nu - E_g\right)^n \qquad (7.1)$$

In the Tauc equation hν is the energy of the incident photon, which varies for a given wavelength, A is a constant and n relates to the manner of the electron transition. The value of n varies depending on the type of transition that occurs (Section 3.1.6.5). The

extinction coefficient can be replaced with reflectance by substituting a modified Kubelka-Munk function (7.2) into the Tauc equation to give (7.3):

$$F(R) = \frac{(1-R)^2}{2R} \qquad (7.2)$$

$$F(R)h\nu = A(h\nu - Eg)^n = (F(R)h\nu)^{1/n} = A\left(h\nu - E_g\right) \qquad (7.3)$$

Where F(R) is the Kubelka-Munk function, R is the reflectance, ε is the extinction coefficient, hν is the energy of the light, A is a constant and E_g is the band gap energy. By plotting $(F(R)h\nu)^{1/n}$ vs hν the band gap can be extrapolated from the graph Figure 7.6b. Direct allowed transitions (n= $^1/_2$) were found for all materials tested. The composite material shows a slight increase in band gap energy compared with the ZnO (Table 7.3). The increased band gap meaning that a lower wavelength of light, and more energy, is necessary for electron transition to occur. $LDH_{initial}$ has a band gap energy of 5.24 indicating poor photocatalytic characteristics. The LDH_{mix} sample has a band gap similar to the ZnO sample due to the fact that there is single phase ZnO crystal phases within the mixture, while the ZnO@LDH sample has inhibited access of the light to the ZnO due to the LDH shell around the material which is the primary reason attributed to the increased band gap energy.

Table 7.3 Band Gap Energy of ZnO@LDH, ZnO and LDH and artificially mixed sample

Sample	Band Gap / eV
ZnO	3.21
ZnO@LDH	3.31
LDH_{mix}	3.22
$LDH_{initial}$	5.24

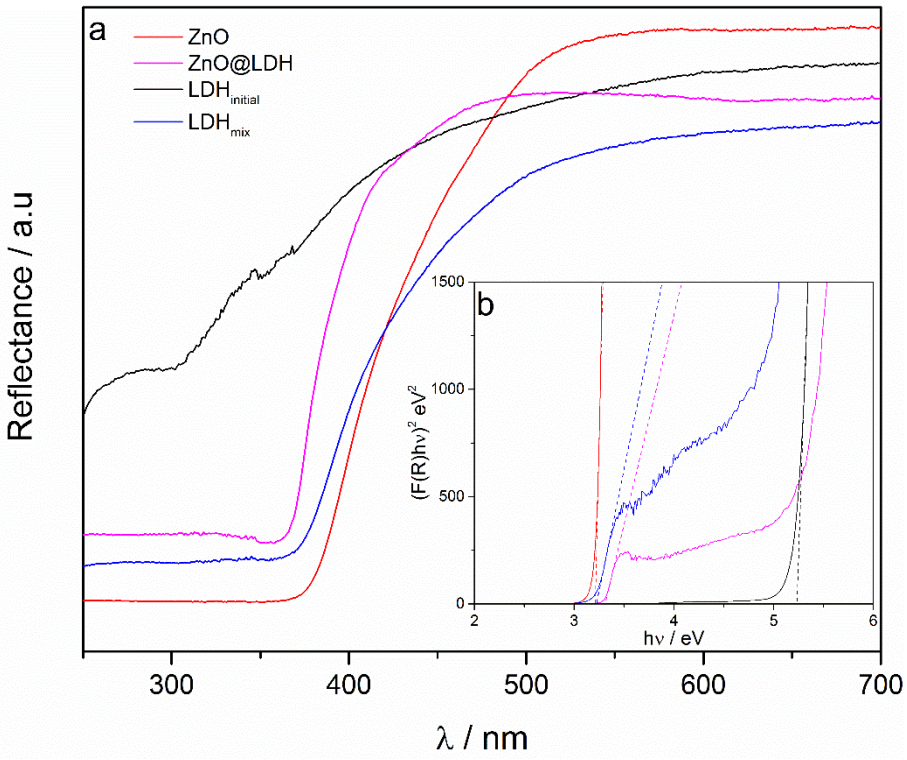


Figure 7.6a) Reflectance and b) Kubelka-Munk function plots

7.3.4 Surface Area Analysis of ZnO, LDH and ZnO@LDH Composite

Nitrogen adsorption isotherms for the determination of specific surface area (S_{BET}) are outlined in Figure 7.7a. The adsorption isotherms are all identified as Type-IV shape isotherms according to IUPAC definition [248].

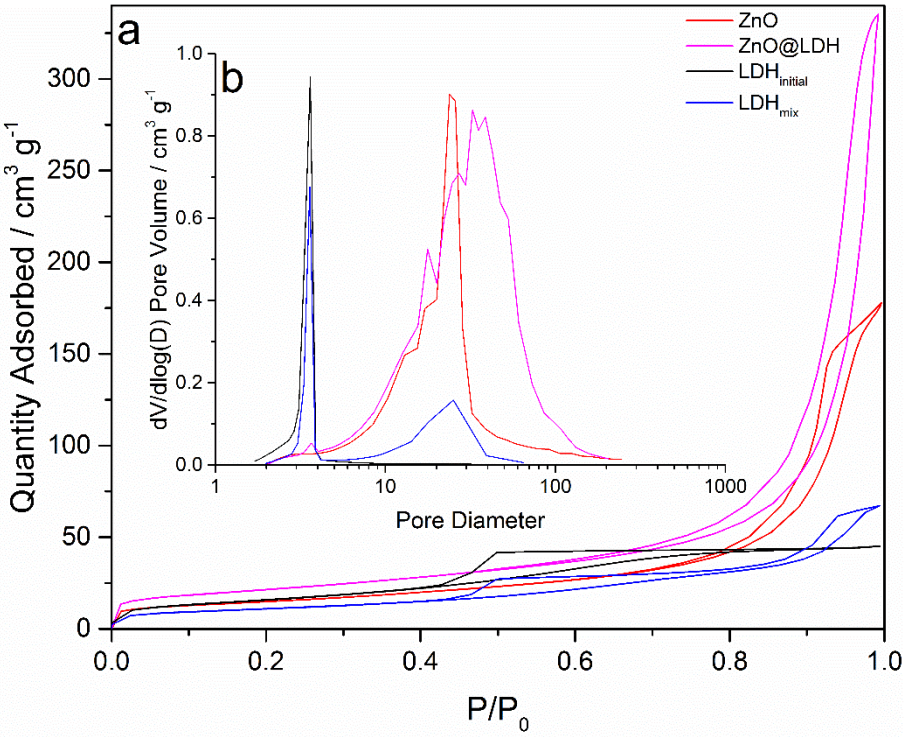


Figure 7.7a) Nitrogen adsorption isotherms and b) pore distribution plots

The ZnO isotherm demonstrates a H1 type hysteresis loop, indicating a network of relatively uniform meso-pores. From TEM and SEM micrographs (Figure 7.4) it is possible to see a '3D' criss-cross like arrangement of particles in the ZnO@LDH sample, yet the 3D structure of platelets is not evident in $LDH_{initial}$ and more face stacked particles are visible with flat surfaces (Figure 7.4). The more open 3D structure of the platelets, resulting from edge-face connections, gives rise to a H1 hysteresis loop that with some characteristics of a H3 type. The H3 hysteresis is indicative of loosely aggregated platelet like particles present in the sample [248]. The isotherm for $LDH_{initial}$ closely resembles H2 and H3 hysteresis. The sharp desorption branch is associated with H2 hysteresis and the inclined tail at high P/P_0 found in H3 loops. This is to be expected as H3 hysteresis is associated with aggregation of platelet-like particles and clays [248]. Of note is the difference in shape between isotherms for ZnO@LDH and LDH_{mix}. The isotherm for LDH_{mix} shows a strong resemblance to both ZnO and $LDH_{initial}$, which is to be expected as

it is a mixture of those two materials. The shape of the ZnO@LDH isotherm however is closer to the ZnO isotherm shape, but also the $Zn_2Al\text{-}CO_3$ isotherm shape, with a large increase in N_2 adsorption at high P/P_0.

Growth of LDHs onto ZnO in the ZnO@LDH, caused an increase in S_{BET} (Table 7.4). The surface area increase indicates that despite larger crystal and particle formation in the composite material the growth arrangement and stacking of ZnO and LDH particles causes a network of meso-pores that results in a total pore volume 7 times greater than the single phase LDH material. The increased surface area coupled with the improved band gap of the ZnO@LDH composite suggests that applications for wastewater remediation could be possible with further research. The surface area of the LDH mix sample is lower than each of the single phase materials, suggesting that dry combination of the powders causes the finer particles to block pores and reduce the effective surface area. The difference in isotherm shape between ZnO@LDH and the LDH_{mix} samples, as well as the increased surface area and pore volume suggests that the composite material is not a mix of two single phases but bonding between ZnO and $Mg_2Al\text{-}CO_3$ has occurred during synthesis.

Table 7.4 Surface area and pore diameter characteristics of ZnO, composite and LDH nanomaterials

Sample	S_{BET} / $m^2\ g^{-1}$	Pore Diameter / nm	Pore Volume / $cm^{-3}\ g^{-1}$
ZnO	53.0±0.1	17.6	0.3
$LDH_{initial}$	58.2±0.3	4.0	0.1
LDH_{mix}	39.6±0.1	7.2	0.1
ZnO@LDH	76.2±0.1	17.0	0.7

7.3.5 Chemical Analysis Nanoparticle Materials

The molecular ratio of the Mg to Al and Zn in the ZnO@LDH composite indicates the proprotion of LDH to ZnO as well as the conversion of the LDH precursors into the brucite-like layers. SEM-EDS analysis of $LDH_{initial}$ indicates that the molecular ratio of Magnesium to Aluminium was 1.97. This value is close to the theoretical Mg/Al in the precusor solutions (Mg/Al=2), while the Mg/Al ratio in ZnO@LDH was 1.3. This change implies a lower conversion of Mg^{2+} compared to $LDH_{initial}$ (Table 7.5).

Table 7.5 Molecular ratio of ZnO@LDH composite

Element	Atomic Fraction	Weight Fraction	Compound Fraction	Formula	Mg/Al
Mg	17.68	16.19	26.4	MgO	1.3
Al	13.55	13.77	27.3	Al_2O_3	
Zn	15.39	37.88	46.34	ZnO	
O	53.39	32.17			

The reduced NaOH in the synthesis of ZnO@LDH may be the cause of the reduced Mg/Al ratio. Alternaltively the unreacted Zn^{2+} may also react in the presence of OH^- and Al^{3+} to produce $Zn_xAl\text{-}CO_3$ or $Mg_xZn_yAl\text{-}CO_3$, as the work in Chapter 4 and Chapter 5 of this thesis indicated, the syntheis of $Zn_2Al\text{-}CO_3$ LDHs is a straightforward process, albeit at 293K compared to 373K as was the case in R_2. However the fraction is unlikely to cause a noticeable impact, as residual Zn^{2+} accounts for 6% of the precursor concentration. ZnO in the reactor down-flow, may partially disolve to produce Zn^{2+} in the reactor and then re-precipitate as $ZnAl\text{-}CO_3$ LDHs.

7.3.6 Thermal Degradation of ZnO, Mg_2Al-CO_3 and Composite Materials

The thermal degradation of the LDH and composite materials can also be used to identify the mass fraction of the LDH and ZnO in the ZnO@LDH composite material. The mass loss profile whilst heating the ZnO illustrates very little mass loss, with surface bound water as the most likely cause of the low (3%) mass loss, while the loss of mass from $LDH_{initial}$ follows a distinct pattern in that there are 2 primary mass loss events which are attributed to the evaporation of surface bound and intercalated water at temperatures up to 400K (Figure 7.8b). The second major mass loss event circa 650K is the dihydroxylation of the brucite-like layers and loss of the interlayer carbonate as CO_2 (Figure 7.8b). The first mass loss accounts for approximately 19% of the mass of $LDH_{initial}$. The dehydroxylation of the layered structure releases 28% of the total starting mass (Figure 7.8a).

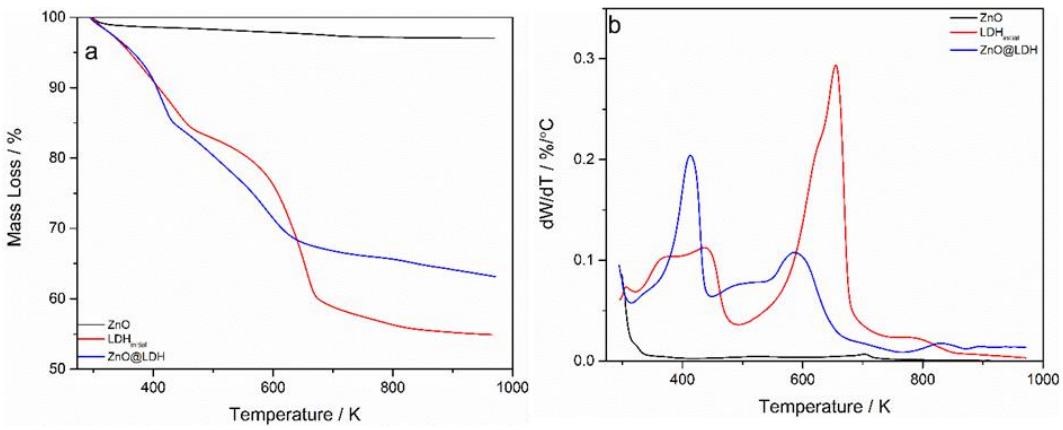


Figure 7.8 Mass loss and derivative mass loss profiles of ZnO, LDHinitial and ZnO@LDH

The mass loss of the ZnO@LDH material follows a different profile, in that the loss of water in the lower temperature range is lower (16%) and the loss of the interlayer anion only accounts for 18% of the original mass. The derivative mass loss profiles also indicate that the rate of water loss is more rapid in the ZnO@LDH occurring at 0.2% K^{-1}

compared to 0.1% K^{-1} in the $LDH_{initial}$ sample. The dehydroxylation of the interlayer anion is much slower in the ZnO@LDH. The loss of hydroxyl groups also occurs at a lower temperature than the breakdown of the $[Mg_2Al(OH)_6]$ in $LDH_{initial}$ (Figure 7.8b). This difference in mass loss profile indicates a change in the structure of the material that is not immediately identifiable from the X-ray diffractograms.

The mass loss profile and total mass lost under heating indicates that the ZnO@LDH sample contains approximately a 0.77 mass fraction of LDH. In contrast the SEM-EDS analysis indicates that the fraction of the material that is LDH is 0.54. Based on the thermal degradation data the mass fraction for the LDH_{mix} sample were used as Mg_2Al-CO_3=0.77 and ZnO=0.23.

The thermal analysis of the ZnO@LDH sample however, strongly indicated that some amount of Zn_2Al-CO_3 LDH was present in the sample (Figure 7.9b). The temperature of major mass loss events are similar in the ZnO@LDH to the peaks in the derivative mass loss profile of Zn_2Al-CO_3. These mass loss events are also present in the thermal degradation of Zn_2Al-CO_3. Further evidence may also be present in the diffractogram in Figure 7.10. The diffractogram in Figure 7.10 illustrates a crystalline Zn_2Al-CO_3 material, more so than the $LDH_{initial}$ sample, and the intense reflections of the Zn_2Al-CO_3 diffraction may be the cause of the increased relative intensity of the LDH reflections compared with the ZnO reflections in the ZnO@LDH diffractogram compared to the LDH_{mix} pattern (Figure 7.2). The data suggests therefore, that although there is some degree of composite synthesis, there is also a situation where Zn_2Al-CO_3 is produced alongside a mixture of ZnO and Mg_2Al-CO_3.

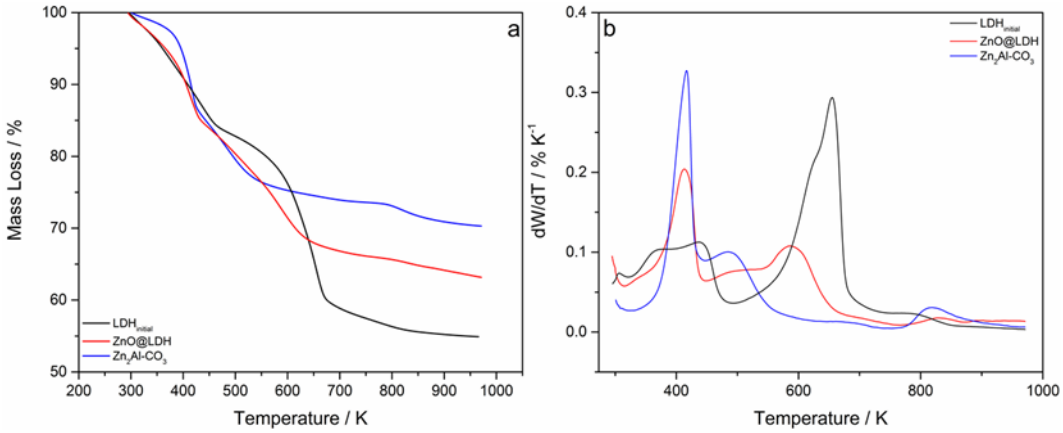


Figure 7.9 Mass loss and derivative mass loss profiles of $LDH_{initial}$ and ZnO@LDH compared with $Zn_2Al\text{-}CO_3$ type LDH

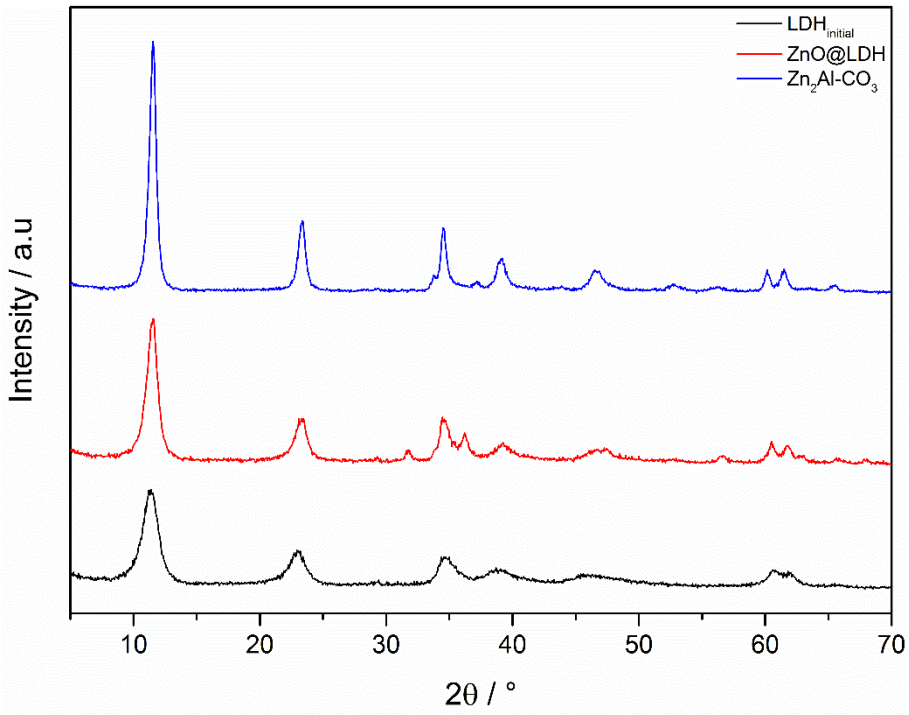


Figure 7.10 X-ray diffractograms of $LDH_{initial}$ ($Mg_2Al\text{-}CO_3$), ZnO@LDH composite and $Zn_2Al\text{-}CO_3$

7.4 Deconvolution of Reactions in the Two-Stage System

The synthesis of the ZnO@LDH composite material is not as simple as it appears, especially when comparing the composite sample with the single phase ZnO and Mg_2Al-

CO_3 ($LDH_{initial}$). There are a number of factors affecting the synthesis of the LDH phase in the composite that are involved in the synthesis of the $LDH_{initial}$ sample. These factors were addressed in a second matrix of experiments that were aimed de-convoluting how they individually impacted the LDH without the presence of the ZnO core. The matrix of experiments is outlined in both Figure 7.11 and Table 7.6.

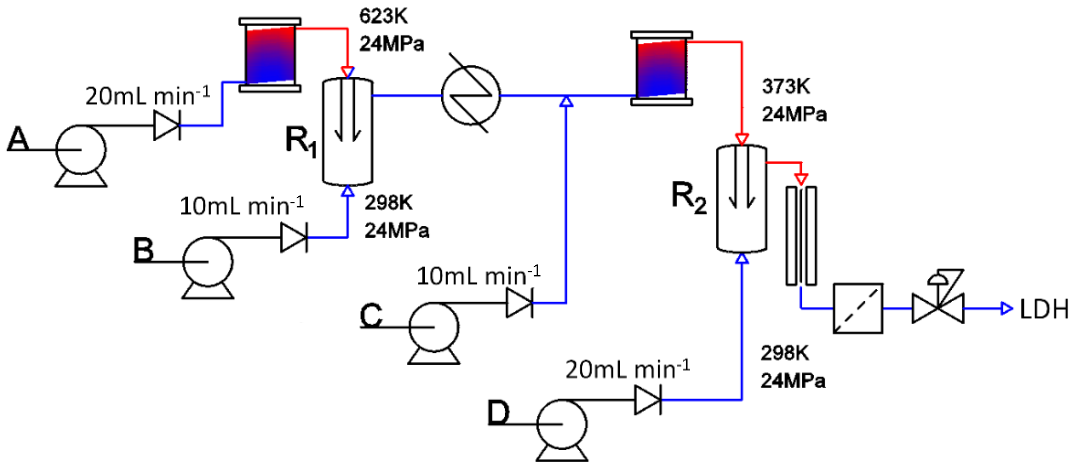


Figure 7.11 Schematic diagram experiments to establish product characteristics of Mg_2Al-CO_3 produced under different conditions in reactor 2 (R_2)

Table 7.6 LDH samples and reaction conditions of deconvolution experiments

Sample	Pump Feed			
	A	B	C	D
LDH_3	H_2O	H_2O	NaOH - 0.25mol L^{-1} Na_2CO_3 - 0.017mol L^{-1}	$Mg(NO_3)_2$ - 0.033mol L^{-1} $Al(NO_3)_3$ - 0.017mol L^{-1}
LDH_4	ZnO Liquor	ZnO Liquor	NaOH - 0.15mol L^{-1} Na_2CO_3 - 0.017mol L^{-1}	$Mg(NO_3)_2$ - 0.033mol L^{-1} $Al(NO_3)_3$ - 0.017mol L^{-1}
LDH_5	H_2O	$NaNO_3$ - 0.05mol L^{-1}	NaOH - 0.15mol L^{-1} Na_2CO_3 - 0.017mol L^{-1}	$Mg(NO_3)_2$ - 0.033mol L^{-1} $Al(NO_3)_3$ - 0.017mol L^{-1}
LDH_6	H_2O	$NaNO_3$ - 0.05mol L^{-1}	NaOH - 0.25mol L^{-1} Na_2CO_3 - 0.017mol L^{-1}	$Mg(NO_3)_2$ - 0.033mol L^{-1} $Al(NO_3)_3$ - 0.017mol L^{-1}
LDH_7	H_2O	$Zn(NO_3)_2$ - 0.003mol L^{-1}	NaOH - 0.15mol L^{-1} Na_2CO_3 - 0.017mol L^{-1}	$Mg(NO_3)_2$ - 0.033mol L^{-1} $Al(NO_3)_3$ - 0.017mol L^{-1}
LDH_8	H_2O	$Zn(NO_3)_2$ - 0.003mol L^{-1}	NaOH - 0.25mol L^{-1} Na_2CO_3 - 0.017mol L^{-1}	$Mg(NO_3)_2$ - 0.033mol L^{-1} $Al(NO_3)_3$ - 0.017mol L^{-1}

The first of the deconvolution experiments were aimed at replicating the LDH synthesis in R_2 compared with the synthesis in R_1. In order to do so, the flow rates, reactor geometry and flow regimes of the subsequent LDH production would need to be similar to that of the composite LDH. There are also the possible effects of residual anions that result in precipitation of other LDH types. The most applicable would be $Zn_2Al\text{-}CO_3$, which is mentioned previously as the mass loss profile of the ZnO@LDH is similar to the thermal mass loss profile of $Zn_2Al\text{-}CO_3$. The residual ions resulting from ZnO synthesis were investigated through the use of reaction liquor from ZnO product from R_1. The effects of residual Zn^{2+} and NO_3^- as individual reacting species were investigated, under varying NaOH concentrations. The NaOH concentration was varied in order to match the synthesis of the individual LDH synthesis in R_2 and the ZnO@LDH synthesis.

7.4.1 Changes to Reaction Flow and Reactor Geometry in LDH Synthesis

The synthesis of LDHs in the two different reactors in the system was investigated following calculations of the Reynolds number in the reactor after mixing. The flow regime in both R_1 and R_2 is laminar (Table 7.7). The Reynolds number is greater in R_2 because the flowrate is double that of the flow in R_1, yet the difference in reactor geometry and tubing size results in a modest increase in Re and the flow regime remains laminar.

Table 7.7 Reynolds number and flow regime of counter reactors

Reactor	Flow rate / mL min^{-1}	Temperature / K	Re	Flow Regime
1	30	373	235	Laminar
2	60	373	297	Laminar

The X-ray diffractograms in Figure 7.12 display similar materials. The crystal domain length of the $LDH_{initial}$ and LDH_3 samples is similar in the ⟨*003*⟩ direction with the CDL calculated from the (*003*) plane equal to 8nm for $LDH_{initial}$ and LDH_3 respectively.

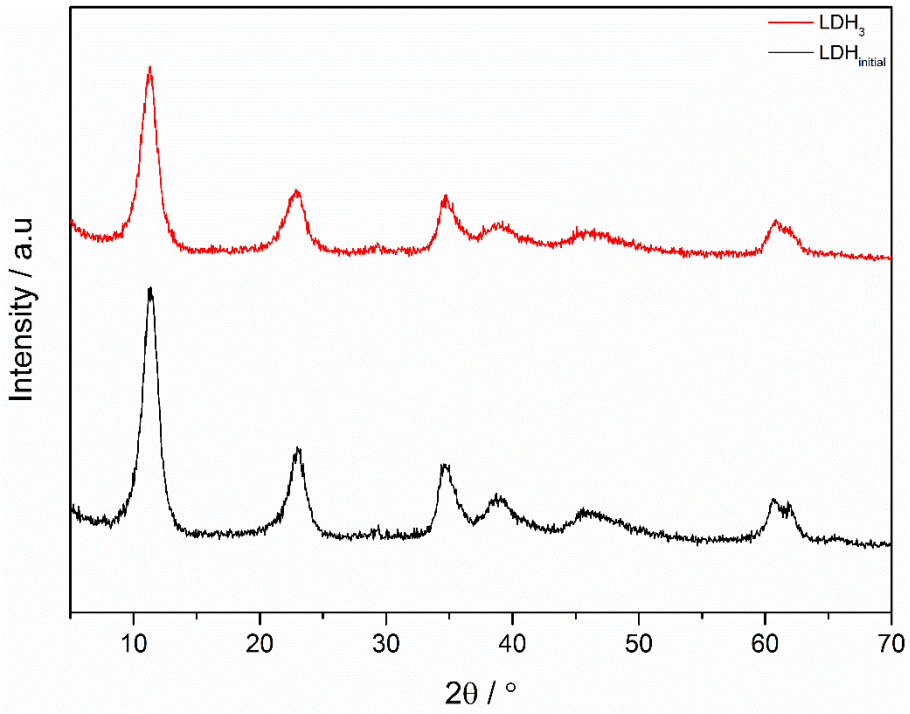


Figure 7.12 Diffractograms for LDHs with different Reynolds numbers in R_1 and R_2

The change in flow regime appears to have affected the surface area of the materials negatively. S_{BET} of LDH_3 is reduced to almost a third of $LDH_{initial}$ (Table 7.8). The cause of such a reduction in specific surface area is unclear. The CDL of the samples is similar at 8nm in the ⟨*003*⟩ plane for both $LDH_{initial}$ and LDH_3.

Table 7.8 S_{BET} and pore characteristics of Mg_2Al-CO_3 synthesised in R_1 and R_2

Sample	Reactor	S_{BET} / $m^2\ g^{-1}$	Pore Diameter / nm	Pore volume / $cm^3\ g^{-1}$
$LDH_{initial}$	R_1	58.2 ± 0.3	3.5	0.07
LDH_3	R_2	20.1 ± 0.1	4.2	0.04

The shape of the nitrogen adsorption isotherms is markedly different between the samples (Figure 7.13). The isotherm of the $LDH_{initial}$ sample is most similar to a Type-IV isotherm with primarily H2 hysteresis, but with some characteristics of H3 [248].This type of H2 hysteresis is more commonly associated with mesoporous silica, where pore-blocking occurs during desorption. The isotherm for LDH_3 however, exhibits a Type-IV shape with H3 hysteresis, which some characteristics of H2 hysteresis [248].

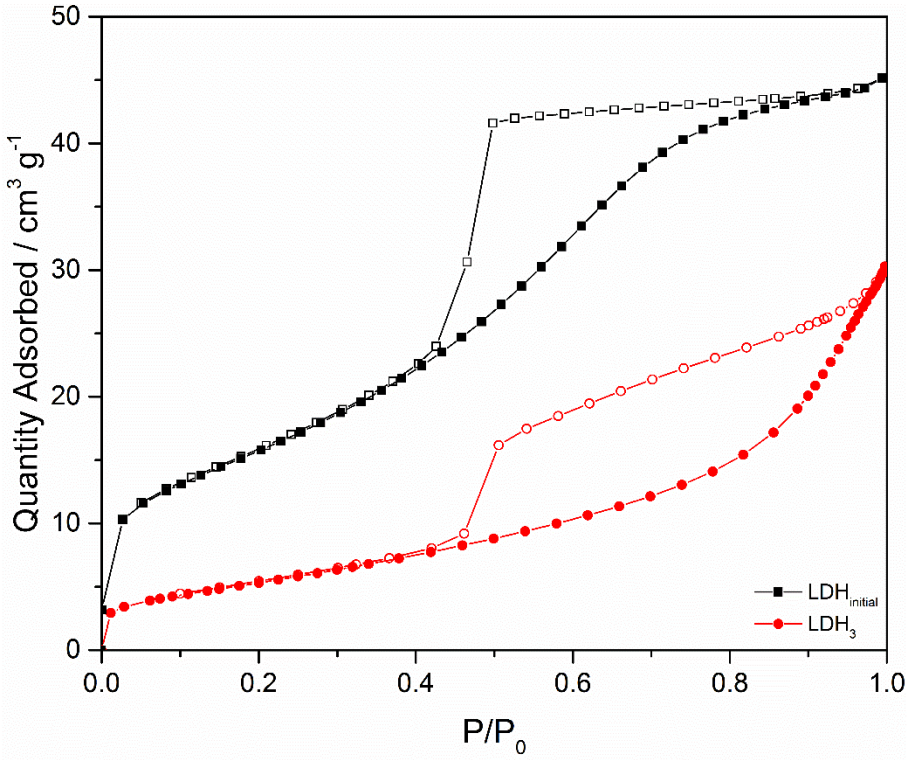


Figure 7.13 Nitrogen adsorption isotherms of LDH samples produced in reactor 1 ($LDH_{initial}$) and reactor 2 (LDH_3)

The adsorption branch at low P/P_0 is similar to a Type-II isotherm however the desorption branch of the isotherm is less steep than H2 hysteresis and is commonly associated with loose agglomerates of platelet-like particles. SEM micrographs of LDH samples produced for comparison of R_1 and R_2, outlined in Figure 7.14, illustrate a

similar morphology between $LDH_{initial}$ and LDH_3. The agglomerates for both materials are micron-sized (Figure 7.14).

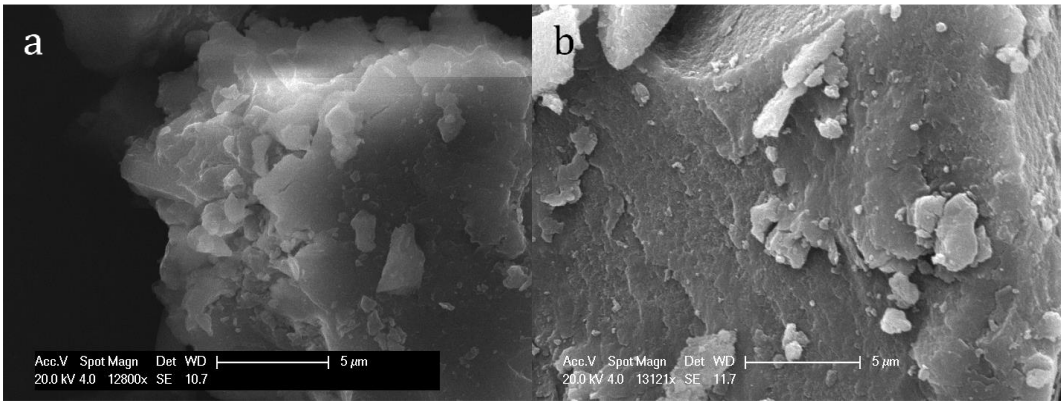


Figure 7.14 SEM micrographs of a) $LDH_{initial}$ and b) LDH_3

7.4.2 Effect of Residual Precursor Ions on LDH Synthesis

ZnO conversion was 94±1% (n=3), which resulted in 72±6mg L^{-1} of Zn entering R_2. There is also the NO_3^- counter ion from the Zn salt in the reaction liquor tin R_2 during ZnO@LDH synthesis. The effect of residual NO_3^- and Zn^{2+} on crystal structure is outlined in (Figure 7.15). Diffraction patterns show decreased crystallinity for samples produced with lower NaOH concentration (LDH_4, LDH_6, and LDH_7).

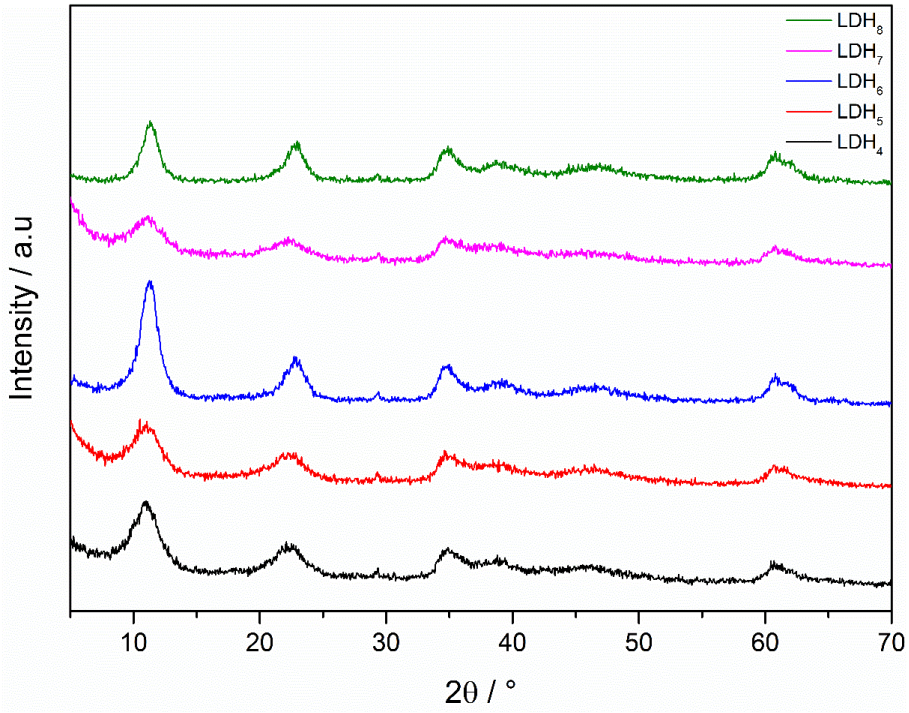


Figure 7.15 Diffraction patterns for isolation experiment LDH samples

The diffraction pattern of LDH_8 is less crystalline that LDH_6, however the relative intensity of reflections compared with the background is larger than the relative intensity of the LDH sample produced with low NaOH levels. The lower NaOH concentration in the LDH synthesis suggests a less crystalline sample. Elemental analysis of the samples by SEM-EDS indicates a significant drop off in the Mg content of the LDH samples produced with low (0.15mol L^{-1}) NaOH concentration (Table 7.9). The major reduction in the Mg content of the brucite-like layers is due primarily to a reduction in $Mg(OH)_2$ precipitation in the LDH as $Mg(OH)_2$ typically precipitates at higher pH ranges than $Al(OH)_3$ and $Zn(OH)_2$ [148] (Figure 7.16).

Table 7.9 Molecular fraction of metals in LDH structures and residual metal content

Sample	LDH Content			
	Mg %	Al %	Zn %	Mg/Al
$LDH_{initial}$	30.30	15.40		1.97
LDH_3	30.19	15.85		1.90
LDH_4	23.42	21.26		1.10
LDH_5	21.22	23.02		0.92
LDH_6	30.88	15.3		2.02
LDH_7	20.25	22.72	1.35	0.89
LDH_8	30.68	14.42	1.3	2.13

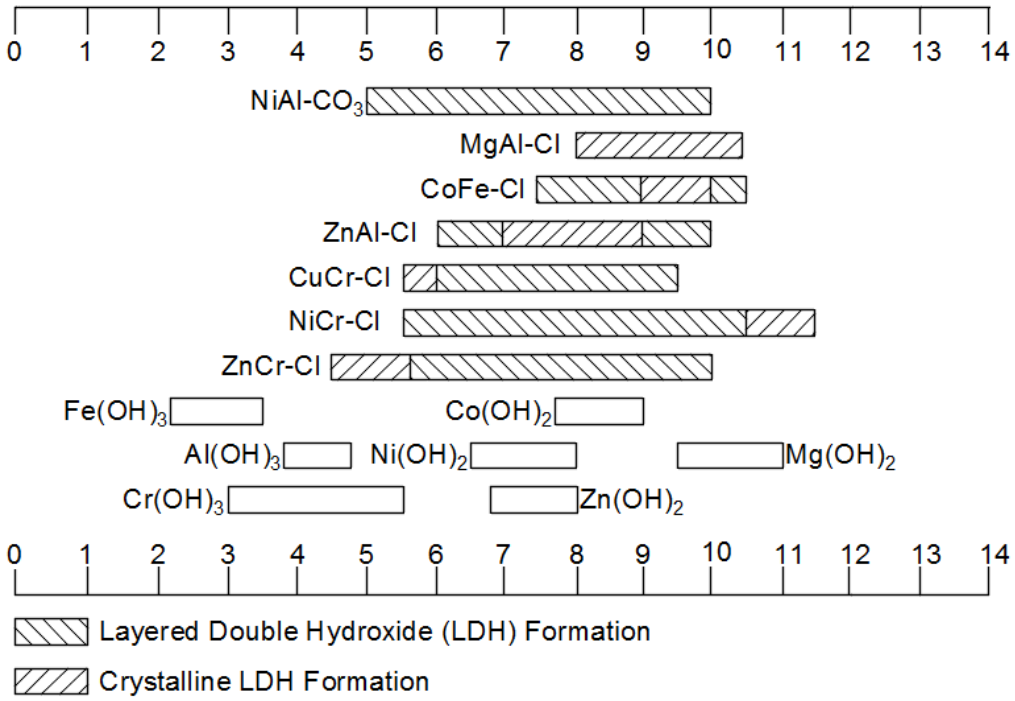


Figure 7.16 pH of Layered double hydroxide (LDH) and metal hydroxide phase precipitation.

Adapted from A. de Roy et al [289] and V. Rives [148]

The excess Al^{3+} causes distortion in the brucite-like sheets due to the imbalances in the electronic charges, as a result of regions of too numerous highly charged Al^{3+} ions located adjacent to each other, and reduced crystallinity. Alternatively; based on the generally accepted idea that LDHs cannot generally form with M^{II}/M^{III} ratios less than 2, approximately, The cause of the reduced crystallinity may be as a result of incomplete precipitation of $Mg(OH)_2$ but excess $Al(OH)_3$. Thus the formation of a mixture of LDH and amorphous $Al(OH)_3$ in the powder. The reduction in the mass fraction of LDH in the powder causes the reduced crystallinity.

Residual Zinc ions appear to have little effect on the crystal structure due to the low feed concentration. This indicates that the ZnO is the primary reason for the formation of the $Zn_2Al\text{-}CO_3$ in the ZnO@LDH composite sample. Nitrate also appears to have no effect on the crystal structure of the samples. Carbonate ions will preferentially form in the interlayer region due to the higher charge density [102], therefore regardless of the NO_3^- concentration, no changes will be observed.

The surface area and morphology of LDHs appear to be unaffected by residual Zn^{2+} or NO_3^- from the simulated ZnO synthesis, but by the concentration of NaOH resulting from the first reaction stage. It can clearly be seen in Table 7.10; samples produced with higher concentration of NaOH (LDH_6 and LDH_8) exhibit a similar S_{BET} to LDH_3. The lower NaOH concentration applied in the synthesis of LDH_4, LDH_5 and LDH_7 results in materials with significantly higher surface area.

Table 7.10 Surface are (S_{BET}) and pore size for samples isolating residual ions from ZnO synthesis

Sample	NaOH / mol L^{-1}	S_{BET} / m^2 g^{-1}	Pore Diameter / nm	Pore volume / cm^3 g^{-1}
LDH_4	0.15	266.82 ± 0.43	16.85	1.36
LDH_5	0.15	270.16 ± 0.52	15.87	1.29
LDH_6	0.25	22.60 ± 0.11	3.89	0.06
LDH_7	0.15	271.68 ± 0.49	14.55	1.20
LDH_8	0.25	26.07 ± 0.17	4.42	0.05

The adsorption isotherms for the LDH samples are all Type-IV (Figure 7.17). In the isotherms of samples LDH_6 and LDH_8, H3 hysteresis is prevalent in samples, whereas a closer resemblance to a combination of H1 and H3 hysteresis is observed in samples LDH_5 and LDH_7. The difference in isotherm and hysteresis shape between samples produced with high and low NaOH in the down-flow feed is also illustrated in SEM micrographs

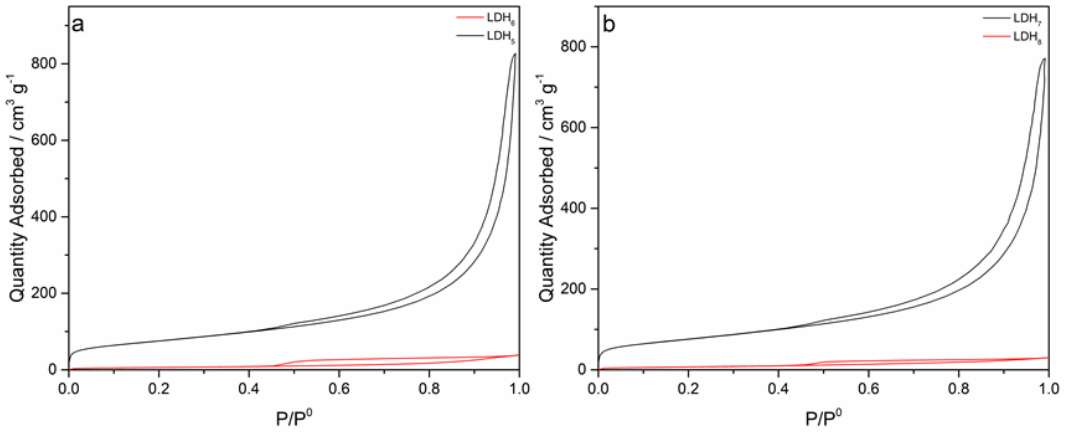


Figure 7.17 Nitrogen adsorption isotherms of LDH samples produced with 0.15mol L^{-1} and 0.25mol L^{-1} NaOH for residual a) Zn^{2+} b) NO_3^-

Figure 7.18 outlines, as an example, the distinct differences in the features of the samples produced with low (LDH_5) and high (LDH_6) NaOH. The LDH_5 sample in Figure 7.18a

displays a fragmented structure consisting of small agglomerates with more gaps between them and the packing of finer particles appears to be looser. The structure of these particles is similar to ZnO, which gives rise to the ink-bottle pore shape and the H1 and H3 hysteresis present in Figure 7.13. In contrast, LDH_6 has a more typical structure seen from the continuous synthesis of $Mg_2Al\text{-}CO_3$ LDHs. Agglomeration and stacking produced block-like structures of large sheets which gives rise to the H3 hysteresis loop present in the Type-VI adsorption isotherms. The fragmented and loose particles generated the exceptional surface areas and larger pore volumes demonstrated by samples produced with 0.15mol l^{-1} NaOH, compared to the LDHs produced at higher NaOH concentrations (0.25mol L^{-1}).

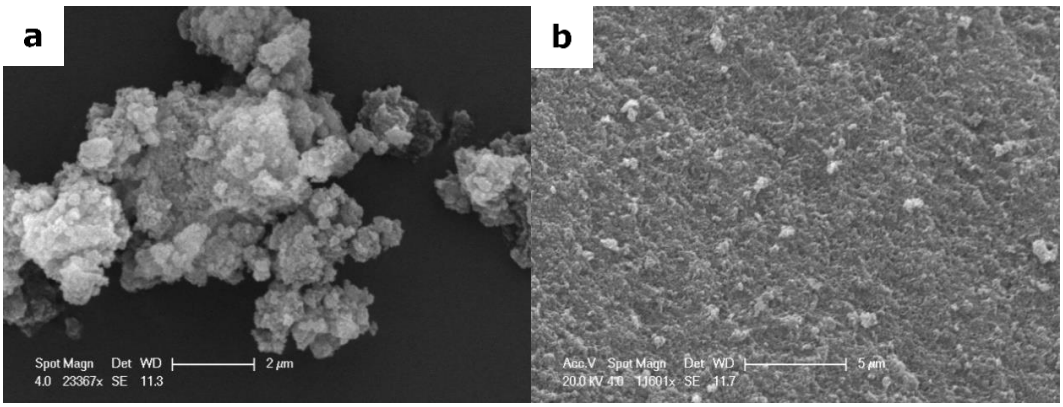


Figure 7.18 SEM micrographs of displaying structural the difference between LDH_5 and LDH_6

Thermal analysis of the LDH samples indicated that there was a difference in thermal stability when the M^{II}/M^{III} ratio becomes disrupted as in samples LDH_4, LDH_5 and LDH_7. Mass loss due to the breakdown of the layered structure occurs between 573K and 673K for samples LDH_6 and LDH_8, mirroring the same mass loss and derivative mass loss profiles of $LDH_{initial}$ (Figure 7.19). Samples produced with low NaOH start to break down below 573K. Water loss is also a much more rapid process occurring typically <373K for LDH_4, LDH_5 and LDH_7.

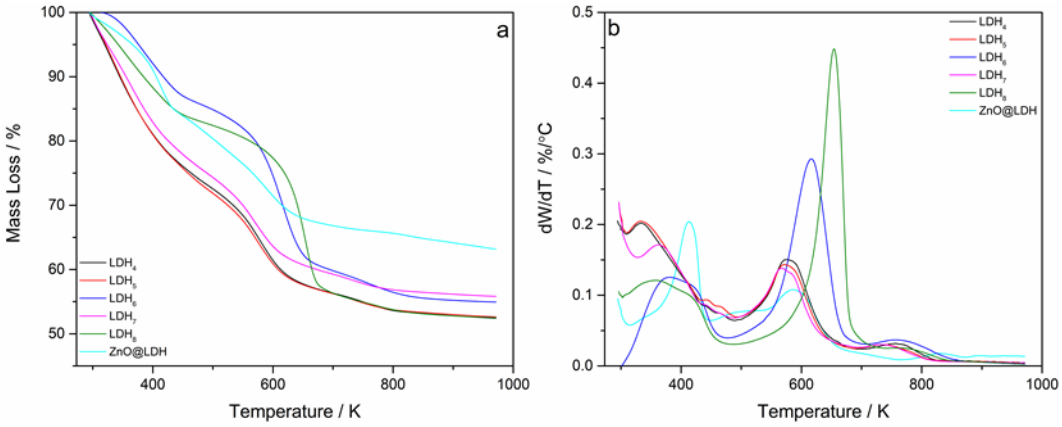


Figure 7.19 Mass loss profile of LDHs produced to isolate precursor effect

The changes in thermal stability are due to the disruption of the layers, caused by the changes in M^{II}/M^{III} ratio, and the possible presence of some amorphous $Al(OH)_3$ in the sample, which contributed to the mass loss structure of the sample. The derivative mass loss profiles of the isolated LDH samples do not exactly match that of ZnO@LDH. The major mass loss below 573K is present in the profiles of both the isolation samples and the ZnO@LDH.

The derivative mass loss from the $Zn_2Al\text{-}CO_3$ is not present in the isolation samples. This is a clear indication that the presence of the zinc oxide in ZnO@LDH, participates in the synthesis of $Zn_2Al\text{-}CO_3$ LDHs in the composite through dissolution and re-precipitation.

7.5 Summary

The results obtained from this research suggest that a one-step continuous synthesis of core-shell ZnO@LDH composite materials has been achieved. However, a single phase $Mg_2Al\text{-}CO_3$ phase in the composite material has not been synthesised. The mass fraction of LDH in the composite material is approximately 0.77 from thermal analysis. The LDH

material in the composite however, is likely to contain a mixture of $Mg_2Al\text{-}CO_3$, $Zn_2Al\text{-}Co_3$ and some $Al(OH)_3$ as a result of variable precipitation rates of the metal hydroxides. The relative Mg/Al ratio of ZnO@LDH is reduced to 1.3 from 1.97 in $LDH_{initial}$. This change is due a combination of factors. Reduced NaOH in the second reactor hinders $Mg(OH)_2$ formation skewing M^{II}/M^{III} ratio, contribution to the possible formation of $Al(OH)_3$.

The presence of ZnO also influenced the formation of $Zn_2Al\text{-}CO_3$ LDH formation. The nitrogen adsorption isotherm displayed by the ZnO@LDH composite material is markedly different from the dry-mixed sample, which has an adsorption isotherm that resembles the individual isotherms of both $LDH_{initial}$ and ZnO. The CDL of ZnO and ZnO@LDH are 25nm and 42nm in the ⟨*112*⟩ plane, respectively. The change in crystal size of ZnO is likely due to some dissolution and re-precipitation of ZnO from smaller elliptical particles into larger rod-shaped particles and some further precipitation and dehydration of residual Zn^{2+} ions.

The surface area of ZnO@LDH is higher than that of the single-phase powders, owing to the difference in the stacking arrangement of the between the single phase LDH and the LDH phase in the ZnO@LDH composite material. The open, 'flower-like' pattern of LDH in the composite material may allow for a better adsorption capacity or adsorption rate compared to the single phase LDH. However, when single phase $Mg_2Al\text{-}CO_3$ LDHs are synthesised at lower NaOH concentration ($OH^-/M^{II}+M^{III}=1.5$); S_{BET} increases by an order of magnitude, to above $250 m^2\ g^{-1}$ regardless of counter ions present. The distortion of layers in the synthesis of LDHs at lower NaOH concentration ($0.15 mol\ L^{-1}$) produced more loosely packed and fragmented powders where pore volume is 20 times greater. The presence of the fragmented structure of the LDH and the presence of amorphous

$Al(OH)_3$ may also contribute to the surface area recorded for the ZnO@LDH and the LDH samples produced with low NaOH concentration.

The continuous synthesis of core-shell composites requires a significant amount of work to fine tune the synthesis conditions to ensure a single phase core and a single phase LDH that are bound through electrostatic attractions to ensure a complete composite synthesis.

8. Conclusions and Recommendations for Further Research

8.1 Summary of Research and Conclusions

8.1.1 Synthesis and Characterisation of LDHs

Synthesis of $Ca_2Al\text{-}NO_3$ and $Zn_2Al\text{-}NO_3$ LDHs was achieved in a counter-current continuous flow reactor. The synthesis of $Ca_2Al\text{-}NO_3$ highlighted the impact of primary reaction variables on the final LDH product. These variables were temperature, pressure and initial NaOH concentration. The effect of these three variables were found to impact on the precipitation of the $Ca_2Al\text{-}NO_3$ LDH samples.

Temperature and pressure impact on the density of the reacting solutions, and therefore the flow rate through the reactor; as well as affecting the reaction itself by driving reactions through increased rates of nucleation and growth. Pressure and temperature are intimately affected by each other. As temperature increases the control over crystal domain length (CDL), through pressure alteration is reduced. This occurs predominantly in the ⟨*002*⟩ crystal plane, while the CDL in the ⟨*030*⟩ crystal plane is more variable across pressures and temperatures between 348K -473K. The changes to CDL arising from the modification of reaction parameters, causes an insignificant change to the low surface area (4m-7m^2 g^{-1}) in the $Ca_2Al\text{-}NO_3$ samples. The changes in temperature, pressure and sodium hydroxide concentration also appear to have little effect on the size of LDH platelets, and there are no decisive trends observed as the mean platelet size ranges from 3-5μm and with the modal diameter equal to 3μm.

The initial NaOH concentration primarily affects nucleation rates as some research as identified, in high supersaturation co-precipitation, smaller crystals form due to the initially high base and therefore rapid nucleation without sustain growth. The highest concentration of NaOH investigated was 1mol L^{-1}. This NaOH concentration in the precursor solution produced LDHs with crystal domain lengths (CDL) measuring of 27nm and 60nm, as calculated from the (*002*) and (*030*) reflections respectively. For samples produced with 0.125M NaOH in the down-flow feed the CDL increases to 53nm and 92nm from the (*002*) and (*030*) reflections respectively. The reducing NaOH causes a shift in prominence of nucleation to growth which is understood to follow a similar pattern as the change from high supersaturation co-precipitation to low supersaturation co-precipitation, where the presence of OH^- is more controlled. The most significant change observed through the manipulation of sodium hydroxide, was the production of $Ca(OH)_2$ and $CaCO_3$. The calcium impurities were the consequence of the excess OH^-, and excess Ca^{2+} in the metal salt feed due to imbalanced M^{II} and M^{III} ions in the precursor solution. These impurities affected the thermal stability and chemical composition of the final LDH powder however the effect on surface area appeared to be minimal

The synthesis of $Zn_2Al\text{-}CO_3$ the initial work into the potential for scaled up synthesis of LDH nanomaterials in continuous modes. Following on from the lack of variability in the characteristics of $Ca_2Al\text{-}NO_3$ LDHs, only one set of reaction conditions was used. The S_{BET} of $Zn_2Al\text{-}CO_3$ was greater than that obtained for $Ca_2Al\text{-}NO_3$. The $Zn_2Al\text{-}CO_3$ material exhibited CDL estimations of 26nm in the ⟨*003*⟩. Platelet size was 120±53nm. The larger platelets in the $Ca_2Al\text{-}NO_3$ are the main contributor that causes the lower surface area in the LDH samples.

The reaction temperature has the greatest impact on continuous hydrothermal LDH synthesis in a broad sense, as high temperatures make the reaction susceptible to metal

oxide synthesis. A combination of temperature and pressure had little impact on bulk material characteristics like surface area and particle size. The impact is on the finer crystal characteristics where the growth and nucleation rates are altered based on manipulation as the temperature and pressure increase the rate of reaction and residence time reduce growth but promote nucleation rates. The precipitation of Ca_2Al-NO_3 was found to be affected by NaOH concentration, and a slight excess of NaOH was found to be optimal in preventing impurity formation while also promoting sufficient nucleation and growth of crystals.

8.1.2 Scale Up of LDH Synthesis

Zn_2Al-CO_3 LDH materials produced by continuous flow synthesis at bench (flow rate=30mL min^{-1}) pilot (flow rate=600mL min^{-1}) and industrial scale (1050L h^{-1}) have been investigated for a variety of material characteristics. The crystal structure of the materials remains similar with differences in CDL. The bench scale sample (B-LDH) shows smaller CDL in both crystal planes compared to the pilot scale (P-LDH) with CDL in the (*003*) plane at 18nm and 26nm for B-LDH and P-LDH respectively, where as the industrial scale LDH (I-LDH) is similar to the bench scale sample. The crystal domain length of the I-LDH was 19±0nm in the ⟨*003*⟩ plane. This change in CDL suggests that a settling period during the P-LDH synthesis process caused the increase observed.

Average platelet size of P-LDH was 177±70nm while the B-LDH was 120±53nm and I-LDH was 165±54nm. The surface area corresponding to each sample was between 50 and 65m^2 g^{-1}. With the industrial scale Zn_2Al-CO_3 sample exhibiting the largest S_{BET} (64.1±0.2m^2 g^{-1}). The larger platelet size of the pilot and industrial samples appears to have a differing impact on surface area and the changes to flow regime during industrial

scale crystallisation may have an effect on the stacking of particles and subsequent surface areas.

8.1.3 Adsorption of reactive Dyes on Calcined LDHs

Adsorption of two types of reactive dye, Reactive Orange 16 (RO16) and Reactive Black 5 (RB5) was investigated. The experiments aimed to identify the applicability of continuously produced Zn_2Al-CO_3 as adsorbents for wastewater remediation.

Calcined Zn_2Al-CO_3 (MMO) adsorbents were assessed for the effectiveness of remediation of RO16 and RB5 in water. Storage in air caused no change to the MMO diffractogram. However, storage in deionised water results in the slow regeneration of the carbonate intercalated Zn_2Al-CO_3 LDH over 6 weeks. This indicates that over prolonged periods of time, CO_2 will dissolve and impact on the MMO causing LDH regeneration and reduction in adsorption capacity. Characterisation of adsorbents, after adsorption, indicates that intercalation of dye molecules is the primary method of adsorption. The intercalation causes the regeneration of the original LDH structure through the memory effect, however the CO_3^{2-} intercalated anion is replaced by the anionic dye molecules, and subsequently swollen interlayer regions

The Langmuir isotherm model indicated that maximum adsorption capacity (q_m), of RO16 (895mg L^{-1}) was higher than RB5 (589mg L^{-1}). This phenomenon is ascribed to the size of the dye molecules and the number of R-SO_3Na functional groups present. Reactive Black 5 has more sulfonate functional groups, and a greater anionic charge resulted in lower amounts being intercalated. The lowest maximum adsorption capacity of RB5 onto Zn_2Al based MMO is greater than most other adsorbents found in published literature, indicating that MMO adsorbents are more applicable than some current remediation methods, based on adsorption capacity.

Addition of competing anions (CO_3^{2-}, SO_4^{2-}, Cl) was found to impact to varying degrees depending on the auxiliary anion in solution. Sodium carbonate had a greater impact than Na_2SO_4 and NaCl. Chloride ions had a negligible effect on adsorption of RB5 and RO16. Carbonate concentration was significant enough at 1g L^{-1} (Na_2CO_3) to reduce adsorption capacity (q_e), and at 10g L^{-1} q_e was reduced to 91±68mg g^{-1} for RB5 and 25±50mg g^{-1} for RO16. The presence of $Na_2CO_3^{2-}$ in particular was problematic because of the high charge density and affinity for intercalation of the carbonate ion.

Thermal regeneration reduced q_e after the first adsorption-regeneration cycle due to residual sulfur and carbonaceous material left in the interlayer region after previous cycles. Washing with Na_2CO_3 was found to mitigate the declining adsorption capacity and aid in dye recovery. More appropriate processes for adsorption-regeneration are needed, as the poor recyclability of the MMO is impractical in spite of the high adsorption capacity.

Adsorption kinetics analysis indicated that the adsorption was best modelled by pseudo 2nd order kinetics. The rate constant increased with higher adsorption temperatures. The intra-particle diffusion model suggests multi-stage adsorption where at higher temperature, ≥293K for RO16 and ≥303K for RB5, intra-particle diffusion and the reformation of the interlayer region the rate is limiting step. At low temperature the film diffusion and surface adsorption is the rate limiting step. Thermodynamic analysis indicated that the adsorption process was spontaneous and chemisorption was the main mode of adsorption, with the intercalation of dye molecules.

The Yoon-Nelson and Thomas models follow a similar linear equation and so generate similar fits for the data. The time to reach 50% breakthrough (τ), was adequately modelled by the Yoon-Nelson equation from the experimental data for dye flowrates of

1.9mL min^{-1} and 3.7mL min^{-1}. The lowest flowrate investigated however, yielded a τ_{cal} (38 minutes) that was equal to half of the τ_{exp} (80 minutes). The Thomas model allows the calculation of the maximum uptake capacity (q_{TH}). The Thomas model uptake capacity is comparable with the equilibrium uptake capacity calculated from the integration of the breakthrough curves (q_{eq}) each were approximately 7mg g^{-1}. The dramatic decrease from 570mg g^{-1} in the batch adsorption compared to the q_{eq} value in column adsorption is attributed to a number of factors. The slow adsorption kinetics, outlined and low EBCT are the main cause of the poor adsorption and modelling of breakthrough curve models. The addition of polymer binder also impacted on the expansion of the layers inhibiting intercalation of the dye molecules. poly(methyl methacrylate) is also hydrophobic, and its presence in the granules will reduce the adsorbent-solute interface and contribute to reduced adsorption. Improved methods for generating column adsorption media area required for further experiments on column adsorption in order to mitigate adsorption decreases between batch and continuous adsorption modes.

8.1.4 Continuous Synthesis of Zinc Oxide@LDH Composites

Continuous synthesis of core-shell ZnO@LDH composite materials was carried out in a two-stage reactor system. A pure Mg_2Al-CO_3 phase in the composite material has not been synthesised, however electron micrographs imply that in areas of localised high pH, the zeta potential of ZnO is negative and the formation of ZnO@LDH composites through electro static attractions did occur.

Thermal analysis indicated that the mass fraction of LDH in the composite material is approximately 0.77, yet the differential mass loss profile matches both Mg_2Al-CO_3 as well as Zn_2Al-CO_3. The relative Mg/Al ratio of ZnO@LDH is reduced to 1.3 from 1.97 in Mg_2Al-

CO_3. This change is due a combination of factors. Reduced NaOH in the second reactor hinders $Mg(OH)_2$ formation, as $Al(OH)_3$ may be produced due to lower NaOH in the reaction, which skewed M^{II}/M^{III} ratio. The presence of ZnO also influences the formation of $Zn_2Al\text{-}CO_3$ LDH formation. Surface area of the ZnO@LDH composite was greater than the single-phase powders, owing to flower like stacking arrangements in the composite.

Single phase $Mg_2Al\text{-}CO_3$ LDHs are synthesised at lower NaOH concentration ($OH^-/M^{II}+M^{III}=1.5$); S_{BET} increases by an order of magnitude, to above $250 m^2\ g^{-1}$. The distortion of layers at lower pH, due to the presence of excess $Al(OH)_3$, produced more loosely packed and fragmented agglomerates where the pore volume was 20 times greater than in standard $Mg_2Al\text{-}CO_3$ LDHs, produced by continuous hydrothermal synthesis. More work is required to optimise the synthesis process, to better coverage of the core with LDH platelets. Work to ensure single phase LDH shells and electrostatic attractions as the method of composite formation are also necessary. Further work on the synthesis of LDHs with varying M^{II}/M^{III} ratios should also be explored in order to maximise the potential for high surface area LDHs.

8.2 Recommendations for Further Research

8.2.1 Continuous Synthesis of Layered Double Hydroxides

The focus of this research was to progress the work that has currently been completed in LDH synthesis; to better understand the controlling variables in the continuous synthesis of LDHs. With improved understanding, synthesis procedures can be progressed from bench scale to reliable industrial scale synthesis. The future of research in this area would likely be to establish a catalogue of LDHs with varying properties than can be effortlessly produced in a continuous mode. Work on LDHs as battery materials

(Ni-Co), photocatalysts (ZnCr-CO_3/ZnTi-CO_3) and as drug delivery devices may benefit from increased LDH availability. A simple rapid approach to synthesis of the LDH materials could be the next steps towards making LDHs a more reliable resource.

Further research on LDH synthesis in pilot and industrial scale reactions, on Zn_2Al-CO_3 and LDHs such as NiCo-CO_3 or ZnTi-CO_3, would be ideal to establish a catalogue of LDHs that can be rapidly produced and processed at industrial scale for more varied applications.

8.2.2 Layered Double Hydroxide Based Adsorbents for Dye Remediation

The work focussing on LDHs as adsorbents was aimed at identifying the capability of LDHs to remove reactive dyes as well as the well documented use of LDHs to remove acidic dyes such as methyl orange (Acid Orange 52). From literature searches there is a significant catalogue of LDH materials from Mg-Al-CO_3 to more exotic ternary LDHs including ZnAlCe and ZnCuAl MgNiAl. The large number of LDHs coupled with a vast range of prospective dyes means that the research in this can be circular; with new LDHs being used on the same dyes or new dyes being adsorbed by the same LDHs. Worthwhile future research will need to utilise industrial dyebath effluent. Water quality analysis will help to identify many of the properties of the wastewater prior to adsorption experimentation. The impact that non-deionised water, salts, organic and heavy metal compounds have on adsorption can be identified, and comparisons against current commercial wastewater remediation methods can be drawn.

An equally important aspect of this area of research is to develop a suitable means of regeneration of the exhausted LDH. The results of regeneration in this research were not favourable for recycling of the adsorbent due to significant reductions in dye removal following regeneration. Recovery of dye rather than destruction would likely be

preferable as resources from waste is a key aspect of waste management. The usefulness of the recovered dye compounds, and the cost benefit compared with destruction, would also need to be assessed.

The final aspect of furthering the research of LDHs as absorbents is to develop a process whereby the LDH materials can be produced or modified into a granular material to allow column adsorption to be completed successfully. The principle issue with the granulation of the calcined $Zn_2Al\text{-}CO_3$ and mix metal oxides was the use of PMMA binder. Most generation methods for LDHs require heating to several hundred degrees Celsius this would melt the binder and likely destroy the granules. There is also a concern that the granulation by polymer binding caused a significant reduction in adsorption capacity and as a result reduced the effectiveness of an excellent powder adsorbent. In-situ growth onto silica beads may provide a solution to this issue, however the continuous growth of LDHs on millimetre scale SiO_2 would be difficult in a continuous mode where pumps and piping is design to handle liquids and colloidal suspensions of nanoparticles. Alternatively, the use of inorganic binders for granulation, may be more beneficial as the thermal stability of many inorganic binders is greater than LDH activation temperatures, and the hydrophobic nature of PMMA will also be mitigated.

8.2.3 Layered Double Hydroxide Composite Materials

Furthering the continuous growth of LDHs onto support materials to enhance the properties of both the LDH and the support is the most difficult aspect of progressing the research in this body of work. Establishing the way in which growth occurs on the support and ensuring that the ratio of core to LDH shell is challenging. There is generally a non-uniform surface for growth and nanoparticle shape and size will impact on the growth of LDHs in-situ. Ratios with excess LDH would render the material useless as

there would be too much of the shell material that would negate the purpose of the core-shell composite. Like-wise, if the core material is in excess the properties of the LDH part of the composite would be lessened.

Further research would likely require a significant amount of experimental work to elucidate the growth patterns of LDHs under different conditions for both core and shell synthesis. Finally the furthering of this research would be to identify new core-shell combinations that possess properties such as enhanced photocatalytic potential, enhanced surface area or electrochemical capacity.

References

[1] F. Cavani, F. Trifiro, A. Vaccari, Hydrotalcite-type Anionic Clays: Preparation, Properties and Applications, Catalysis Today 11(2) (1991) 173-301.

[2] R. Xu, W. Pang, Q. Huo, Modern Inorganic Synthetic Chemistry, Modern Inorganic Synthetic Chemistry (2011) 1-590.

[3] S. Miyata, A. Okada, Synthesis of Hydrotalcite-Like Compounds and their Physicochemical Properties - Systems Mg^{2+}-Al^{3+}-SO_4^{2-} and Mg^{2+}-Al^{3+}-CrO_4^{-}, Clays and Clay Minerals 25(1) (1977) 14-18.

[4] S. Miyata, Physico-chemical Properties of Synthetic Hydrotalcites in Relation to Composition, Clays Clay Miner 28(1) (1980) 50-56.

[5] M.A. Gonzalez, I. Pavlovic, R. Rojas-Delgado, C. Barriga, Removal of Cu^{2+}, Pb^{2+} and Cd^{2+} by layered double hydroxide-humate hybrid. Sorbate and sorbent comparative studies, Chemical Engineering Journal 254 (2014) 605-611.

[6] M.A. Gonzalez, I. Pavlovic, C. Barriga, Cu(II), Pb(II) and Cd(II) sorption on different layered double hydroxides. A kinetic and thermodynamic study and competing factors, Chemical Engineering Journal 269 (2015) 221-228.

[7] K. Grover, S. Komarneni, H. Katsuki, Uptake of arsenite by synthetic layered double hydroxides, Water Research 43(15) (2009) 3884-3890.

[8] S. Miyata, T. Kumura, H. Hattori, K. Tanabe, Physico-chemical Properties and Structure of Magnesia-alumina, Nippon Kagaku Zassi 92(6) (1971) 514-519.

[9] S.M. Auerbach, K.A. Carrado, P.K. Dutta, Handbook of layered materials, M. Dekker, New York, 2004.

[10] Q. Wang, S. Tang, E. Lester, D. O'Hare, Synthesis of ultrafine layered double hydroxide (LDHs) nanoplates using a continuous-flow hydrothermal reactor, Nanoscale 5(1) (2013) 114-117.

[11] P.W. Dunne, C.L. Starkey, A.S. Munn, S.V.Y. Tang, O. Luebben, I. Shvets, A.G. Ryder, Y. Casamayou-Boucau, L. Morrison, E.H. Lester, Bench- and pilot-scale continuous-flow hydrothermal production of barium strontium titanate nanopowders, Chemical Engineering Journal 289 (2016) 433-441.

[12] P.W. Dunne, A.S. Munn, C.L. Starkey, T.A. Huddle, E.H. Lester, Continuous-flow hydrothermal synthesis for the production of inorganic nanomaterials, Philosophical Transactions of the Royal Society A-Mathematical Physical and Engineering Sciences 373(2057) (2015) 21.

[13] I.A. Alaton, I.A. Balcioglu, D.W. Bahnemann, Advanced oxidation of a reactive dyebath effluent: comparison of O_3, H_2O_2/UV-C and TiO_2/UV-A processes, Water Research 36(5) (2002) 1143-1154.

[14] N. Daneshvar, D. Salari, A.R. Khataee, Photocatalytic degradation of azo dye acid red 14 in water: investigation of the effect of operational parameters, Journal of Photochemistry and Photobiology a-Chemistry 157(1) (2003) 111-116.

[15] P.K. Malik, Use of activated carbons prepared from sawdust and rice-husk for adsorption of acid dyes: a case study of Acid Yellow 36, Dyes and Pigments 56(3) (2003) 239-249.

[16] N. Daneshvar, D. Salari, A.R. Khataee, Photocatalytic degradation of azo dye acid red 14 in water on ZnO as an alternative catalyst to TiO_2, Journal of Photochemistry and Photobiology a-Chemistry 162(2-3) (2004) 317-322.

[17] G. Tchobanoglous, H.D. Stensel, R. Tsuchihashi, F.L. Burton, M. Abu-Orf, G. Bowden, W. Pfrang, Metcalf & Eddy, Wastewater engineering : treatment and resource recovery, Fifth edition / ed., McGraw-Hill Education, New York, NY, 2014.

[18] P. Kanekar, S. Sarnaik, An Activated-Sludge Process To Reduce the Pollution Load of a Dye-Industry Waste, Environmental Pollution 70(1) (1991) 27-33.

[19] G.M. Walker, L.R. Weatherley, Adsorption of acid dyes on to granular activated carbon in fixed beds, Water Research 31(8) (1997) 2093-2101.

[20] M.F.R. Pereira, S.F. Soares, J.J.M. Orfao, J.L. Figueiredo, Adsorption of dyes on activated carbons: influence of surface chemical groups, Carbon 41(4) (2003) 811-821.

[21] V. Dulman, C. Simion, A. Barsanescu, I. Bunia, V. Neagu, Adsorption of Anionic Textile Dye Acid Green 9 from Aqueous Solution onto Weak or Strong Base Anion Exchangers, Journal of Applied Polymer Science 113(1) (2009) 615-627.

[22] M. Wawrzkiewicz, Removal of CI Basic Blue 3 dye by sorption onto cation exchange resin, functionalized and non-functionalized polymeric sorbents from aqueous solutions and wastewaters, Chemical Engineering Journal 217 (2013) 414-425.

[23] R. Jiraratananon, A. Sungpet, P. Luangsowan, Performance evaluation of nanofiltration membranes for treatment of effluents containing reactive dye and salt, Desalination 130(2) (2000) 177-183.

[24] I. Koyuncu, Reactive dye removal in dye/salt mixtures by nanofiltration membranes containing vinylsulphone dyes: Effects of feed concentration and cross flow velocity, Desalination 143(3) (2002) 243-253.

[25] C. Peng, J. Dai, J.Y. Yu, J. Yin, Calcined Mg-Fe layered double hydroxide as an absorber for the removal of methyl orange, Aip Advances 5(5) (2015) 057138-1-13.

[26] H. Zaghouane-Boudiaf, M. Boutahala, L. Arab, Removal of methyl orange from aqueous solution by uncalcined and calcined MgNiAl layered double hydroxides (LDHs), Chemical Engineering Journal 187 (2012) 142-149.

[27] P. Zhang, G.R. Qian, H.S. Shi, X.X. Ruan, J. Yang, R.L. Frost, Mechanism of interaction of hydrocalumites (Ca/Al-LDH) with methyl orange and acidic scarlet GR, Journal of Colloid and Interface Science 365(1) (2012) 110-116.

[28] K. Morimoto, K. Tamura, N. Iyi, J.H. Ye, H. Yamada, Adsorption and photodegradation properties of anionic dyes by layered double hydroxides, Journal of Physics and Chemistry of Solids 72(9) (2011) 1037-1045.

[29] C.G. Silva, Y. Bouizi, V. Fornes, H. Garcia, Layered Double Hydroxides as Highly Efficient Photocatalysts for Visible Light Oxygen Generation from Water, Journal of the American Chemical Society 131(38) (2009) 13833-13839.

[30] M.F. Shao, J.B. Han, M. Wei, D.G. Evans, X. Duan, The synthesis of hierarchical Zn-Ti layered double hydroxide for efficient visible-light photocatalysis, Chemical Engineering Journal 168(2) (2011) 519-524.

[31] S.J. Xia, F.X. Liu, Z.M. Ni, J.L. Xue, P.P. Qian, Layered double hydroxides as efficient photocatalysts for visible-light degradation of Rhodamine B, Journal of Colloid and Interface Science 405 (2013) 195-200.

[32] S. Kandula, P. Jeevanandam, Synthesis of Silica@Ni-Co Mixed Metal Oxide Core-Shell Nanorattles and Their Potential Use as Effective Adsorbents for Waste Water Treatment, European Journal of Inorganic Chemistry (25) (2015) 4260-4274.

[33] Y. Lin, Z.K. Zeng, J.R. Zhu, Y. Wei, S. Chen, X. Yuan, L. Liu, Facile synthesis of ZnAl-layered double hydroxide microspheres with core-shell structure and their enhanced adsorption capability, Materials Letters 156 (2015) 169-172.

[34] Y. Al-Degs, M.A.M. Khraisheh, S.J. Allen, M.N. Ahmad, Effect of carbon surface chemistry on the removal of reactive dyes from textile effluent, Water Research 34(3) (2000) 927-935.

[35] N. Kannan, M.M. Sundaram, Kinetics and mechanism of removal of methylene blue by adsorption on various carbons - a comparative study, Dyes and Pigments 51(1) (2001) 25-40.

[36] W.X. Zhang, L. Dong, H. Yan, H.J. Li, Z.W. Jiang, X.W. Kan, H. Yang, A.M. Li, R.S. Cheng, Removal of methylene blue from aqueous solutions by straw based adsorbent in a fixed-bed column, Chemical Engineering Journal 173(2) (2011) 429-436.

[37] C. Namasivayam, D. Kavitha, Removal of Congo Red from water by adsorption onto activated carbon prepared from coir pith, an agricultural solid waste, Dyes and Pigments 54(1) (2002) 47-58.

[38] W.Y. Huang, X. Yu, D. Li, Adsorption removal of Congo red over flower-like porous microspheres derived from Ni/Al layered double hydroxide, RSC Advances 5(103) (2015) 84937-84946.

[39] M.O. Gessner, R. Hinkelmann, G. Nutzmann, M. Jekel, G. Singer, J. Lewandowski, T. Nehls, M. Barjenbruch, Urban water interfaces, Journal of Hydrology 514 (2014) 226-232.

[40] Directive 2000/60/EC of the European Parliament and of the Council of 23 October 2000 establishing a framework for Community action in the field of water policy, in: E.

Commission (Ed.) L 327/1, Official Journal of the European Communities, Brussels, 2000.

[41] Council Directive of 21 May 1991 concerning urban waste water treatment, in: E. Commission (Ed.) L 135/52, Official Journal of the European Communities, Brussels, 1991.

[42] Directive 2013/39/EU of the European Parliament and of the Council of 12 August 2013 amending Directives 2000/60/EC and 2008/105/EC as regards priority substances in the field of water policy, in: E. Commission (Ed.) L 226/1, Official Journal of the European Union, Brussels, 2013.

[43] T. Shao, River in China turns red, 2011. https://edition.cnn.com/2011/12/16/world/asia/china-river-of-red/index.html. (Accessed 11/02/2018 2018).

[44] J. Yardley, Bangladesh Pollution, Told in Colors and Smells, 2013. http://www.nytimes.com/2013/07/15/world/asia/bangladesh-pollution-told-in-colors-and-smells.html. (Accessed 10/02/2018 2018).

[45] M. Clark, Handbook of Textile and Industrial Dyeing, Volume 1 - Principles, Processes and Types of Dyes, Woodhead Publishing (2011).

[46] M. Clark, Handbook of Textile and Industrial Dyeing, Volume 2 - Applications of Dyes, Woodhead Publishing (2011).

[47] R.M. Christie, Colour Chemistry (2nd Edition), Royal Society of Chemistry, 2016.

[48] R. Nayak, R. Padhye, Garment Manufacturing Technology, Elsevier, 2015.

[49] M. Tewari, The Role of Price and Cost Competitiveness in Apparel Exports, Post-MFA: A Review Indian Council for Research on International Economic Relations, 2005, pp. 1-62.

[50] P. Dicken, Global Shift: Reshaping the Global Economic Map in the 21st Century, 4th ed., Sage, London, 2003.

[51] V.K. Garg, R. Kumar, R. Gupta, Removal of malachite green dye from aqueous solution by adsorption using agro-industry waste: a case study of Prosopis cineraria, Dyes and Pigments 62(1) (2004) 1-10.

[52] D. Brown, Effect of Colorants in the Aquatic Environment, Ecotoxicology and Environmental Safety 13(2) (1987) 139-147.

[53] C. O'Neill, F.R. Hawkes, D.L. Hawkes, N.D. Lourenco, H.M. Pinheiro, W. Delee, Colour in textile effluents - sources, measurement, discharge consents and simulation: a review, Journal of Chemical Technology and Biotechnology 74(11) (1999) 1009-1018.

[54] S. Rangabhashiyam, N. Anu, N. Selvaraju, Sequestration of dye from textile industry wastewater using agricultural waste products as adsorbents, Journal of Environmental Chemical Engineering 1(4) (2013) 629-641.

[55] P. Schoeberl, A. Brik, R. Braun, W. Fuchs, Treatment and recycling of textile wastewater - case study and development of a recycling concept, Desalination 171(2) (2005) 173-183.

[56] P.C. Vandevivere, R. Bianchi, W. Verstraete, Review: Treatment and reuse of wastewater from the textile wet-processing industry: Review of emerging technologies, Journal of Chemical Technology and Biotechnology 72(4) (1998) 289-302.

[57] R.M. Christie, Environmental Aspects of Textile Dyeing, 1st Edition ed., Woodhead Publishing, 2007.

[58] M.A.M. Salleh, D.K. Mahmoud, W. Karim, A. Idris, Cationic and anionic dye adsorption by agricultural solid wastes: A comprehensive review, Desalination 280(1-3) (2011) 1-13.

[59] S.W. Oh, M.N. Kang, M.W. Cho, M.W. Lee, Detection of carcinogenic amines from dyestuffs or dyed substrates, Dyes and Pigments 33(2) (1997) 119-135.

[60] M. Ejder-Korucu, A. Gürses, Ç. Doğar, S.K. Sharma, M. Açıkyıldız, Removal of Organic Dyes from Industrial Effluents: An Overview of Physical and Biotechnological Applications, Green Chemistry for Dyes Removal from Wastewater, John Wiley & Sons, Inc.2015, pp. 1-34.

[61] F.R. Spellman, Handbook of water and wastewater treatment plant operations, Third edition. ed., CRC Press/Taylor & Francis Group, Boca Raton, 2014.

[62] A. Reife, H.S. Freeman, Environmental chemistry of dyes and pigments, Wiley, New York, 1996.

[63] G.M. Shaul, T.J. Holdsworth, C.R. Dempsey, K.A. Dostal, Fate of water soluble azo dyes in the activated sludge process, Chemosphere 22(1–2) (1991) 107-119.

[64] F.P. van der Zee, G. Lettinga, J.A. Field, Azo dye decolourisation by anaerobic granular sludge, Chemosphere 44(5) (2001) 1169-1176.

[65] T. Panswad, W. Luangdilok, Decolorization of reactive dyes with different molecular structures under different environmental conditions, Water Research 34(17) (2000) 4177-4184.

[66] P. Nigam, I.M. Banat, D. Singh, R. Marchant, Microbial process for the decolorization of textile effluent containing azo, diazo and reactive dyes, Process Biochemistry 31(5) (1996) 435-442.

[67] M.F. Coughlin, B.K. Kinkle, P.L. Bishop, Degradation of acid orange 7 in an aerobic biofilm, Chemosphere 46(1) (2002) 11-19.

[68] S. Chinwekitvanich, M. Tuntoolvest, T. Panswad, Anaerobic decolorization of reactive dyebath effluents by a two-stage UASB system with tapioca as a co-substrate, Water Research 34(8) (2000) 2223-2232.

[69] H. An, Y. Qian, X.S. Gu, W.Z. Tang, Biological treatment of dye wastewaters using an anaerobic-oxic system, Chemosphere 33(12) (1996) 2533-2542.

[70] C.X. Wang, A. Yediler, D. Lienert, Z.J. Wang, A. Kettrup, Ozonation of an azo dye CI Remazol Black 5 and toxicological assessment of its oxidation products, Chemosphere 52(7) (2003) 1225-1232.

[71] M. Koch, A. Yediler, D. Lienert, G. Insel, A. Kettrup, Ozonation of hydrolyzed azo dye reactive yellow 84 (CI), Chemosphere 46(1) (2002) 109-113.

[72] N. Azbar, T. Yonar, K. Kestioglu, Comparison of various advanced oxidation processes and chemical treatment methods for COD and color removal from a polyester and acetate fiber dyeing effluent, Chemosphere 55(1) (2004) 35-43.

[73] T. Yonar, G.K. Yonar, K. Kestioglu, N. Azbar, Decolorisation of textile effluent using homogeneous photochemical oxidation processes, Coloration Technology 121(5) (2005) 258-264.

[74] S. Meric, D. Kaptan, T. Olmez, Color and COD removal from wastewater containing Reactive Black 5 using Fenton's oxidation process, Chemosphere 54(3) (2004) 435-441.

[75] M. Muruganandham, M. Swaminathan, Photochemical oxidation of reactive azo dye with UV-H_2O_2 process, Dyes and Pigments 62(3) (2004) 269-275.

[76] C.H. Liao, S.F. Kang, F.A. Wu, Hydroxyl radical scavenging role of chloride and bicarbonate ions in the H_2O_2/UV process, Chemosphere 44(5) (2001) 1193-1200.

[77] A.R. Khataee, M.B. Kasiri, Photocatalytic degradation of organic dyes in the presence of nanostructured titanium dioxide: Influence of the chemical structure of dyes, Journal of Molecular Catalysis a-Chemical 328(1-2) (2010) 8-26.

[78] P.F. Ji, J.L. Zhang, F. Chen, M. Anpo, Study of adsorption and degradation of acid orange 7 on the surface of CeO_2 under visible light irradiation, Applied Catalysis B-Environmental 85(3-4) (2009) 148-154.

[79] S. Sakthivel, B. Neppolian, M.V. Shankar, B. Arabindoo, M. Palanichamy, V. Murugesan, Solar photocatalytic degradation of azo dye: comparison of photocatalytic efficiency of ZnO and TiO_2, Solar Energy Materials and Solar Cells 77(1) (2003) 65-82.

[80] M.A. Behnajady, N. Modirshahla, N. Daneshvar, M. Rabbani, Photocatalytic degradation of an azo dye in a tubular continuous-flow photoreactor with immobilized TiO_2 on glass plates, Chemical Engineering Journal 127(1-3) (2007) 167-176.

[81] M. Muruganandham, M. Swaminathan, Solar photocatalytic degradation of a reactive azo dye in TiO_2-suspension, Solar Energy Materials and Solar Cells 81(4) (2004) 439-457.

[82] K. Byrappa, A.K. Subramani, S. Ananda, K.M.L. Rai, R. Dinesh, M. Yoshimura, Photocatalytic degradation of rhodamine B dye using hydrothermally synthesized ZnO, Bulletin of Materials Science 29(5) (2006) 433-438.

[83] R. Comparelli, E. Fanizza, M.L. Curri, P.D. Cozzoli, G. Mascolo, A. Agostiano, UV-induced photocatalytic degradation of azo dyes by organic-capped ZnO nanocrystals immobilized onto substrates, Applied Catalysis B-Environmental 60(1-2) (2005) 1-11.

[84] E. Alventosa-DeLara, S. Barredo-Damas, E. Zuriaga-Agusti, M.I. Alcaina-Miranda, M.I. Iborra-Clar, Ultrafiltration ceramic membrane performance during the treatment of model solutions containing dye and salt, Separation and Purification Technology 129 (2014) 96-105.

[85] N. Saffaj, M. Persin, S.A. Younssi, A. Albizane, M. Bouhria, H. Loukili, H. Dach, A. Larbot, Removal of salts and dyes by low $ZnAl_2O_4$-TiO_2 ultrafiltration membrane deposited on support made from raw clay, Separation and Purification Technology 47(1-2) (2005) 36-42.

[86] Y. He, G.M. Li, H. Wang, J.F. Zhao, H.X. Su, Q.Y. Huang, Effect of operating conditions on separation performance of reactive dye solution with membrane process, Journal of Membrane Science 321(2) (2008) 183-189.

[87] T.H. Kim, C. Park, S. Kim, Water recycling from desalination and purification process of reactive dye manufacturing industry by combined membrane filtration, Journal of Cleaner Production 13(8) (2005) 779-786.

[88] J.Y. Lin, W.Y. Ye, H.M. Zeng, H. Yang, J.N. Shen, S. Darvishmanesh, P. Luis, A. Sotto, B. Van der Bruggen, Fractionation of direct dyes and salts in aqueous solution using loose nanofiltration membranes, Journal of Membrane Science 477 (2015) 183-193.

[89] D.W. Hendricks, Water treatment unit processes : physical and chemical, Taylor & Francis, Boca Raton, FL, 2005.

[90] B.H. Hameed, A.T.M. Din, A.L. Ahmad, Adsorption of methylene blue onto bamboo-based activated carbon: Kinetics and equilibrium studies, Journal of Hazardous Materials 141(3) (2007) 819-825.

[91] Y. Al-Degs, M.A.M. Khraisheh, S.J. Allen, M.N. Ahmad, G.M. Walker, Competitive adsorption of reactive dyes from solution: Equilibrium isotherm studies in single and multisolute systems, Chemical Engineering Journal 128(2-3) (2007) 163-167.

[92] Y.S. Al-Degs, M.I. El-Barghouthi, A.H. El-Sheikh, G.A. Walker, Effect of solution pH, ionic strength, and temperature on adsorption behavior of reactive dyes on activated carbon, Dyes and Pigments 77(1) (2008) 16-23.

[93] G. Newcombe, M. Drikas, Adsorption of NOM onto activated carbon: Electrostatic and non-electrostatic effects, Carbon 35(9) (1997) 1239-1250.

[94] Y.S. Al-Degs, M.A.M. Khraisheh, S.J. Allen, M.N. Ahmad, Adsorption characteristics of reactive dyes in columns of activated carbon, Journal of Hazardous Materials 165(1-3) (2009) 944-949.

[95] A.A. Ahmad, B.H. Hameed, Fixed-bed adsorption of reactive azo dye onto granular activated carbon prepared from waste, Journal of Hazardous Materials 175(1-3) (2010) 298-303.

[96] Z. Aksu, F. Gonen, Biosorption of phenol by immobilized activated sludge in a continuous packed bed: prediction of breakthrough curves, Process Biochemistry 39(5) (2004) 599-613.

[97] M. Jafari, M.R. Rahimi, M. Ghaedi, H. Javadian, A. Asfaram, Fixed-bed column performances of azure-II and auramine-O adsorption by Pinus eldarica stalks activated carbon and its composite with zno nanoparticles: Optimization by response surface methodology based on central composite design, Journal of Colloid and Interface Science 507 (2017) 172-189.

[98] R.P. Han, D.D. Ding, Y.F. Xu, W.H. Zou, Y.F. Wang, Y.F. Li, L. Zou, Use of rice husk for the adsorption of congo red from aqueous solution in column mode, Bioresource Technology 99(8) (2008) 2938-2946.

[99] R.P. Han, Y. Wang, X. Zhao, Y.F. Wang, F.L. Xie, J.M. Cheng, M.S. Tang, Adsorption of methylene blue by phoenix tree leaf powder in a fixed-bed column: experiments and prediction of breakthrough curves, Desalination 245(1-3) (2009) 284-297.

[100] D.C.K. Ko, J.F. Porter, G. McKay, Optimised correlations for the fixed-bed adsorption of metal ions on bone char, Chemical Engineering Science 55(23) (2000) 5819-5829.

[101] M. Greluk, Z. Hubicki, Efficient removal of Acid Orange 7 dye from water using the strongly basic anion exchange resin Amberlite IRA-958, Desalination 278(1-3) (2011) 219-226.

[102] L.M. Parker, N.B. Milestone, R.H. Newman, The use of Hydrotalcite as an Anion Absorbent, Industrial & Engineering Chemistry Research 34(4) (1995) 1196-1202.

[103] S.L. Xu, Z.R. Chen, B.W. Zhang, J.H. Yu, F.Z. Zhang, D.G. Evans, Facile preparation of pure CaAl-layered double hydroxides and their application as a hardening accelerator in concrete, Chemical Engineering Journal 155(3) (2009) 881-885.

[104] L. Raki, J.J. Beaudoin, L. Mitchell, Layered double hydroxide-like materials: nanocomposites for use in concrete, Cement and Concrete Research 34(9) (2004) 1717-1724.

[105] Q. Wang, J.P. Undrell, Y.S. Gao, G.P. Cai, J.C. Buffet, C.A. Wilkie, D. O'Hare, Synthesis of Flame-Retardant Polypropylene/LDH-Borate Nanocomposites, Macromolecules 46(15) (2013) 6145-6150.

[106] Y.S. Gao, J.W. Wu, Q. Wang, C.A. Wilkie, D. O'Hare, Flame retardant polymer/layered double hydroxide nanocomposites, Journal of Materials Chemistry A 2(29) (2014) 10996-11016.

[107] S.J. Kim, Y. Lee, D.K. Lee, J.W. Lee, J.K. Kang, Efficient Co-Fe layered double hydroxide photocatalysts for water oxidation under visible light, Journal of Materials Chemistry A 2(12) (2014) 4136-4139.

[108] X.Y. Han, K.G. Fang, J. Zhou, L. Zhao, Y.H. Sun, Synthesis of higher alcohols over highly dispersed Cu-Fe based catalysts derived from layered double hydroxides, Journal of Colloid and Interface Science 470 (2016) 162-171.

[109] L.A. Lv, W. Wang, M. Wei, H.J. Cheng, Bromide ion removal from contaminated water by calcined and uncalcined MgAl-CO_3 layered double hydroxides, Journal of Hazardous Materials 152(3) (2008) 1130-1137.

[110] Y. Zhang, X.L. Li, Preparation of Zn-Al CLDH to Remove Bromate from Drinking Water, Journal of Environmental Engineering 140(7) (2014) 7.

[111] M. Dadwhal, M. Sahimi, T.T. Tsotsis, Adsorption Isotherms of Arsenic on Conditioned Layered Double Hydroxides in the Presence of Various Competing Ions, Industrial & Engineering Chemistry Research 50(4) (2011) 2220-2226.

[112] Y.W. You, H.T. Zhao, G.F. Vance, Removal of arsenite from aqueous solutions by anionic clays, Environmental Technology 22(12) (2001) 1447-1457.

[113] Y. Du, N. Rees, D. O'Hare, A study of phosphate absorption by magnesium iron hydroxycarbonate, Dalton Transactions (39) (2009) 8197-8202.

[114] B. Saha, L. Griffin, H. Blunden, Adsorptive separation of phosphate oxyanion from aqueous solution using an inorganic adsorbent, Environmental Geochemistry and Health 32(4) (2010) 341-347.

[115] S. Paikaray, M.J. Hendry, J. Essilfie-Dughan, Controls on arsenate, molybdate, and selenate uptake by hydrotalcite-like layered double hydroxides, Chemical Geology 345 (2013) 130-138.

[116] R.L. Goswamee, P. Sengupta, K.G. Bhattacharyya, D.K. Dutta, Adsorption of Cr(VI) in layered double hydroxides, Applied Clay Science 13(1) (1998) 21-34.

[117] N.N. Das, J. Konar, M.K. Mohanta, S.C. Srivastava, Adsorption of Cr(VI) and Se(IV) from their aqueous solutions onto Zr^{4+}-substituted ZnAl/MgAl-layered double hydroxides: effect of Zr^{4+} substitution in the layer, Journal of Colloid and Interface Science 270(1) (2004) 1-8.

[118] S.L. Wang, R.J. Hseu, R.R. Chang, P.N. Chiang, J.H. Chen, Y.M. Tzou, Adsorption and thermal desorption of Cr(VI) on Li/Al layered double hydroxide, Colloids and Surfaces a-Physicochemical and Engineering Aspects 277(1-3) (2006) 8-14.

[119] L. Lv, J. He, M. Wei, D.G. Evans, X. Duan, Factors influencing the removal of fluoride from aqueous solution by calcined Mg-Al-CO_3 layered double hydroxides, Journal of Hazardous Materials 133(1-3) (2006) 119-128.

[120] L. Lv, J. He, M. Wei, D.G. Evans, Z.L. Zhou, Treatment of high fluoride concentration water by MgAl-CO_3 layered double hydroxides: Kinetic and equilibrium studies, Water Research 41(7) (2007) 1534-1542.

[121] S. Mandal, S. Mayadevi, Adsorption of fluoride ions by Zn-Al layered double hydroxides, Applied Clay Science 40(1-4) (2008) 54-62.

[122] J. Orthman, H.Y. Zhu, G.Q. Lu, Use of anion clay hydrotalcite to remove coloured organics from aqueous solutions, Separation and Purification Technology 31(1) (2003) 53-59.

[123] L. El Gaini, M. Lakraimi, E. Sebbar, A. Meghea, M. Bakasse, Removal of indigo carmine dye from water to Mg-Al-CO_3-calcined layered double hydroxides, Journal of Hazardous Materials 161(2-3) (2009) 627-632.

[124] G. Bascialla, A.E. Regazzoni, Immobilization of anionic dyes by intercalation into hydrotalcite, Colloids and Surfaces a-Physicochemical and Engineering Aspects 328(1-3) (2008) 34-39.

[125] R. Extremera, I. Pavlovic, M.R. Perez, C. Barriga, Removal of acid orange 10 by calcined Mg/Al layered double hydroxides from water and recovery of the adsorbed dye, Chemical Engineering Journal 213 (2012) 392-400.

[126] Z.M. Ni, S.J. Xia, L.G. Wang, F.F. Xing, G.X. Pan, Treatment of methyl orange by calcined layered double hydroxides in aqueous solution: Adsorption property and kinetic studies, Journal of Colloid and Interface Science 316(2) (2007) 284-291.

[127] L.P. Nong, C.L. Xiao, W. Jiang, Azo dye removal from aqueous solution by organic-inorganic hybrid dodecanoic acid modified layered Mg-Al hydrotalcite, Korean Journal of Chemical Engineering 28(3) (2011) 933-938.

[128] L.H. Ai, C.Y. Zhang, L.Y. Meng, Adsorption of Methyl Orange from Aqueous Solution on Hydrothermal Synthesized Mg-Al Layered Double Hydroxide, Journal of Chemical and Engineering Data 56(11) (2011) 4217-4225.

[129] F.P. de Sa, B.N. Cunha, L.M. Nunes, Effect of pH on the adsorption of Sunset Yellow FCF food dye into a layered double hydroxide (CaAl-LDH-NO_3), Chemical Engineering Journal 215 (2013) 122-127.

[130] M.X. Zhu, Y.P. Li, M. Xie, H.Z. Xin, Sorption of an anionic dye by uncalcined and calcined layered double hydroxides: a case study, Journal of Hazardous Materials 120(1-3) (2005) 163-171.

[131] R. Marangoni, M. Bouhent, C. Taviot-Gueho, F. Wypych, F. Leroux, Zn_2Al layered double hydroxides intercalated and adsorbed with anionic blue dyes: A physico-chemical characterization, Journal of Colloid and Interface Science 333(1) (2009) 120-127.

[132] Y.M. Zheng, N. Li, W.D. Zhang, Preparation of nanostructured microspheres of Zn-Mg-Al layered double hydroxides with high adsorption property, Colloids and Surfaces a-Physicochemical and Engineering Aspects 415 (2012) 195-201.

[133] D.D. Asouhidou, K.S. Triantafyllidis, N.K. Lazaridis, K.A. Matis, Adsorption of reactive dyes from aqueous solutions by layered double hydroxides, Journal of Chemical Technology and Biotechnology 87(4) (2012) 575-582.

[134] P.P. Wu, T. Wu, W.W. He, L.L. Sun, Y.J. Li, D.J. Sun, Adsorption properties of dodecylsulfate-intercalated layered double hydroxide for various dyes in water, Colloids and Surfaces a-Physicochemical and Engineering Aspects 436 (2013) 726-731.

[135] Q.L. Wu, A. Olafsen, O.B. Vistad, J. Roots, P. Norby, Delamination and restacking of a layered double hydroxide with nitrate as counter anion, Journal of Materials Chemistry 15(44) (2005) 4695-4700.

[136] Photofunctional Layered Materials, Springer International Publishing. 2015.

[137] K.V. Kumar, S. Sivanesan, Isotherm parameters for basic dyes onto activated carbon: Comparison of linear and non-linear method, Journal of Hazardous Materials 129(1-3) (2006) 147-150.

[138] C.Y. Chen, Photocatalytic Degradation of Azo Dye Reactive Orange 16 by TiO_2, Water Air and Soil Pollution 202(1-4) (2009) 335-342.

[139] X. Duan, D.G. Evans, Layered double hydroxides, Springer, Berlin ; New York, 2006.

[140] K. Abderrazek, F.S. Najoua, E. Srasra, Synthesis and characterization of Zn-Al LDH: Study of the effect of calcination on the photocatalytic activity, Applied Clay Science 119 (2016) 229-235.

[141] L.H. Zhang, Z.G. Xiong, L. Li, R. Burt, X.S. Zhao, Uptake and degradation of Orange II by zinc aluminum layered double oxides, Journal of Colloid and Interface Science 469 (2016) 224-230.

[142] M. Suarez-Quezada, G. Romero-Ortiz, V. Suarez, G. Morales-Mendoza, L. Lartundo-Rojas, E. Navarro-Ceron, F. Tzompantzi, S. Robles, R. Gomez, A. Mantilla, Photodegradation of phenol using reconstructed Ce doped Zn/Al layered double hydroxides as photocatalysts, Catalysis Today 271 (2016) 213-219.

[143] J.Y. Zhu, Z.L. Zhu, H. Zhang, H.T. Lu, Y.L. Qiu, L.Y. Zhu, S. Kuppers, Enhanced photocatalytic activity of Ce-doped Zn-Al multi-metal oxide composites derived from layered double hydroxide precursors, Journal of Colloid and Interface Science 481 (2016) 144-157.

[144] K.M. Parida, L. Mohapatra, Carbonate intercalated Zn/Fe layered double hydroxide: A novel photocatalyst for the enhanced photo degradation of azo dyes, Chemical Engineering Journal 179 (2012) 131-139.

[145] K. Parida, L. Mohapatra, Recent progress in the development of carbonate-intercalated Zn/Cr LDH as a novel photocatalyst for hydrogen evolution aimed at the utilization of solar light, Dalton Transactions 41(4) (2012) 1173-1178.

[146] N. Baliarsingh, K.M. Parida, G.C. Pradhan, Effects of Co, Ni, Cu, and Zn on Photophysical and Photocatalytic Properties of Carbonate Intercalated M-II/Cr LDHs for Enhanced Photodegradation of Methyl Orange, Industrial & Engineering Chemistry Research 53(10) (2014) 3834-3841.

[147] S.J. Xia, F.X. Liu, Z.M. Ni, W. Shi, J.L. Xue, P.P. Qian, Ti-based layered double hydroxides: Efficient photocatalysts for azo dyes degradation under visible light, Applied Catalysis B-Environmental 144 (2014) 570-579.

[148] V. Rives, Layered double hydroxides : present and future, Nova Science Publishers, Huntington, N.Y., 2001.

[149] R. Chitrakar, Y. Makita, A. Sonoda, T. Hirotsu, Fe-Al layered double hydroxides in bromate reduction: Synthesis and reactivity, Journal of Colloid and Interface Science 354(2) (2011) 798-803.

[150] R. Chitrakar, A. Sonoda, Y. Makita, T. Hirotsu, Synthesis and bromate reduction of sulfate intercalated Fe(II)-Al(III) layered double hydroxides, Separation and Purification Technology 80(3) (2011) 652-657.

[151] J. Das, B.S. Patra, N. Baliarsingh, K.M. Parida, Adsorption of phosphate by layered double hydroxides in aqueous solutions, Applied Clay Science 32(3-4) (2006) 252-260.

[152] S. Tezuka, R. Chitrakar, A. Sonoda, K. Ooi, T. Tomida, Studies on selective adsorbents for oxo-anions. Nitrate ion-exchange properties of layered double hydroxides with different metal atoms, Green Chemistry 6(2) (2004) 104-109.

[153] J. Plank, Z. Dai, P.R. Andres, Preparation and characterization of new Ca-Al-polycarboxylate layered double hydroxides, Materials Letters 60(29-30) (2006) 3614-3617.

[154] A. Tsujimura, M. Uchida, A. Okuwaki, Synthesis and sulfate ion-exchange properties of a hydrotalcite-like compound intercalated by chloride ions, Journal of Hazardous Materials 143(1-2) (2007) 582-586.

[155] V.R.L. Constantino, T.J. Pinnavaia, Basic Properties of $Mg_{1-x}^{2+}Al_x^{3+}$ Layered Double Hydroxides Intercalated by Carbonate, Hydroxide, Chloride and Sulfate Anions, Inorganic Chemistry 34(4) (1995) 883-892.

[156] M. Ogawa, H. Kaiho, Homogeneous precipitation of uniform hydrotalcite particles, Langmuir 18(11) (2002) 4240-4242.

[157] Y. Zhao, F. Li, R. Zhang, D.G. Evans, X. Duan, Preparation of layered double-hydroxide nanomaterials with a uniform crystallite size using a new method involving separate nucleation and aging steps, Chemistry of Materials 14(10) (2002) 4286-4291.

[158] G.R. Wang, D.M. Rao, K.T. Li, Y.J. Lin, UV Blocking by Mg-Zn-Al Layered Double Hydroxides for the Protection of Asphalt Road Surfaces, Industrial & Engineering Chemistry Research 53(11) (2014) 4165-4172.

[159] L. Shi, D.Q. Li, S.F. Li, J.R. Wang, D.G. Evans, X. Duan, Structure, flame retarding and smoke suppressing properties of Zn-Mg-Al-CO_3 layered double hydroxides, Chinese Science Bulletin 50(11) (2005) 1101-1104.

[160] F. Li, X.R. Jiang, D.G. Evans, X. Duan, Structure and basicity of mesoporous materials from Mg/Al/In layered double hydroxides prepared by separate nucleation and aging steps method, Journal of Porous Materials 12(1) (2005) 55-63.

[161] M.S. Yang, E. Tuckley, J.C. Buffet, D. O'Hare, Rapid, efficient phase pure synthesis of Ca_2AlNO_3 layered double hydroxide, Journal of Materials Chemistry A 4(2) (2016) 500-504.

[162] G. Hu, D. O'Hare, Unique layered double hydroxide morphologies using reverse microemulsion synthesis, Journal of the American Chemical Society 127(50) (2005) 17808-17813.

[163] G. Hu, N. Wang, D. O'Hare, J.J. Davis, Synthesis of magnesium aluminium layered double hydroxides in reverse microemulsions, Journal of Materials Chemistry 17(21) (2007) 2257-2266.

[164] Q. Wang, D. O'Hare, Large-scale synthesis of highly dispersed layered double hydroxide powders containing delaminated single layer nanosheets, Chemical Communications 49(56) (2013) 6301-6303.

[165] M.S. Yang, O. McDermott, J.C. Buffet, D. O'Hare, Synthesis and characterisation of layered double hydroxide dispersions in organic solvents, RSC Advances 4(93) (2014) 51676-51682.

[166] C.P. Chen, A. Wangriya, J.C. Buffet, D. O'Hare, Tuneable ultra high specific surface area Mg/Al-CO_3 layered double hydroxides, Dalton Transactions 44(37) (2015) 16392-16398.

[167] C.P. Chen, M.S. Yang, Q. Wang, J.C. Buffet, D. O'Hare, Synthesis and characterisation of aqueous miscible organic-layered double hydroxides, Journal of Materials Chemistry A 2(36) (2014) 15102-15110.

[168] C.P. Chen, C.F.H. Byles, J.C. Buffet, N.H. Rees, Y. Wu, D. O'Hare, Core-shell zeolite@aqueous miscible organic-layered double hydroxides, Chemical Science 7(2) (2016) 1457-1461.

[169] S. Abello, J. Perez-Ramirez, Tuning nanomaterials' characteristics by a miniaturized in-line dispersion-precipitation method: Application to hydrotalcite synthesis, Advanced Materials 18(18) (2006) 2436-2439.

[170] S. Abello, S. Mitchell, M. Santiago, G. Stoica, J. Perez-Ramirez, Perturbing the properties of layered double hydroxides by continuous coprecipitation with short residence time, Journal of Materials Chemistry 20(28) (2010) 5878-5887.

[171] J.M. Oh, S.H. Hwang, J.H. Choy, The effect of synthetic conditions on tailoring the size of hydrotalcite particles, Solid State Ionics 151(1-4) (2002) 285-291.

[172] F. Kovanda, D. Kolousek, Z. Cilova, V. Hulinsky, Crystallization of synthetic hydrotalcite under hydrothermal conditions, Applied Clay Science 28(1-4) (2005) 101-109.

[173] T. Adschiri, K. Kanazawa, K. Arai, Rapid and Continuous Hydrothermal Crystallization of Metal-Oxide Particle in Supercritical Water, Journal of the American Ceramic Society 75(4) (1992) 1019-1022.

[174] T. Adschiri, K. Kanazawa, K. Arai, Rapid and Continuous Hydrothermal Synthesis of Boehmite Particles in Subcritical and Supercritical Water, Journal of the American Ceramic Society 75(9) (1992) 2615-2618.

[175] T. Adschiri, Y. Hakuta, K. Arai, Hydrothermal synthesis of metal oxide fine particles at supercritical conditions, Industrial & Engineering Chemistry Research 39(12) (2000) 4901-4907.

[176] E. Lester, P. Blood, J. Denyer, D. Giddings, B. Azzopardi, M. Poliakoff, Reaction engineering: The supercritical water hydrothermal synthesis of nano-particles, Journal of Supercritical Fluids 37(2) (2006) 209-214.

[177] H. Zhang, D.K. Pan, K. Zou, J. He, X. Duan, A novel core-shell structured magnetic organic-inorganic nanohybrid involving drug-intercalated layered double hydroxides coated on a magnesium ferrite core for magnetically controlled drug release, Journal of Materials Chemistry 19(19) (2009) 3069-3077.

[178] H. Zhang, D.K. Pan, X. Duan, Synthesis, Characterization, and Magnetically Controlled Release Behavior of Novel Core-Shell Structural Magnetic Ibuprofen-Intercalated LDH Nanohybrids, Journal of Physical Chemistry C 113(28) (2009) 12140-12148.

[179] C.P. Chen, R. Felton, J.C. Buffet, D. O'Hare, Core-shell SiO_2@LDHs with tuneable size, composition and morphology, Chemical Communications 51(16) (2015) 3462-3465.

[180] C.P. Chen, P.H. Wang, T.T. Lim, L.H. Liu, S.M. Liu, R. Xu, A facile synthesis of monodispersed hierarchical layered double hydroxide on silica spheres for efficient removal of pharmaceuticals from water, Journal of Materials Chemistry A 1(12) (2013) 3877-3880.

[181] L. Guo, X. Zhang, Q. Chen, C. Ruan, Y. Leng, Enhanced removal performance by the core-shell zeolites/MgFe-layered double hydroxides (LDHs) for municipal wastewater treatment, Environmental Science and Pollution Research 23(7) (2016) 6749-6757.

[182] F.Y. Ning, M.F. Shao, C.L. Zhang, S.M. Xu, M. Wei, X. Duan, Co_3O_4@layered double hydroxide core/shell hierarchical nanowire arrays for enhanced supercapacitance performance, Nano Energy 7 (2014) 134-142.

[183] X. Li, Z.C. Yang, W. Qi, Y.T. Li, Y. Wu, S.X. Zhou, S.M. Huang, J. Wei, H.J. Li, P. Yao, Binder-free Co_3O_4@NiCoAl-layered double hydroxide core-shell hybrid architectural nanowire arrays with enhanced electrochemical performance, Applied Surface Science 363 (2016) 381-388.

[184] M.F. Shao, F.Y. Ning, M. Wei, D.G. Evans, X. Duan, Hierarchical Nanowire Arrays Based on ZnO Core-Layered Double Hydroxide Shell for Largely Enhanced Photoelectrochemical Water Splitting, Advanced Functional Materials 24(5) (2014) 580-586.

[185] N.T.H. Trang, H.V. Ngoc, N. Lingappan, D.J. Kang, A comparative study of supercapacitive performances of nickel cobalt layered double hydroxides coated on ZnO nanostructured arrays on textile fibre as electrodes for wearable energy storage devices, Nanoscale 6(4) (2014) 2434-2439.

[186] Q.S. Guo, Q.H. Zhang, H.Z. Wang, Z.F. Liu, Z. Zhao, Core-shell structured ZnO@Cu-Zn-Al layered double hydroxides with enhanced photocatalytic efficiency for CO_2 reduction, Catalysis Communications 77 (2016) 118-122.

[187] M. Hadnadjev-Kostic, T. Vulic, R. Marinkovic-Neducin, Solar light induced rhodamine B degradation assisted by TiO_2-Zn-Al LDH based photocatalysts, Advanced Powder Technology 25(5) (2014) 1624-1633.

[188] Y.B. Dou, S.T. Zhang, T. Pan, S.M. Xu, A.W. Zhou, M. Pu, H. Yan, J.B. Han, M. Wei, D.G. Evans, X. Duan, TiO_2@ Layered Double Hydroxide Core-Shell Nanospheres with Largely Enhanced Photocatalytic Activity Toward O_2 Generation, Advanced Functional Materials 25(15) (2015) 2243-2249.

[189] E.M. Seftel, M. Niarchos, C. Mitropoulos, M. Mertens, E.F. Vansant, P. Cool, Photocatalytic removal of phenol and methylene-blue in aqueous media using TiO_2@LDH clay nanocomposites, Catalysis Today 252 (2015) 120-127.

[190] D. Chen, Y. Li, J. Zhang, J.Z. Zhou, Y. Guo, H. Liu, Magnetic Fe_3O_4/ZnCr-layered double hydroxide composite with enhanced adsorption and photocatalytic activity, Chemical Engineering Journal 185 (2012) 120-126.

[191] R. Rusdi, A.A. Rahman, N.S. Mohamed, N. Kamarudin, N. Kamarulzaman, Preparation and band gap energies of ZnO nanotubes, nanorods and spherical nanostructures, Powder Technology 210(1) (2011) 18-22.

[192] N.M. Makwana, C.J. Tighe, R.I. Gruar, P.F. McMillan, J.A. Darr, Pilot plant scale continuous hydrothermal synthesis of nano-titania; effect of size on photocatalytic activity, Materials Science in Semiconductor Processing 42 (2016) 131-137.

[193] D.R. Modeshia, R.I. Walton, Solvothermal synthesis of perovskites and pyrochlores: crystallisation of functional oxides under mild conditions, Chemical Society Reviews 39(11) (2010) 4303-4325.

[194] P.W. Dunne, C.L. Starkey, M. Gimeno-Fabra, E.H. Lester, The rapid size- and shape-controlled continuous hydrothermal synthesis of metal sulphide nanomaterials, Nanoscale 6(4) (2014) 2406-2418.

[195] B.L. Cushing, V.L. Kolesnichenko, C.J. O'Connor, Recent advances in the liquid-phase syntheses of inorganic nanoparticles, Chemical Reviews 104(9) (2004) 3893-3946.

[196] J.H. Bang, K.S. Suslick, Applications of Ultrasound to the Synthesis of Nanostructured Materials, Advanced Materials 22(10) (2010) 1039-1059.

[197] A. Gedanken, Using sonochemistry for the fabrication of nanomaterials, Ultrasonics Sonochemistry 11(2) (2004) 47-55.

[198] A. Cabañas, J. Li, P. Blood, T. Chudoba, W. Lojkowski, M. Poliakoff, E. Lester, Synthesis of nanoparticulate yttrium aluminum garnet in supercritical water–ethanol mixtures, The Journal of Supercritical Fluids 40(2) (2007) 284-292.

[199] E. Lester, G. Aksomaityte, J. Li, S. Gomez, J. Gonzalez-Gonzalez, M. Poliakoff, Controlled continuous hydrothermal synthesis of cobalt oxide (Co_3O_4) nanoparticles, Progress in Crystal Growth and Characterization of Materials 58(1) (2012) 3-13.

[200] M. Gimeno-Fabra, P. Dunne, D. Grant, P. Gooden, E. Lester, Continuous flow synthesis of tungsten oxide (WO_3) nanoplates from tungsten (VI) ethoxide, Chemical Engineering Journal 226 (2013) 22-29.

[201] P.J. Blood, J.P. Denyer, B.J. Azzopardi, M. Poliakoff, E. Lester, A versatile flow visualisation technique for quantifying mixing in a binary system: application to continuous supercritical water hydrothermal synthesis (SWHS), Chemical Engineering Science 59(14) (2004) 2853-2861.

[202] E. Lester, P.J. Blood, J.P. Denyer, B.J. Azzopardi, J. Li, M. Poliakoff, Impact of reactor geometry on continuous hydrothermal synthesis mixing, Materials Research Innovations 14(1) (2010) 19-26.

[203] A. Cabanas, J. Li, P. Blood, T. Chudoba, W. Lojkowski, M. Poliakoff, E. Lester, Synthesis of nanoparticulate yttrium aluminum garnet in supercritical water-ethanol mixtures, Journal of Supercritical Fluids 40(2) (2007) 284-292.

[204] R.I. Gruar, C.J. Tighe, J.A. Darr, Scaling-up a Confined Jet Reactor for the Continuous Hydrothermal Manufacture of Nanomaterials, Industrial & Engineering Chemistry Research 52(15) (2013) 5270-5281.

[205] C.J. Tighe, R.Q. Cabrera, R.I. Gruar, J.A. Darr, Scale Up Production of Nanoparticles: Continuous Supercritical Water Synthesis of Ce-Zn Oxides, Industrial & Engineering Chemistry Research 52(16) (2013) 5522-5528.

[206] C.J. Denis, C.J. Tighe, R.I. Gruar, N.M. Makwana, J.A. Darr, Nucleation and Growth of Cobalt Oxide Nanoparticles in a Continuous Hydrothermal Reactor under Laminar and Turbulent Flow, Crystal Growth & Design 15(9) (2015) 4256-4265.

[207] Y. Hakuta, S. Onai, H. Terayama, T. Adschiri, K. Arai, Production of ultra-fine ceria particles by hydrothermal synthesis under supercritical conditions, Journal of Materials Science Letters 17(14) (1998) 1211-1213.

[208] A. Cabanas, J.A. Darr, E. Lester, M. Poliakoff, A continuous and clean one-step synthesis of nano-particulate $Ce_{1-x}Zr_xO_2$ solid solutions in near-critical water, Chemical Communications (11) (2000) 901-902.

[209] H. Hobbs, S. Briddon, E. Lester, The synthesis and fluorescent properties of nanoparticulate ZrO_2 doped with Eu using continuous hydrothermal synthesis, Green Chemistry 11(4) (2009) 484-491.

[210] F. Moro, S.V.Y. Tang, F. Tuna, E. Lester, Magnetic properties of cobalt oxide nanoparticles synthesised by a continuous hydrothermal method, Journal of Magnetism and Magnetic Materials 348 (2013) 1-7.

[211] Z.C. Zhang, S. Brown, J.B.M. Goodall, X.L. Weng, K. Thompson, K.N. Gong, S. Kellici, R.J.H. Clark, J.R.G. Evans, J.A. Darr, Direct continuous hydrothermal synthesis of high surface area nanosized titania, Journal of Alloys and Compounds 476(1-2) (2009) 451-456.

[212] F. Demoisson, M. Ariane, R. Piolet, F. Bernard, Original Supercritical Water Device for Continuous Production of Nanopowders, Advanced Engineering Materials 13(6) (2011) 487-493.

[213] F. Demoisson, R. Piolet, F. Bernard, Hydrothermal Synthesis of ZnO Crystals from Zn(OH)(2) Metastable Phases at Room to Supercritical Conditions, Crystal Growth & Design 14(11) (2014) 5388-5396.

[214] F. Demoisson, R. Piolet, M. Ariane, A. Leybros, F. Bernard, Influence of the pH on the ZnO nanoparticle growth in supercritical water: Experimental and simulation approaches, Journal of Supercritical Fluids 95 (2014) 75-83.

[215] F. Demoisson, R. Piolet, F. Bernard, Hydrothermal growth of ZnO nanostructures in supercritical domain: Effect of the metal salt concentration ($Zn(NO_3)_2$) in alkali medium (KOH), Journal of Supercritical Fluids 97 (2015) 268-274.

[216] M. Sondergaard, E.D. Bojesen, M. Christensen, B.B. Iversen, Size and Morphology Dependence of ZnO Nanoparticles Synthesized by a Fast Continuous Flow Hydrothermal Method, Crystal Growth & Design 11(9) (2011) 4027-4033.

[217] A. McLaren, T. Valdes-Solis, G.Q. Li, S.C. Tsang, Shape and Size Effects of ZnO Nanocrystals on Photocatalytic Activity, Journal of the American Chemical Society 131(35) (2009) 12540-12541.

[218] B.B. He, Two-dimensional X-ray diffraction, Wiley, Hoboken, N.J., 2009.

[219] R.I. Masel, Principles of adsorption and reaction on solid surfaces, Wiley, New York, 1996.

[220] R. Kohli, K.L. Mittal, Developments in Surface Contamination and Cleaning, Volume 1 - Fundamentals and Applied Aspects (2nd Edition), Elsevier, 2015.

[221] T. Oku, Structure Analysis of Advanced Nanomaterials - Nanoworld by High-Resolution Electron Microscopy, De Gruyter, 2014.

[222] H.Y. Zhu, R. Jiang, J. Yao, F.Q. Fu, J.B. Li, Novel ZnO/Zn-Cr hydrotalcite-like anionic clay as a high-performance and recyclable material for efficient photocatalytic removal of organic dye under simulated solar irradiation, Research on Chemical Intermediates 42(5) (2016) 4359-4372.

[223] T. Numai, Fundamentals of Semiconductor Lasers, Fundamentals of Semiconductor Lasers, 2nd Edition 93 (2015) 89-186.

[224] R. López, R. Gómez, Band-gap energy estimation from diffuse reflectance measurements on sol–gel and commercial TiO_2: a comparative study, Journal of Sol-Gel Science and Technology 61(1) (2012) 1-7.

[225] Y.W. Guo, Z.L. Zhu, Y.L. Qiu, J.F. Zhao, Enhanced adsorption of acid brown 14 dye on calcined Mg/Fe layered double hydroxide with memory effect, Chemical Engineering Journal 219 (2013) 69-77.

[226] H. Abdolmohammad-Zadeh, E. Ghorbani, Z. Talleb, Zinc-aluminum layered double hydroxide as a nano-sorbent for removal of Reactive Yellow 84 dye from textile wastewater effluents, Journal of the Iranian Chemical Society 10(6) (2013) 1103-1112.

[227] A. Guzman-Vargas, E. Lima, G.A. Uriostegui-Ortega, M.A. Oliver-Tolentino, E.E. Rodriguez, Adsorption and subsequent partial photodegradation of methyl violet 2B on Cu/Al layered double hydroxides, Applied Surface Science 363 (2016) 372-380.

[228] F.B.D. Saiah, B.L. Su, N. Bettahar, Removal of Evans Blue by using Nickel-Iron Layered Double Hydroxide (LDH) Nanoparticles: Effect of Hydrothermal Treatment Temperature on Textural Properties and Dye Adsorption, Macromolecular Symposia 273 (2008) 125-134.

[229] A. Sari, M. Tuzen, Kinetic and equilibrium studies of biosorption of Pb(II) and Cd(II) from aqueous solution by macrofungus (Amanita rubescens) biomass, Journal of Hazardous Materials 164(2-3) (2009) 1004-1011.

[230] M. Dogan, M. Alkan, Adsorption kinetics of methyl violet onto perlite, Chemosphere 50(4) (2003) 517-528.

[231] R.H. Perry, D.W. Green, Perry's chemical engineers' handbook, 8th ed., McGraw-Hill, New York, 2008.

[232] Q.Q. Zhou, F.F. Chen, W. Wu, R. Bu, W. Li, F. Yang, Reactive orange 5 removal from aqueous solution using hydroxyl ammonium ionic liquids/layered double hydroxides intercalation composites, Chemical Engineering Journal 285 (2016) 198-206.

[233] C. Zhang, S.G. Yang, H.Z. Chen, H. He, C. Sun, Adsorption behavior and mechanism of reactive brilliant red X-3B in aqueous solution over three kinds of hydrotalcite-like LDHs, Applied Surface Science 301 (2014) 329-337.

[234] P.S. Ghosal, A.K. Gupta, An insight into thermodynamics of adsorptive removal of fluoride by calcined Ca-Al-(NO3) layered double hydroxide, RSC Advances 5(128) (2015) 105889-105900.

[235] Y. Liu, Is the Free Energy Change of Adsorption Correctly Calculated?, Journal of Chemical & Engineering Data 54(7) (2009) 1981-1985.

[236] W.X. Zhang, H. Yan, H.J. Li, Z.W. Jiang, L. Dong, X.W. Kan, H. Yang, A.M. Li, R.S. Cheng, Removal of dyes from aqueous solutions by straw based adsorbents: Batch and column studies, Chemical Engineering Journal 168(3) (2011) 1120-1127.

[237] H.C. Thomas, Heterogeneous ion exchange in a flowing system, Journal of the American Chemical Society 66 (1944) 1664-1666.

[238] G.S. Bohart, E.Q. Adams, Some aspects of the behavior of charcoal with respect to chlorine, Journal of the American Chemical Society 42 (1920) 523-544.

[239] M.C. de Hoces, G.B. Garcia, A.R. Galvez, M.A. Martin-Lara, Effect of the Acid Treatment of Olive Stone on the Biosorption of Lead in a Packed-Bed Column, Industrial & Engineering Chemistry Research 49(24) (2010) 12587-12595.

[240] Y.H. Yoon, J.H. Nelson, Application of Gas-Adsorption Kinetics .1. A Theoretical - Model for Respirator Cartridge Service Life, American Industrial Hygiene Association Journal 45(8) (1984) 509-516.

[241] Y.H. Yoon, J.H. Nelson, Application of Gas-Adsorption Kinetics .2. A Theoretical - Model for Respirator Cartridge Service Life and its Practical Applications, American Industrial Hygiene Association Journal 45(8) (1984) 517-524.

[242] E.W. Lemmon, M.O. McLinden, D.G. Friend, "Thermophysical Properties of Fluid Systems" in NIST Chemistry WebBook, NIST Standard Reference Database Number 69, in: P.J. Linstrom, W.G. Mallard (Eds.) National Institute of Standards and Technology, Gaithersburg MD.

[243] S.G. Khristov, Collision theory and statistical theory of chemical reactions, Springer-Verlag, Berlin ; New York, 1980.

[244] G. Renaudin, M. Francois, The lamellar double-hydroxide (LDH) compound with composition $3CaO{\cdot}Al_2O_3{\cdot}Ca(NO_3)_2{\cdot}10H_2O$, Acta Crystallographica Section C-Crystal Structure Communications 55 (1999) 835-838.

[245] R. Rojas, Copper, lead and cadmium removal by Ca Al layered double hydroxides, Applied Clay Science 87 (2014) 254-259.

[246] J.T. Kloprogge, L. Hickey, R.L. Frost, The effects of synthesis pH and hydrothermal treatment on the formation of zinc aluminum hydrotalcites, Journal of Solid State Chemistry 177(11) (2004) 4047-4057.

[247] E.M. Seftel, E. Popovici, M. Mertens, K. Witte, G. Tendeloo, P. Cool, E.F. Vansant, Zn-Al layered double hydroxides: Synthesis, characterization and photocatalytic application, Microporous and Mesoporous Materials 113(1-3) (2008) 296-304.

[248] M. Thommes, K. Kaneko, A.V. Neimark, J.P. Olivier, F. Rodriguez-Reinoso, J. Rouquerol, K.S.W. Sing, Physisorption of gases, with special reference to the evaluation of surface area and pore size distribution (IUPAC Technical Report), Pure and Applied Chemistry 87(9-10) (2015) 1051-1069.

[249] M. Maugey, W. Neri, C. Zakri, A. Derre, A. Nnicaud, L. Noe, M. Chorro, P. Launois, M. Monthioux, P. Poulin, Substantial improvement of nanotube processability by freeze-drying, Journal of Nanoscience and Nanotechnology 7(8) (2007) 2633-2639.

[250] Y.J. Li, B.Y. Gao, T. Wu, W.S. Chen, X. Li, B.A. Wang, Adsorption kinetics for removal of thiocyanate from aqueous solution by calcined hydrotalcite, Colloids and Surfaces a-Physicochemical and Engineering Aspects 325(1-2) (2008) 38-43.

[251] L. Yang, M. Dadwhal, Z. Shahrivari, M. Ostwal, P.K.T. Liu, M. Sahimi, T.T. Tsotsis, Adsorption of arsenic on layered double hydroxides: Effect of the particle size, Industrial & Engineering Chemistry Research 45(13) (2006) 4742-4751.

[252] R. Chitrakar, S. Tezuka, A. Sonoda, K. Sakane, K. Ooi, T. Hirotsu, Adsorption of phosphate from seawater on calcined MgMn-layered double hydroxides, Journal of Colloid and Interface Science 290(1) (2005) 45-51.

[253] M. Chetia, R.L. Goswamee, S. Banerjee, S. Chatterjee, L. Singh, R.B. Srivastava, H.P. Sarma, Arsenic removal from water using calcined Mg-Al layered double hydroxide, Clean Technologies and Environmental Policy 14(1) (2012) 21-27.

[254] H. Morioka, Y. Shimizu, M. Sukenobu, K. Ito, E. Tanabe, T. Shishido, K. Takehira, Partial oxidation of methane to synthesis gas over supported Ni catalysts prepared from Ni-Ca/Al-layered double hydroxide, Applied Catalysis a-General 215(1-2) (2001) 11-19.

[255] C. Rodriguez-Navarro, E. Ruiz-Agudo, A. Luque, A.B. Rodriguez-Navarro, M. Ortega-Huertas, Thermal decomposition of calcite: Mechanisms of formation and textural evolution of CaO nanocrystals, American Mineralogist 94(4) (2009) 578-593.

[256] M.R. Perez, I. Crespo, M.A. Ulibarri, C. Barriga, V. Rives, J.M. Fernandez, Influence of divalent metal on the decomposition products of hydrotalcite-like ternary systems M-II-Al-Cr (M-II = Zn, Cd), Materials Chemistry and Physics 132(2-3) (2012) 375-386.

[257] K. Yang, L.G. Yan, Y.M. Yang, S.J. Yu, R.R. Shan, H.Q. Yu, B.C. Zhu, B. Du, Adsorptive removal of phosphate by Mg-Al and Zn-Al layered double hydroxides: Kinetics, isotherms and mechanisms, Separation and Purification Technology 124 (2014) 36-42.

[258] X. Cheng, X.R. Huang, X.Z. Wang, D.Z. Sun, Influence of calcination on the adsorptive removal of phosphate by Zn-Al layered double hydroxides from excess sludge liquor, Journal of Hazardous Materials 177(1-3) (2010) 516-523.

[259] J.B. Zhou, S.L. Yang, J.G. Yu, Z. Shu, Novel hollow microspheres of hierarchical zinc-aluminum layered double hydroxides and their enhanced adsorption capacity for phosphate in water, Journal of Hazardous Materials 192(3) (2011) 1114-1121.

[260] Z.P. Xu, S.K. Saha, P.S. Braterman, N. D'Souza, The effect of Zn, Al layered double hydroxide on thermal decomposition of poly(vinyl chloride), Polymer Degradation and Stability 91(12) (2006) 3237-3244.

[261] W. Ma, N.N. Zhao, G. Yang, L.Y. Tian, R. Wang, Removal of fluoride ions from aqueous solution by the calcination product of Mg-Al-Fe hydrotalcite-like compound, Desalination 268(1-3) (2011) 20-26.

[262] H.F. Zhang, D.F. Liu, Y. Yao, B.Q. Zhang, Y.S. Lin, Stability of ZIF-8 membranes and crystalline powders in water at room temperature, Journal of Membrane Science 485 (2015) 103-111.

[263] L. Yang, Z. Shahrivari, P.K.T. Liu, M. Sahimi, T.T. Tsotsis, Removal of trace levels of arsenic and selenium from aqueous solutions by calcined and uncalcined layered double hydroxides (LDH), Industrial & Engineering Chemistry Research 44(17) (2005) 6804-6815.

[264] P. Koilraj, S. Kannan, Aqueous fluoride removal using ZnCr layered double hydroxides and their polymeric composites: Batch and column studies, Chemical Engineering Journal 234 (2013) 406-415.

[265] D.L. Zhao, G.D. Sheng, J. Hu, C.L. Chen, X.K. Wang, The adsorption of Pb(II) on Mg_2Al layered double hydroxide, Chemical Engineering Journal 171(1) (2011) 167-174.

[266] Y.S. Ho, G. McKay, Pseudo-second order model for sorption processes, Process Biochemistry 34(5) (1999) 451-465.

[267] J.F. Corbett, Pseudo first-order kinetics, Journal of Chemical Education 49(10) (1972) 663.

[268] C.S. Lei, M. Pi, P.Y. Kuang, Y.Q. Guo, F.G. Zhang, Organic dye removal from aqueous solutions by hierarchical calcined Ni-Fe layered double hydroxide: Isotherm, kinetic and mechanism studies, Journal of Colloid and Interface Science 496 (2017) 158-166.

[269] H.A. Hamid, Y. Jenidi, W. Thielemans, C. Somerfield, R.L. Gomes, Predicting the capability of carboxylated cellulose nanowhiskers for the remediation of copper from water using response surface methodology (RSM) and artificial neural network (ANN) models, Industrial Crops and Products 93 (2016) 108-120.

[270] F. Marrakchi, M.J. Ahmed, W.A. Khanday, M. Asif, B.H. Hameed, Mesoporous carbonaceous material from fish scales as low-cost adsorbent for reactive orange 16 adsorption, Journal of the Taiwan Institute of Chemical Engineers 71 (2017) 47-54.

[271] F. Marrakchi, W.A. Khanday, M. Asif, B.H. Hameed, Cross-linked chitosan/sepiolite composite for the adsorption of methylene blue and reactive orange 16, International Journal of Biological Macromolecules 93 (2016) 1231-1239.

[272] J.C. Huang, C.Y. Kuo, C.H. Wu, Y.H. Lin, Adsorption of CI Reactive Red 2 by ZnAl-layered double hydroxides: kinetics, equilibrium, and thermodynamics, Desalination and Water Treatment 70 (2017) 372-379.

[273] D.M. Lewis, Dyes, Reactive, Kirk-Othmer Encyclopedia of Chemical Technology, John Wiley & Sons, 2004.

[274] P. Pengthamkeerati, T. Satapanajaru, O. Singchan, Sorption of reactive dye from aqueous solution on biomass fly ash, Journal of Hazardous Materials 153(3) (2008) 1149-1156.

[275] M.S. Tanyildizi, Modeling of adsorption isotherms and kinetics of reactive dye from aqueous solution by peanut hull, Chemical Engineering Journal 168(3) (2011) 1234-1240.

[276] R. Patel, S. Suresh, Kinetic and equilibrium studies on the biosorption of reactive black 5 dye by Aspergillus foetidus, Bioresource Technology 99(1) (2008) 51-58.

[277] K. Vijayaraghavan, Y.S. Yun, Biosorption of C.I. Reactive Black 5 from aqueous solution using acid-treated biomass of brown seaweed Laminaria sp, Dyes and Pigments 76(3) (2008) 726-732.

[278] Z. Aksu, S. Tezer, Biosorption of reactive dyes on the green alga Chlorella vulgaris, Process Biochemistry 40(3-4) (2005) 1347-1361.

[279] O. Ozdemir, B. Armagan, M. Turan, M.S. Celik, Comparison of the adsorption characteristics of azo-reactive dyes on mezoporous minerals, Dyes and Pigments 62(1) (2004) 49-60.

[280] Z. Eren, F.N. Acar, Adsorption of Reactive Black 5 from an aqueous solution: equilibrium and kinetic studies, Desalination 194(1-3) (2006) 1-10.

[281] E. Guibal, E. Touraud, J. Roussy, Chitosan interactions with metal ions and dyes: Dissolved-state vs. solid-state application, World Journal of Microbiology & Biotechnology 21(6-7) (2005) 913-920.

[282] C.P. Chen, P. Gunawan, R. Xu, Self-assembled Fe_3O_4-layered double hydroxide colloidal nanohybrids with excellent performance for treatment of organic dyes in water, Journal of Materials Chemistry 21(4) (2011) 1218-1225.

[283] M.F. Shao, F.Y. Ning, J.W. Zhao, M. Wei, D.G. Evans, X. Duan, Preparation of Fe_3O_4@SiO_2@Layered Double Hydroxide Core-Shell Microspheres for Magnetic Separation of Proteins, Journal of the American Chemical Society 134(2) (2012) 1071-1077.

[284] S. Tang, G.H. Chia, H.K. Lee, Magnetic core-shell iron(II,III) oxide@layered double oxide microspheres for removal of 2,5-dihydroxybenzoic acid from aqueous solutions, Journal of Colloid and Interface Science 437 (2015) 316-323.

[285] I. Clark, P.W. Dunne, R.L. Gomes, E. Lester, Continuous hydrothermal synthesis of Ca_2Al-NO_3 layered double hydroxides: The impact of reactor temperature, pressure and NaOH concentration on crystal characteristics, Journal of Colloid and Interface Science 504 (2017) 492-499.

[286] B. Cheng, E.T. Samulski, Hydrothermal synthesis of one-dimensional ZnO nanostructures with different aspect ratios, Chemical Communications (8) (2004) 986-987.

[287] K.M. Lee, C.W. Lai, K.S. Ngai, J.C. Juan, Recent developments of zinc oxide based photocatalyst in water treatment technology: A review, Water Research 88 (2016) 428-448.

[288] R. Marsalek, Particle Size and Zeta Potential of ZnO, APCBEE Procedia 9 (2014) 13-17.

[289] A. de Roy, C. Forano, K.E. Malki, J.-P. Besse, Anionic Clays: Trends in Pillaring Chemistry, in: M.L. Occelli, H.E. Robson (Eds.), Expanded Clays and Other Microporous Solids, Springer US, Boston, MA, 1992, pp. 108-169.

[290] D.A. Armbruster, T. Pry, Limit of Blank, Limit of Detection and Limit of Quantitation, The Clinical Biochemist Reviews 29(Suppl 1) (2008) S49-S52.

Appendix

UV-Vis Limit of Detection and Calibration Curves

Limit of detection (LoD) and Limit of quantitation (LoQ) for the UV-Vis spectrophotometer were analysed by the testing of blank samples. Twenty blank samples were analysed at λ=338nm. The mean and standard deviation were taken from the absorbance readings. The LoD was then taken as a multiple of three times the standard deviation from the blank samples and the LoQ as an order of magnitude higher than the standard deviation [290]. For the analysis of RO16 at λ=338nm, the LoD was taken as 0.001 while the LoQ was taken as 0.005.

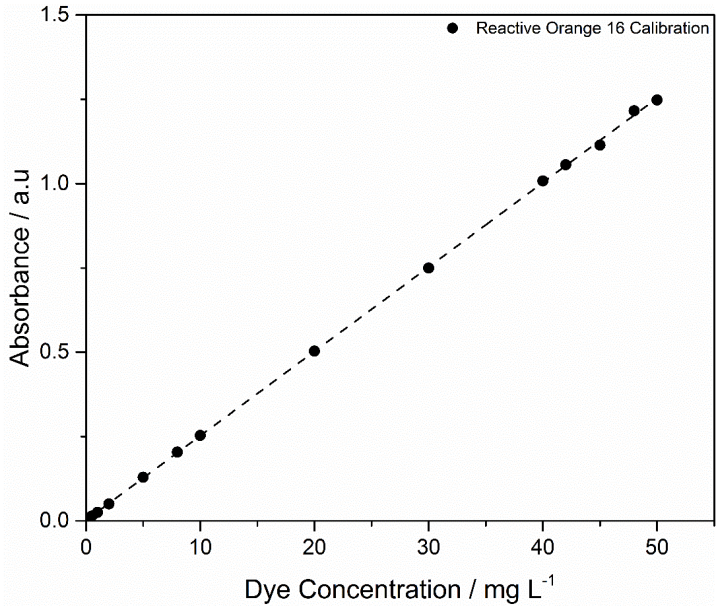


Figure A. 1 Calibration curve for Reactive Orange 16

Calibration curves were generated using the Reactive Orange 16 dye powder. On an accurate balance (10μg), the mass of RO16 dye required for 1000mg L^{-1} was carefully weighed, accounting for the mass of sodium content in the dye molecule and the 70% dye content in the powder. The solution was made to 1L and dilutions from this stock

solution were taken to generate a calibration curve within a linear range of 0.1mg L^{-1} to 50mg L^{-1}.

Table A. 1 Calibration absorbance data for RO16

Dye Concentration mg L-1	Absorbance 1	Absorbance 2	Absorbance 3	Average
50	1.248	1.247	1.248	1.248
48	1.216	1.214	1.217	1.216
45	1.114	1.113	1.114	1.114
42	1.056	1.056	1.056	1.056
40	1.008	1.009	1.008	1.008
30	0.751	0.749	0.75	0.75
20	0.503	0.503	0.502	0.503
10	0.253	0.254	0.253	0.253
8	0.204	0.205	0.204	0.204
5	0.129	0.128	0.127	0.129
2	0.051	0.049	0.051	0.05
1	0.025	0.026	0.024	0.025
0.5	0.014	0.014	0.014	0.014
0.2	0.006	0.006	0.006	0.006
0.1	0.005	0.005	0.005	0.005

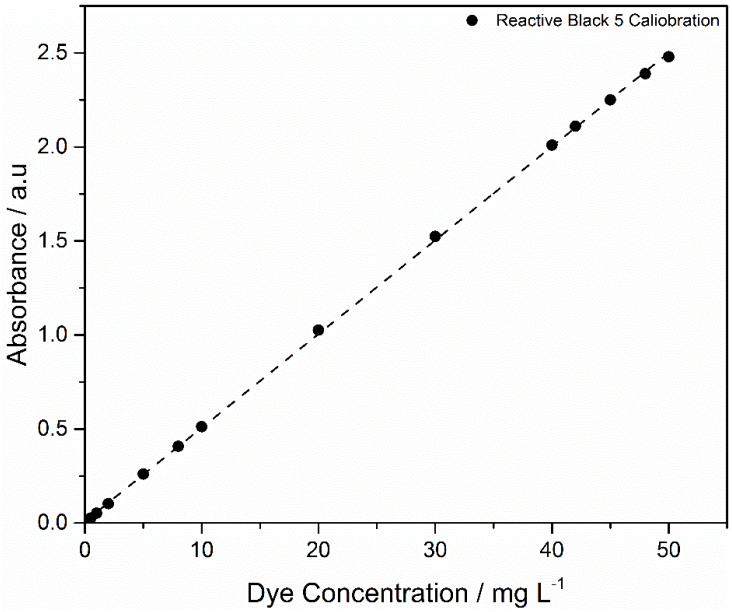


Figure A. 2 Calibration curve for Reactive Black 5

Calibration curves were generated using the Reactive Black 5 dye powder. On the same accurate balance (10µg) as was used for RO16 calibration, the mass of RB5 dye required for 1000mg L^{-1} was carefully weighed, accounting for the mass of sodium content in the dye molecule and the 50% dye content in the powder.

Table A. 2 Calibration absorbance data RB5

Dye Concentration mg L^{-1}	Absorbance 1	Absorbance 2	Absorbance 3	Average
50	2.481	2.48	2.478	2.480
48	2.400	2.400	2.380	2.390
45	2.249	2.25	2.25	2.250
42	2.109	2.111	2.109	2.110
40	2.012	2.011	2.009	2.010
30	1.524	1.522	1.525	1.524
20	1.027	1.026	1.026	1.026
10	0.512	0.513	0.511	0.512
8	0.408	0.408	0.407	0.408
5	0.261	0.26	0.26	0.26
2	0.103	0.102	0.103	0.103
1	0.052	0.052	0.052	0.052
0.5	0.026	0.025	0.026	0.026
0.2	0.011	0.012	0.011	0.011
0.1	0.006	0.006	0.006	0.006